NASA CONTRACTOR REPORT

NASA CR-521

NASA CR-521

AN EXPERIMENTAL INVESTIGATION OF THE FLOW FIELDS ABOUT DELTA AND DOUBLE-DELTA WINGS AT LOW SPEEDS

by William H. Wentz, Jr., and Michael C. McMahon

Prepared by

WICHITA STATE UNIVERSITY

Wichita, Kans.

for

NATIONAL AERONAUTICS AND SPACE ADMINISTRATION • WASHINGTON, D. C. • AUGUST 1966

NASA CR-521

AN EXPERIMENTAL INVESTIGATION OF THE FLOW FIELDS ABOUT DELTA AND DOUBLE-DELTA WINGS AT LOW SPEEDS

By William H. Wentz, Jr., and Michael C. McMahon

Prepared under Grant No. NGR 17-003-003 by
WICHITA STATE UNIVERSITY
Wichita, Kans.

for

NATIONAL AERONAUTICS AND SPACE ADMINISTRATION

For sale by the Clearinghouse for Federal Scientific and Technical Information
Springfield, Virginia 22151 – Price $4.00

SUMMARY

A low-speed wind tunnel investigation was conducted to determine the flow fields about delta and double-delta wings. Semi-span models consisting of a 62° sweep delta wing-body and a 75°/62° double-delta wing-body were tested at a Reynolds number per foot of 1.0×10^6. Detailed surveys of the three-dimensional velocity fields above the wings are presented. In addition, three-component force data, pressure distributions, surface tuft patterns and oil streak patterns are presented and discussed. It is concluded that the principal effect of the strake on the double-delta configuration is to increase the vortex strength over the wing, resulting in an increase in normal force developed for a given angle of attack.

SYMBOLS

a	wing semi-span at any chordwise station x
A	aspect ratio, $\frac{(\text{span})^2}{(\text{wing area})}$
b	wing maximum semi-span
c	wing chord
$\bar{c}$	wing mean geometric chord, $\frac{\int_0^b c^2\, dy}{\int_0^b c\, dy}$
C_L	lift coefficient, $\frac{L}{qS}$
C_D	drag coefficient, $\frac{D}{qS}$
C_M	pitching moment coefficient, $\frac{M}{qS\bar{c}}$
D	drag force
L	lift force
M	pitching moment
p	pressure
q	dynamic pressure, $\frac{1}{2}\ \rho V_\infty^2$
S	wing area
V	velocity
x	coordinate in chordwise direction
y	coordinate in spanwise direction
z	coordinate perpendicular to wing chord plane
α	angle of attack

Subscripts

∞	free stream conditions
62	pertaining to 62° delta wing
i	induced

Introduction

The advent of supersonic aircraft has dictated the use of thin, sharp-edged, highly-swept wings. These wings, however, suffer from two low-speed problems which limit landing and takeoff speeds: maximum lift-drag ratio occurs at a low value of lift coefficient resulting in speedwise instability when flying at low speeds, and a forward movement of the neutral point reduces pitching stability.

The theory for the lift developed by highly-swept delta wings at low speeds was first developed by Jones (ref. 6) for small angles of attack, and later extended by Brown and Michael (ref. 2) and Mangler and Smith (ref. 1) to include the non-linear effects of assumed leading edge vortex systems. Most delta wings at high angles develop less lift than predicted by these latter methods. Only in rather special cases (such as ref. 7) have the theoretical lifts been achieved. While the primary and secondary vortex systems associated with delta wings at low speeds have been observed qualitatively, little quantitative data exist for these flow fields.

The recent supersonic commercial transport airplane competition has brought about great interest in delta wings with an increased sweep angle along the inboard portion, i.e., double-delta wings (see ref. 4). The interactions of inboard and outboard panel vortex systems are not included in either of the lifting theories mentioned above. The purpose of the present investigation was to obtain quantitative flow field information for a delta wing at high-angle low-speed conditions,

and to determine the effects of adding a high sweep strake to the wing (making a double-delta configuration).

WIND TUNNEL MODELS AND INSTRUMENTATION

MODELS

Two half-models consisting of wing and fuselage were tested (figs. 1a, 1b): a 62° delta configuration and a 75°/62° double-delta. The basic delta has a 62° leading edge sweep and is cropped slightly. The wing sections are biconvex with 2.5% maximum thickness to chord. This gives sharp leading and trailing edges with included angles of only 6°. The wing has no camber or twist.

The second wing is a double-delta wing derived from the basic wing by the addition of a symmetric 75° sweep leading edge strake which fairs into the basic delta thickness contour at the 50% root chord location. (Both model configurations utilize the same aft panel.)

The wing panels are constructed of aluminum. The 62° delta is fitted with 64 static pressure taps on one surface and the 75°/62° double delta has 71 taps. The fuselage is a simple body of revolution constructed of mahogany. The wings mount 1/4 diameter below the fuselage centerline. No fillets were used at the wing-fuselage junctures. Because of the symmetry of the wings, both upper and lower surface pressure distributions were obtained from the same static pressure holes by a repositioning of the wings relative to the fuselages.

Both semi-span models were installed adjacent to a 10- by 10-ft. reflection plane which was mounted three inches above the tunnel floor in order to minimize the reflection plane

boundary layer adjacent to the model. Preliminary wind tunnel tests using a rude semi-span model were conducted early in the program to ascertain that the reflection plane boundary layer would not significantly interact with the wing flow field at lift coefficients of the order of unity. During these investigations reflection plane surface tufts and oil streaks were observed to determine whether the low pressure field of the wind would induce any significant flow from the reflection plane boundary layer onto the wing upper surface.

A clearance gap between the fuselage and the reflection plane was maintained at 0.05 inch to prevent interference under loaded conditions. During initial exploratory investigations, gaps up to 0.25 inch were determined to have negligible influence on force measurements.

INSTRUMENTATION

At the outset it was recognized that one of the principal problems in an investigation of this sort would be to develop velocity instrumentation capable of measuring accurately the highly deviated flow field. After some preliminary calibrations, a rather small combination pitot-yaw probe was selected. The probe is a 1/8 inch diameter tube with a truncated conic shaped tip. The tip has five pressure ports; a center total and four statics located at 90° intervals around the total. The probe stem is fitted with a small drive motor which permits remote rotation $\pm$ 180° in the sidewash direction. The entire apparatus was calibrated for upwash angles of $\pm$ 45°. In operation the

probe was rotated to null the Δp sensed by the sidewash holes. Probe sidewash angle as well as upwash Δp and p_{total} were then recorded. From these data and the calibration information, the three-dimensional direction and magnitude of the unknown velocity were obtained.

The velocity probe was mounted on a stand parallel with the wing surface (figs. 3a through 3d). The stand permitted manual positioning of the probe in a plane parallel to the wing chord plane (x, y plane). A linear actuator permitted remote traversing perpendicular to the wing (z-direction) for distances up to about 15 inches. (See figure 2 for coordinate system.) The five velocity probe pressures were read by electrical transducers and printed directly onto IBM cards. The experimental values were then reduced using the IBM 1620 computer. Overall accuracies are estimated to be $\pm$ 2° for upwash and sidewash angles and $\pm$ 2% for velocity.

TESTS AND CORRECTIONS

Experimental tests were conducted in the Wichita State University 7- by 10-ft. wind tunnel, a low speed, closed circuit tunnel. All tests were conducted at a dynamic pressure of 40 psf which corresponds to a Reynolds number per foot of 1.0×10^6. Lift, drag and pitching moment data were obtained from both models in 2° increments from -10° to +40° angle of attack, using the tunnel main balance system. Since this information is utilized in conjunction with measured pressure and flow field data, jet boundary corrections were not applied to the bulk of the force data. The following correction was

applied to the data indicated in figs. 19a and 19b, which compare measured normal force coefficients with theory:

$$\Delta\alpha_i = 0.756\ C_L \text{ (degrees)}$$

The blockage correction was negligible. The method of comparing measured induced drag with theory (figs. 20a and 20b) obviates the need to apply boundary corrections.

Static pressure distributions were obtained for upper and lower surfaces of both wings from -10° to +40° in 5° increments. Upper surface tuft and oil streak photos were obtained at the same angles.

Flow field upper surface velocity distributions were obtained at 5°, 10° and 20° angles of attack using the velocity probe. The 5° and 10° angles were selected to bracket the strake vortex "rollup" observed on the double-delta wing in early oil streak and tuft photos. (See page 12 for a discussion of this phenomena.) The 20° angle was selected as being near a lift coefficient of unity, which represents somewhat near the present upper limit of useful C_L for wings of this type. A probe image was constructed and an image calibration was obtained to correct the indicated upwash angles at positions very close to the wing. This correction amounts to -4.2° at zero gap and is less than -0.5° for z-distances greater than 0.4 inches.

DISCUSSION OF FLOW FIELD DATA

The flow fields about slender sharp-edged delta wings are characterized by three more or less distinct types of flow discussed by Winter in 1936 (ref. 3):

1. At very small angles, unseparated flow with Prandtl type lift.

2. At intermediate angles, leading edge separation with vortices washing over the upper surface creating additional lift.

3. At high angles, separated wake type flow.

In flow of type 2 it has been observed by many investigators that a secondary separation occurs along a line outboard of the vortex, due to the adverse pressure gradient imposed on the cross-flow boundary layer. It is flow of type 2 that is of primary interest in the present investigations.

FLOW FIELD CHARACTERISTICS - DELTA WING

The data for the basic delta wing are all in substantial agreement with the patterns discussed above.

Pressure Distributions (figs. 4a through 4i)

Pressure data at angles of attack from 5° to 20° show a sharp ridge of negative pressure in close proximity to the leading edge. In the range from 10° to 20° the effects of secondary separation are apparent and the growth of the separated region is seen. At 25° the wing appears to be entirely separated and from 25° to 40° the upper surface suction actually decreases. The maximum lift coefficient occurs at 30°.

Comparisons of the measured pressure distributions with the theories of refs. 1 and 2 are shown in figs. 6a and 6b. The effects of the secondary separation in reducing nose suction and moving the leading edge vortex inboard are obvious. A displacement of the lifting vortex from the wing surface near the trailing edge is evidenced by the reduced suction developed over the aft stations.

Streaks and Surface Tufts (figs. 7a through 7g, 9a through 9i)

Streak photos show that the secondary separation line moves inboard with increasing angle of attack. Surface tufts clearly mark the position of the lifting vortex and secondary separation. At 20° angle of attack, evidence of separation near the trailing edge appears. At 25° the separation has progressed considerably, and at 30° the flow appears completely separated.

Flow Field Maps (figs. 11a through 11u, 13a through 13i)

The upper surface flow field velocity maps for 5° angle of attack show the presence of a vortex sheet or elliptical core of vorticity extending over roughly the outer third of the wing semi-span. At 10° and 20° angles the circulation components of velocity have become progressively stronger and the patterns are nearly circular. Centers of rotation move upward and inboard as angle of attack is increased. The reversed rotation vortex usually attributed to secondary separation is visible only in the extreme aft position at 20° angle of attack. Figures 13a through 13i are presented to illustrate the flow in planes below the vortex, near the

plane of the vortex, and above the vortex.

Forces and Moments (figs. 16a through 16c, 19a, 20a)

Conventional lift, drag, and moment coefficient data are presented. Measured normal force coefficients are compared with the theories of refs. 1 and 2, on fig. 19a. For these comparisons, the theoretical normal force coefficients were calculated assuming that the area aft of the wing tip crop point develops no normal force. As seen, the normal force developed increases in a greater than linear fashion with angle of attack, but is substantially less than the value predicted by either theory. The rather sharp stall observed in these tests is not characteristic of delta wings. It is believed to be due to some boundary effect, possibly a reflection plane boundary layer interaction (see page 6). Since the stall occurs at angles well beyond the region of primary interest, (α up to 20°) no attempt was made to isolate the cause.

The induced drag data show good agreement with calculated $C_{D_i} = C_L \tan \alpha$, (fig. 20a) illustrating that the resultant force developed by a wing with leading edge separation is essentially a normal force.

The moment data exhibit a non-linear increase in pitching moment with lift coefficient (pitch-up), for lift coefficients above 0.3. Since this is considerably below $C_{L_{max}}$, the pitch-up represents the practical limit on C_L (or minimum flying speed) for wings of this type.

FLOW FIELD CHARACTERISTICS - DOUBLE-DELTA WING

Flow fields of the double-delta wing are characterized

by the presence of two leading edge vortex systems. At 5° angle of attack the two systems appear to be more or less independent. Between 5° and 10° the two systems interact, and for angles of 10° and greater, the flow appears to be characterized by a single primary vortex which forms along the strake leading edge and deflects outboard at the leading edge breakpoint. The result is a stronger circulation over the aft panel than would otherwise be present, and a corresponding increase in normal force.

Pressure Distributions (figs. 5a through 5i)

The upper surface pressure at 5° angle of attack shows two distinct negative pressure ridges, indicating the presence of two vortex cores. At 10° and 20° a single ridge is evident, which bends distinctly at the leading edge break. This ridge peaks at the wing apex and again near the leading edge break. At 20° angle of attack a valley of reduced suction appears near the trailing edge and at 25° this valley has progressed forward to nearly the leading edge break point. At 30° and higher angles, the pressure ridge is much flatter than at lower angles, and the aft panel peak has disappeared.

Streaks and Surface Tufts (figs. 8a through 8h, 10a through 10i)

Streak and surface photos at 5° indicate clearly the presence of the two separate vortex systems. At 10°, only one vortex is evident over the aft panel. A streak photo at 7° indicates that the rollup of strake and aft panel vortex systems is progressing forward from the trailing edge.

At 20° and 25° angles of attack the streak photos exhibit a double separation line in the vicinity of the trailing edge (figs. 8e and 8f). The wedge-shaped area between these double lines coincides with the position of the reduced suction valley mentioned above (figs. 5e and 5f). The tufts in this wedge region are distinctly oscillating (fig. 10f), whereas tufts in other areas outboard of the secondary separation line are steady and oriented essentially parallel to the leading edge. It appears that propagation of this wedge forward as angle of attack is increased results in a transformation from vortex type flow to wake type flow.

Flow Field Maps (figs. 12a through 12aa, 14a through 14i, 15)

Flow field maps at 5° angle of attack exhibit the vortex sheet character observed with the delta wing. In addition, however, a vortex emanating from the strake appears as a separate circular pattern over the aft panel. At 10° and 20° angles only one vortex center appears, indicating that rollup has occurred. The upward and inboard movement of the vortex centers and increased circulation with increasing angle of attack are clearly indicated. Fig. 15 includes some lower surface flow field measurements which show greatly reduced sidewash components.

Forces and Moments (figs. 17a through 17l, 19b, 20b)

These data show generally the same trends evident with the delta wing. The remarks made on page 11 concerning the stall characteristics and induced drag are applicable here as well. In this case pitch-up occurs at a C_L of about 0.4.

COMPARISON OF DOUBLE-DELTA AND DELTA WINGS (figs. 18a through 18c)

In order to compare directly the forces and moments developed by the two wings, the following parameters are used:

$$\text{lift:} \quad \frac{C_L}{A} = \frac{L}{q\ (\text{span})^2}$$

$$\text{drag:} \quad \frac{C_D}{A} = \frac{D}{q\ (\text{span})^2}$$

$$\text{pitching moment:} \quad \frac{C_M}{A}\left[\frac{\bar{c}}{\bar{c}_{62}}\right] = \frac{M}{q\ (\text{span})^2\ \bar{c}_{62}}$$

The data in this form show that the delta and double-delta develop the same lift up to an angle of attack of about 5°. The strake vortex observed at 5° (discussed above) apparently contributes a negligible amount of lift. Close examination of the flow field velocity maps shows that the strength of the strake vortex is quite small. Beyond 5° the double-delta wing develops greater lift.

The drag data show that the delta and double-delta wings have the same drag for a given lift up to a C_L/A of about 0.45. Beyond this point the delta wing develops less drag for a given lift than the double-delta wing. The lower drag for the double-delta wing is due to the lower angle required for a given lift, since C_{D_i}/A is essentially equal to $(C_L/A) \tan \alpha$, as discussed previously (page 11).

The moment data are compared in fig. 18c. For this

comparison the moment data of the double-delta wing have been referred to a position which gives it the same stability as the delta wing at zero lift. On this basis, the pitch characteristics of the two wings are identical for values of C_L/A less than 0.5. The pitch-up tendency for both wings begins at a C_L/A of about 0.25. Above C_L/A of 0.5, the double-delta pitches up at a greater rate, indicating the effects of the strake lift.

An interesting feature of the flow fields is the comparison of the positions of the vortex centers (as nearly as they can be defined by observations of the velocity maps). These comparisons (for example figs. 11u and 12aa) show no really significant changes of vortex position due to the addition of the strake. Correlation of pressure and streak information in figs. 21a through 22c shows that the secondary separation is consistently located just outboard of the minimum pressure ridge, as would be anticipated from boundary layer theory.

A secondary vortex with reversed sense of rotation has been observed by numerous investigators (for example ref. 5). The secondary vortex is clearly shown in the velocity map of fig. 11u, for the delta wing, but was not observed on the double-delta wing. This vortex may have been present in other cases, but if so, it was too small in magnitude to be observed.

CONCLUSIONS

1. Delta wing flow fields measured in the present investigation deviate significantly from idealized mathematical models because secondary separation causes discrepancies in vortex locations, and grossly affects pressure distributions.

2. The resultant forces developed by both wings are essentially normal forces, in accordance with theory.

3. Normal forces developed by both wings are significantly less than predicted by existing theories.

4. At moderate to high angles of attack the double-delta wing strake vortex rolls up with the aft panel vortex, with a resultant increase in circulation and normal force developed over the aft panel.

5. Vortex core positions and secondary separation are not grossly affected by the addition of the strake. The principal influence is to increase the strength of the circulation.

REFERENCES

1. Mangler, K. W. and Smith, J. H. B.: A Theory of Slender Wings with Leading Edge Separation, Proc. Royal Soc., London Series A, Vol. 251, 1959, p. 200.

2. Brown, Clinton E. and Michael, W. H., Jr.: On Slender Wings with Leading Edge Separation. NACA TN 3430, April, 1955.

3. Winter, H.: Flow Phenomena on Plates and Airfoils of Short Span. NACA TM 798, July, 1936.

4. Heppe, R. R. and Hong, J.: The Double-Delta Supersonic Transport. AIAA Paper No. 64-602, August, 1964.

5. Bergesen, A. J. and Porter, J. D.: An Investigation of the Flow Around Slender Delta Wings with Leading Edge Separation. ONR Report No. 510, Princeton Univ. Press, May, 1960.

6. Jones, R. T.: Properties of Low-Aspect Ratio Pointed Wings at Speeds Below and Above the Speed of Sound. NACA Report 834, 1946.

7. Alexander, A. J.: Experiments on a Delta Wing Using Leading Edge Blowing to Remove the Secondary Separation. College of Aeronautics, Cranfield, Report No. 161, May 1963.

LIST OF FIGURES

WING SECTION:

$\bar{C}$ = 40.25 inches
Aspect Ratio 1.80
Symmetric Circular Arc
Maximum Thickness .025 Chord
Wing Area 6.60 sq ft (semi-span)

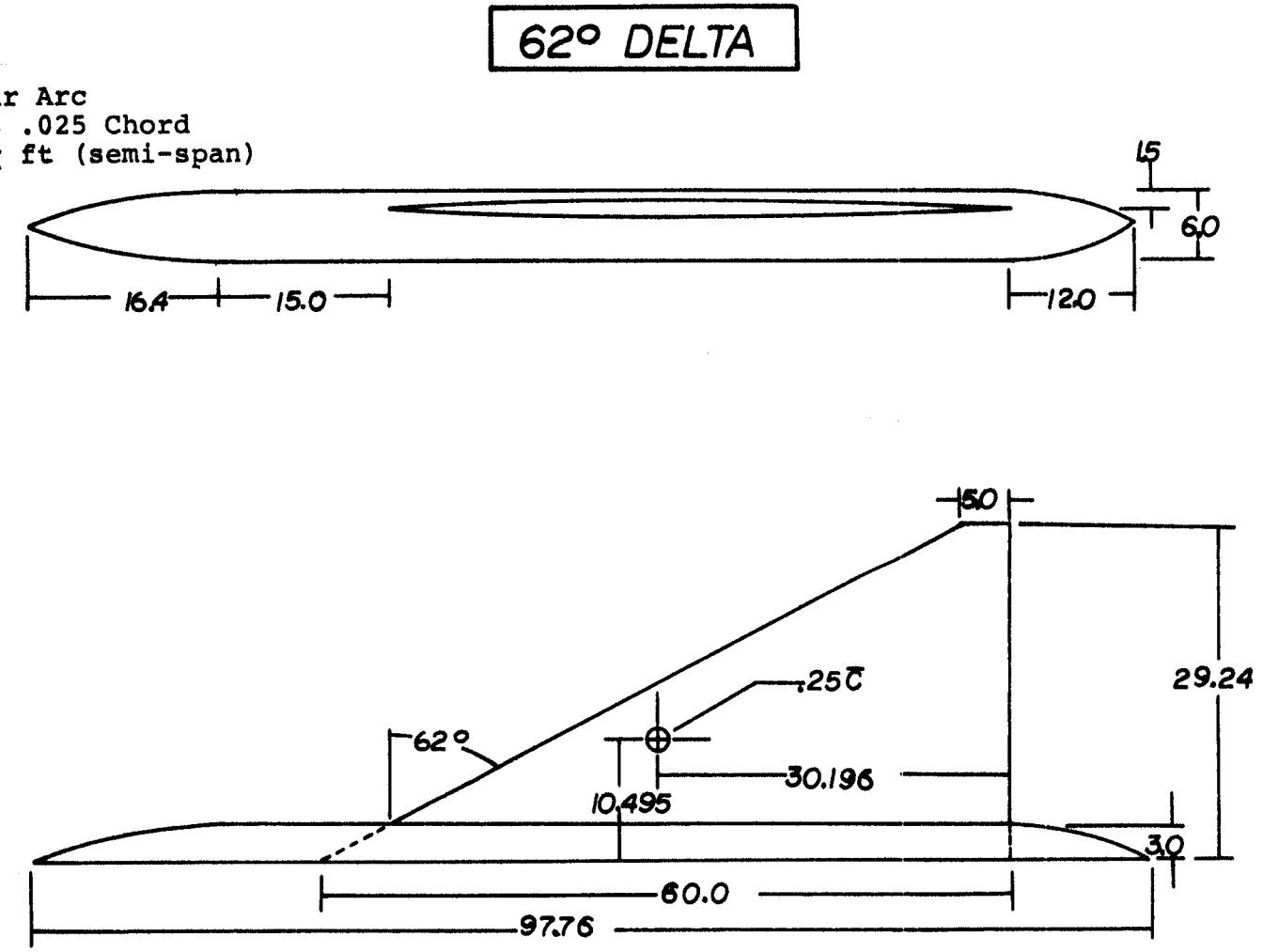

Figure 1a.- 62° delta configuration.

75°/62° DOUBLE-DELTA

$\bar{C}$ = 48.75 inches
Aspect Ratio 1.61
Wing Area 7.39 sq ft (semi-span)

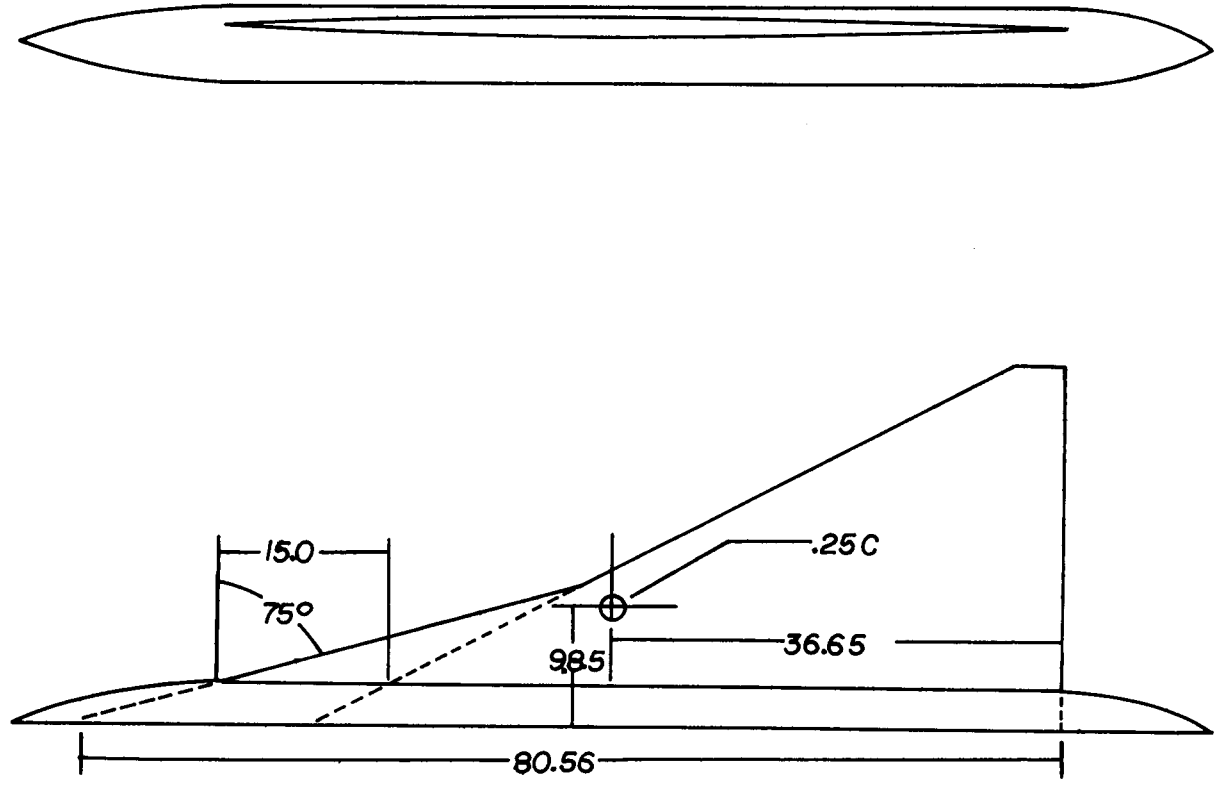

Figure 1b.- 75°/62° double-delta configuration.

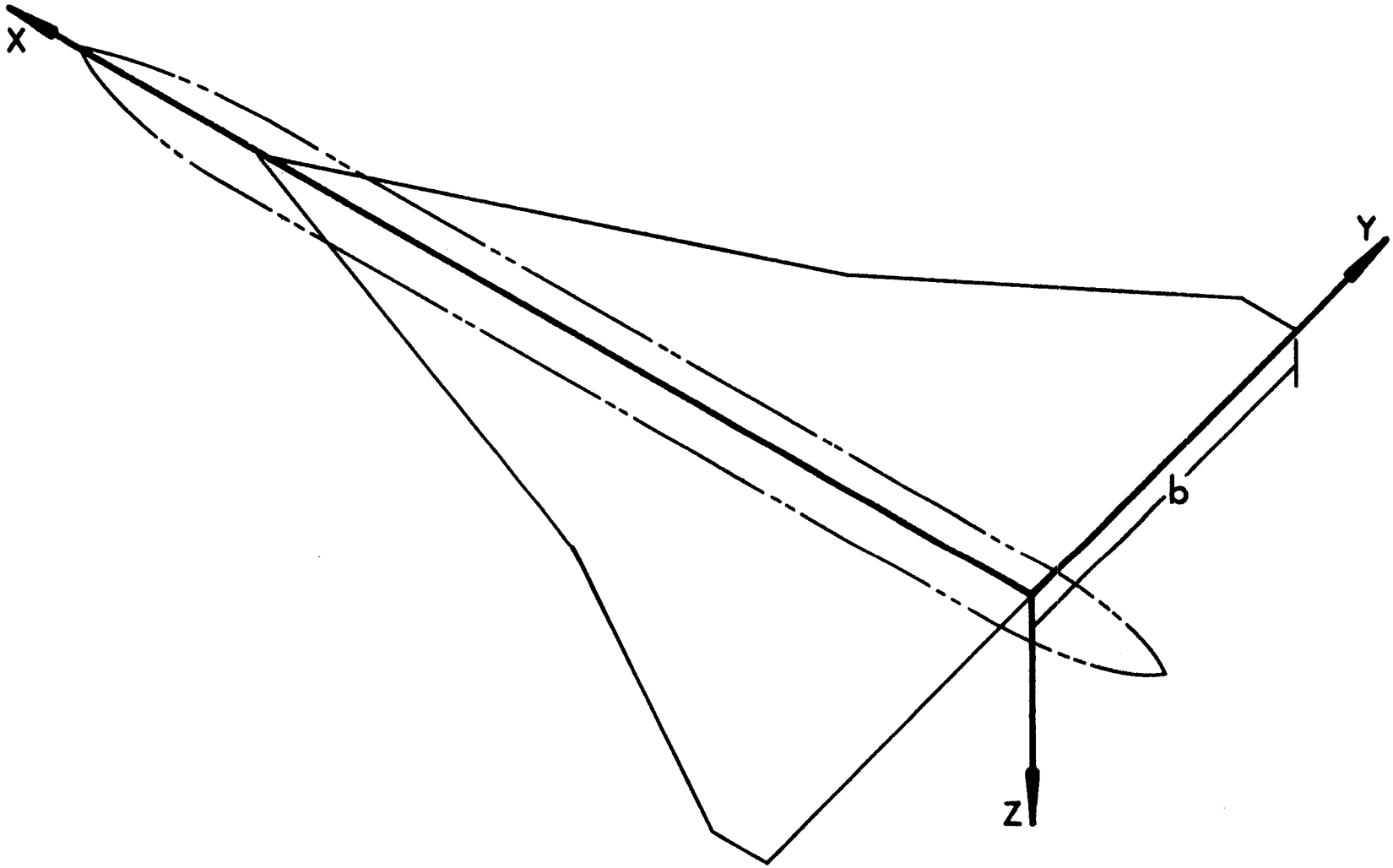

Figure 2.- Coordinate system.

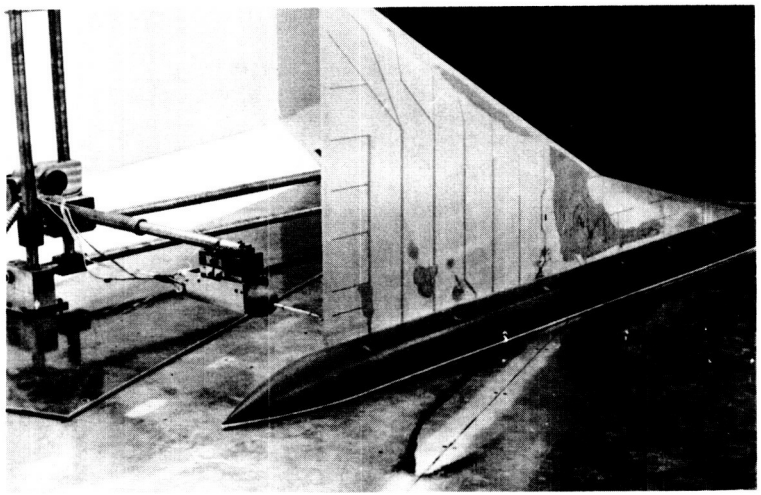

Figure 3a.

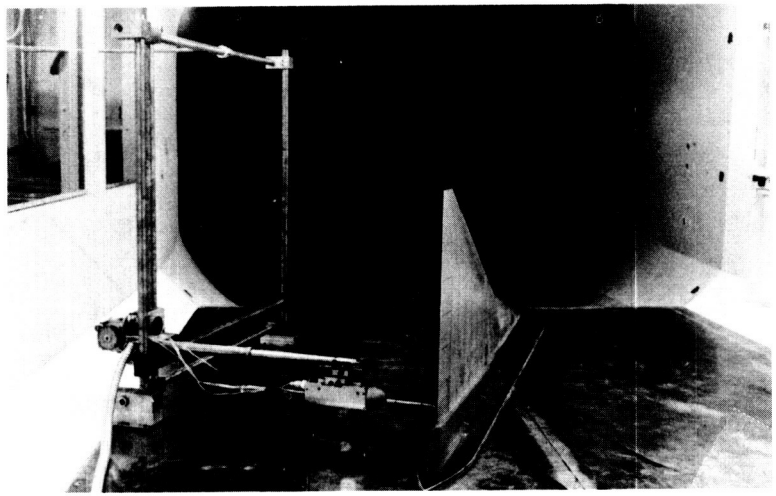

Figure 3b.

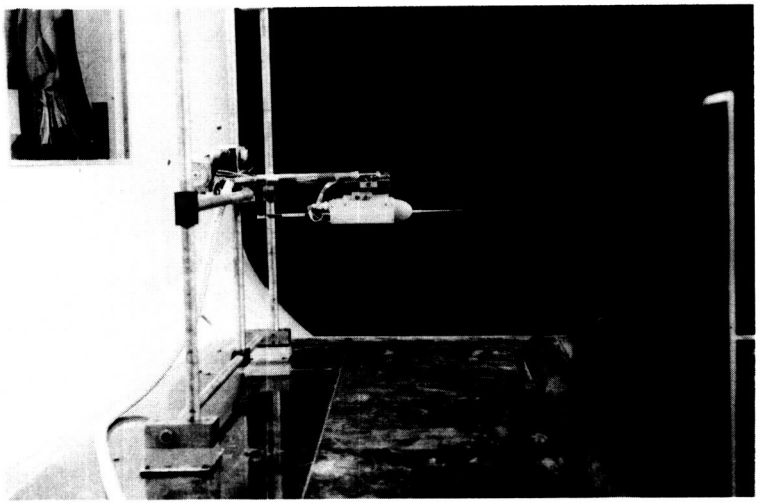

Figure 3c.

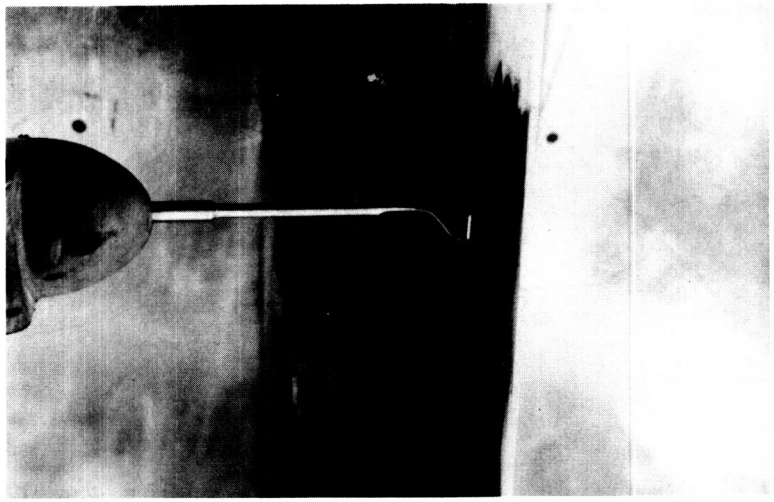

Figure 3d.

Figures 3a, 3b, 3c, 3d.- Configuration photos.

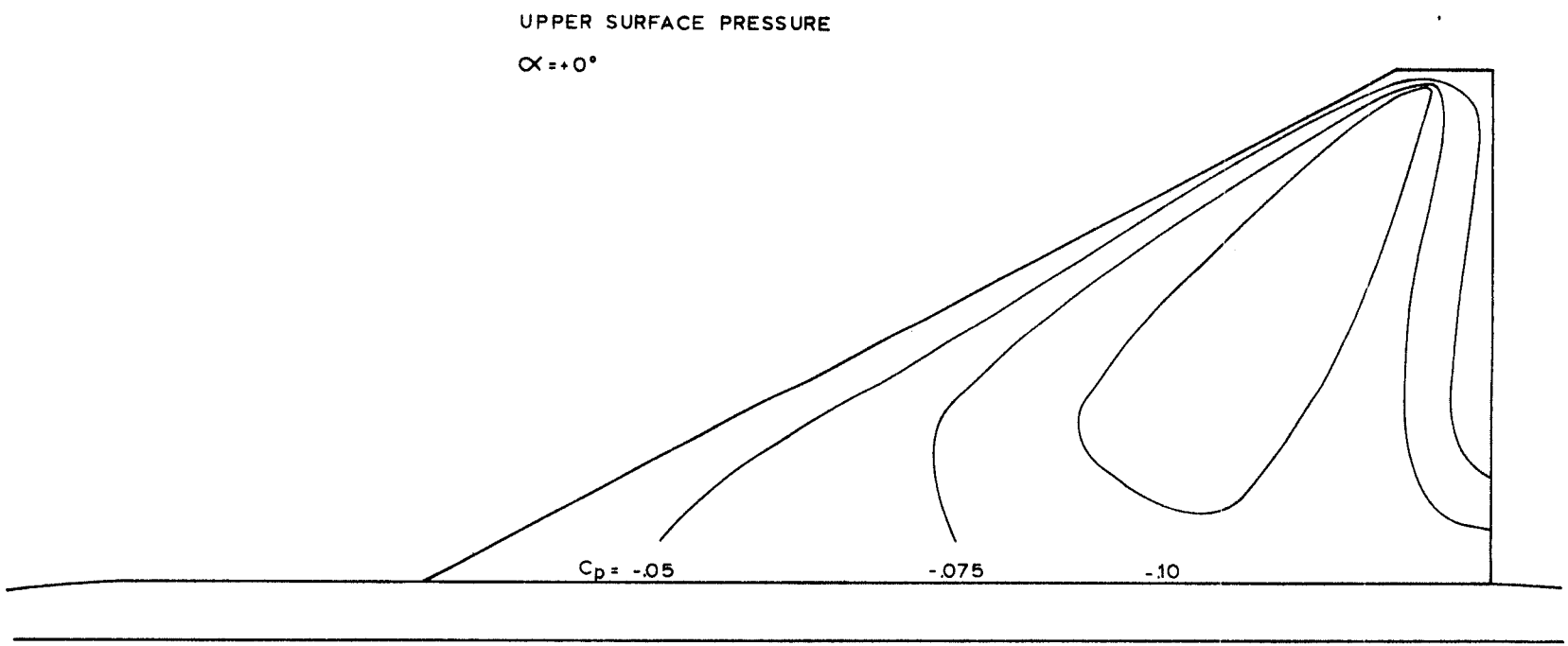

Figure 4a.- Pressure distribution. $\alpha = +0^{\circ}$.

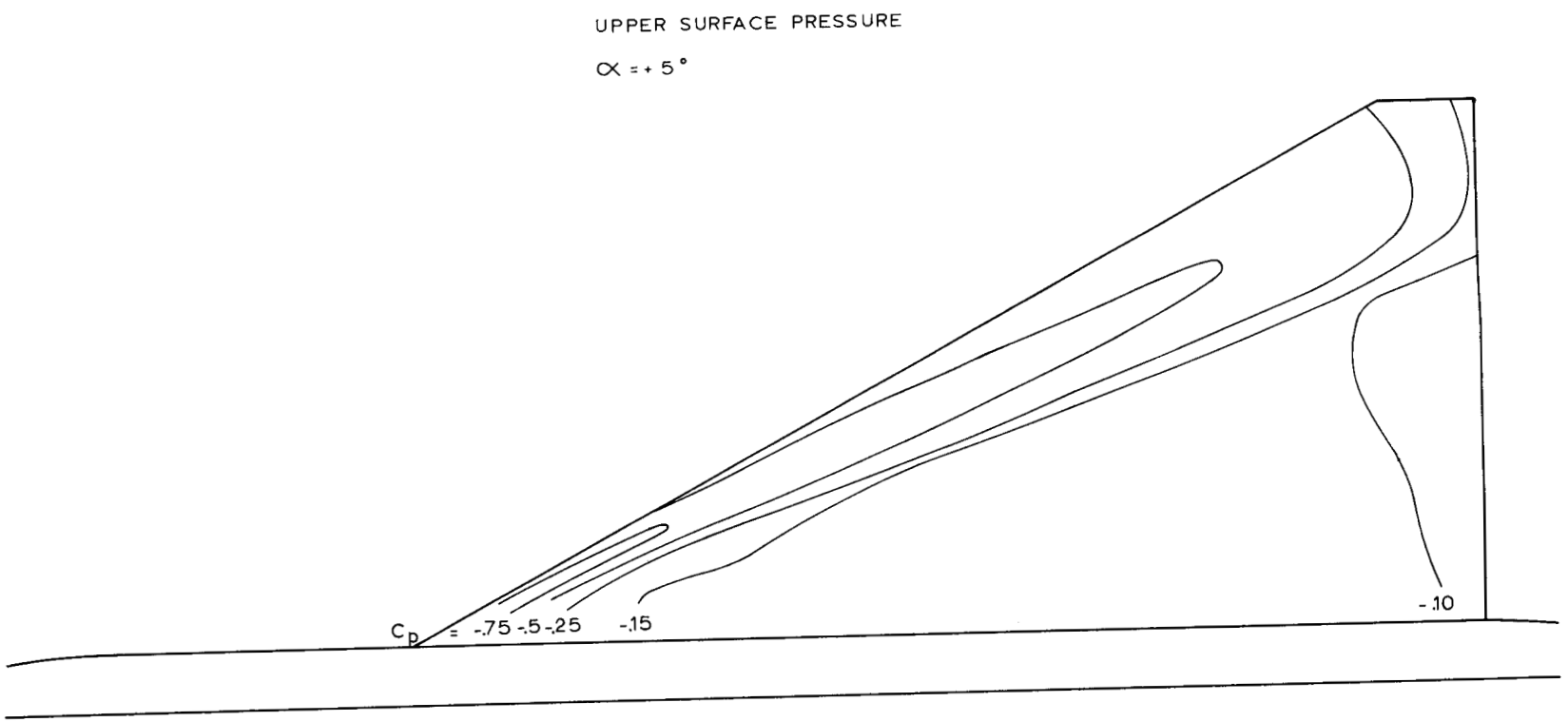

Figure 4b.- Pressure distribution. $\alpha = +5^{o}$.

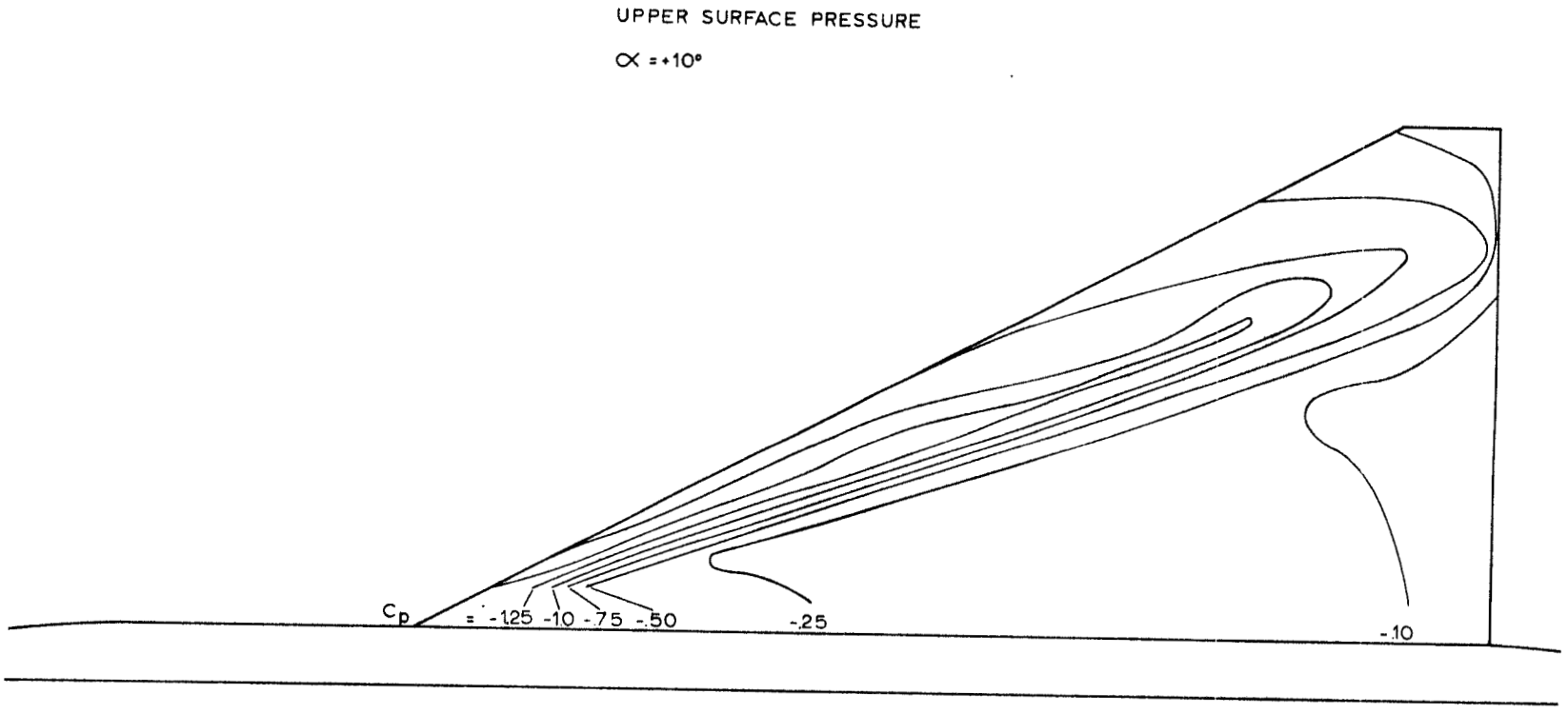

Figure 4c.- Pressure distribution. $\alpha = +10^{\circ}$.

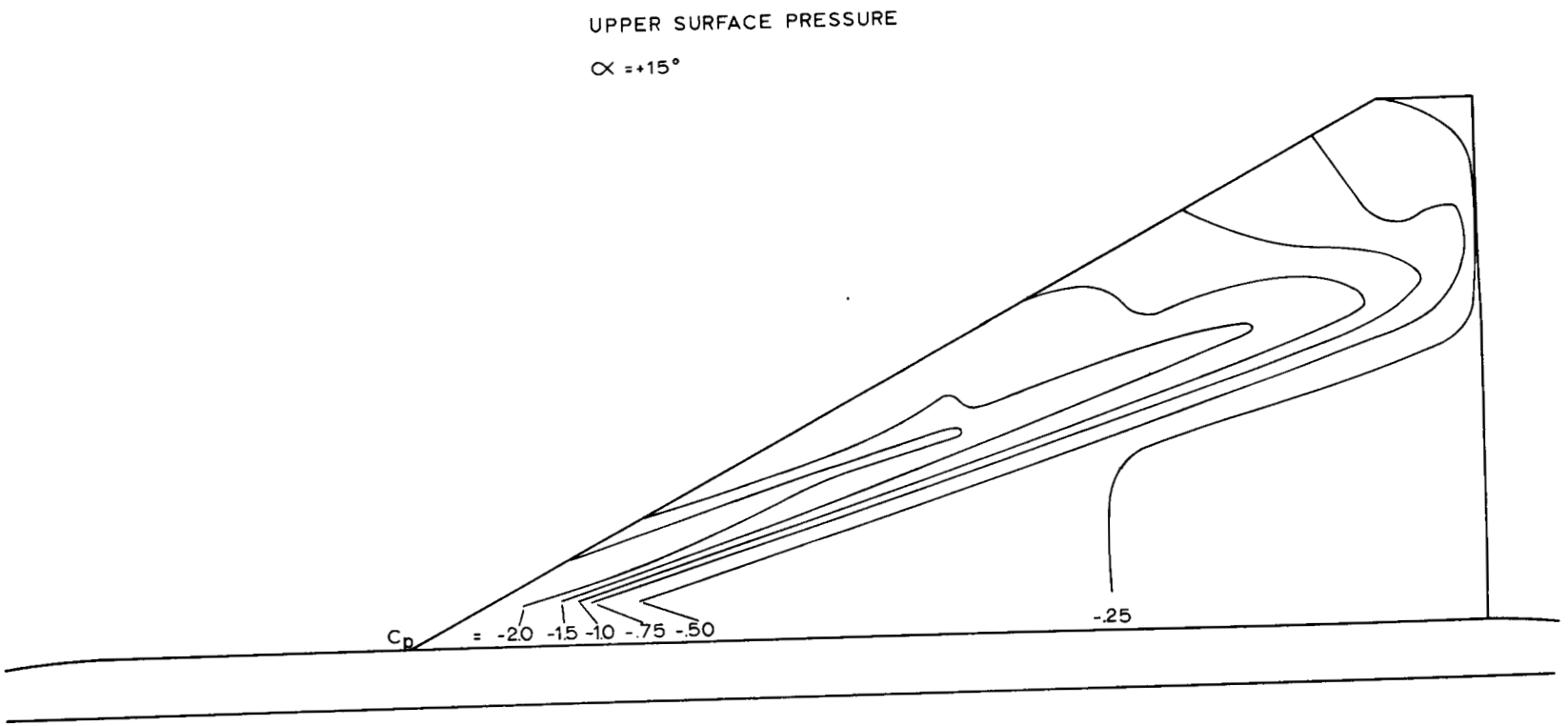

Figure 4d.- Pressure distribution. $\alpha = +15^{o}$.

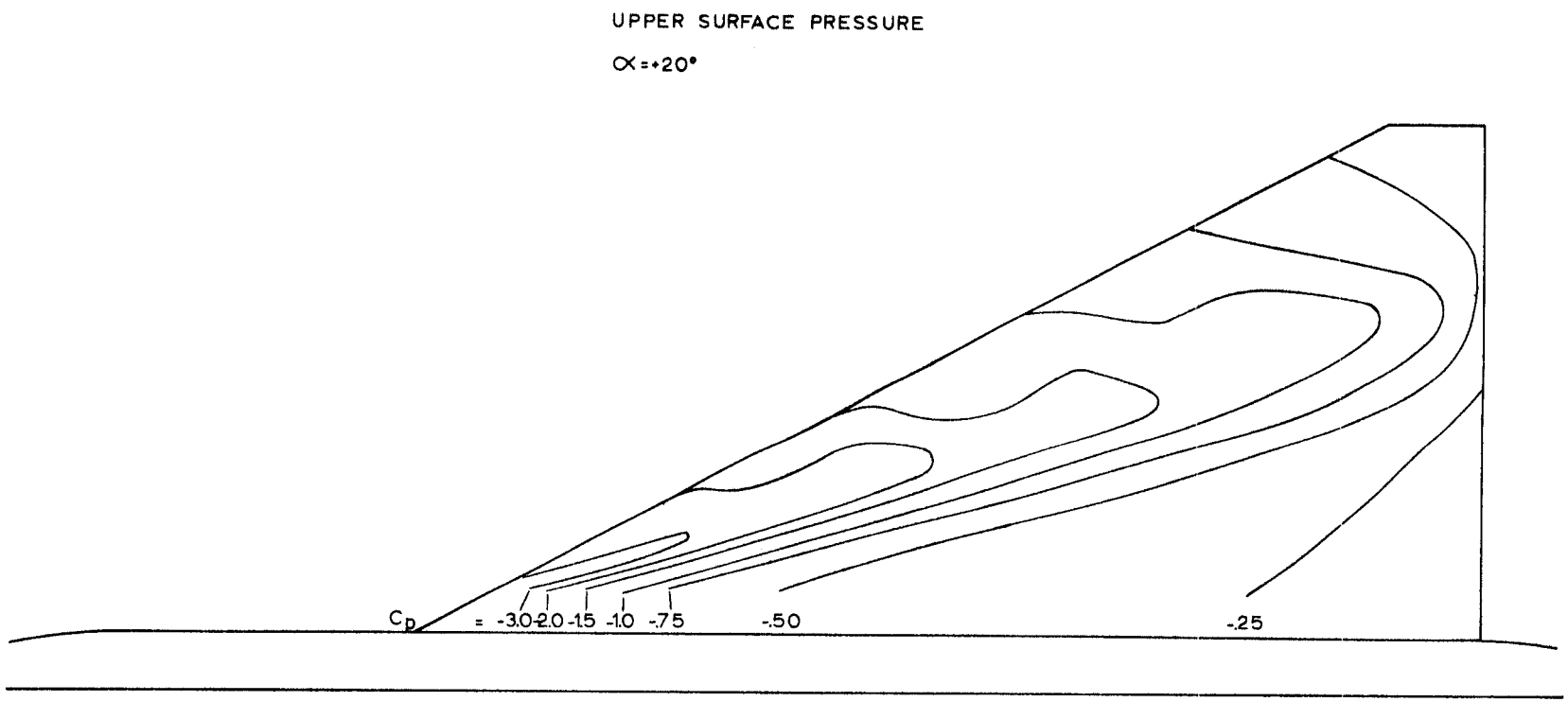

Figure 4e.- Pressure distribution. $\alpha = +20^{\circ}$.

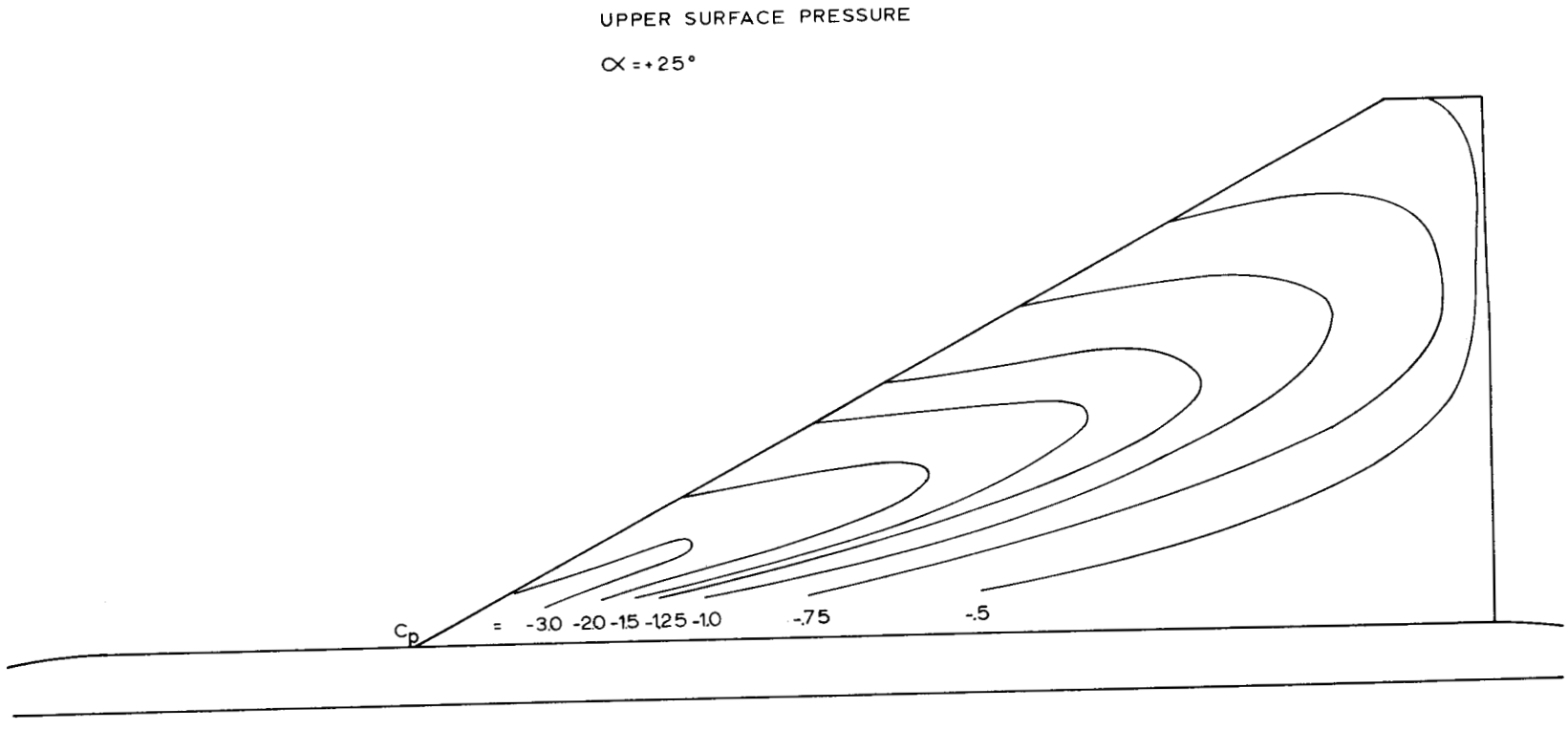

Figure 4f.- Pressure distribution. $\alpha = +25^{o}$.

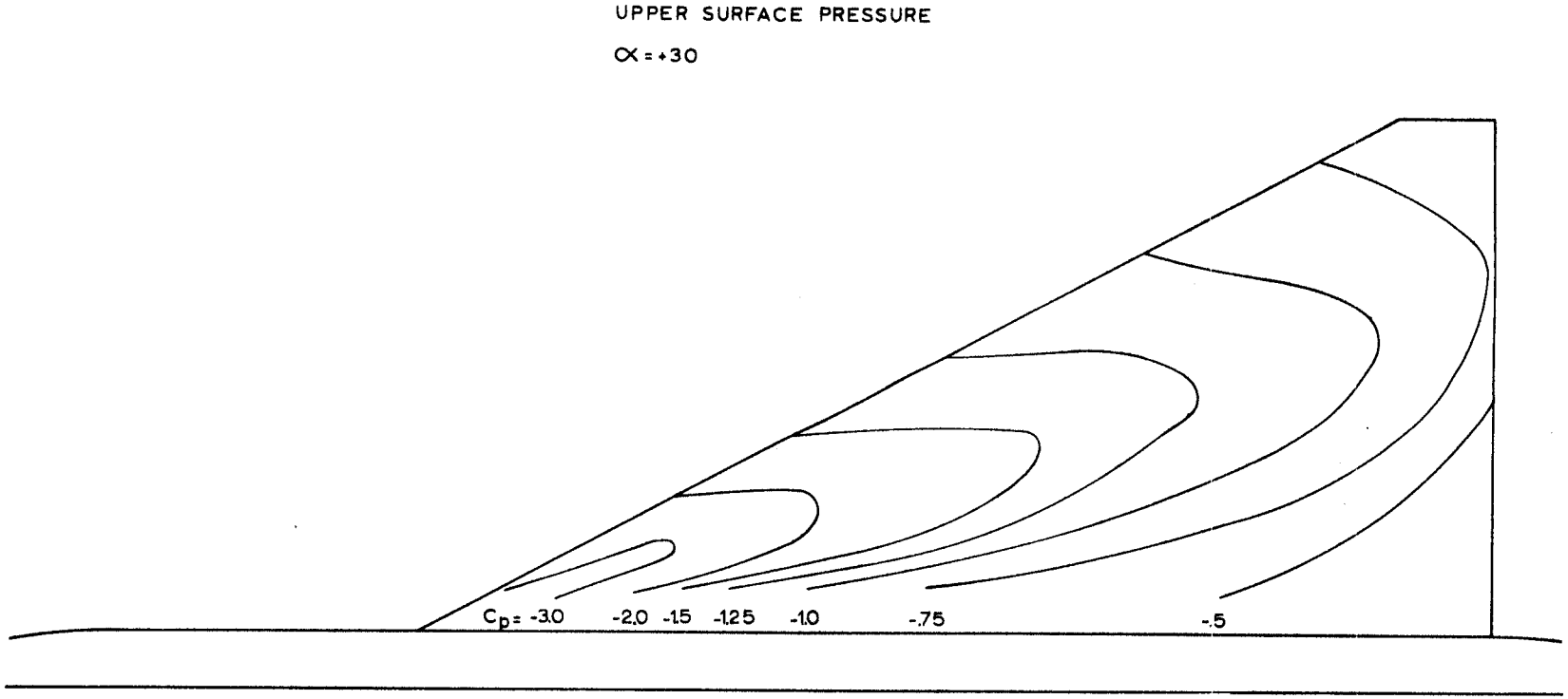

Figure 4g.- Pressure distribution. $\alpha = +30^{\circ}$.

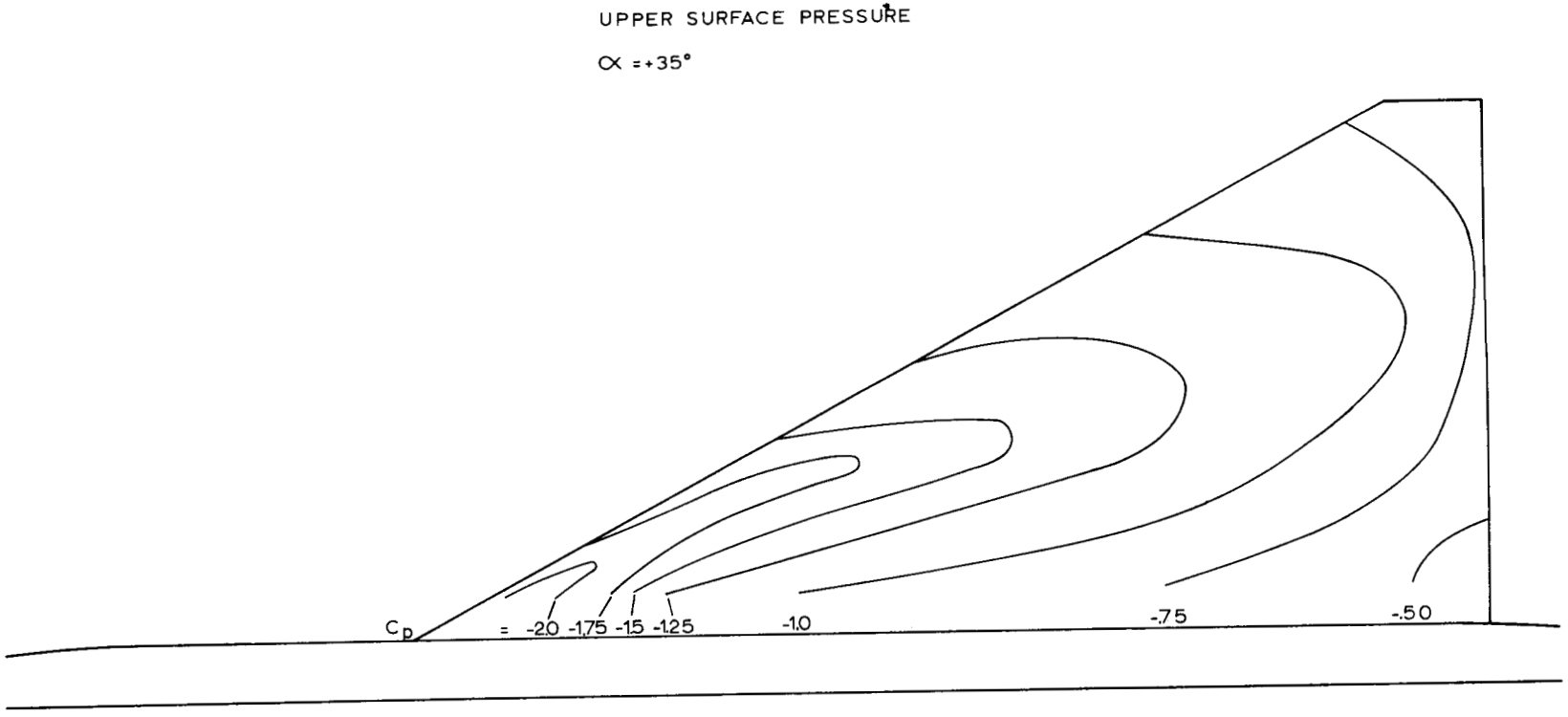

Figure 4h.- Pressure distribution. $\alpha = +35^{\circ}$.

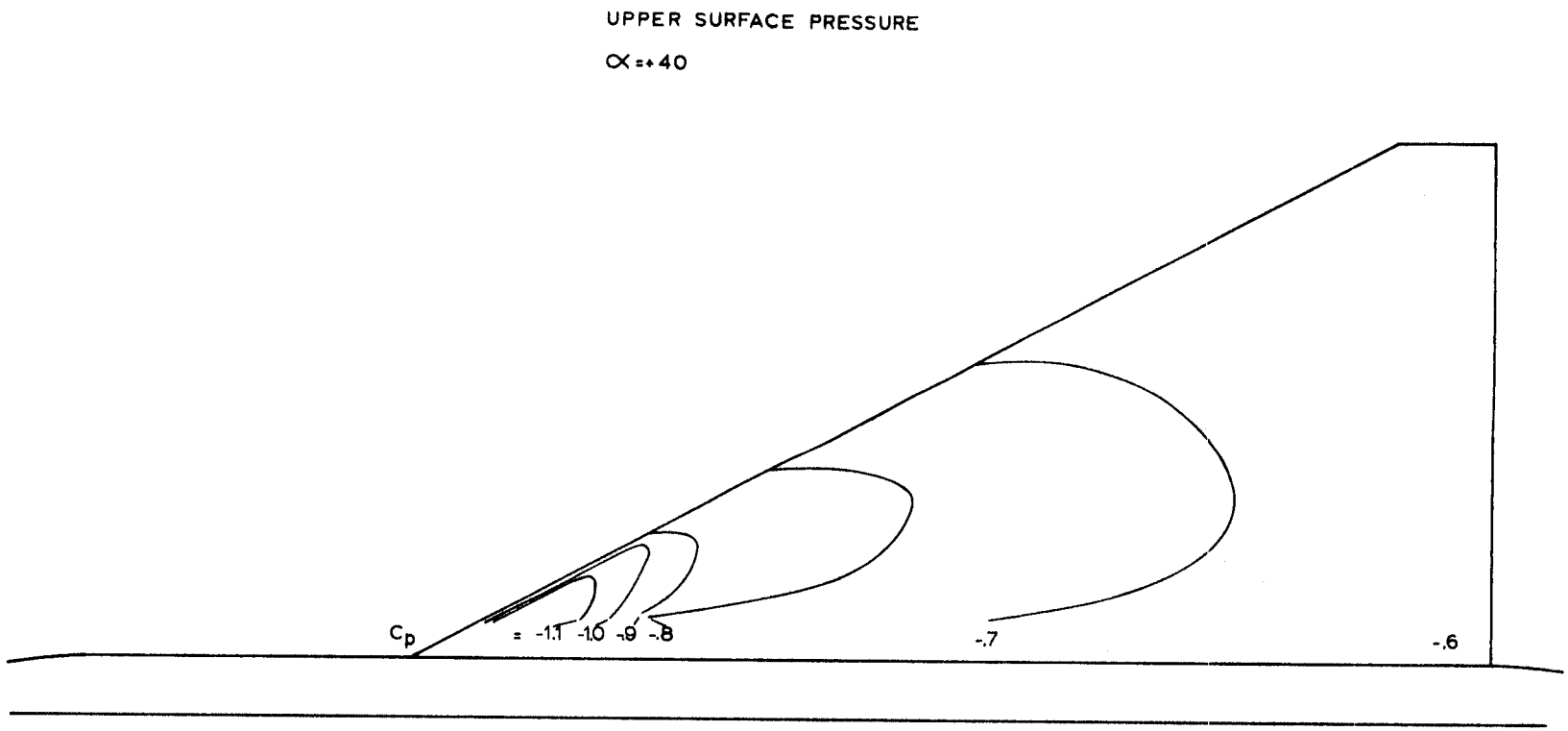

Figure 41.- Pressure distribution. $\alpha = +40^{\circ}$.

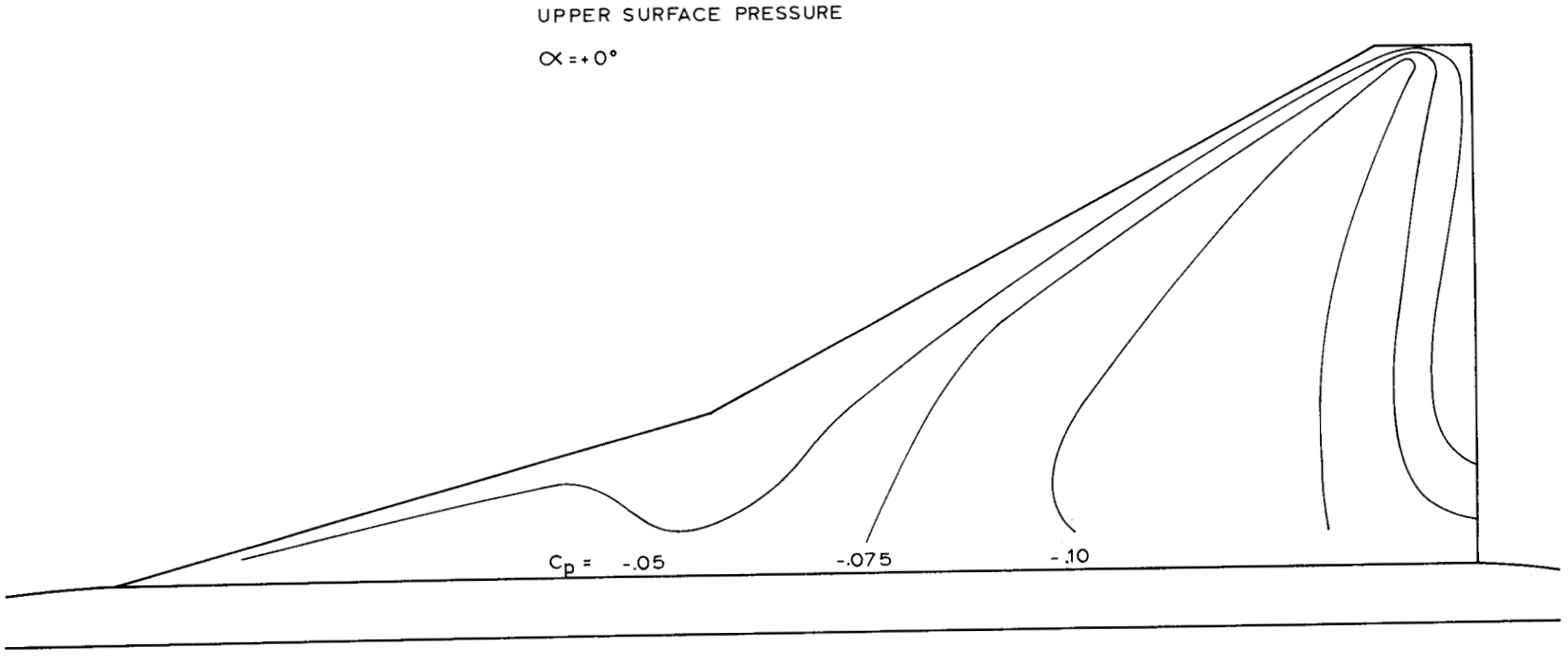

Figure 5a.- Pressure distribution. $\alpha = +0^{\circ}$.

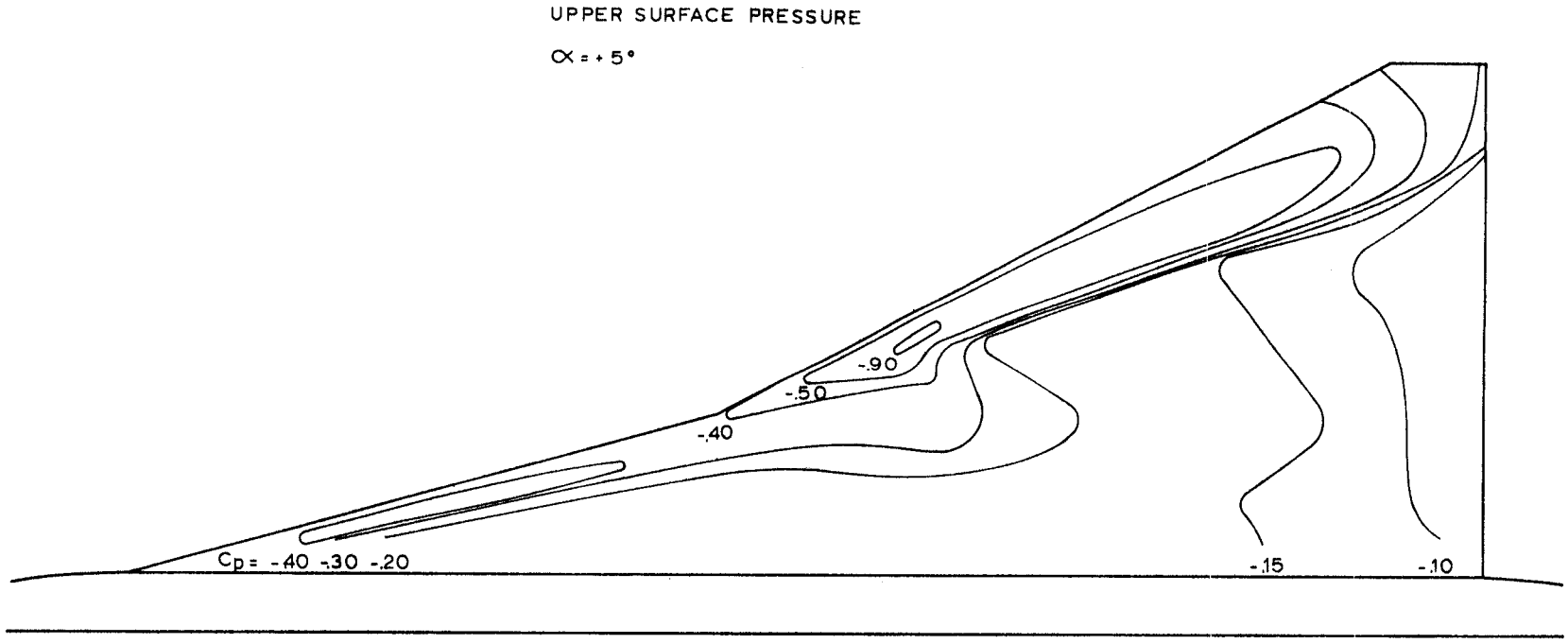

Figure 5b.- Pressure distribution. $\alpha = +5^{\circ}$.

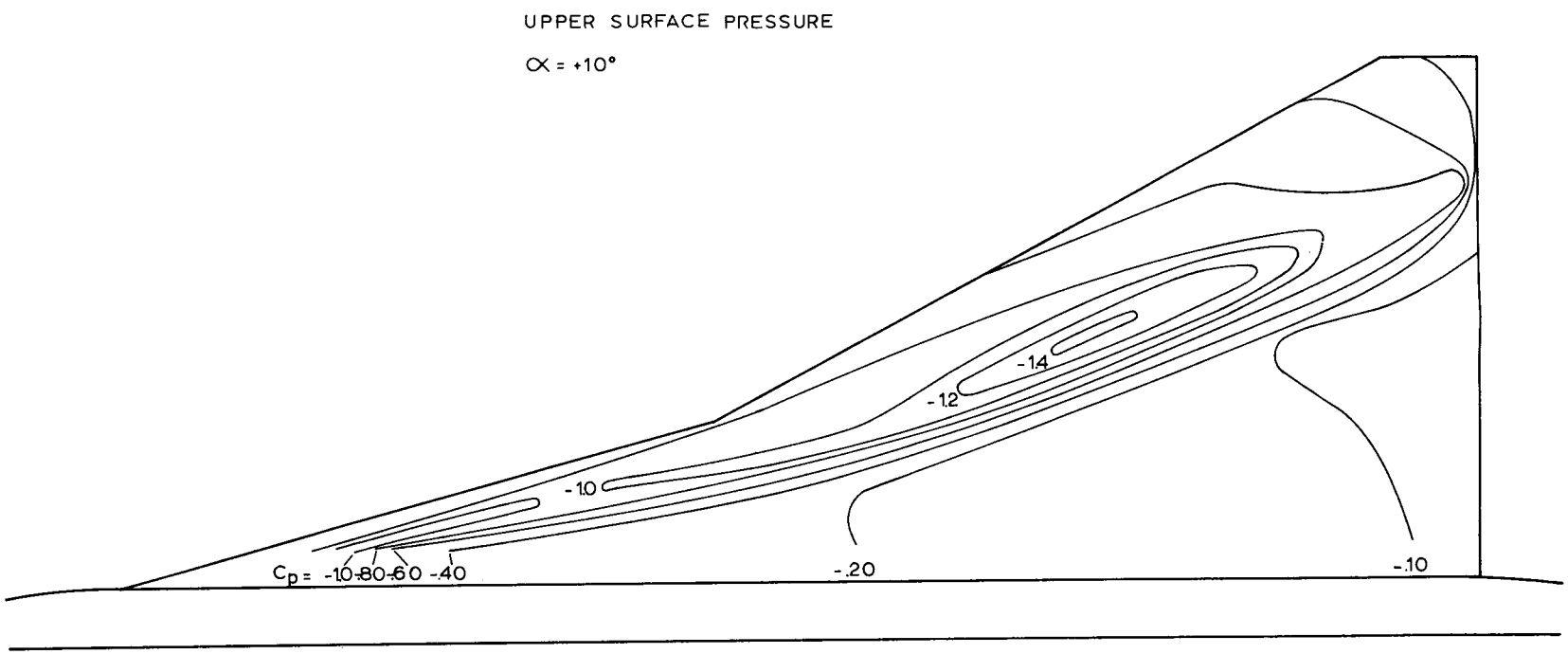

Figure 5c.- Pressure distribution. $\alpha = +10^{o}$.

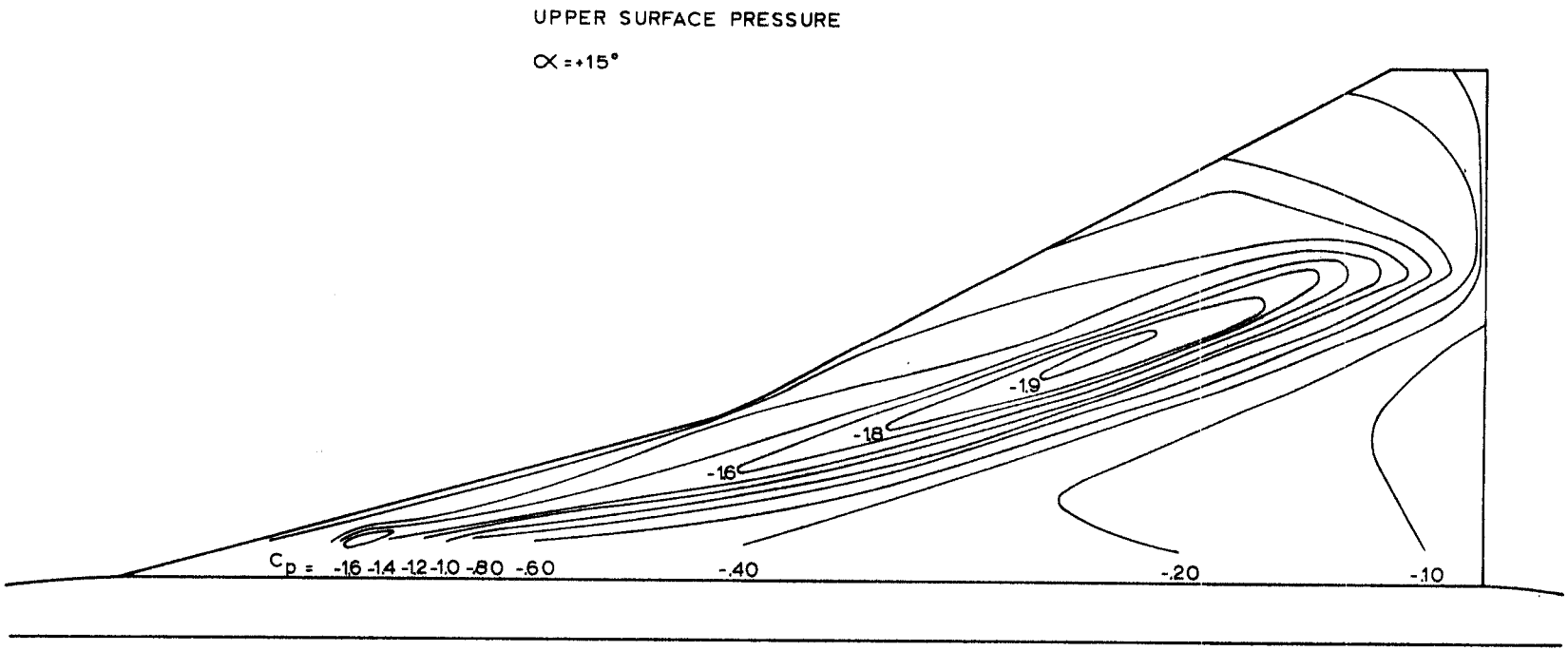

Figure 5d.- Pressure distribution. $\alpha = +15^{\circ}$.

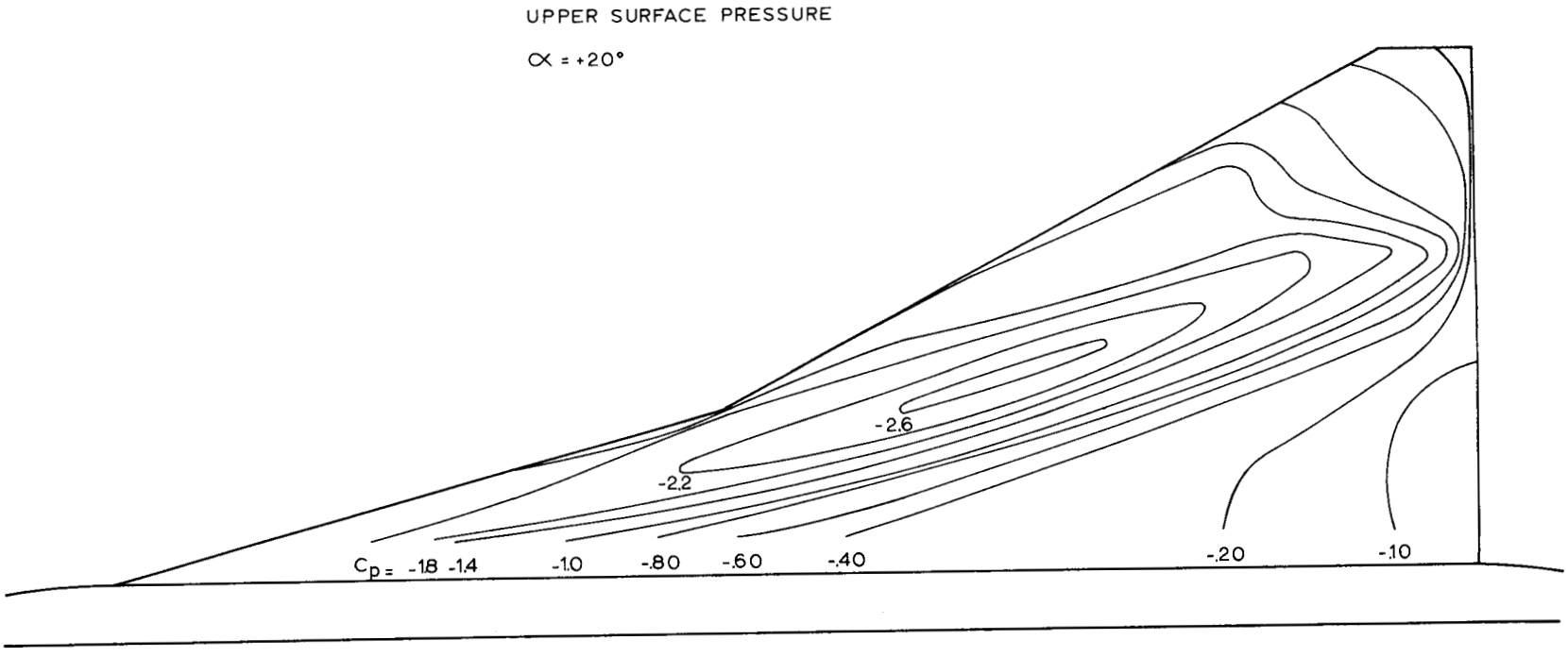

Figure 5e.- Pressure distribution. $\alpha = +20^{\circ}$.

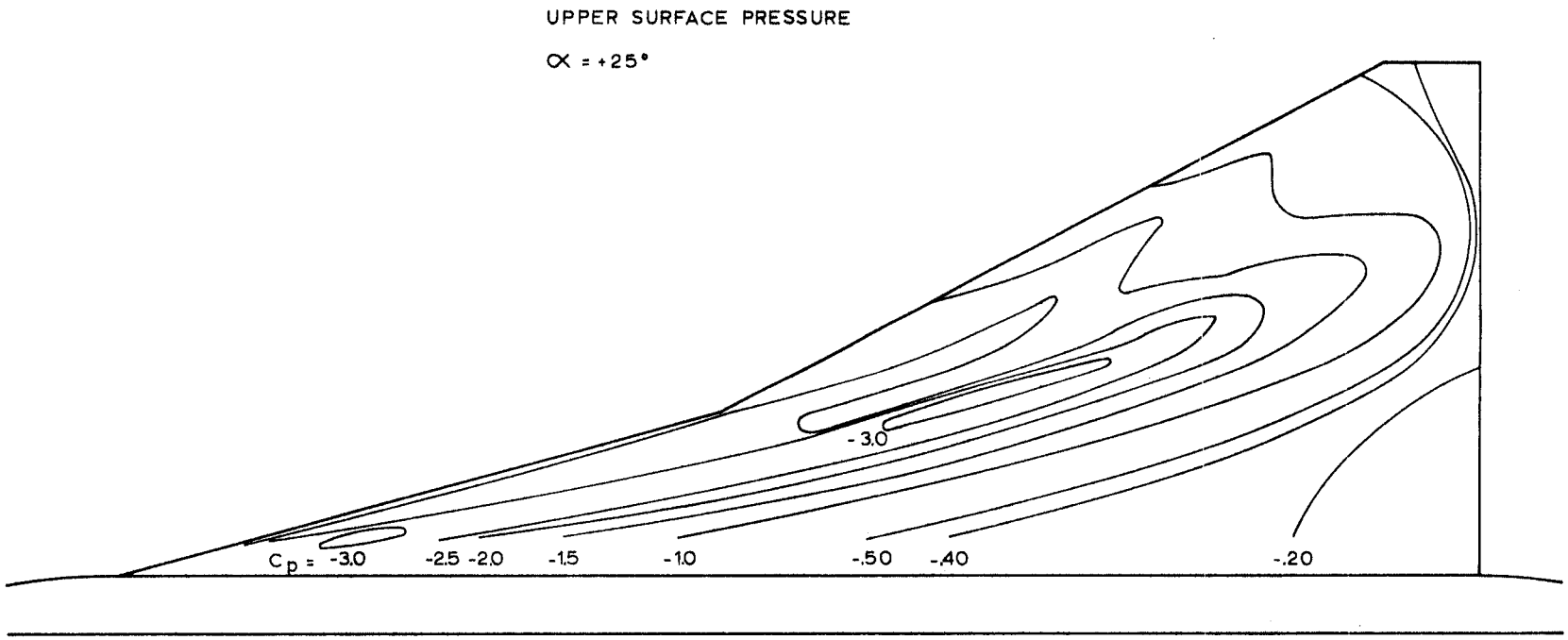

Figure 5f.- Pressure distribution. $\alpha = +25^{\circ}$.

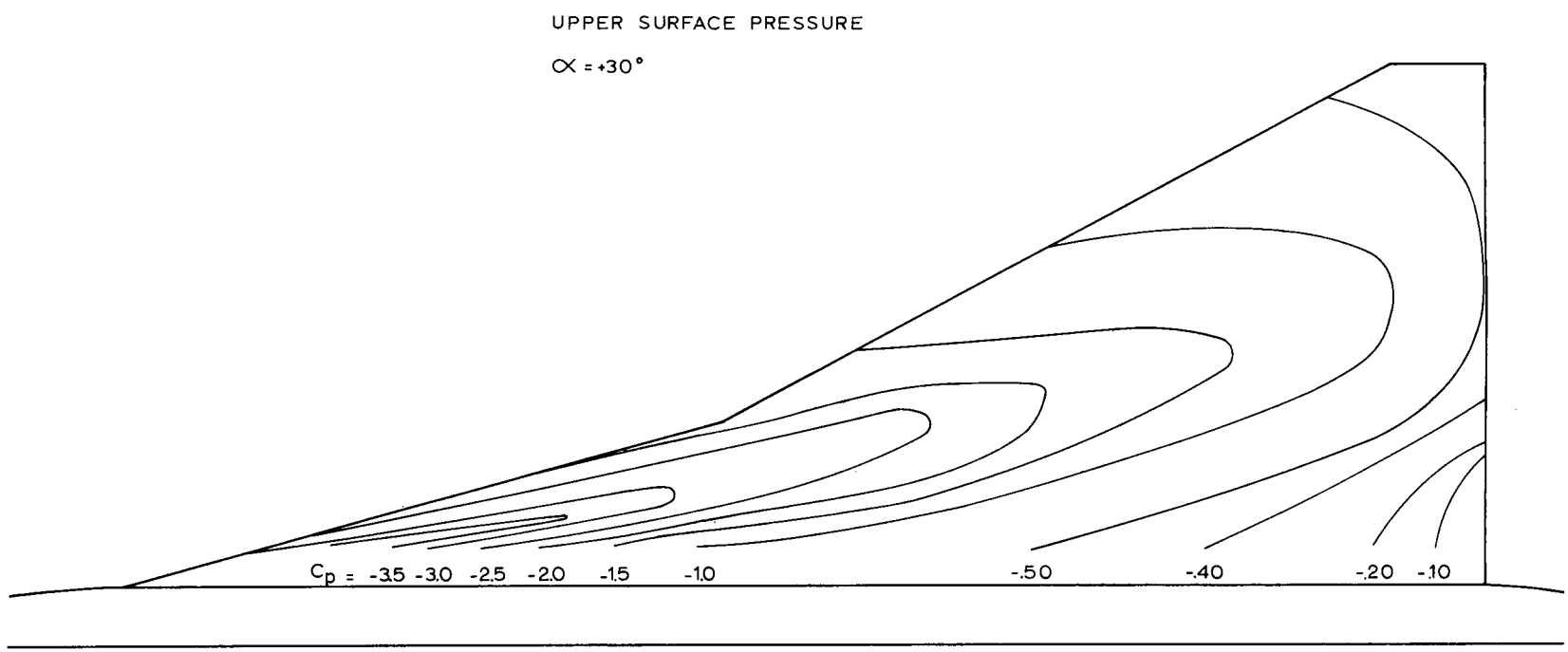

Figure 5g.- Pressure distribution. $\alpha = +30^{\circ}$.

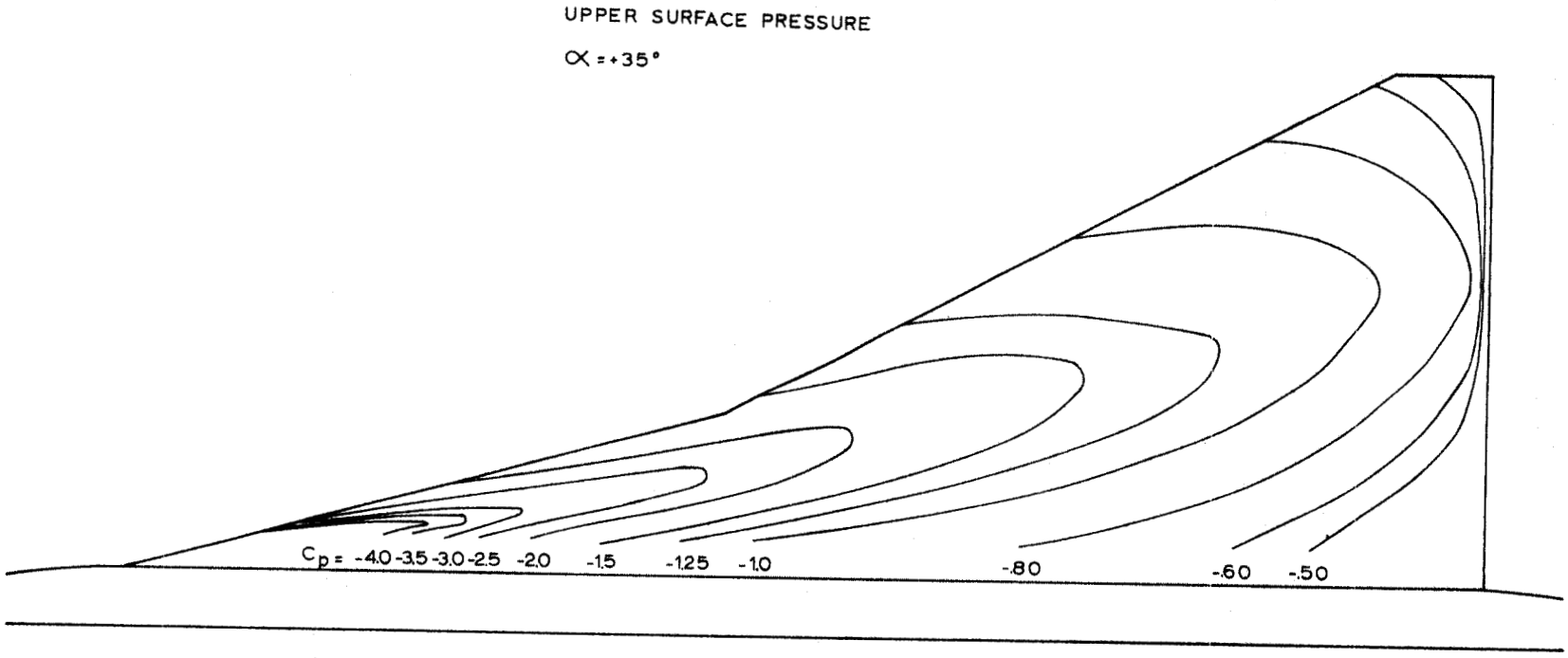

Figure 5h.- Pressure distribution. $\alpha = +35^{\circ}$.

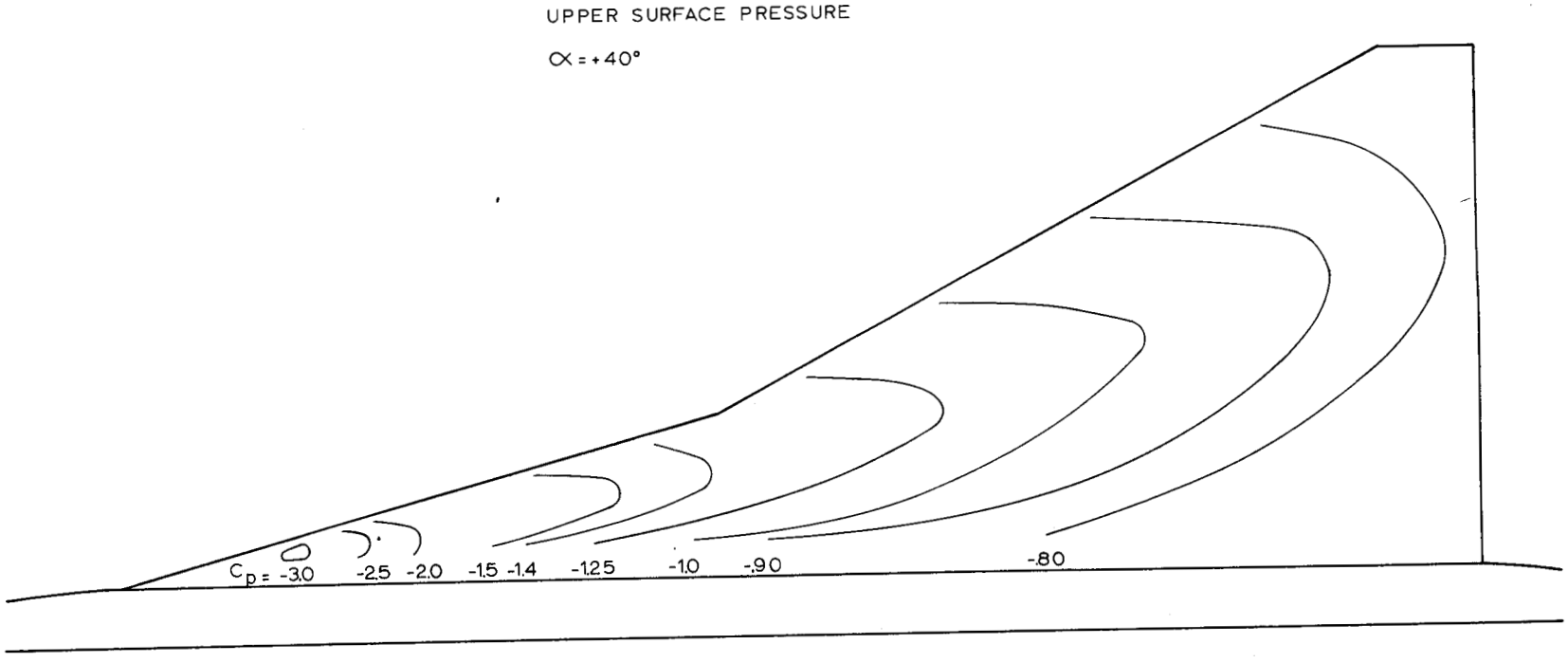

Figure 5i.- Pressure distribution. $\alpha = +40^{\circ}$.

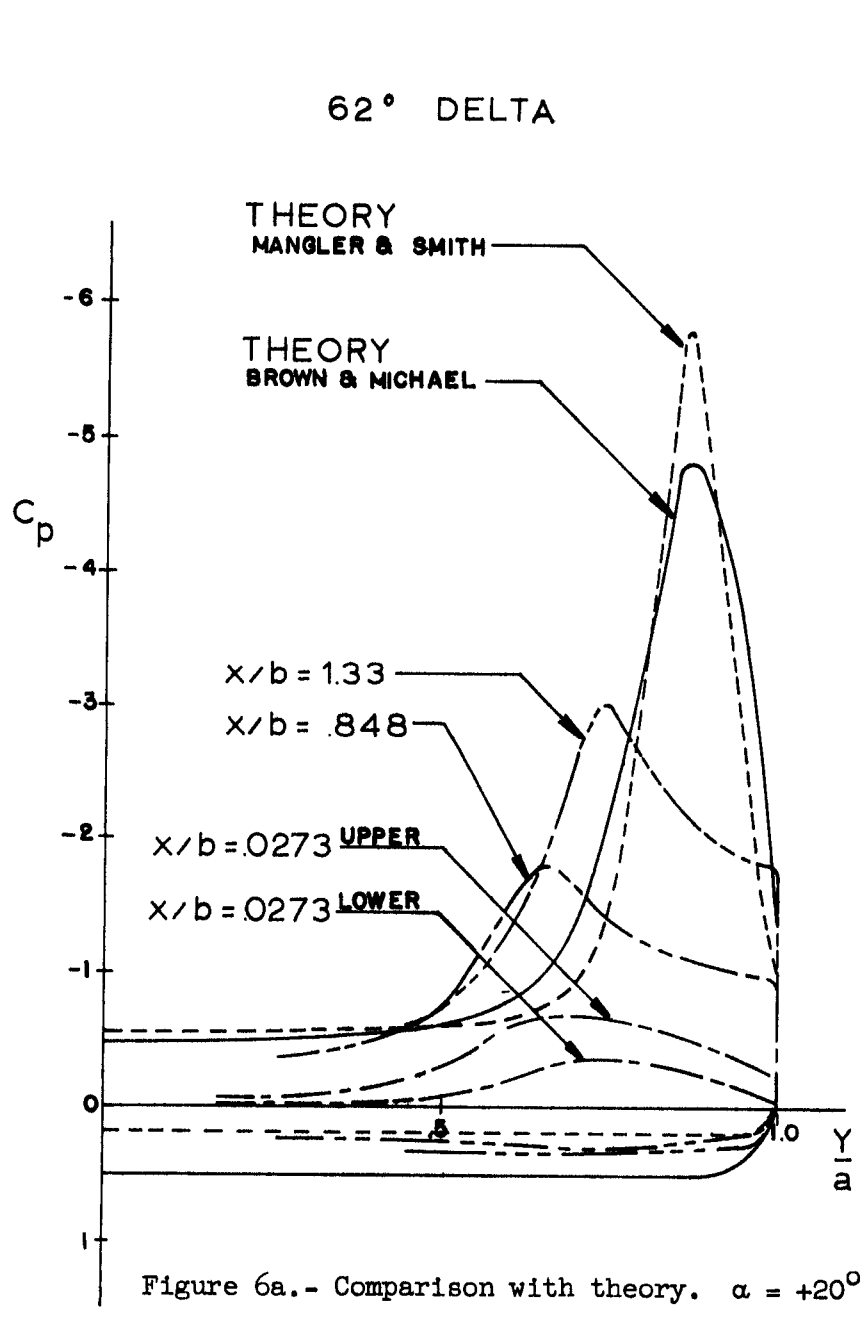

Figure 6a.- Comparison with theory. $\alpha = +20^{\circ}$.

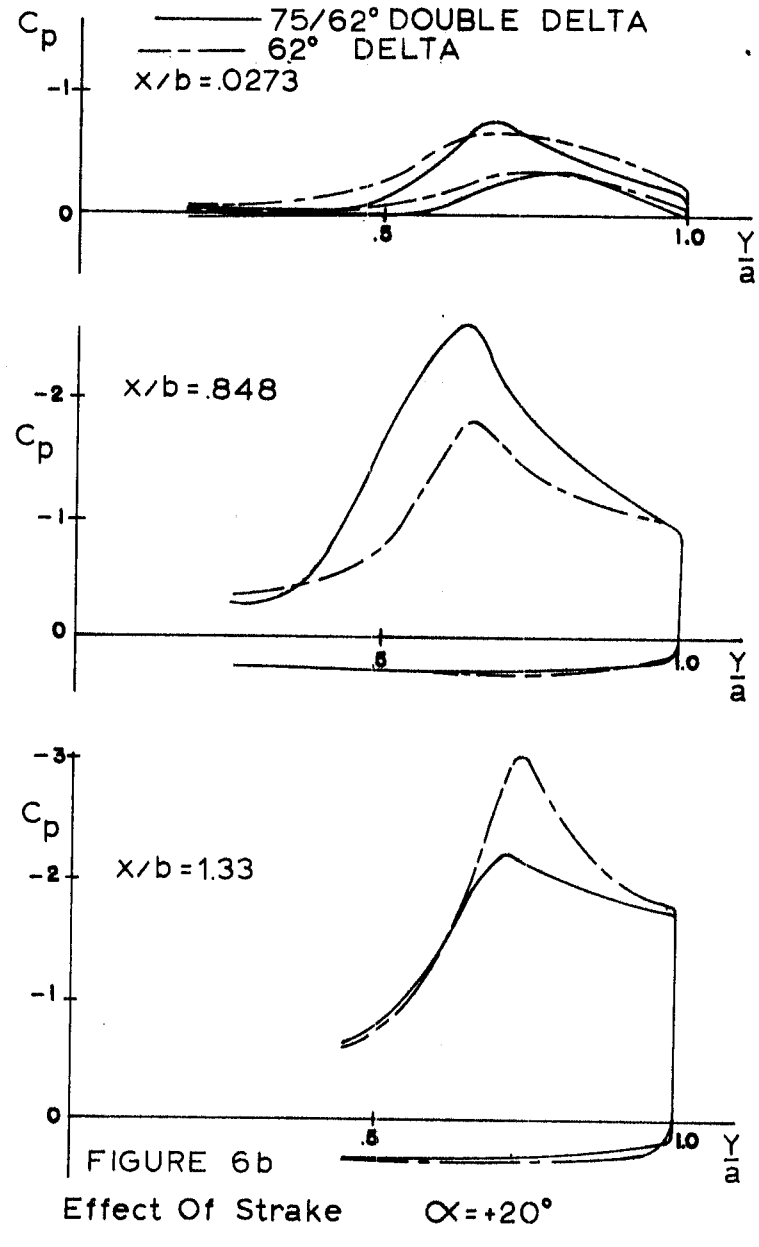

FIGURE 6b

Effect Of Strake $\alpha = +20^{\circ}$

Figure 6b.- Effect of strake. $\alpha = +20^{\circ}$.

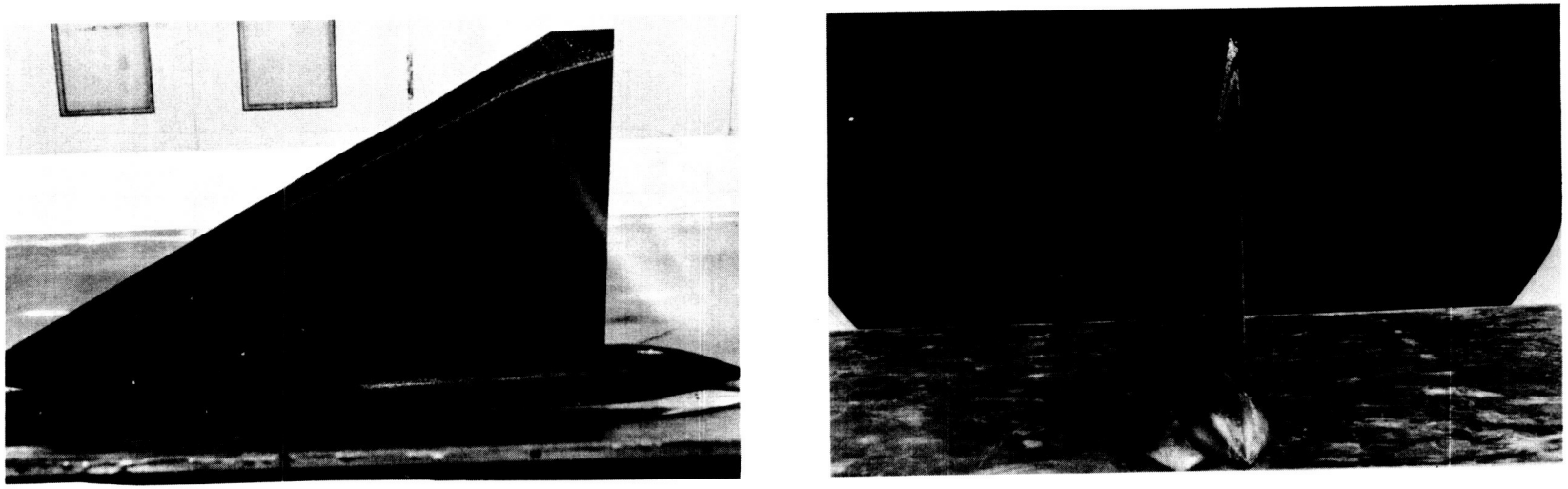

Figure 7a.- $\alpha = +5^{\circ}$.

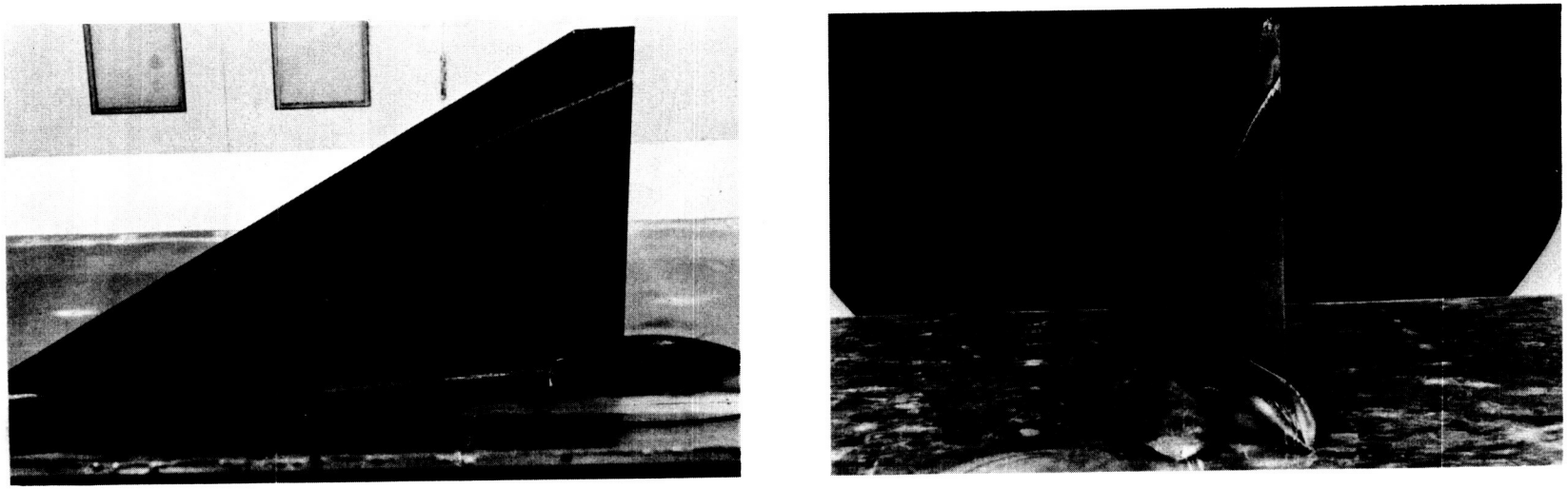

Figure 7b.- $\alpha = +10^{\circ}$.

Figures 7a, 7b.- Streak photos 62° delta wing.

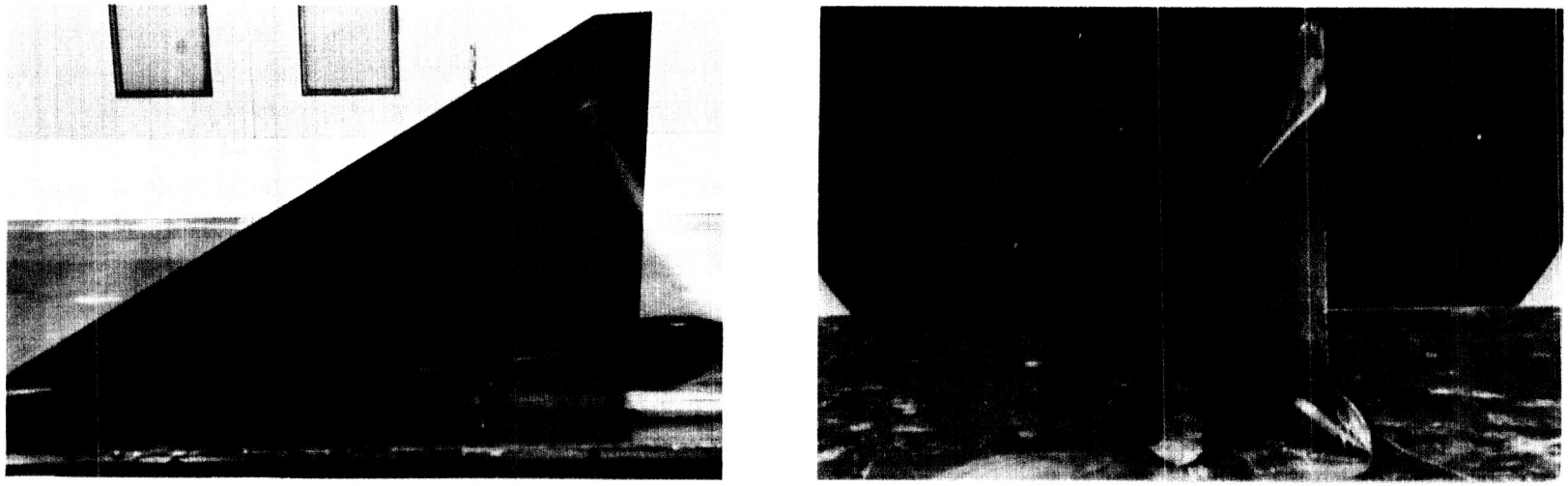

Figure 7c.- $\alpha = +15^{\circ}$.

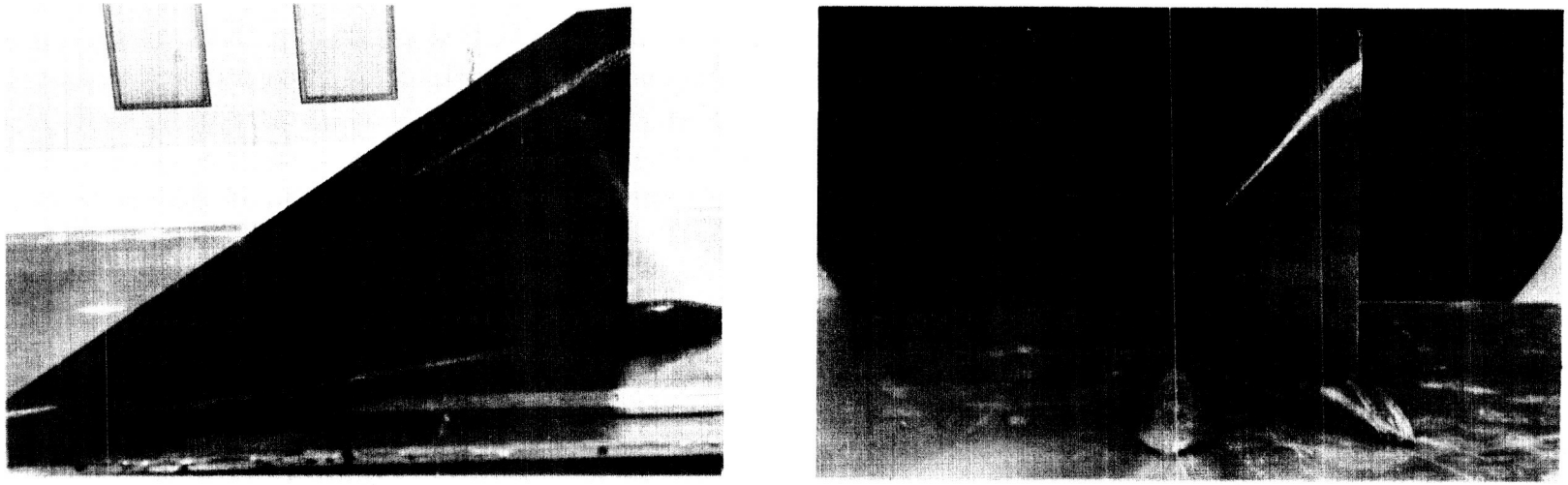

Figure 7d.- $\alpha = +20^{\circ}$.

Figures 7c, 7d.- Streak photos 62° delta wing.

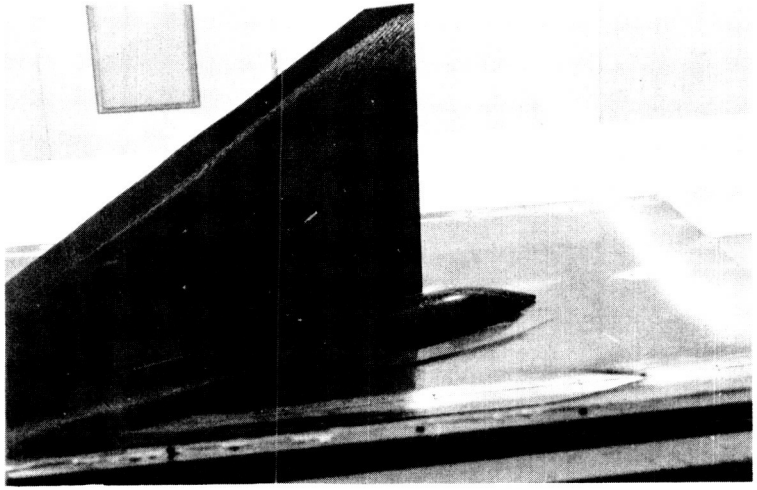

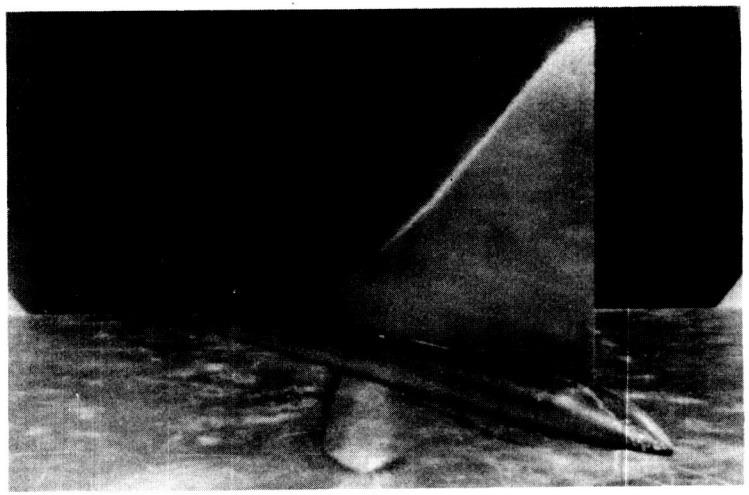

Figure 7e.- $\alpha = +25^{\circ}$.

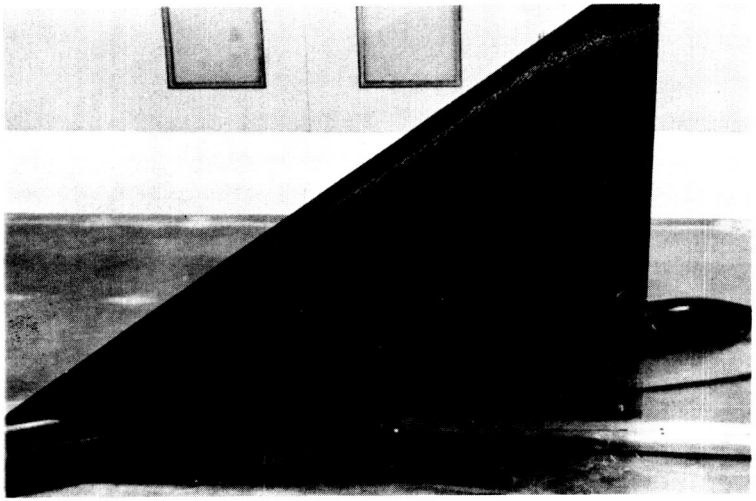

Figure 7f.- $\alpha = +30^{\circ}$.

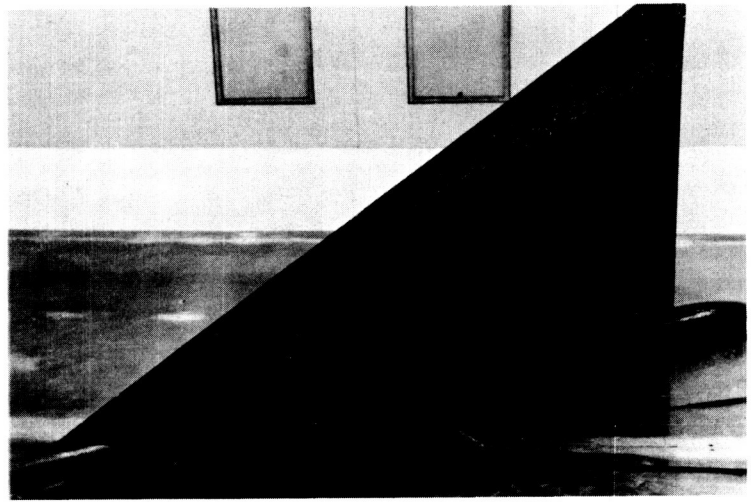

Figure 7g.- $\alpha = +35^{\circ}$.

Figures 7e, 7f, 7g.- Streak photos 62° delta wing.

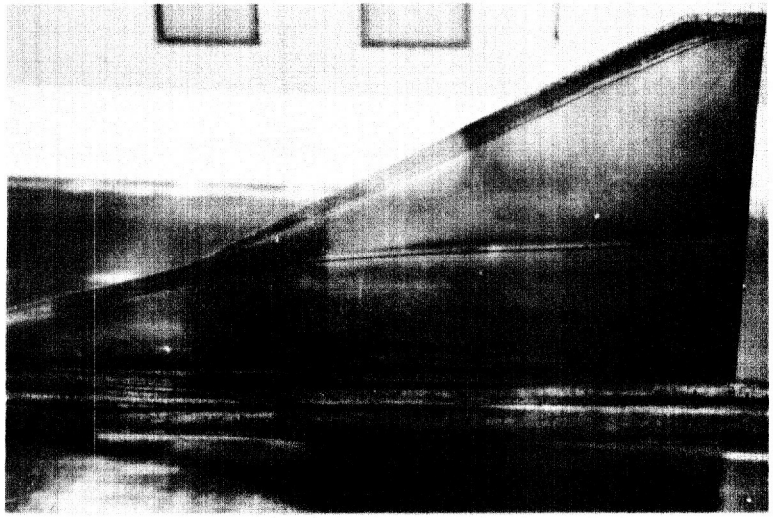

Figure 8a.- $\alpha = 5^{\circ}$

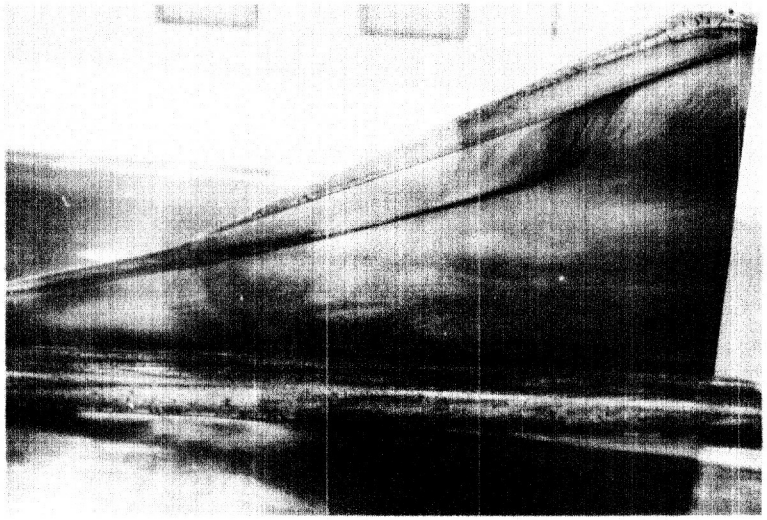

Figure 8b.- $\alpha = 7^{\circ}$.

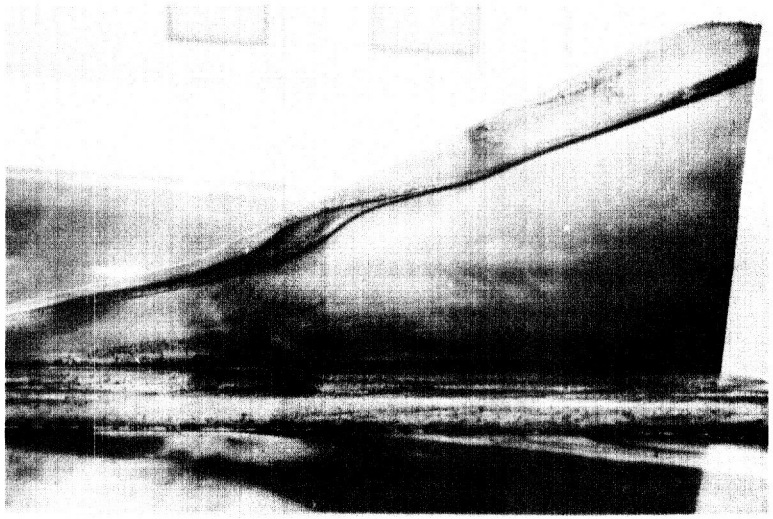

Figure 8c.- $\alpha = 10^{\circ}$.

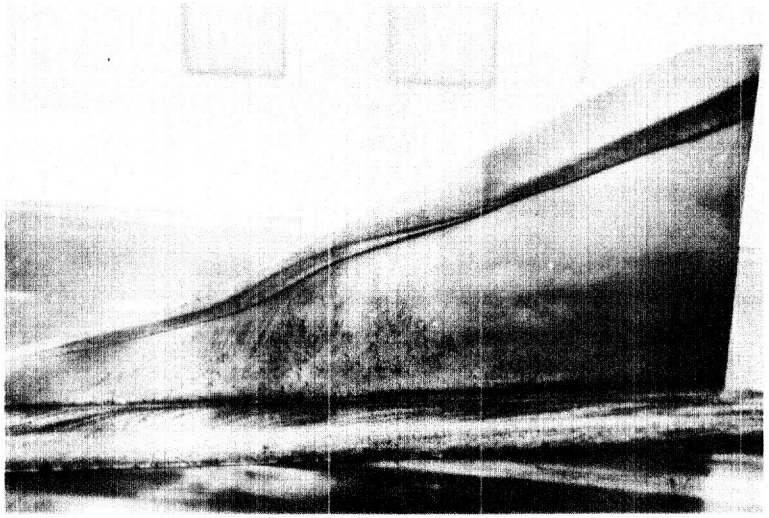

Figure 8d.- $\alpha = 15^{\circ}$.

Figures 8a, 8b, 8c, 8d.- Streak photos $75^{\circ}/62^{\circ}$ double-delta wing.

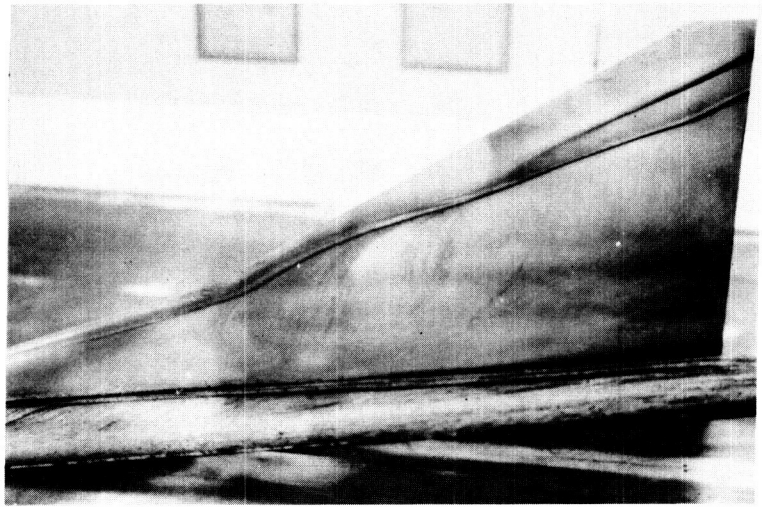

Figure 8e.- $\alpha = 20^{\circ}$.

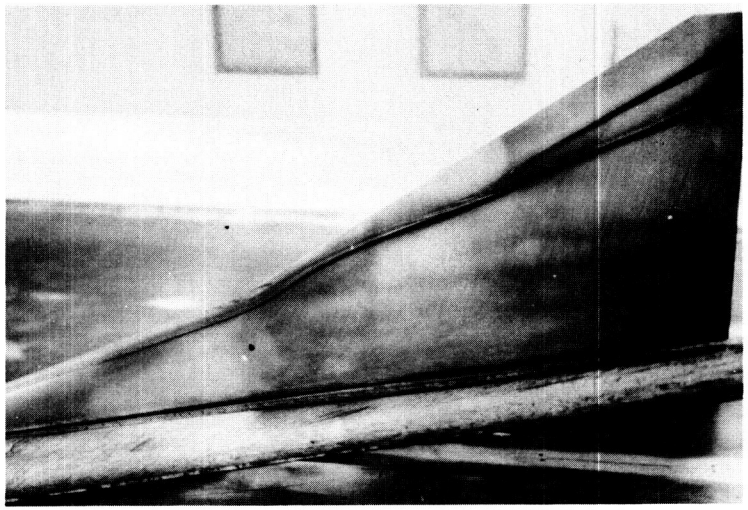

Figure 8f.- $\alpha = 25^{\circ}$.

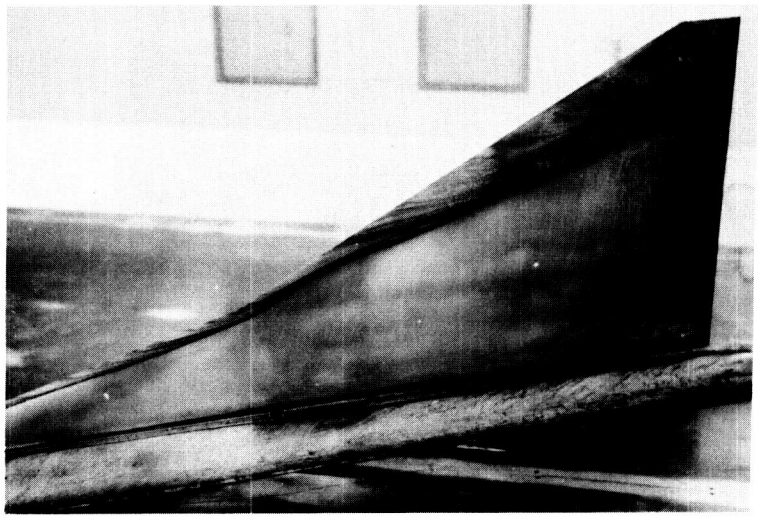

Figure 8g.- $\alpha = 30^{\circ}$.

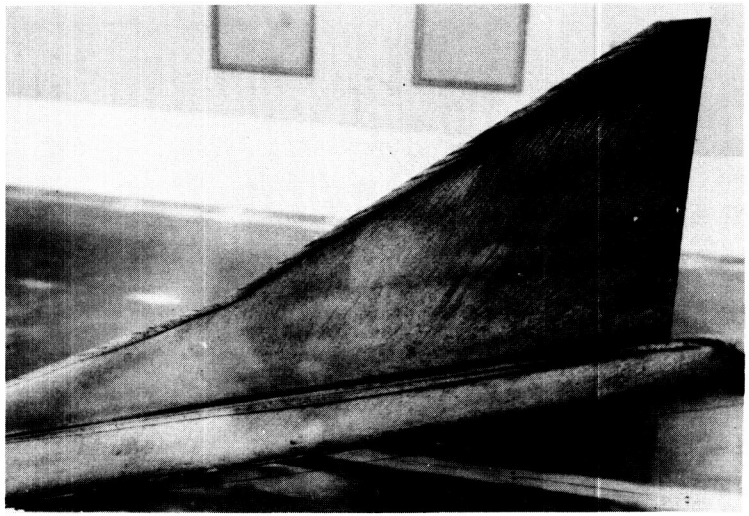

Figure 8h.- $\alpha = 35^{\circ}$.

Figures 8e, 8f, 8g, 8h.- Streak photos $75^{\circ}/62^{\circ}$ double-delta wing.

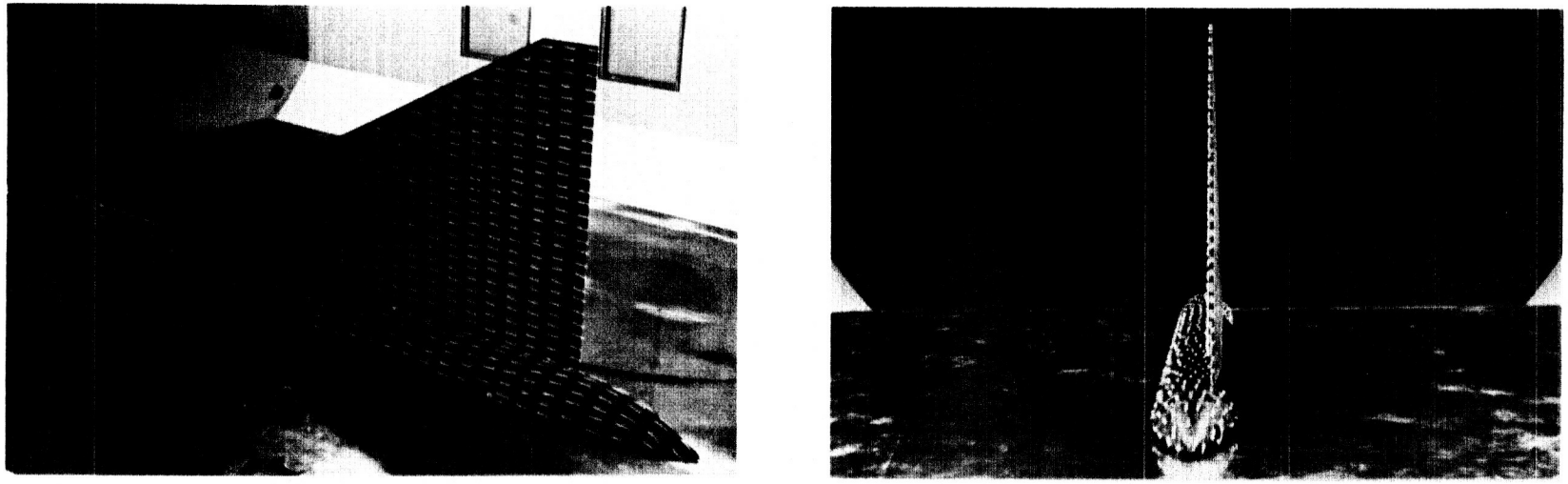

Figure 9a.- $\alpha = 0^{\circ}$.

Figure 9b.- $\alpha = 5^{\circ}$.

Figures 9a, 9b.- Tuft photos 62° delta wing.

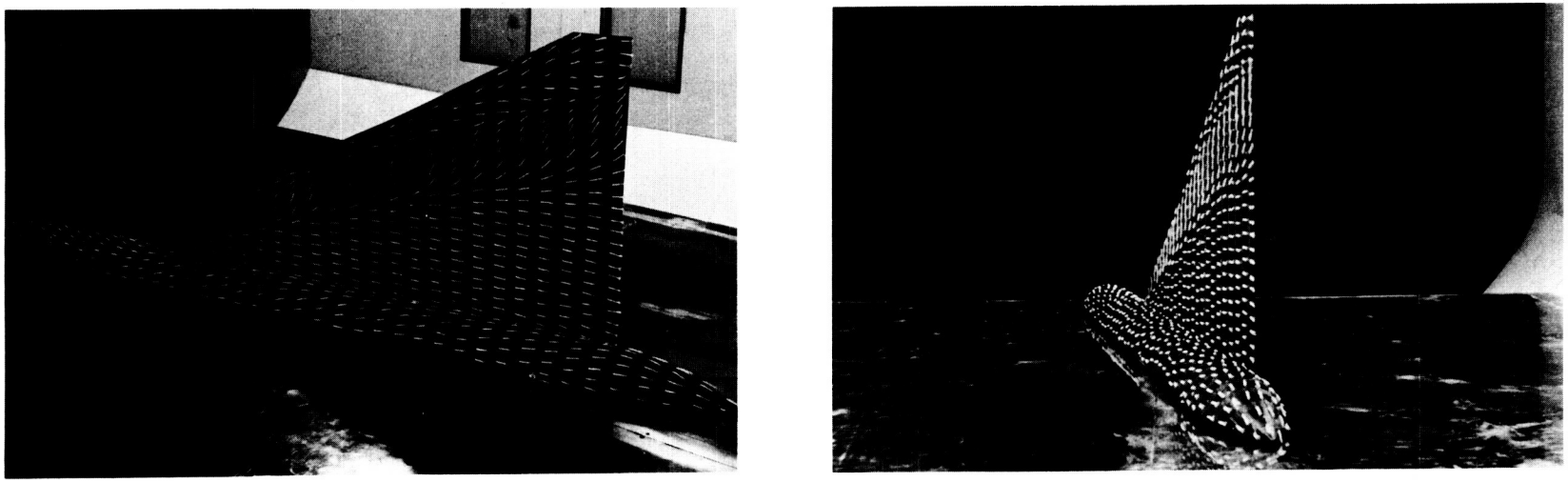

Figure 9c.- $\alpha = 10^{\circ}$.

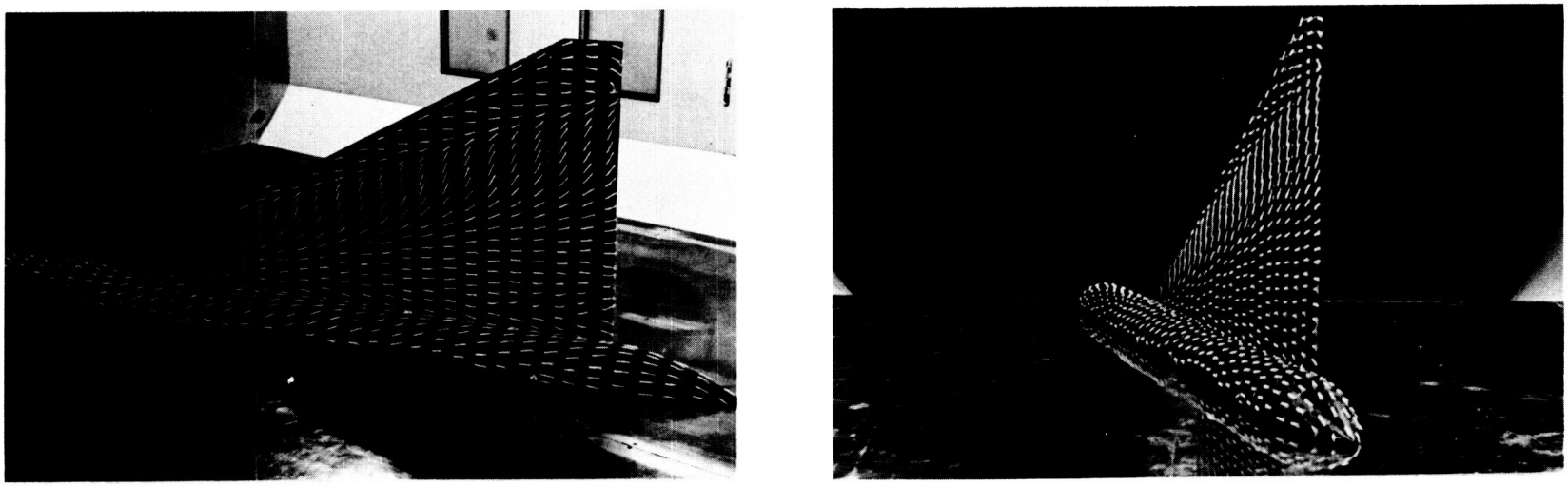

Figure 9d.- $\alpha = 15^{\circ}$.

Figures 9c, 9d.- Tuft photos 62° delta wing.

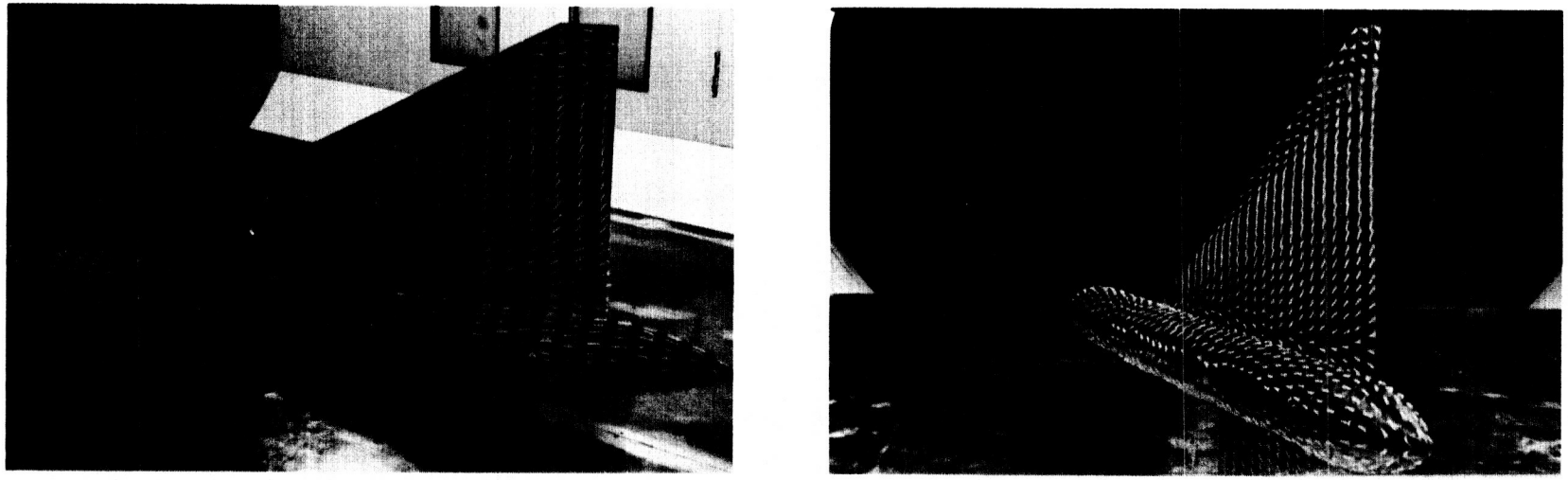

Figure 9e.- $\alpha = 20^{\circ}$.

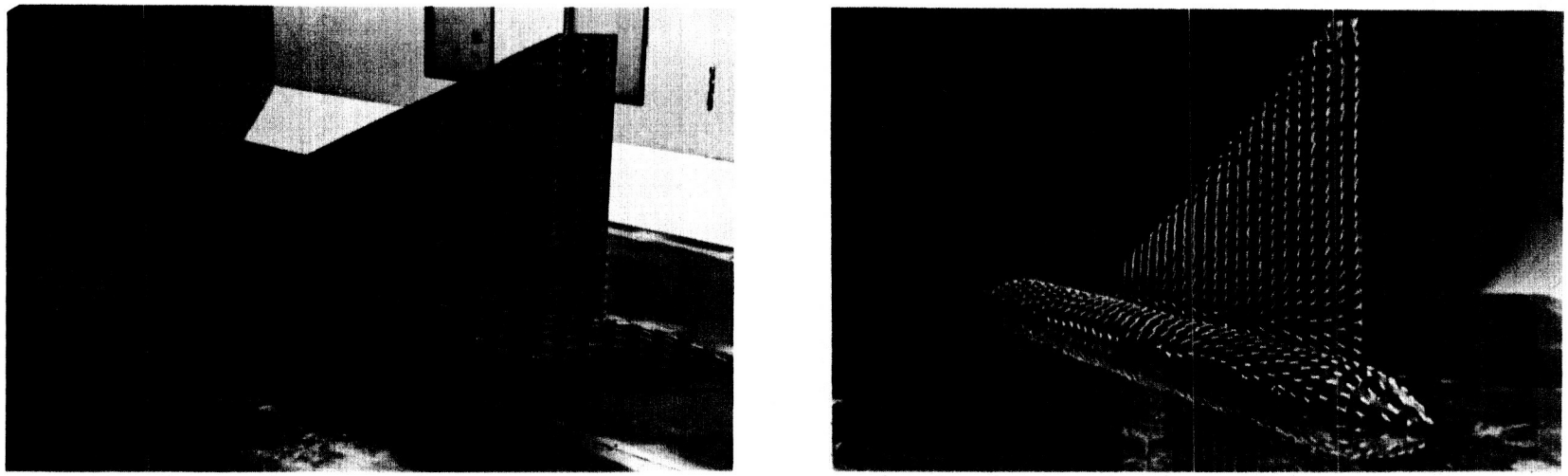

Figure 9f.- $\alpha = 25^{\circ}$.

Figures 9e, 9f.- Tuft photos 62° delta wing.

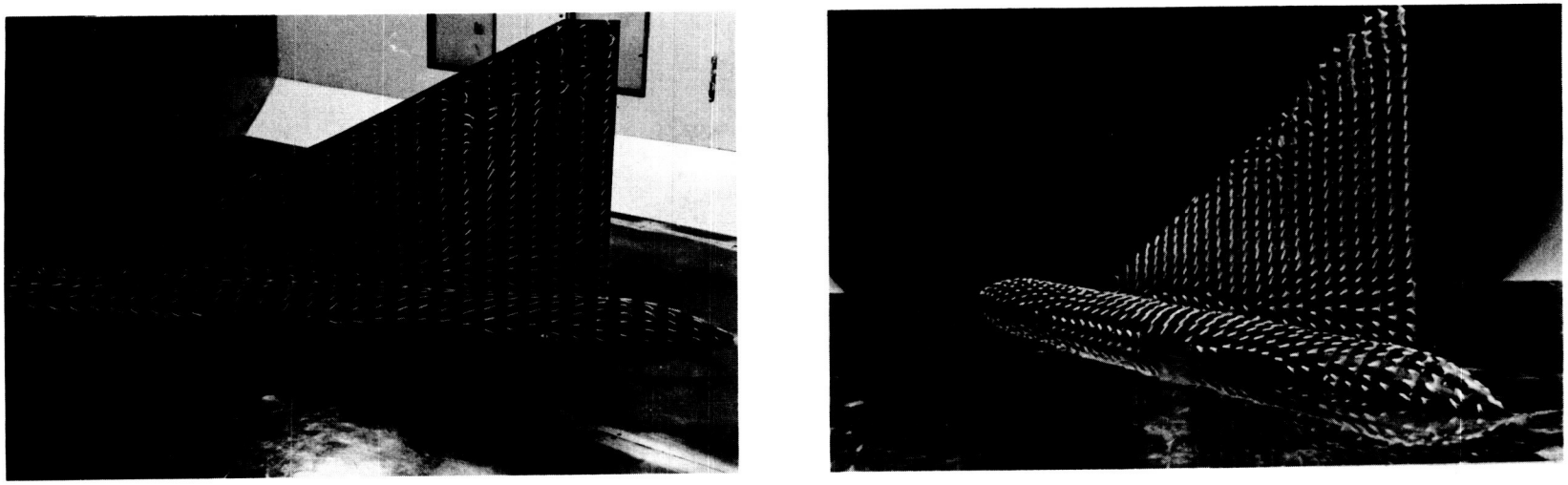

Figure 9g.- $\alpha = 30^{\circ}$.

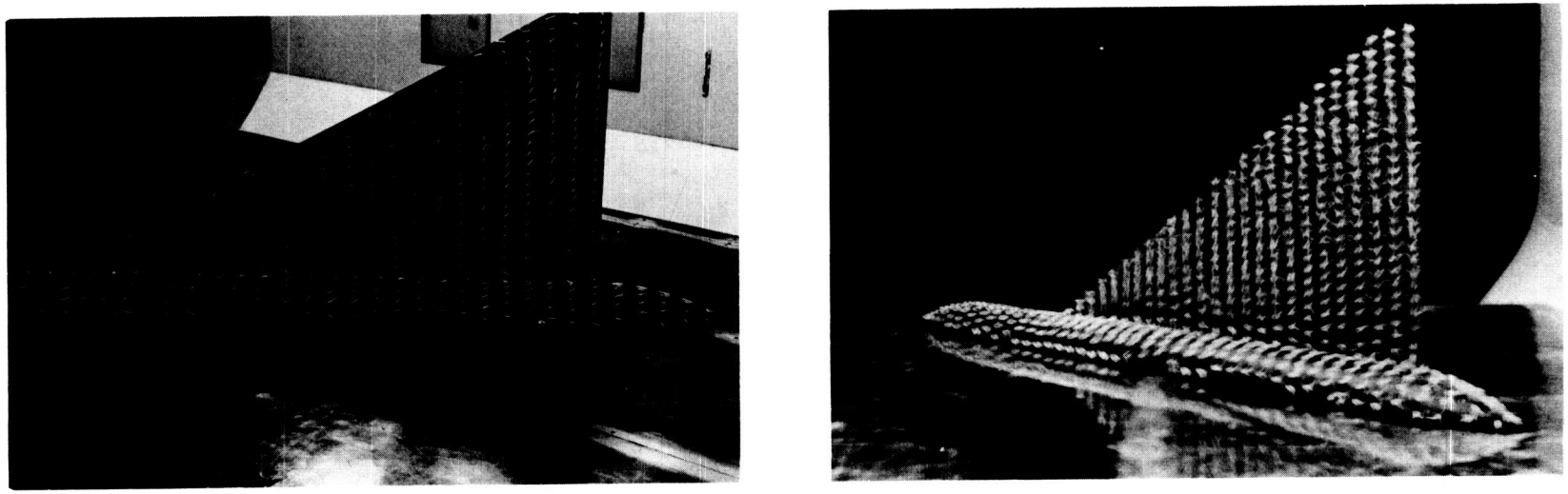

Figure 9h.- $\alpha = 35^{\circ}$.

Figures 9g, 9h.- Tuft photos 62° delta wing.

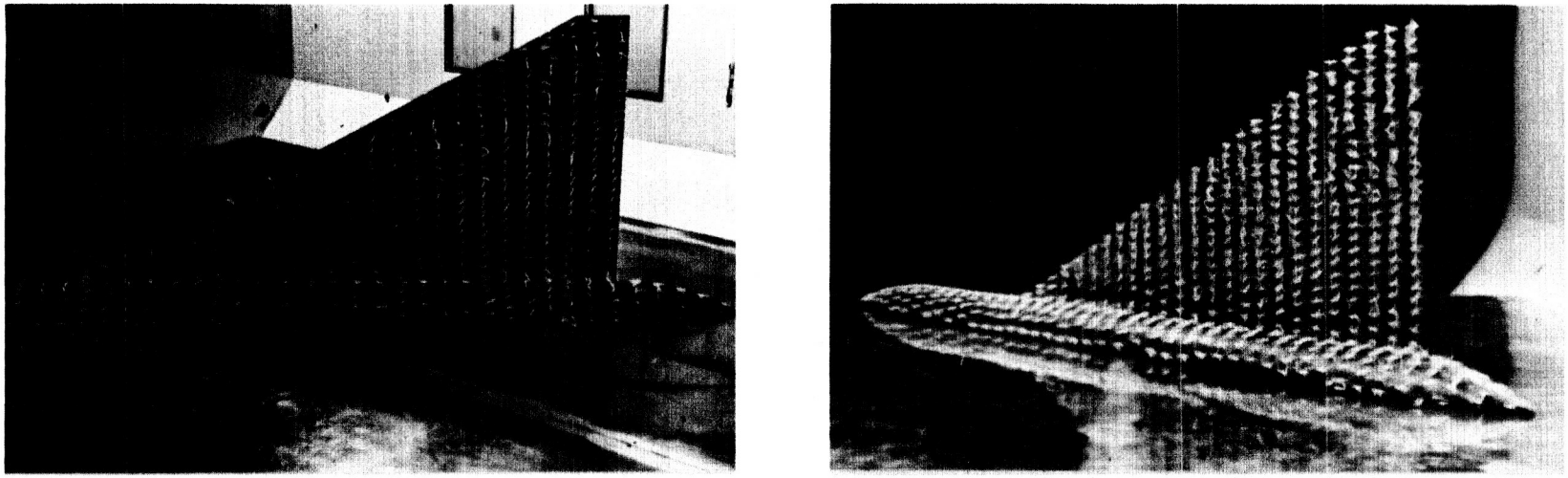

Figure 9i.- $\alpha = 40^{\circ}$.

Figure 9i.- Tuft photos 62° delta wing.

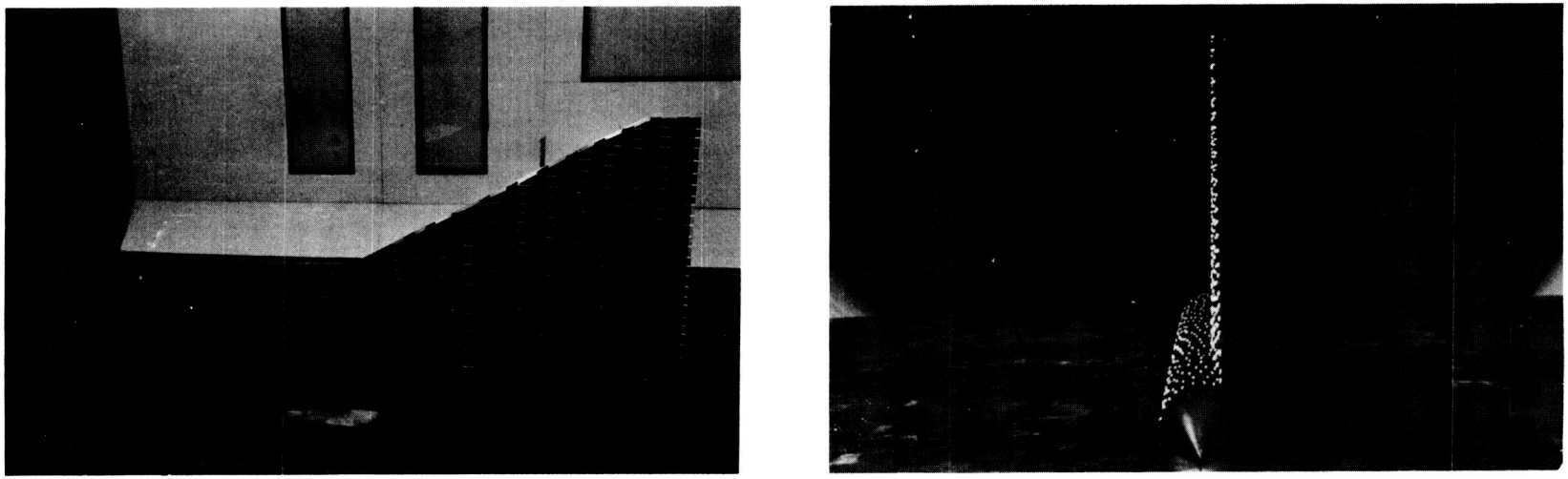

Figure 10a.- $\alpha = 0^{\circ}$.

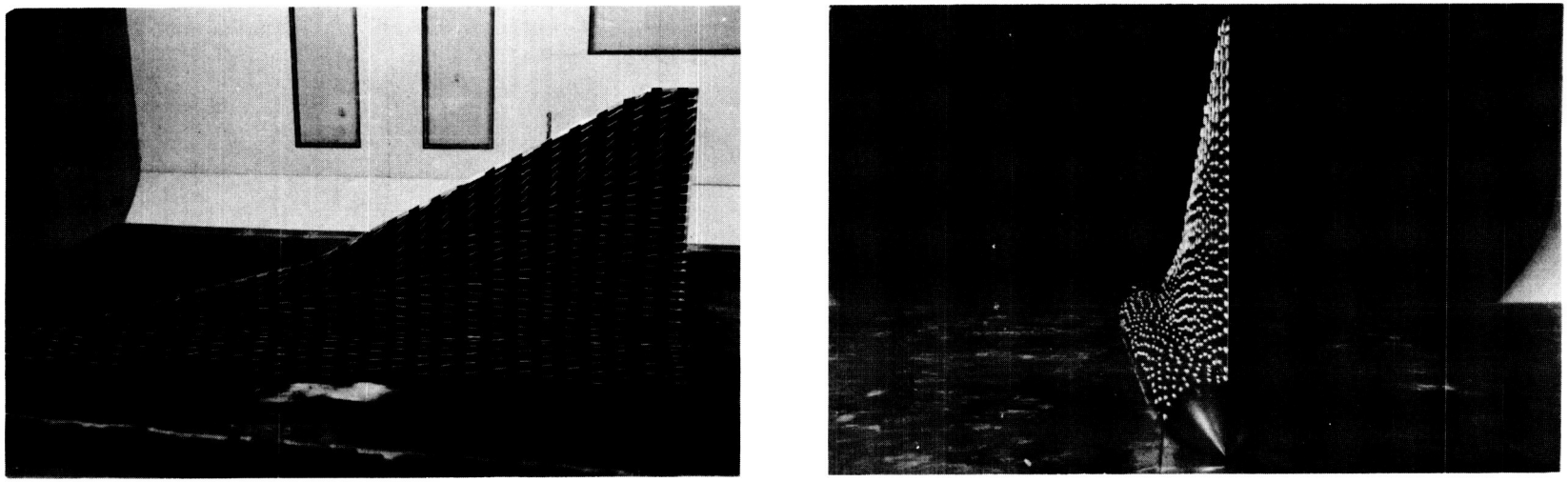

Figure 10b.- $\alpha = 5^{\circ}$.

Figures 10a, 10b.- Tuft photos $75^{\circ}/62^{\circ}$ double-delta wing.

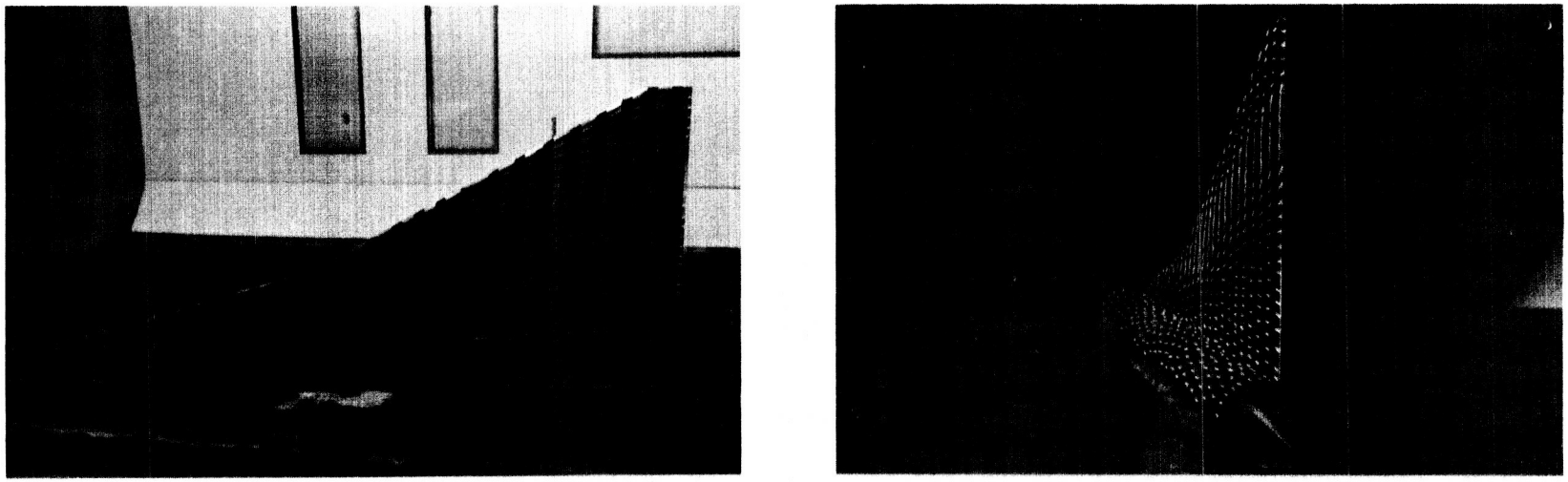

Figure 10c.- $\alpha = 10^{\circ}$.

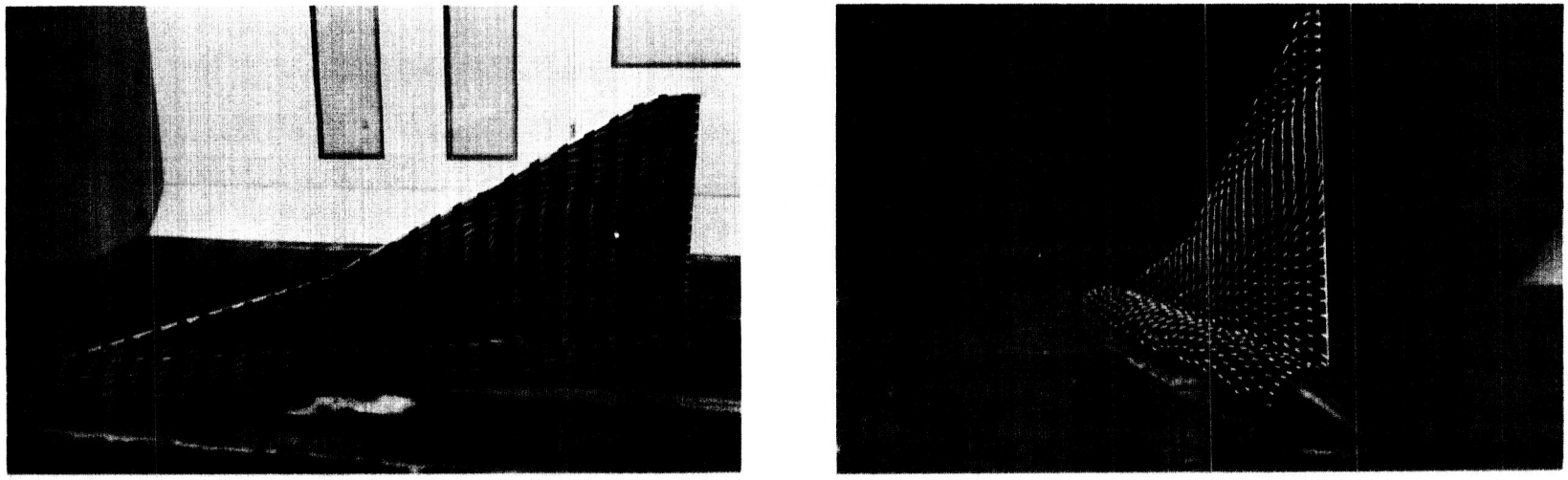

Figure 10d.- $\alpha = 15^{\circ}$.

Figures 10c, 10d.- Tuft photos $75^{\circ}/62^{\circ}$ double-delta wing.

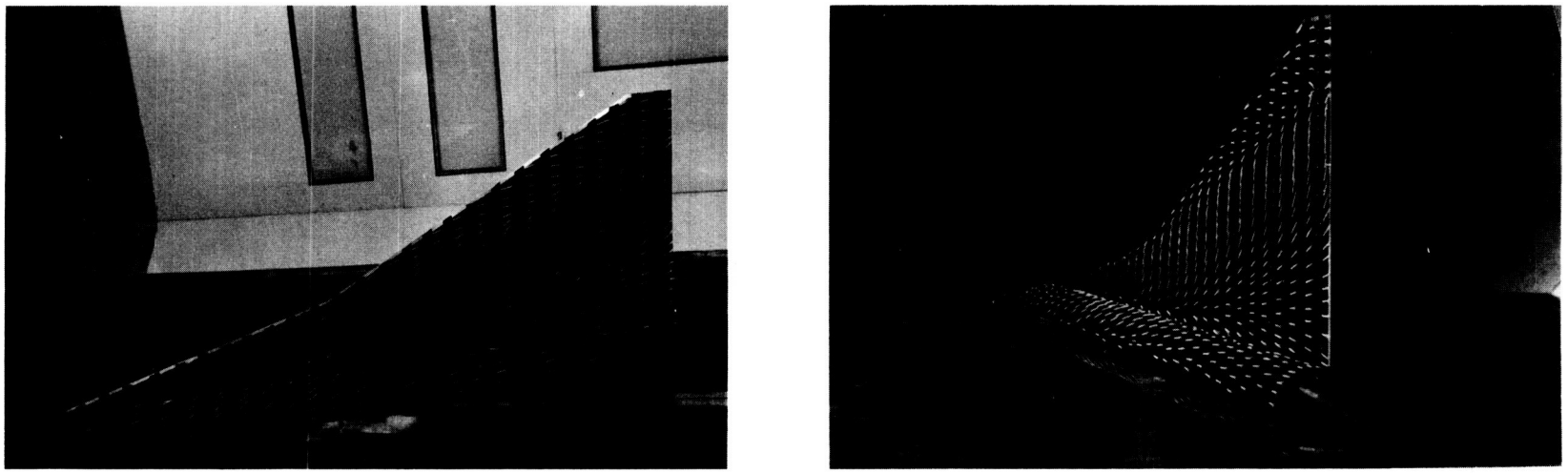

Figure 10e.- $\alpha = 20^{\circ}$.

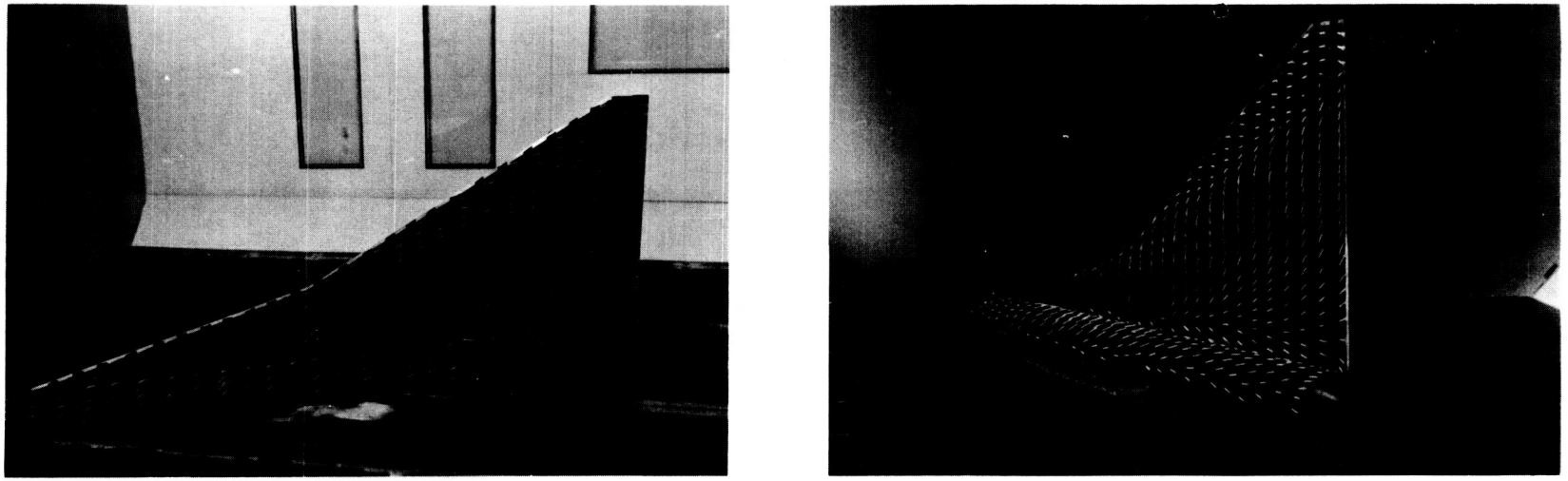

Figure 10f.- $\alpha = 25^{\circ}$.

Figures 10e, 10f.- Tuft photos $75^{\circ}/62^{\circ}$ double-delta wing.

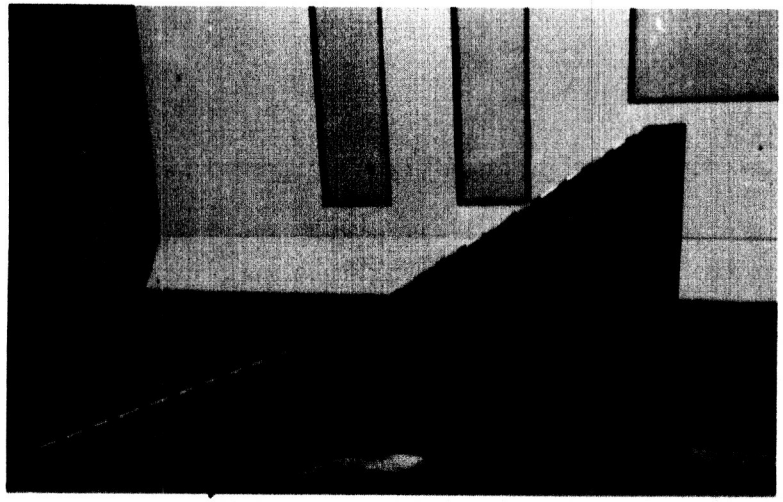

Figure 10g.- $\alpha = 30^{\circ}$.

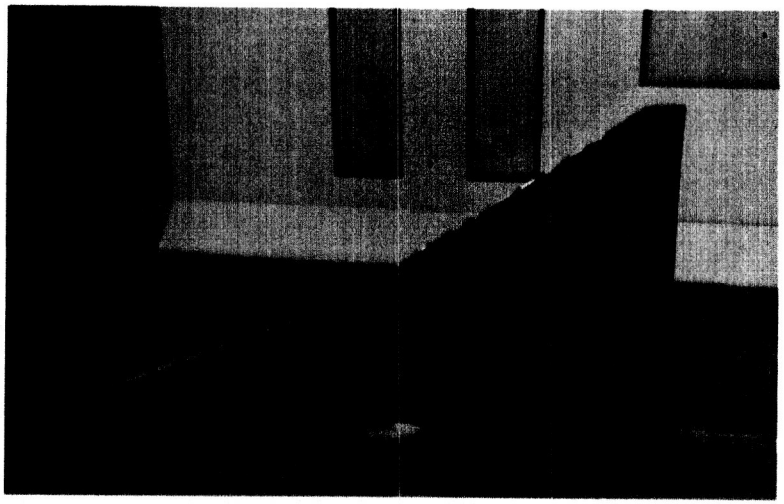

Figure 10h.- $\alpha = 35^{\circ}$.

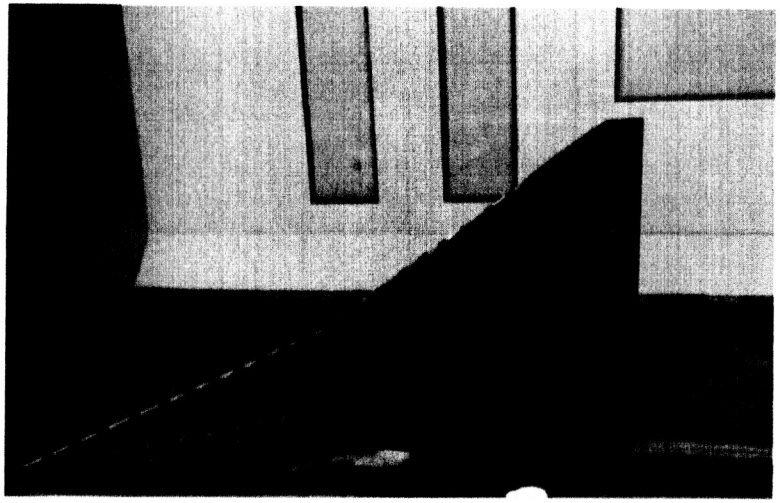

Figure 10i.- $\alpha = 40^{\circ}$.

Figures 10g, 10h, 10i.- Tuft photos $75^{\circ}/62^{\circ}$ double-delta wing.

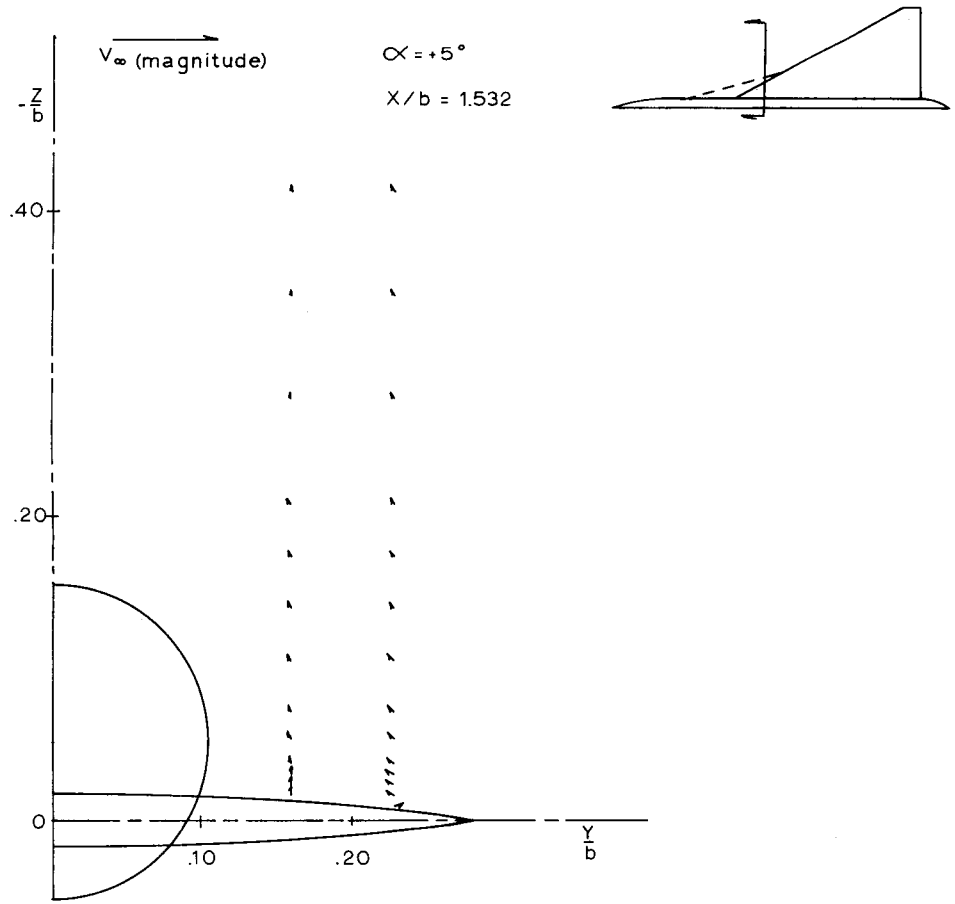

Figure 11a.- Upper surface flow field. $\alpha = 5^{o}$; x/b = 1.532.

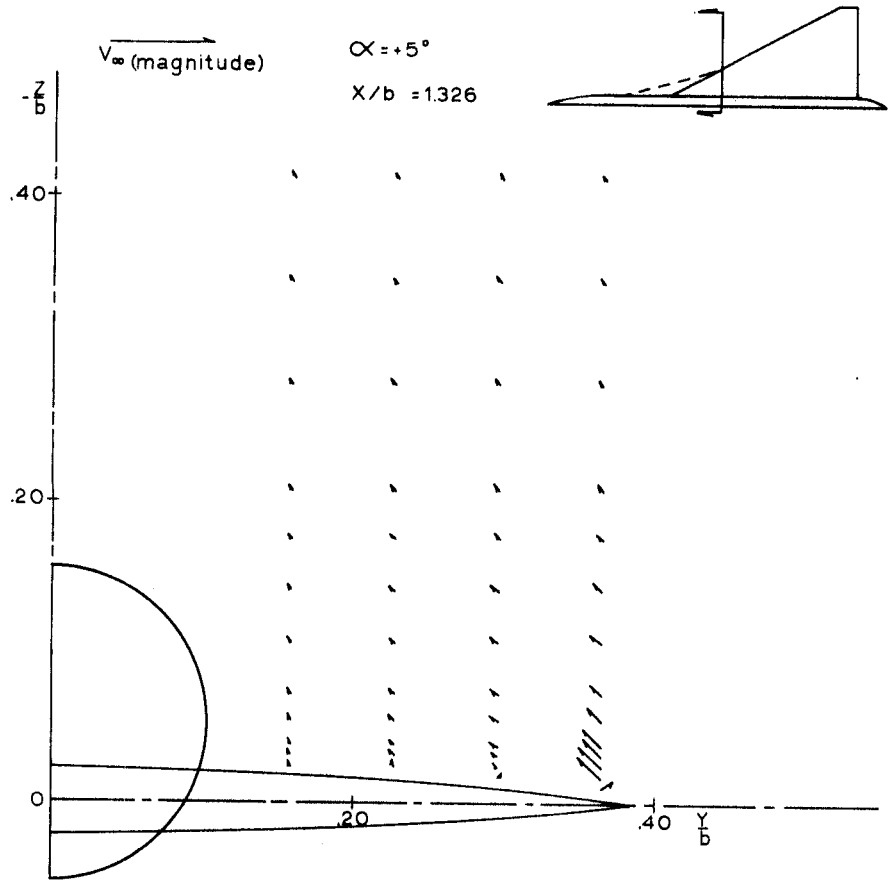

Figure 11b.- Upper surface flow field. $\alpha = 5^{\circ}$; x/b = 1.326.

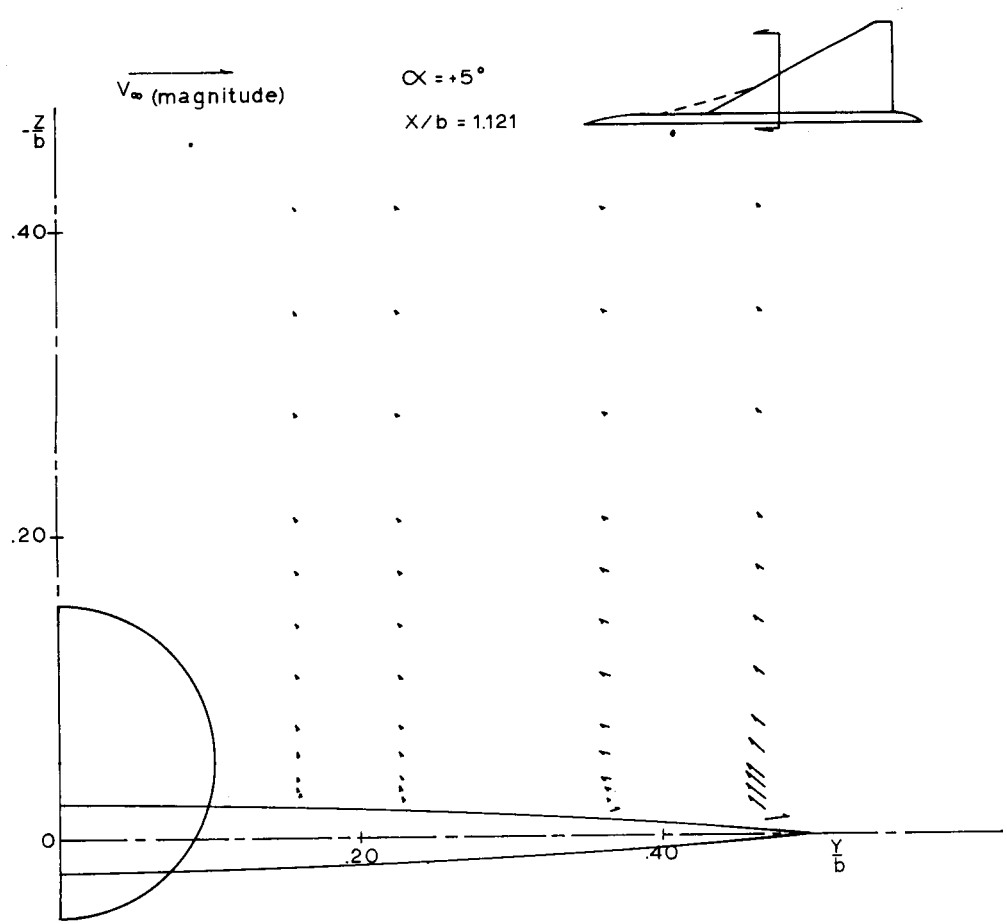

Figure 11c.- Upper surface flow field. $\alpha = 5^{o}$; x/b = 1.121.

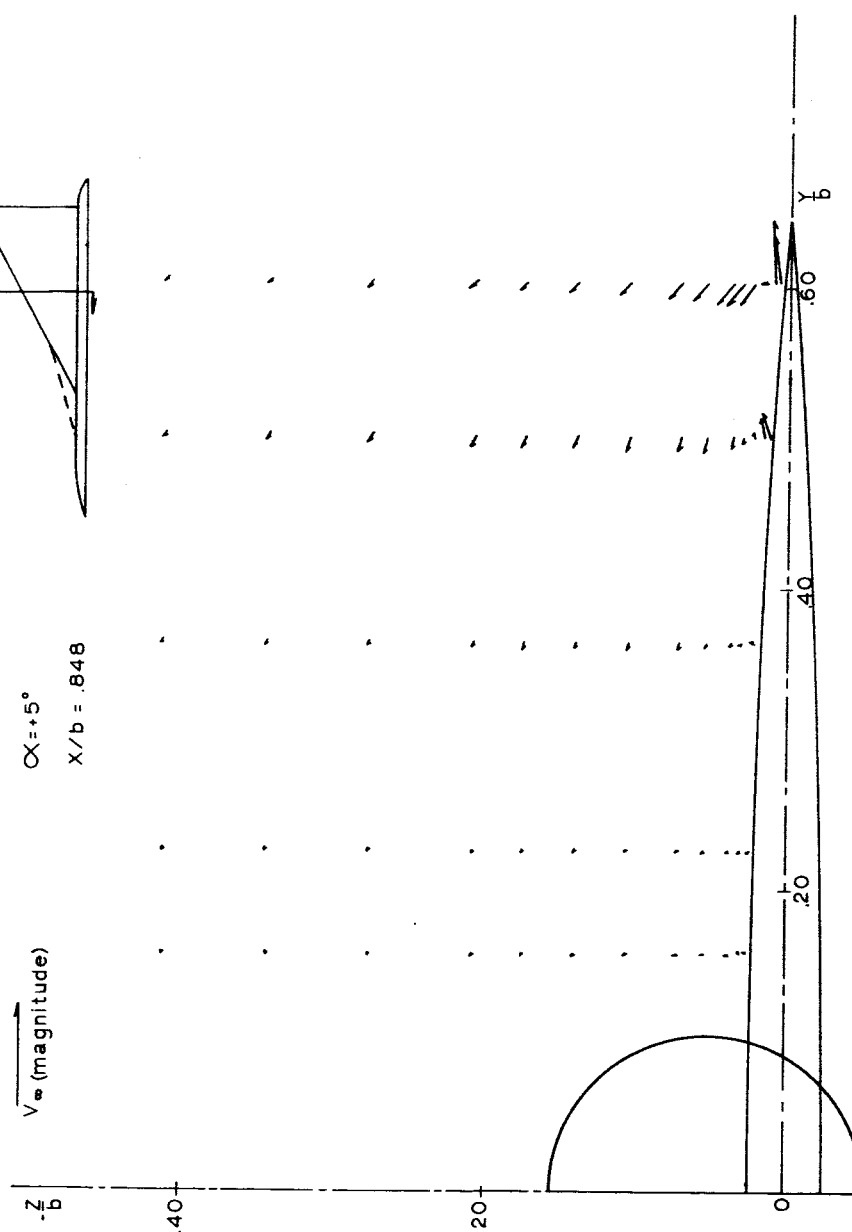

Figure 11d.- Upper surface flow field. $\alpha = 5°$; $x/b = 0.848$.

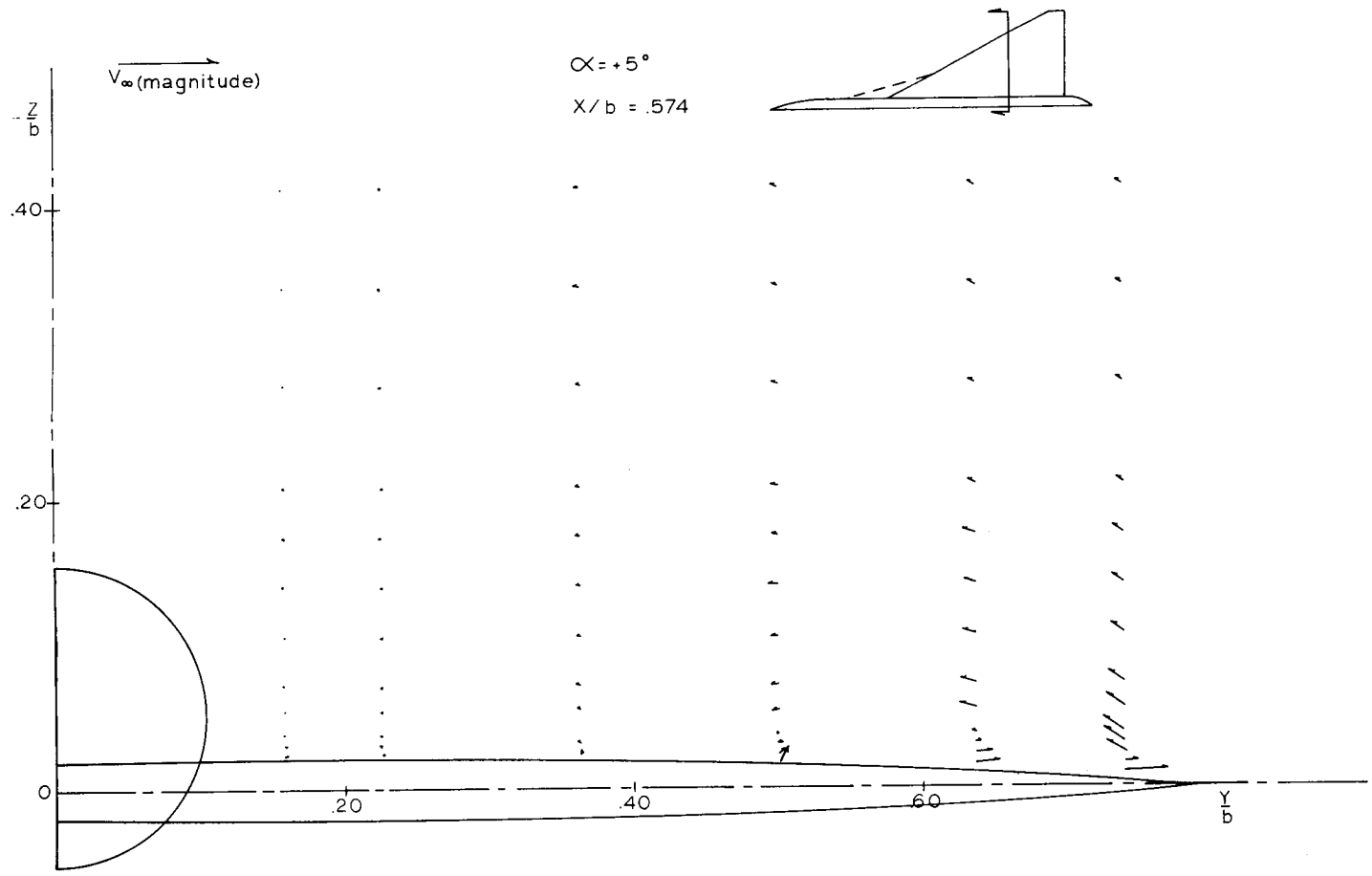

Figure 11e.- Upper surface flow field. $\alpha = 5^{\circ}$; x/b = 0.574.

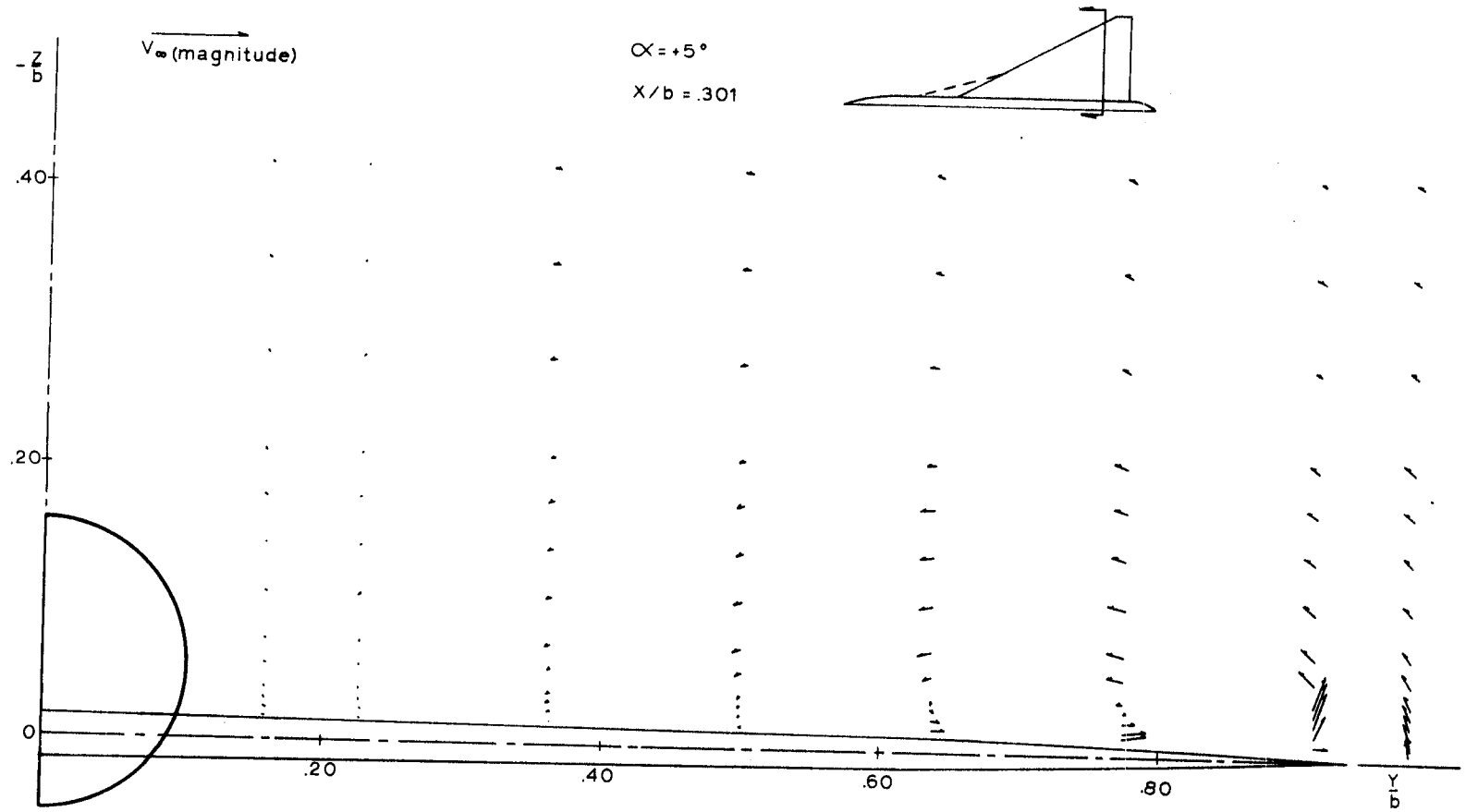

Figure 11f.- Upper surface flow field. $\alpha = 5^{o}$; x/b = 0.301.

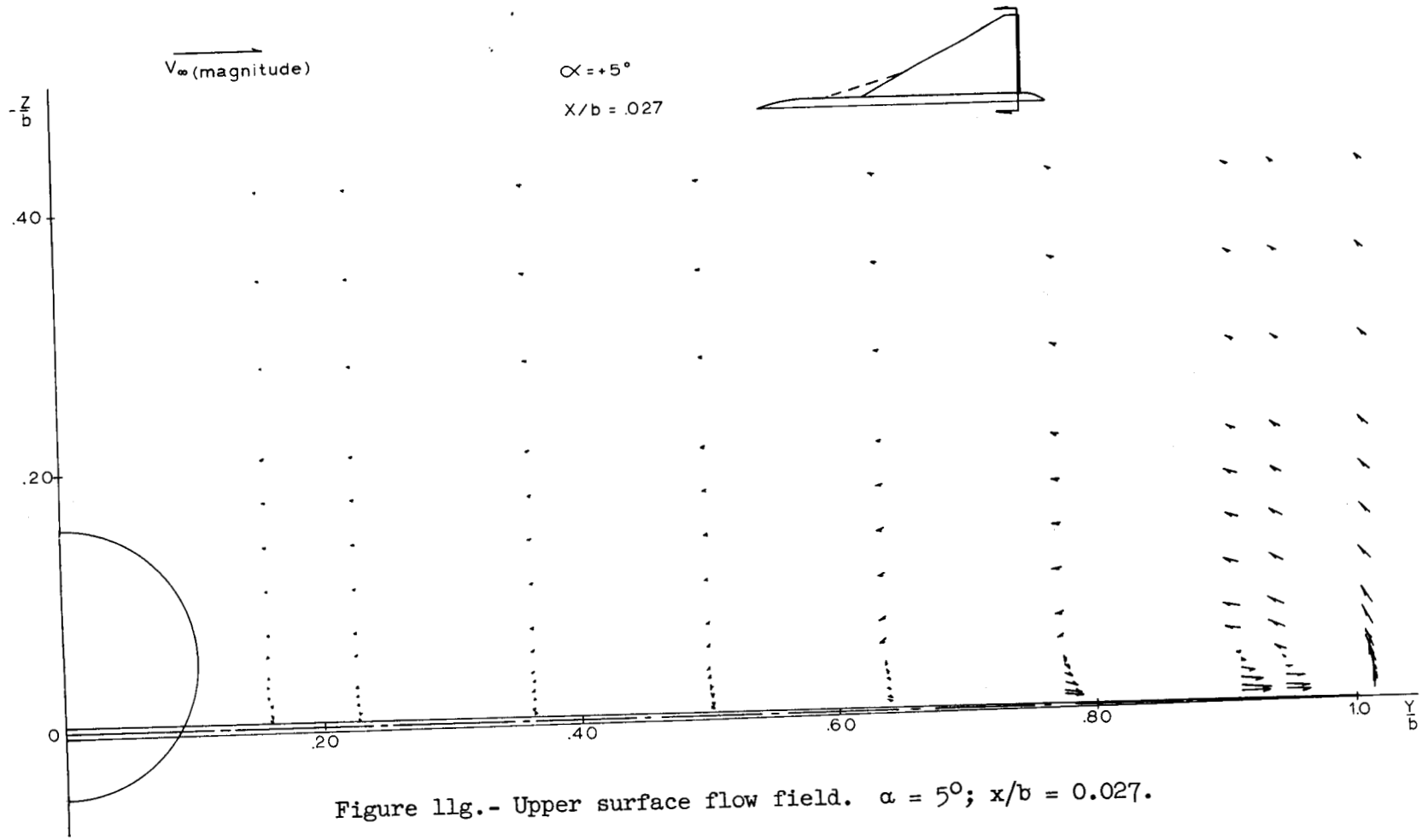

Figure 11g.- Upper surface flow field. $\alpha = 5^{\circ}$; x/b = 0.027.

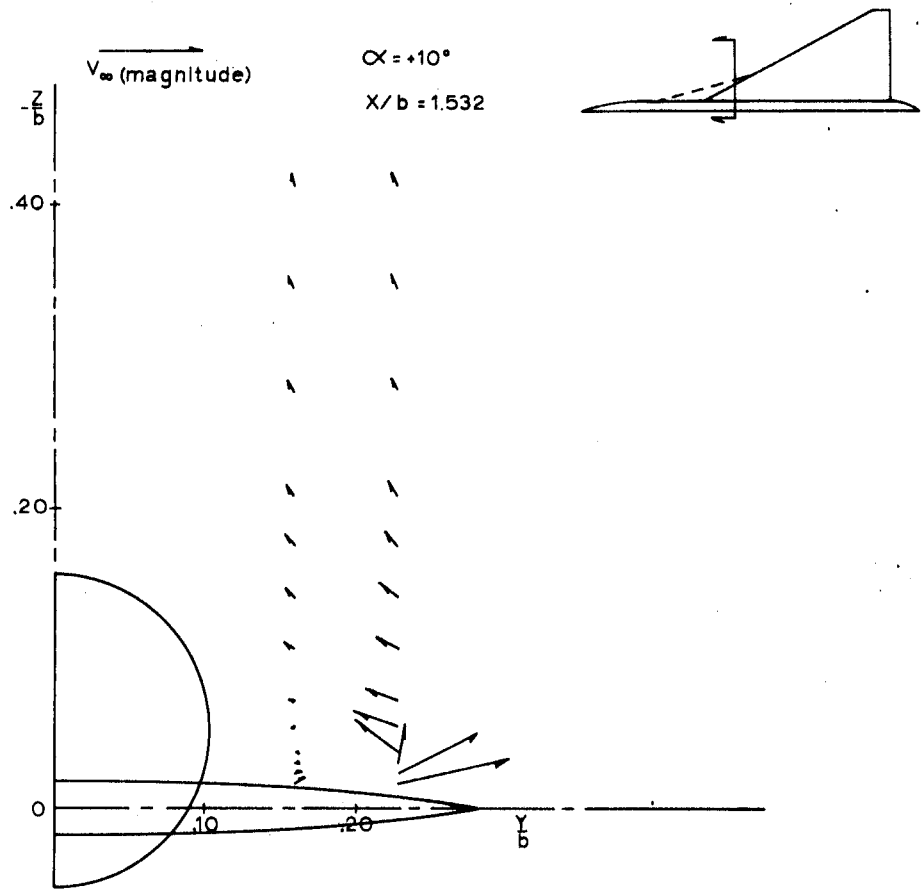

Figure 11h.- Upper surface flow field. $\alpha = 10^{\circ}$; $x/b = 1.532$.

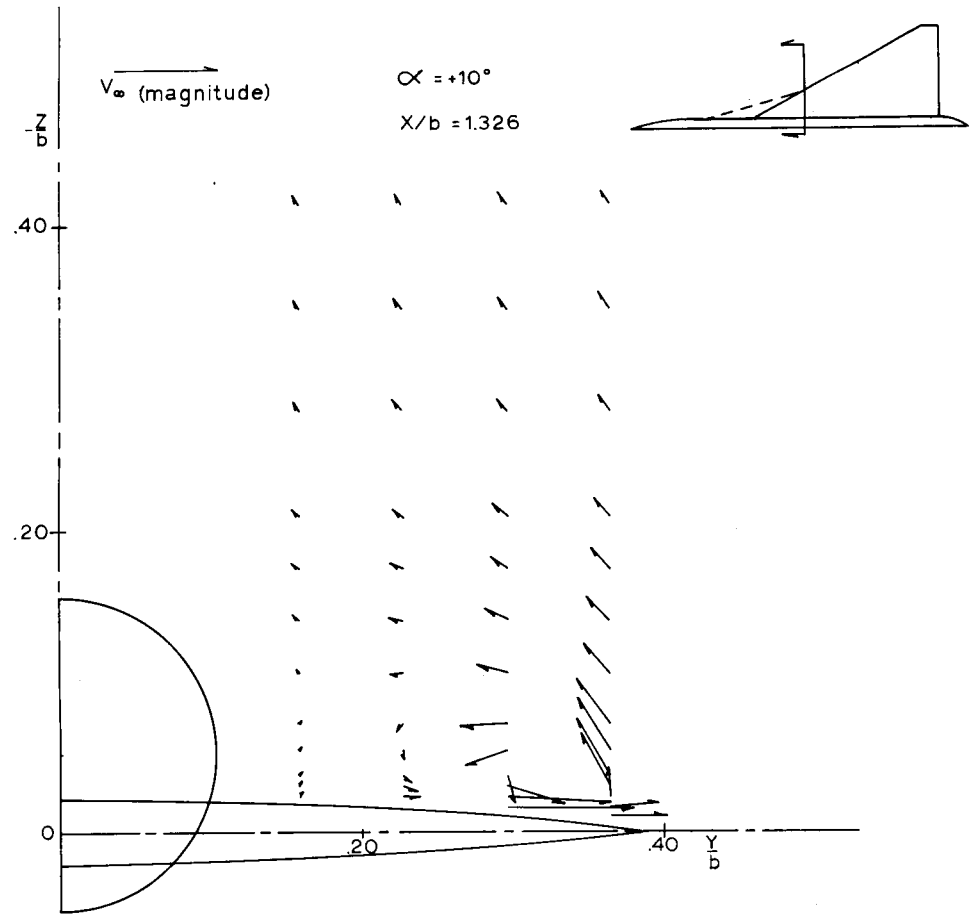

Figure 11i.- Upper surface flow field. $\alpha = 10^{o}$; x/b = 1.326.

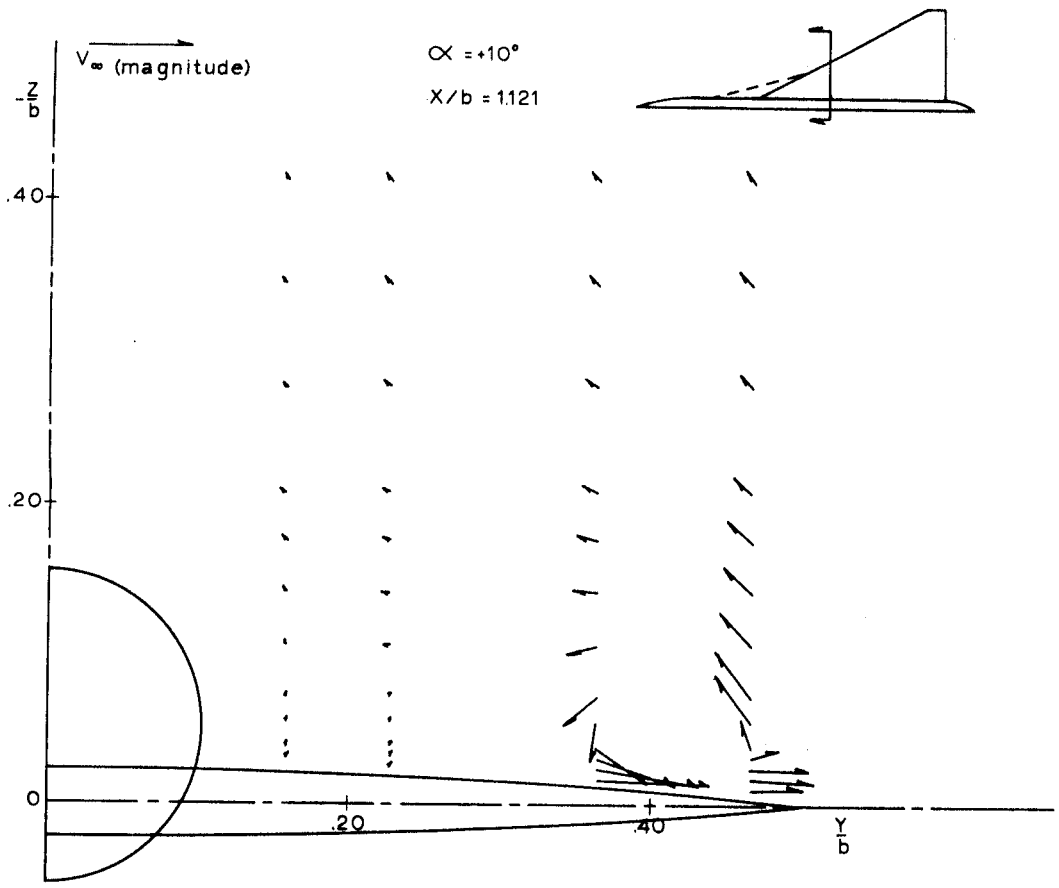

Figure 11j.- Upper surface flow field. $\alpha = 10^{\circ}$; $x/b = 1.121$.

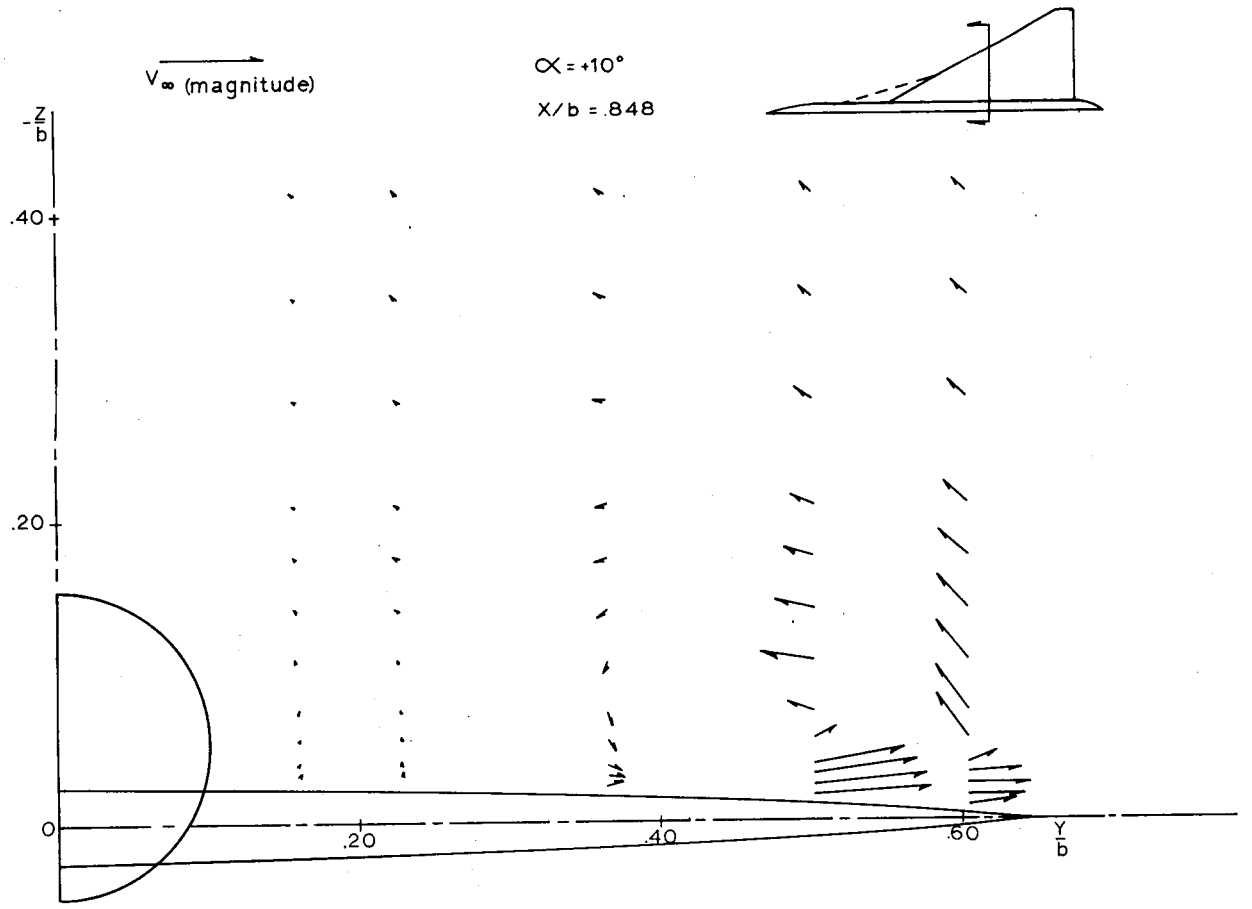

Figure 11k.- Upper surface flow field. $\alpha = 10^{o}$; x/b = 0.848.

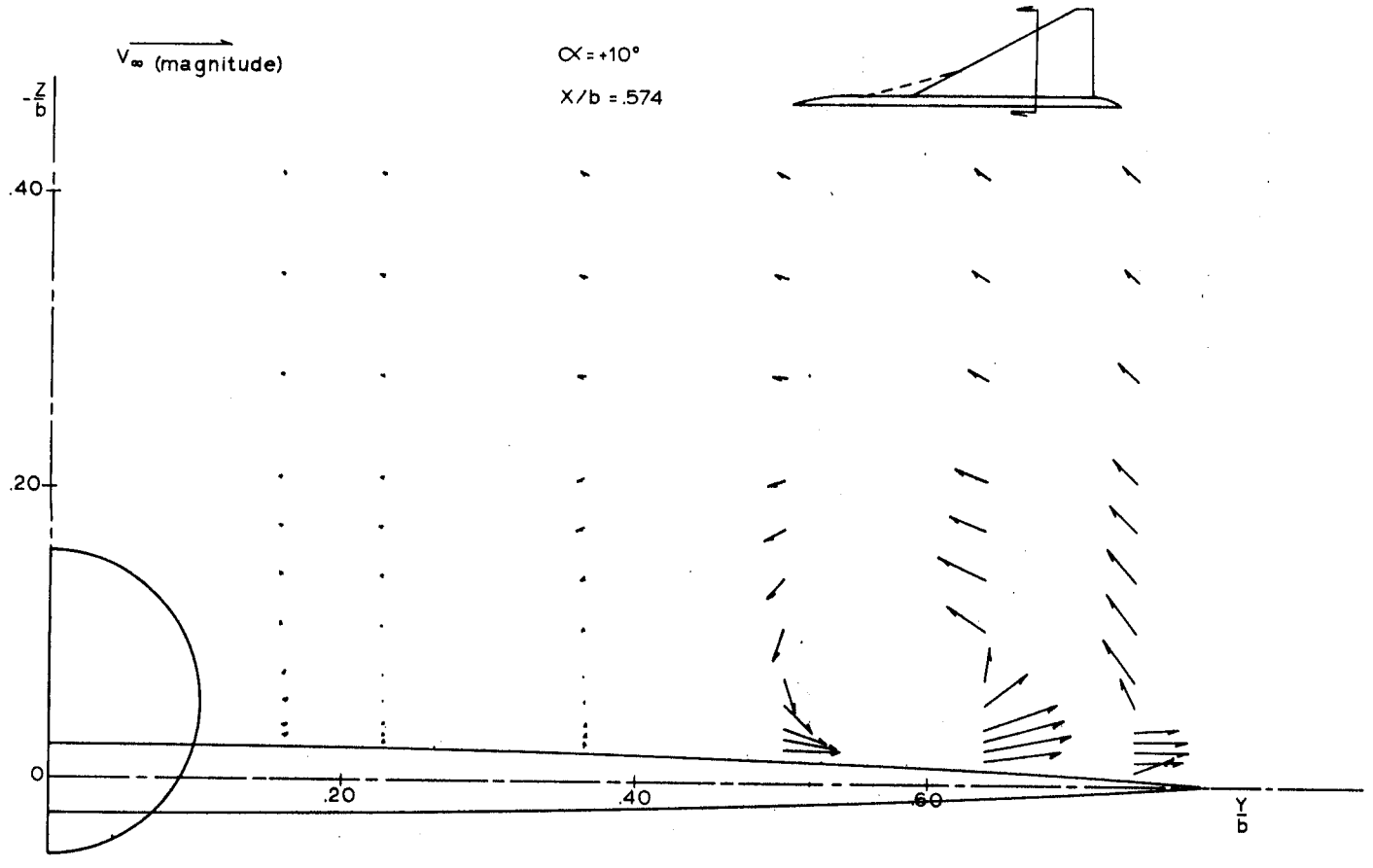

Figure 111.- Upper surface flow field. $\alpha = 10^{o}$; $x/b = 0.574$.

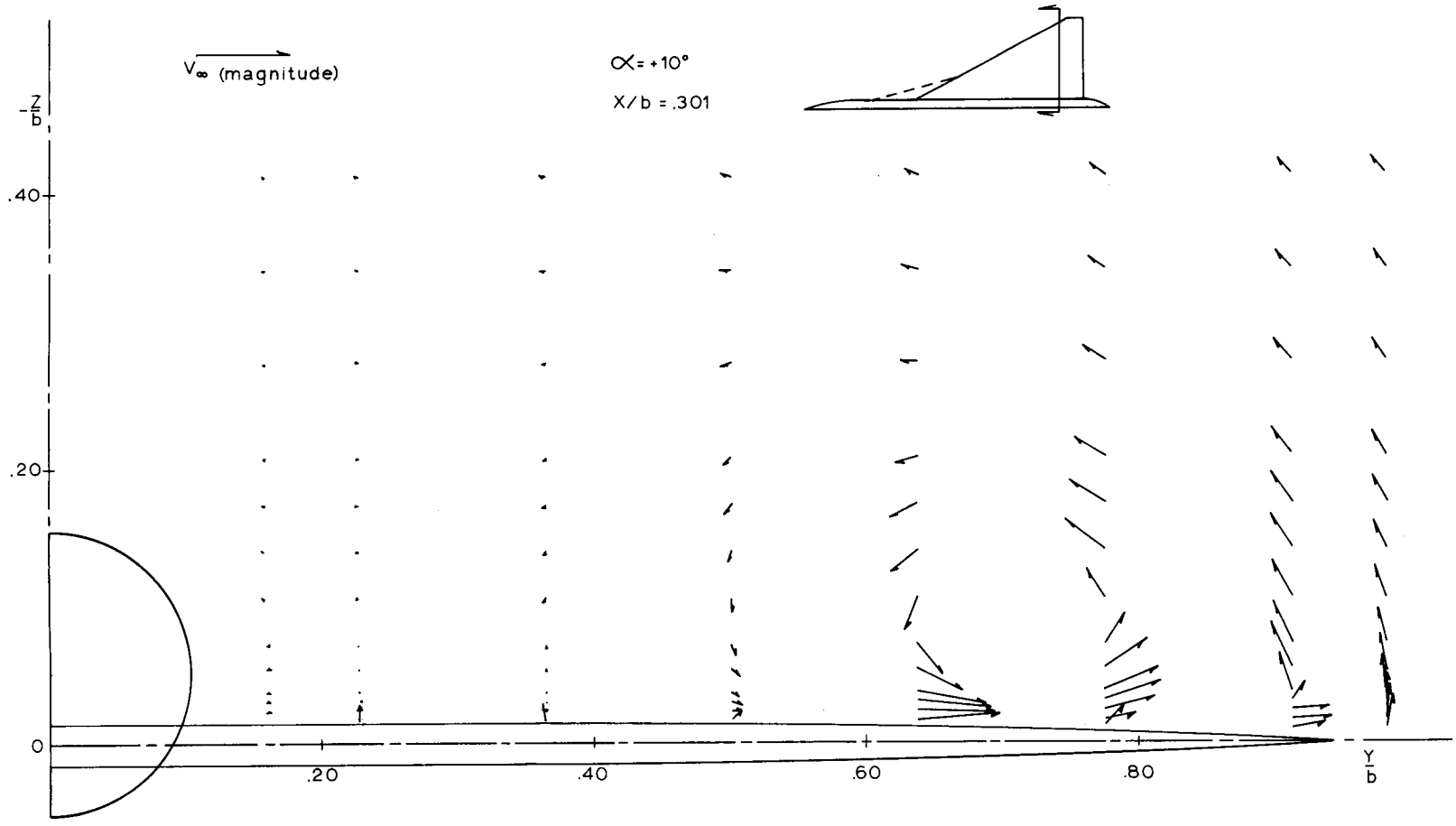

Figure 11m.- Upper surface flow field. $\alpha = 10^{\circ}$; $x/b = 0.301$.

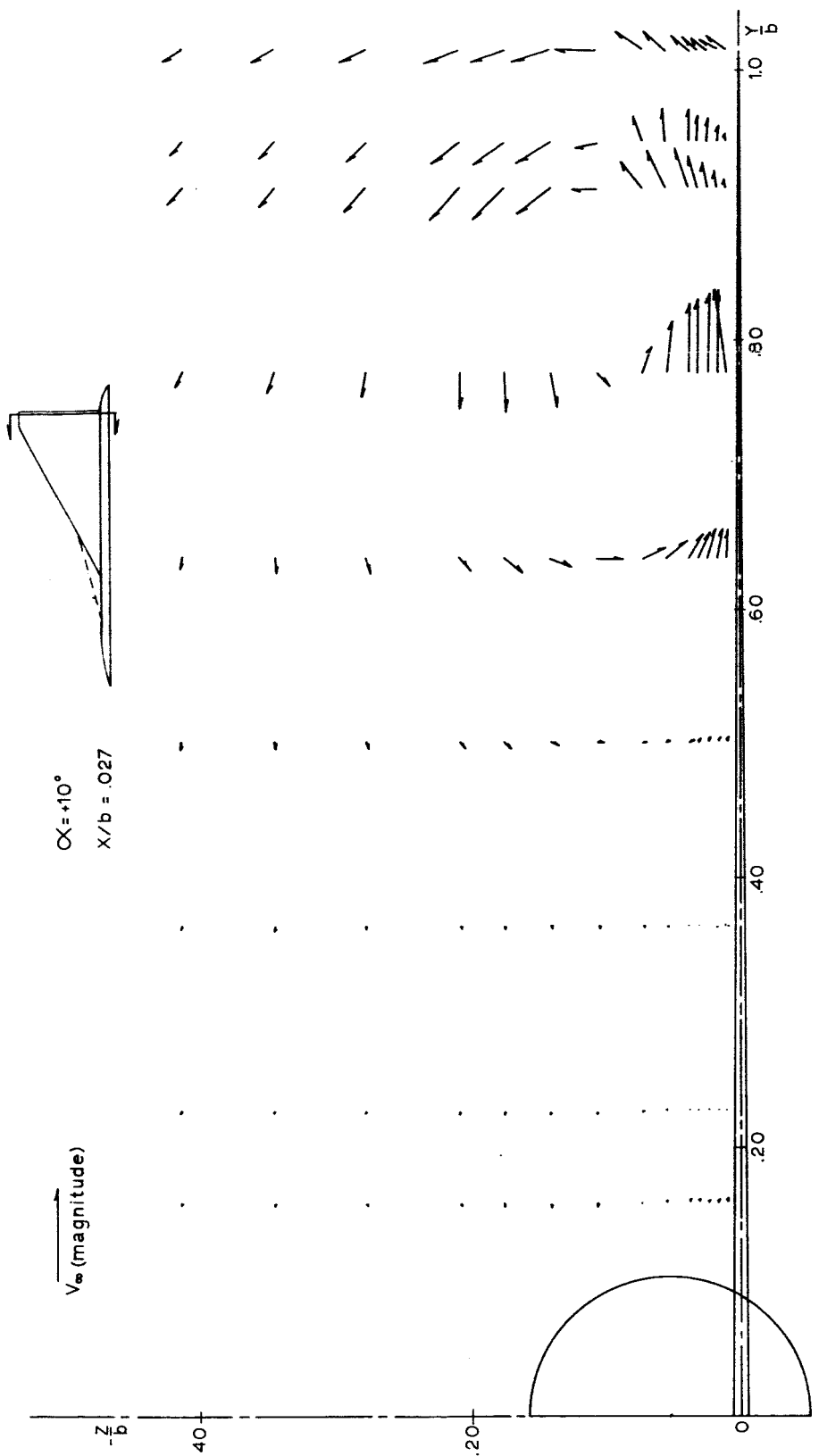

Figure 11n.- Upper surface flow field. $\alpha = 10^{\circ}$; x/b = 0.027.

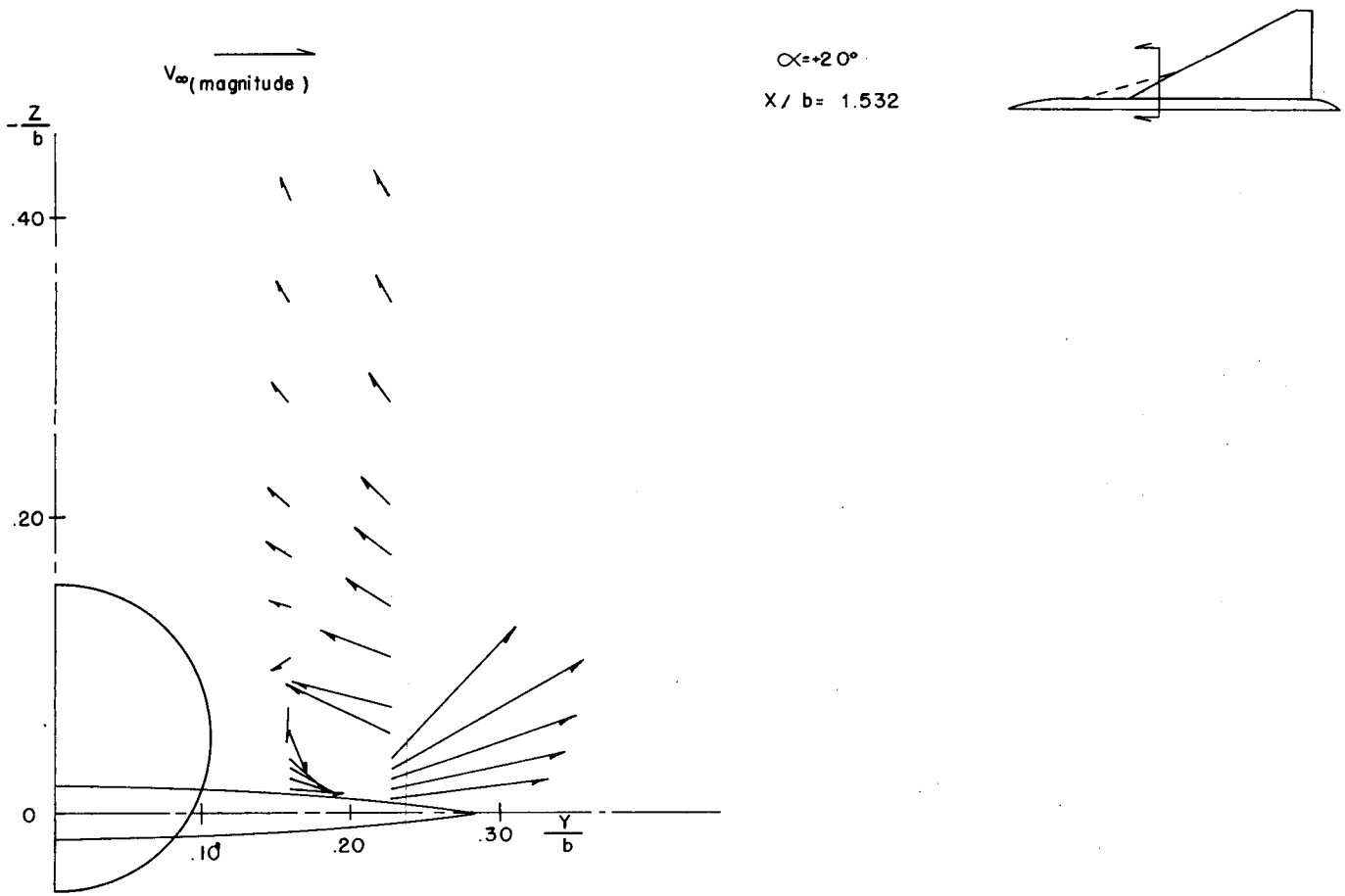

Figure 11o.- Upper surface flow field. $\alpha = 20^{\circ}$; $x/b = 1.532$.

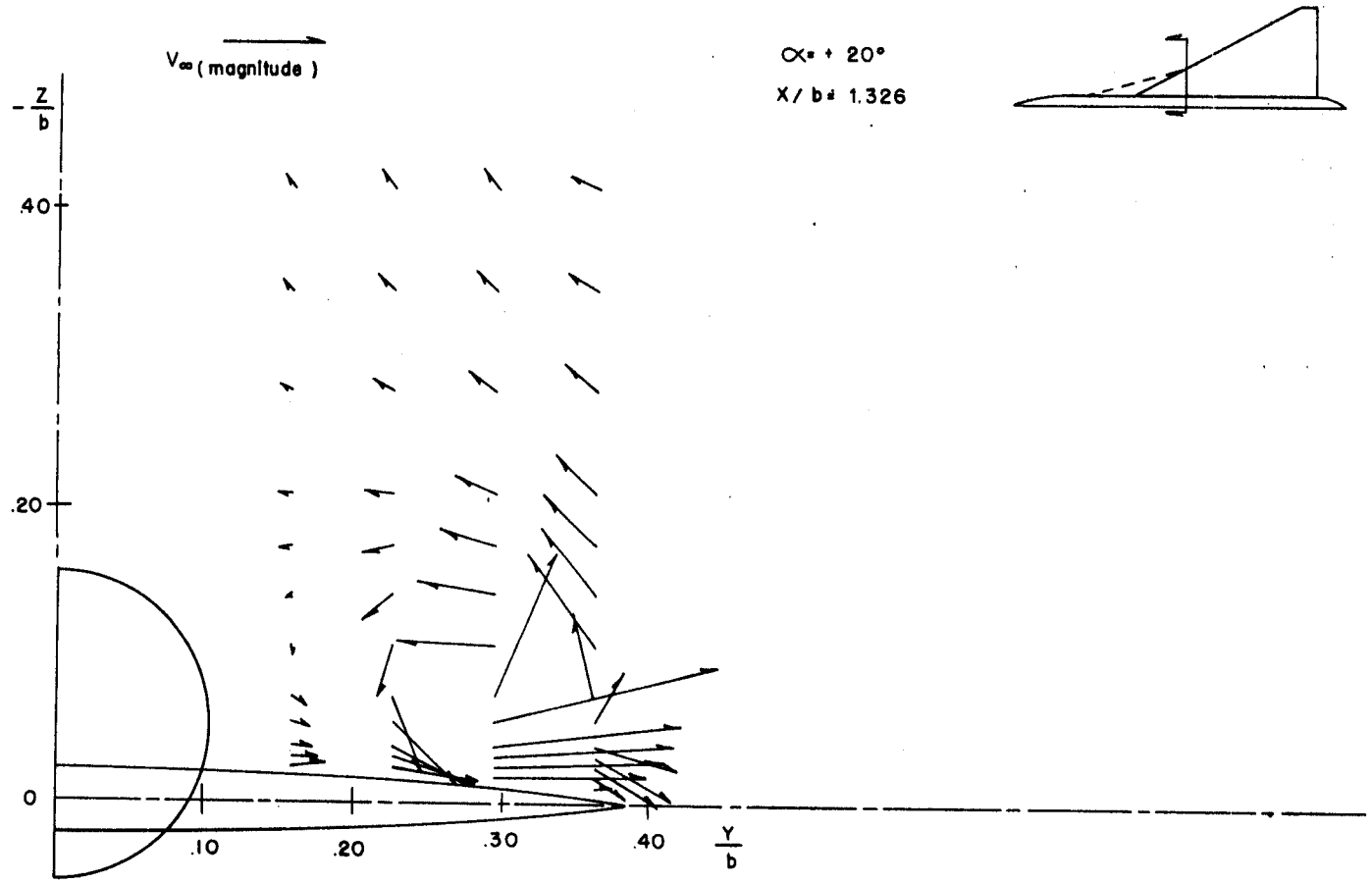

Figure 11p.- Upper surface flow field. $\alpha = 20^{\circ}$; $x/b = 1.326$.

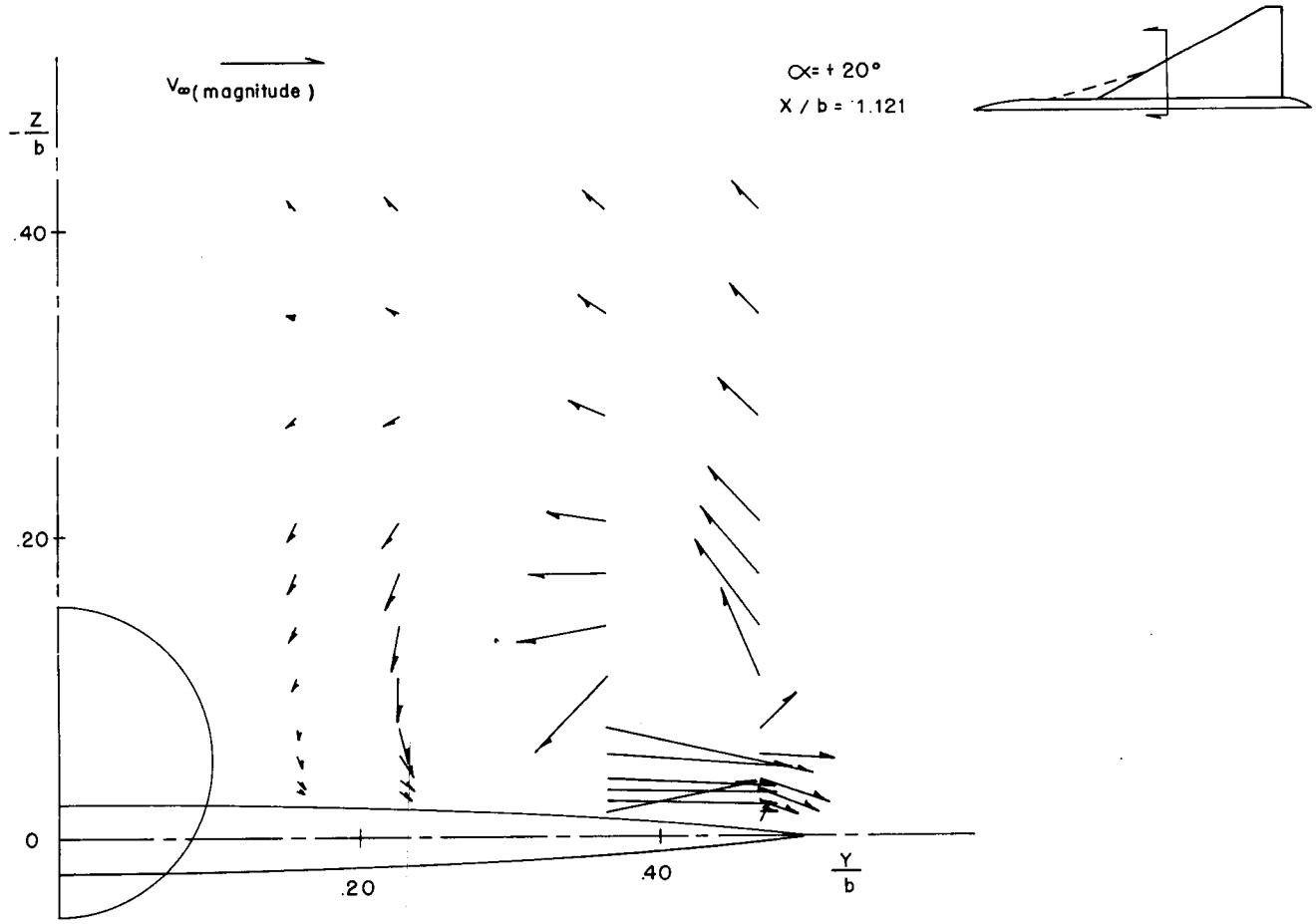

Figure 11q.- Upper surface flow field. $\alpha = 20^{\circ}$; $x/b = 1.121$.

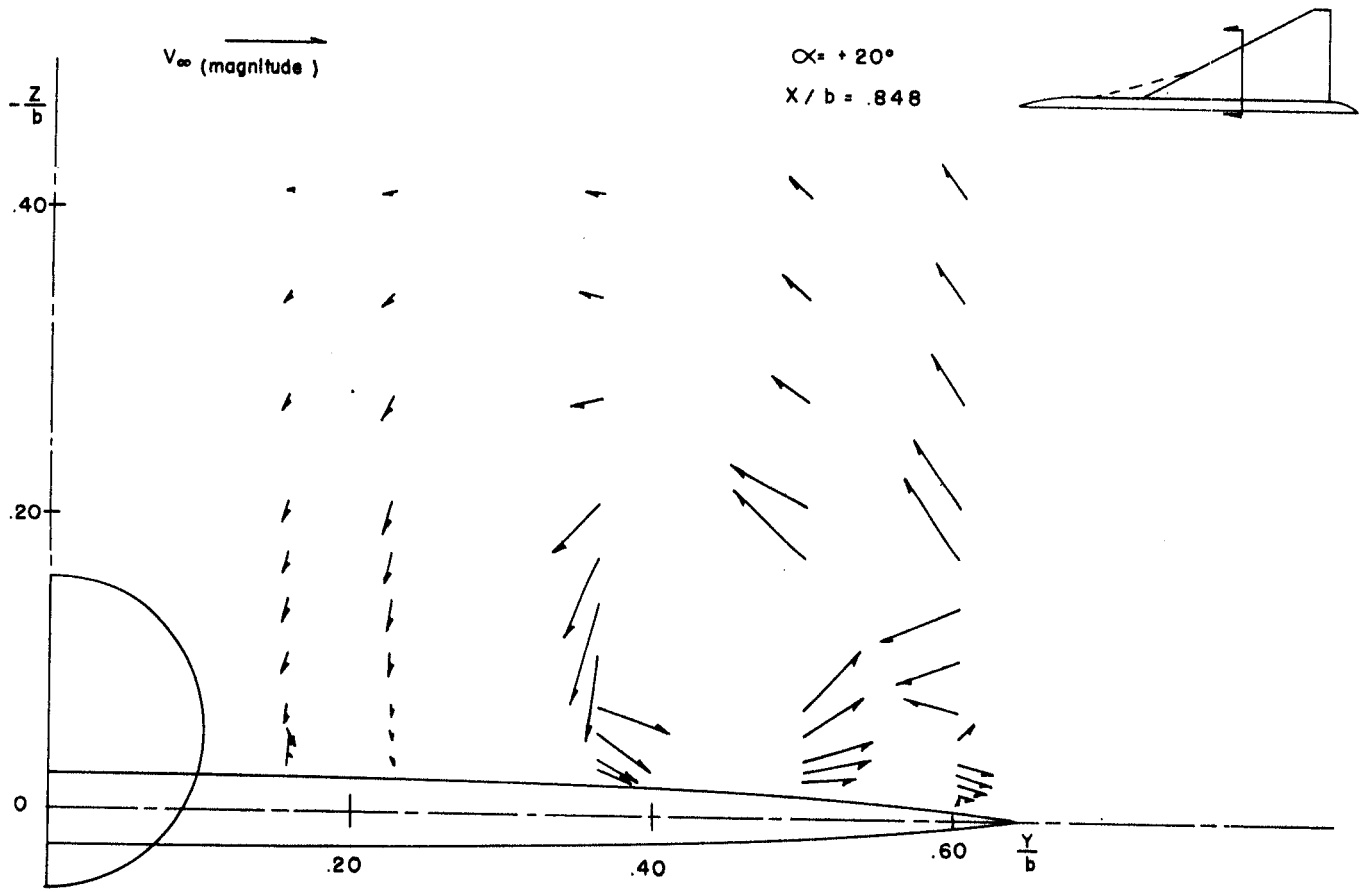

Figure 11r.- Upper surface flow field. $\alpha = 20^{\circ}$; $x/b = 0.848$.

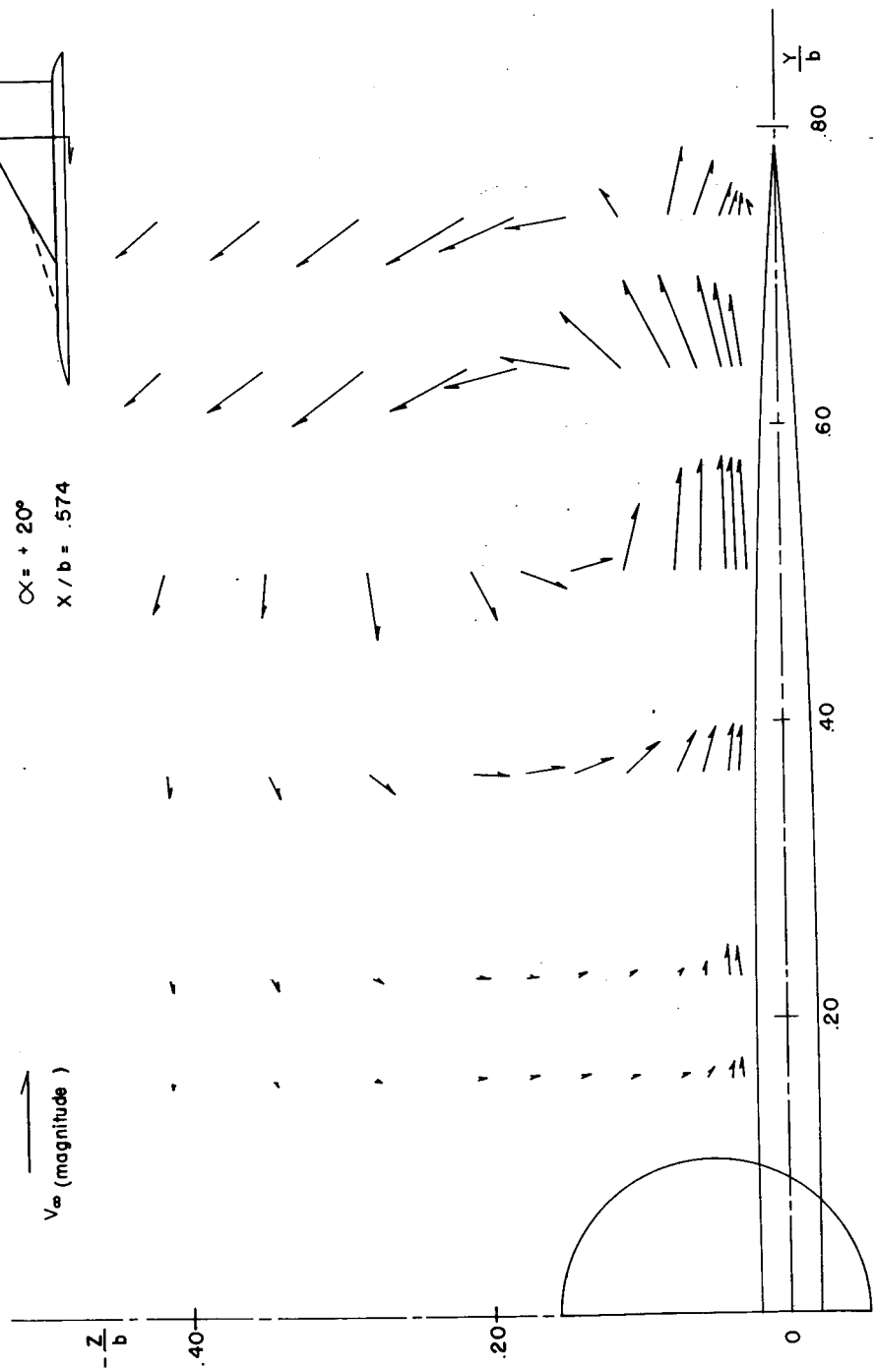

Figure 11s.- Upper surface flow field. $\alpha = 20^{\circ}$; $x/b = 0.574$.

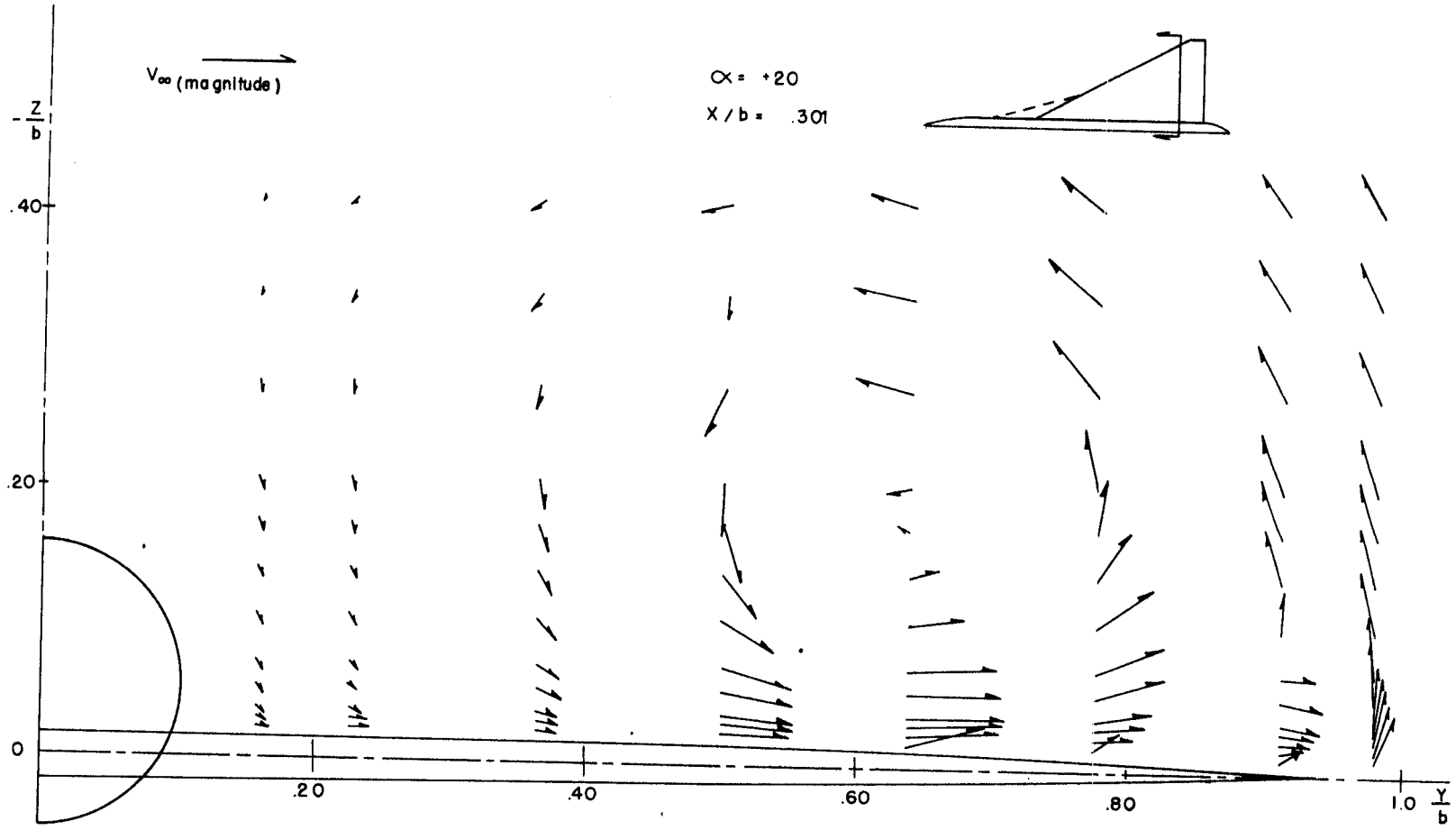

Figure 11t.- Upper surface flow field. $\alpha = 20^{\circ}$; $x/b = 0.301$.

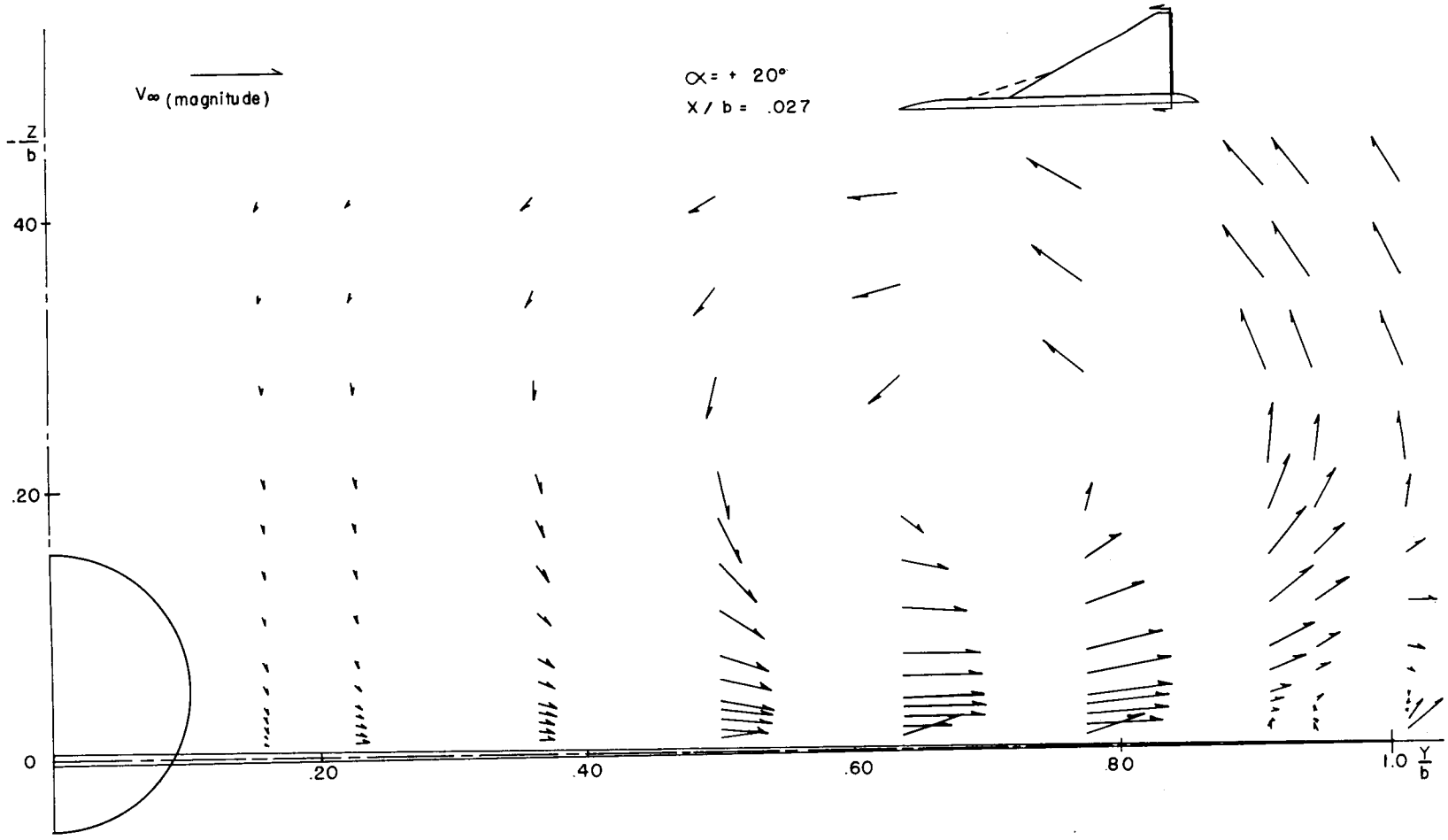

Figure 11u.- Upper surface flow field. $\alpha = 20^{\circ}$; $x/b = 0.027$.

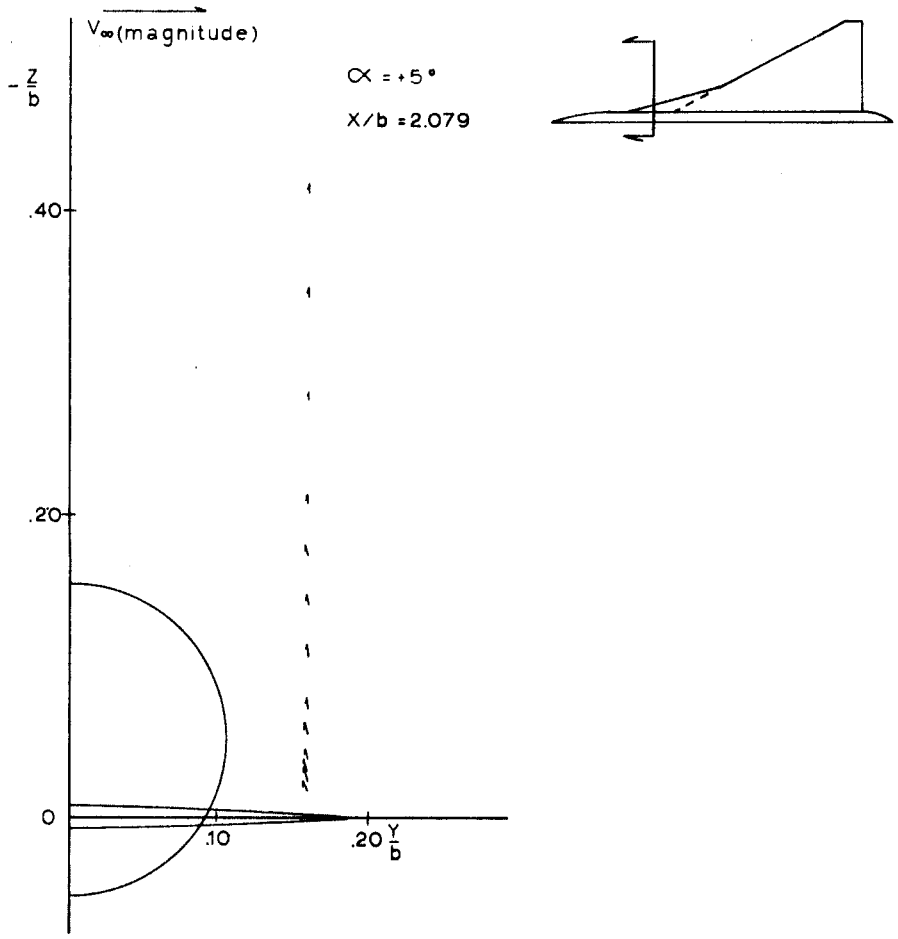

Figure 12a.- Upper surface flow field. $\alpha = 5^{\circ}$; x/b = 2.079.

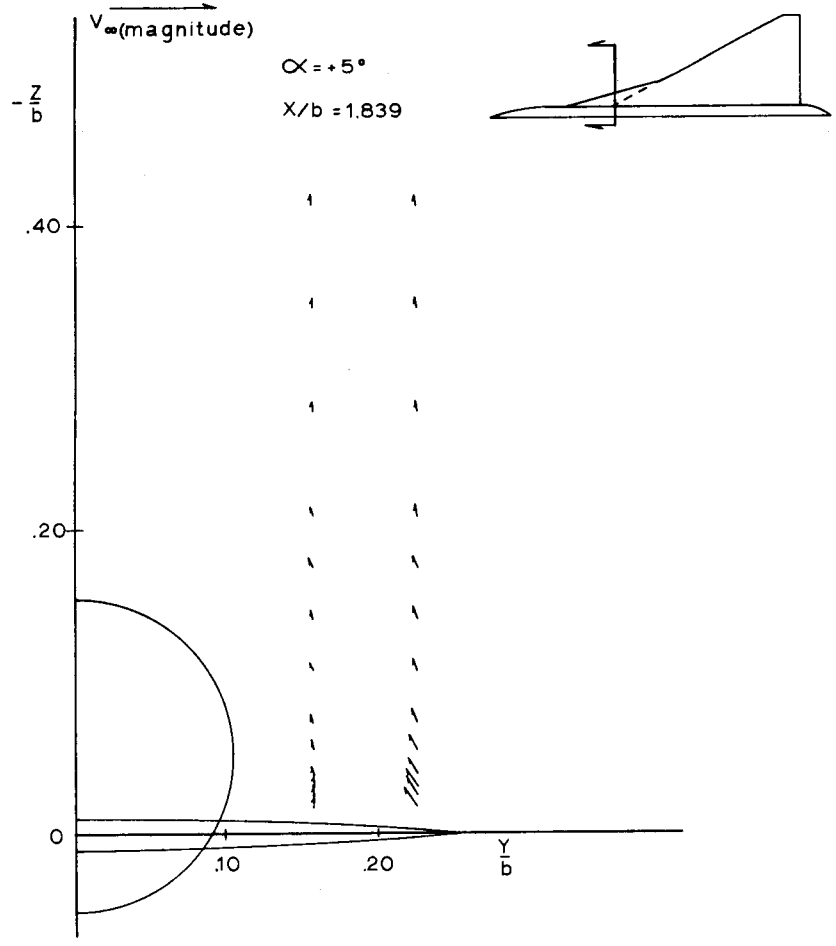

Figure 12b.- Upper surface flow field. $\alpha = 5^{\circ}$; x/b = 1.839.

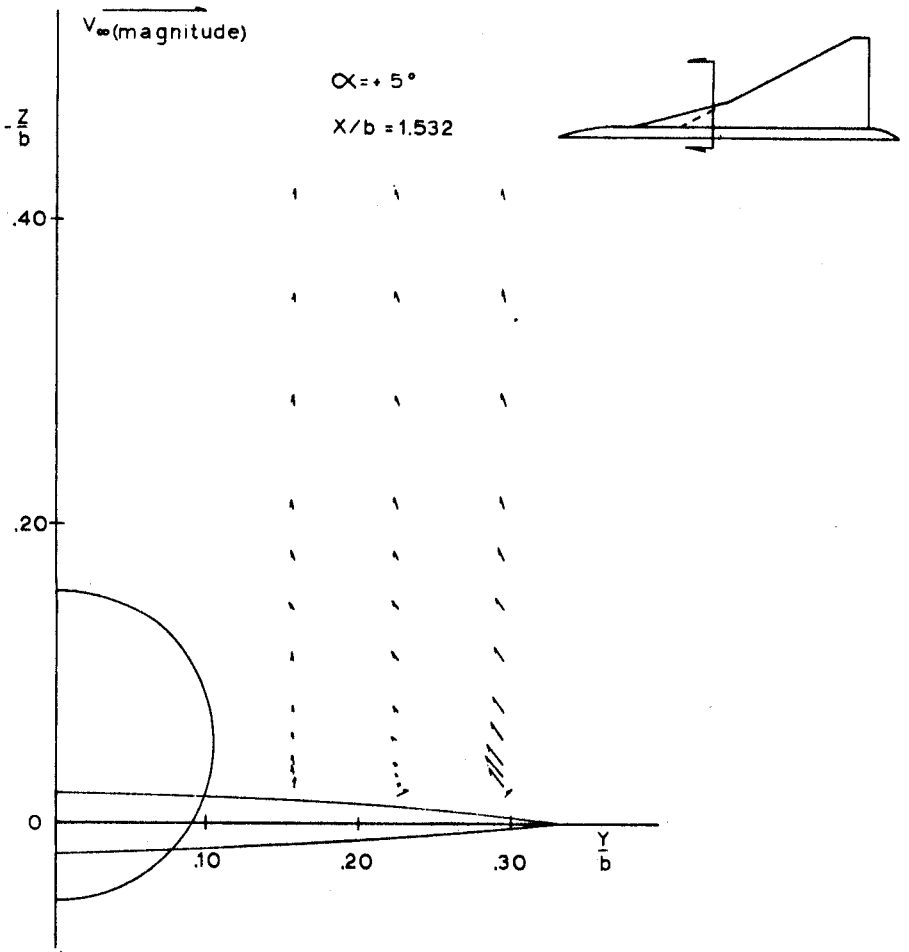

Figure 12c.- Upper surface flow field. $\alpha = 5^{o}$; x/b = 1.532.

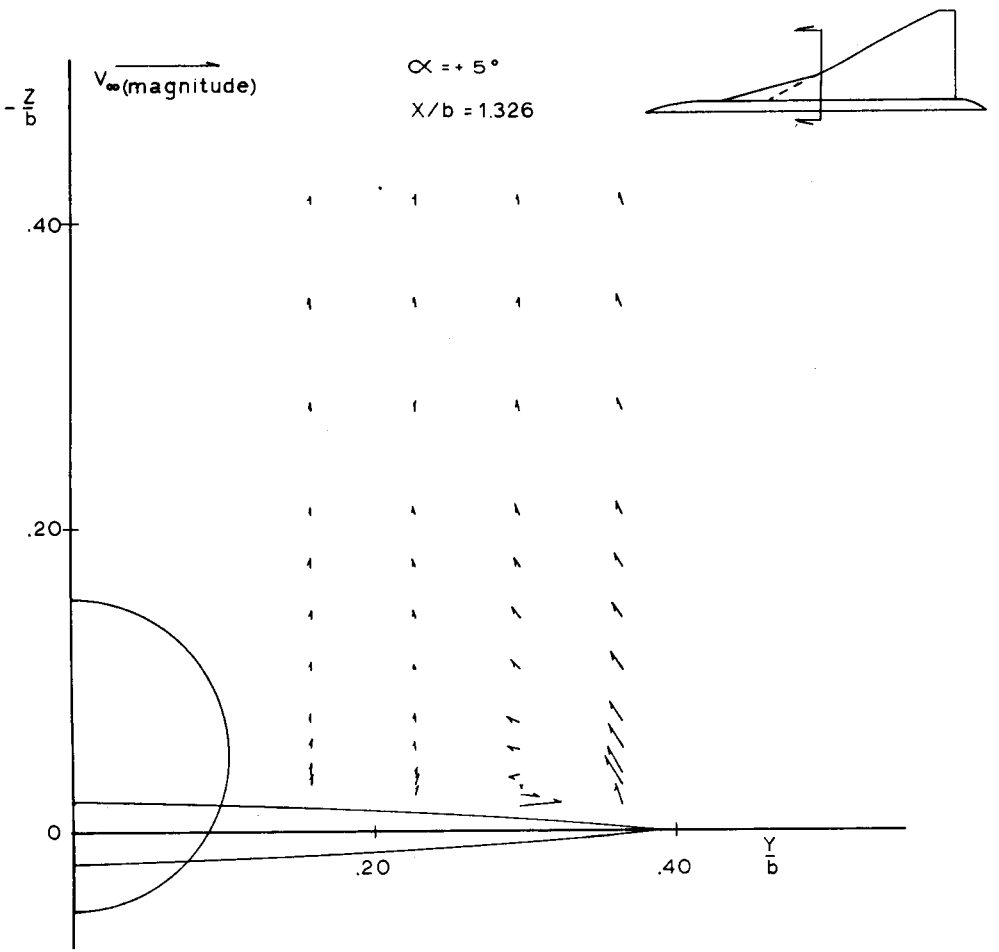

Figure 12d.- Upper surface flow field. $\alpha = 5^{\circ}$; $x/b = 1.326$.

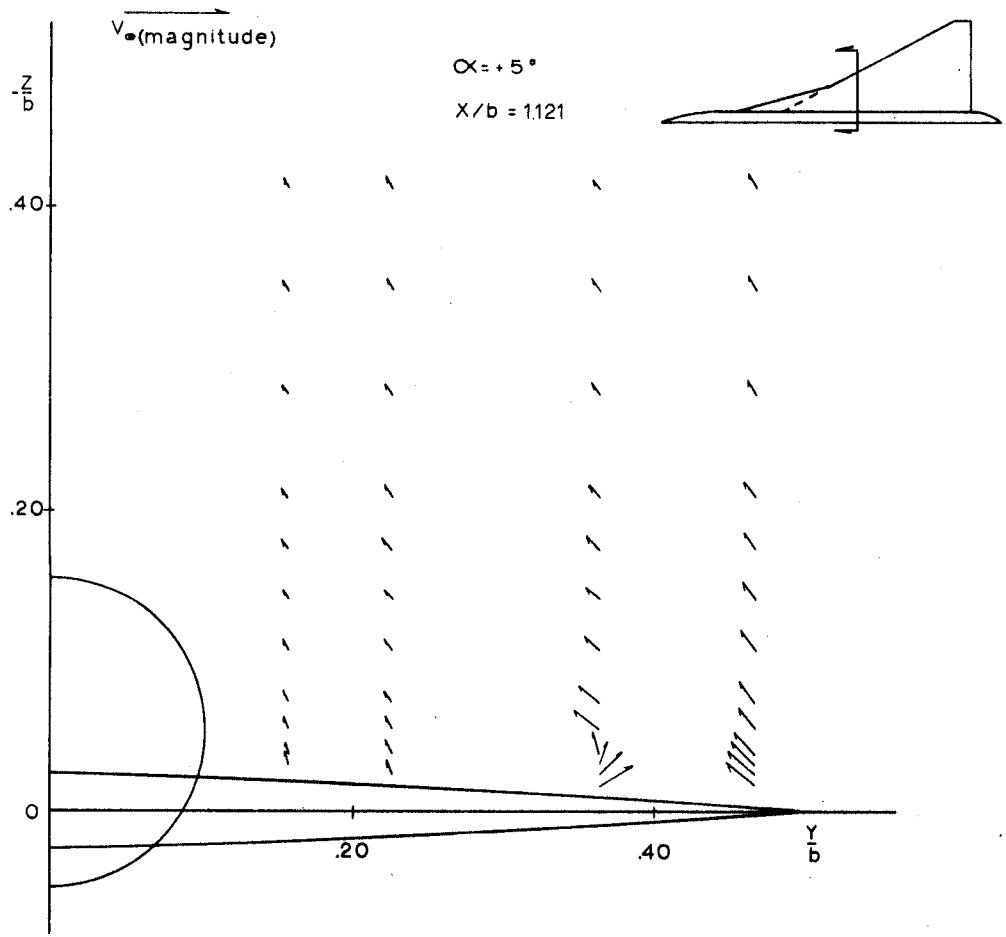

Figure 12e.- Upper surface flow field. $\alpha = 5^{\circ}$; $x/b = 1.121$.

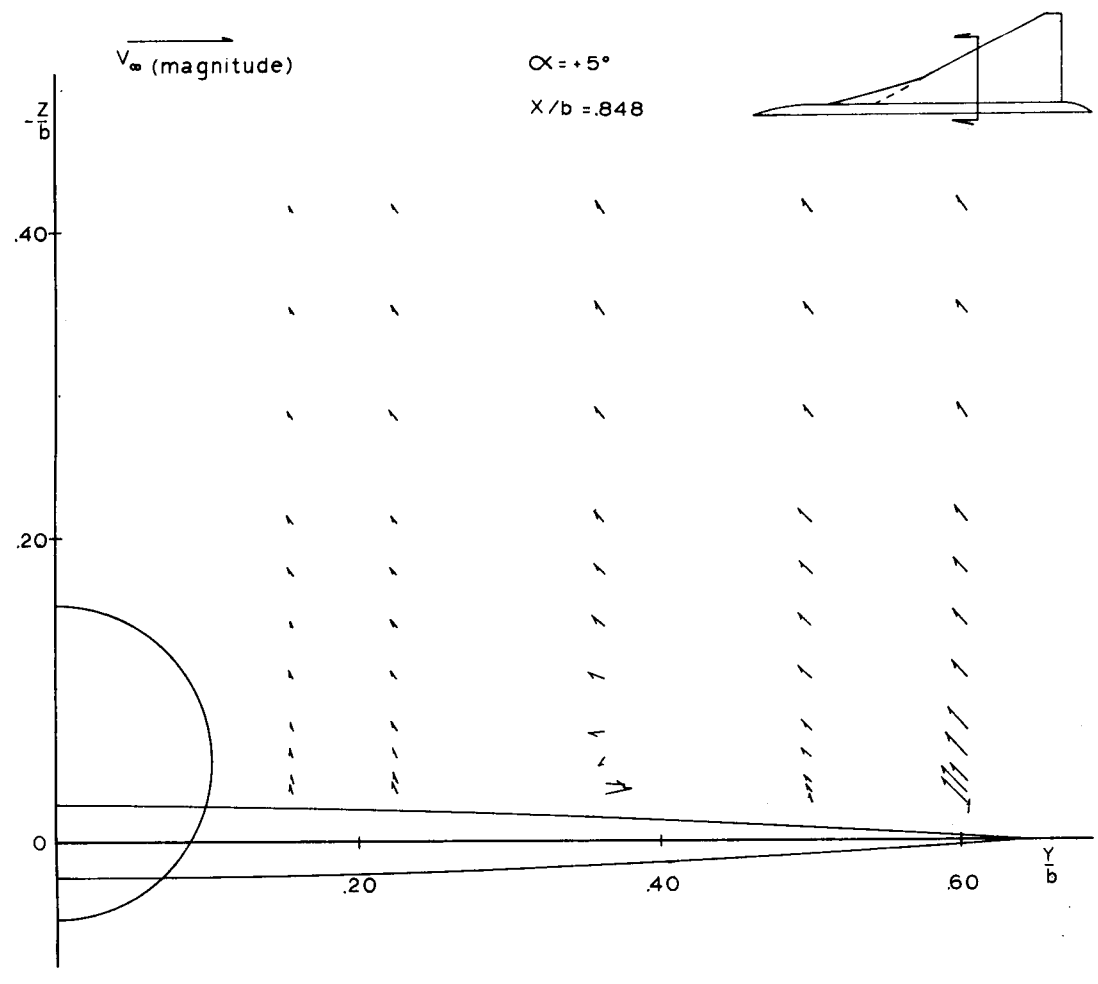

Figure 12f.- Upper surface flow field. $\alpha = 5^{o}$; x/b = 0.848.

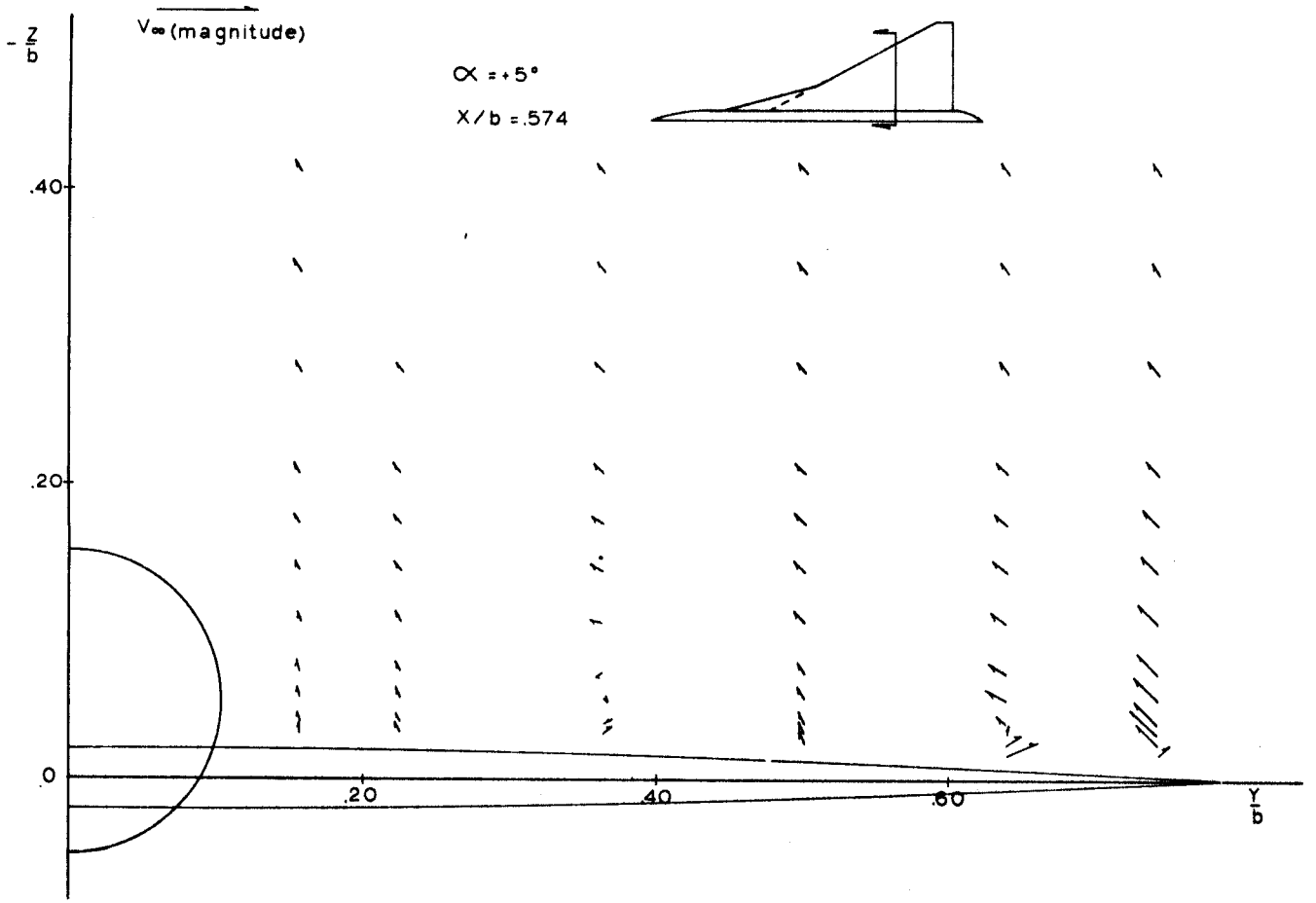

Figure 12g.- Upper surface flow field. $\alpha = 5^{o}$; $x/b = 0.574$.

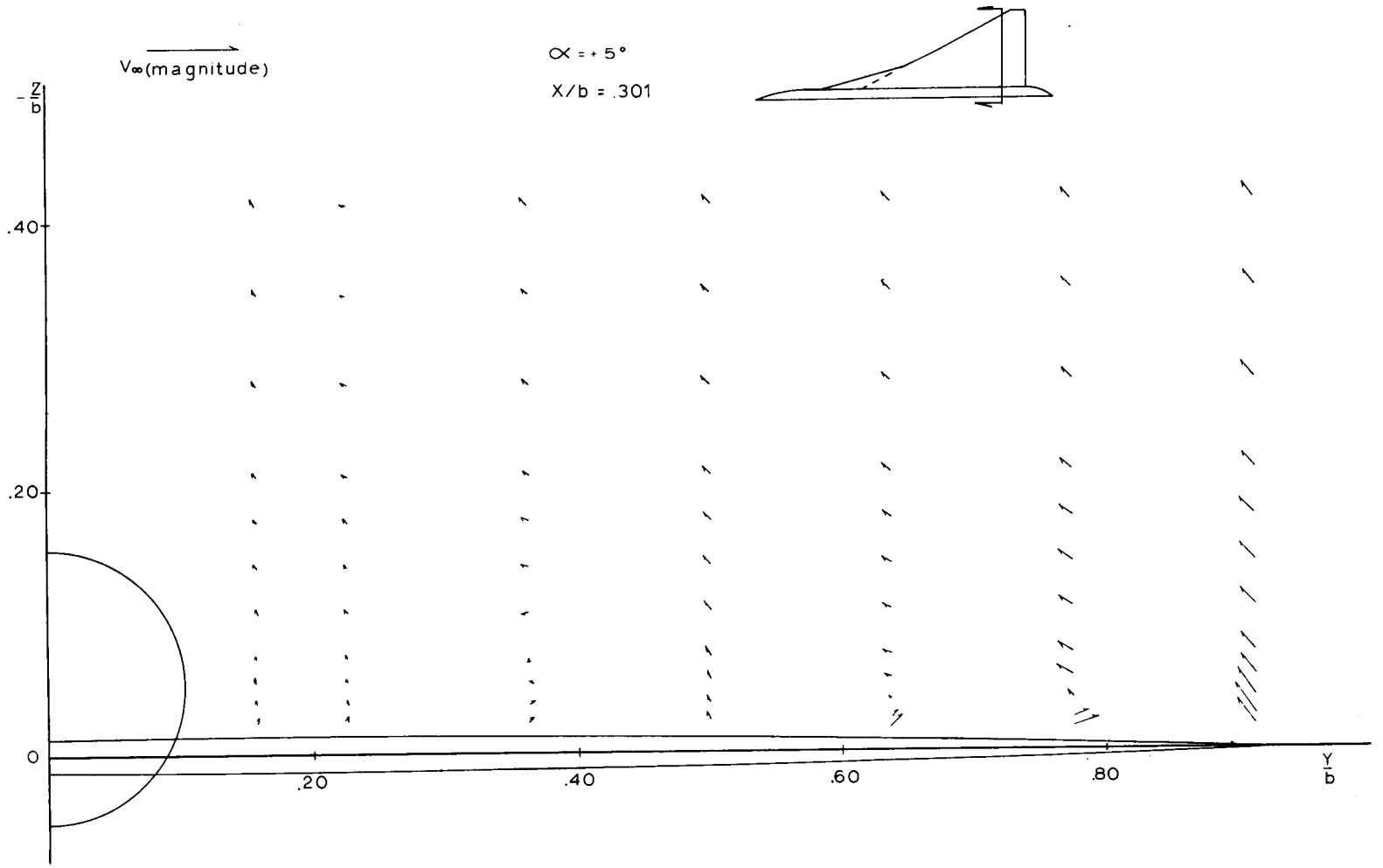

Figure 12h.- Upper surface flow field. $\alpha = 5^{o}$; x/b = 0.301.

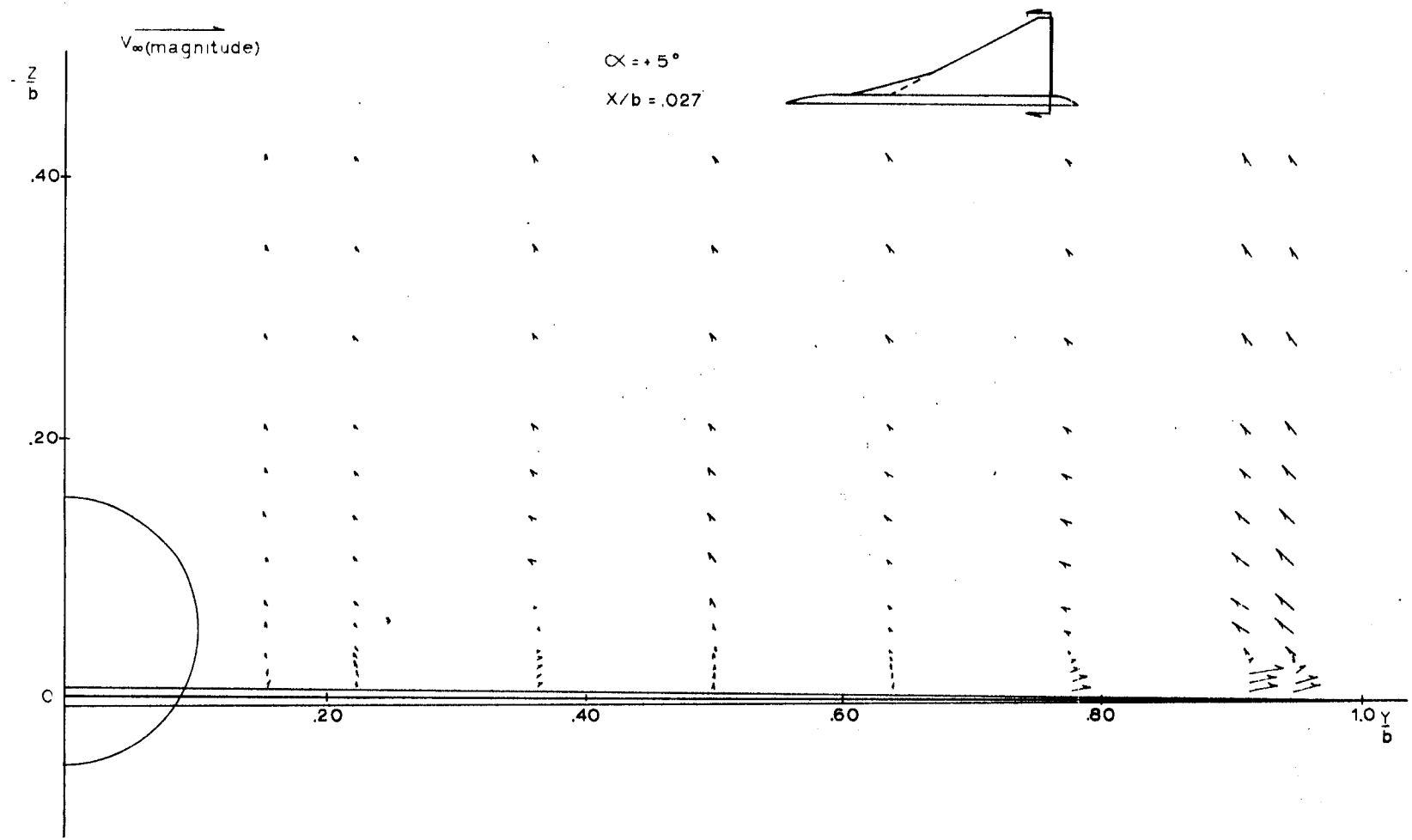

Figure 121.- Upper surface flow field. $\alpha = 5^{\circ}$; $x/b = 0.027$.

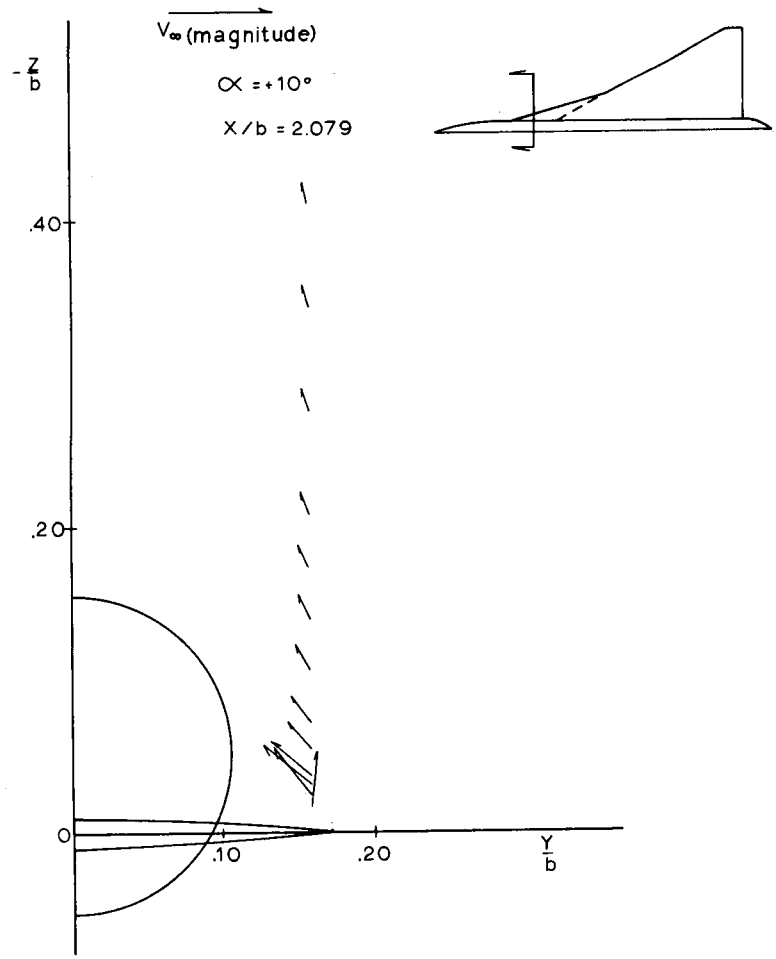

Figure 12j.- Upper surface flow field. $\alpha = 10^{o}$; x/b = 2.079.

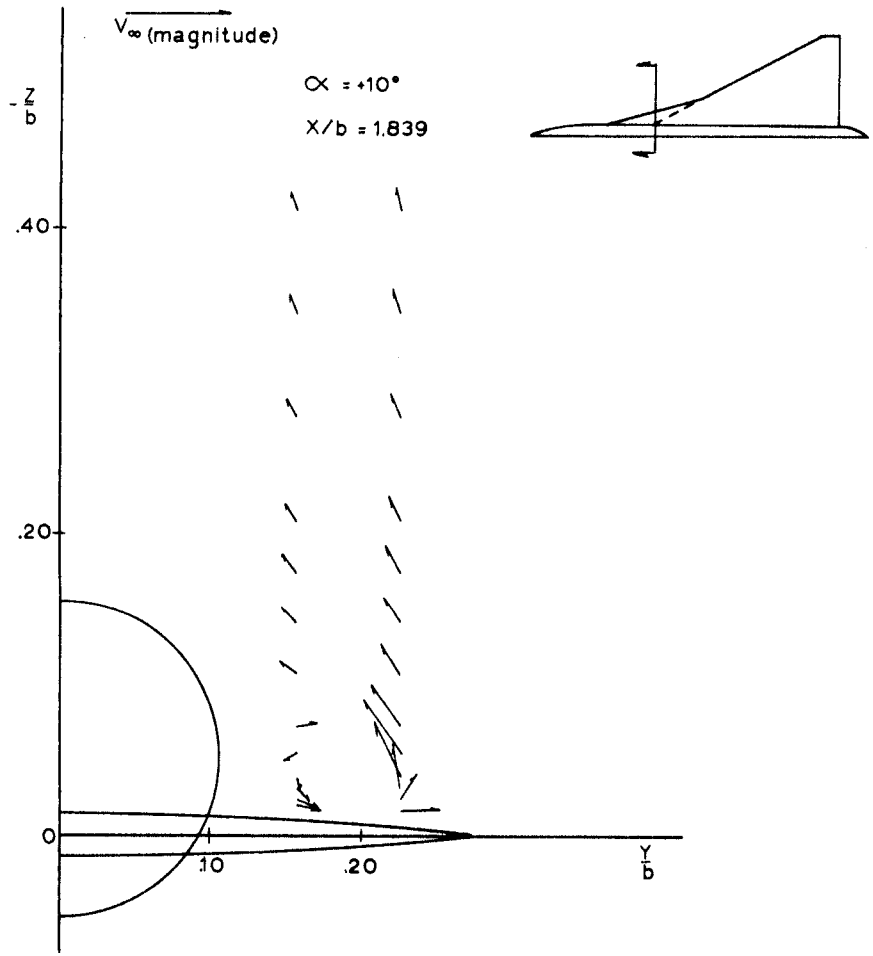

Figure 12k.- Upper surface flow field. $\alpha = 10^{o}$; x/b = 1.839.

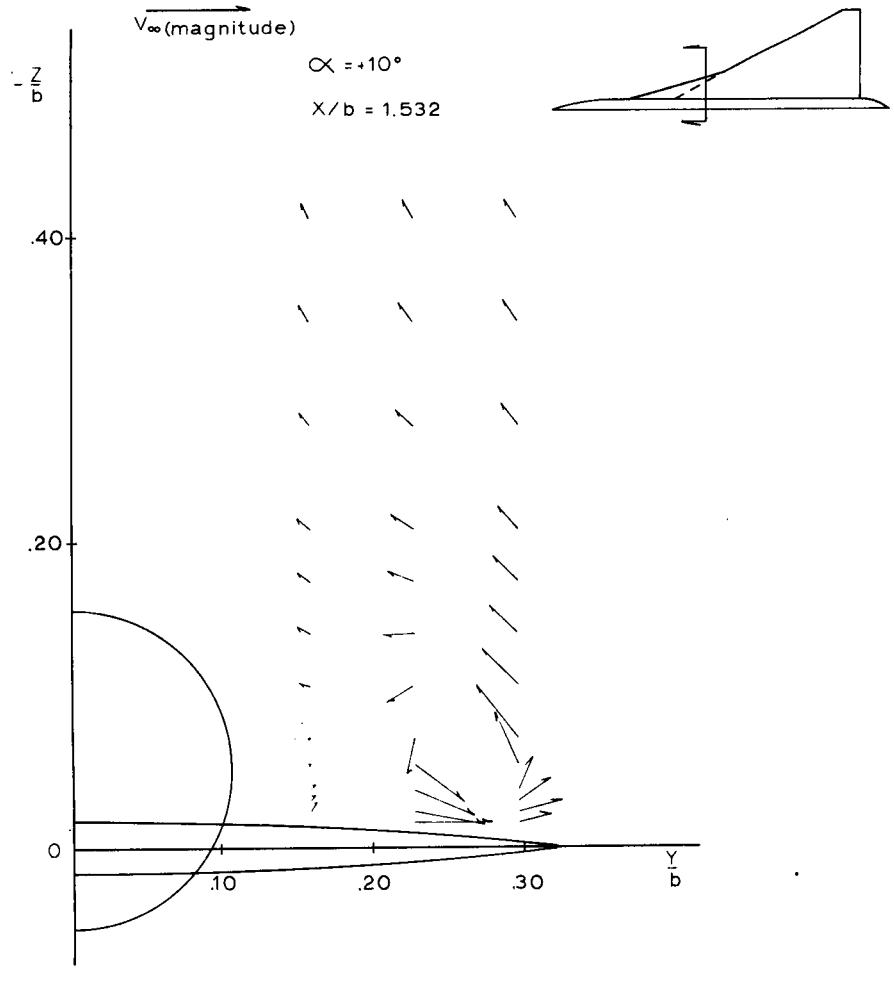

Figure 121.- Upper surface flow field. $\alpha = 10^{\circ}$; $x/b = 1.532$.

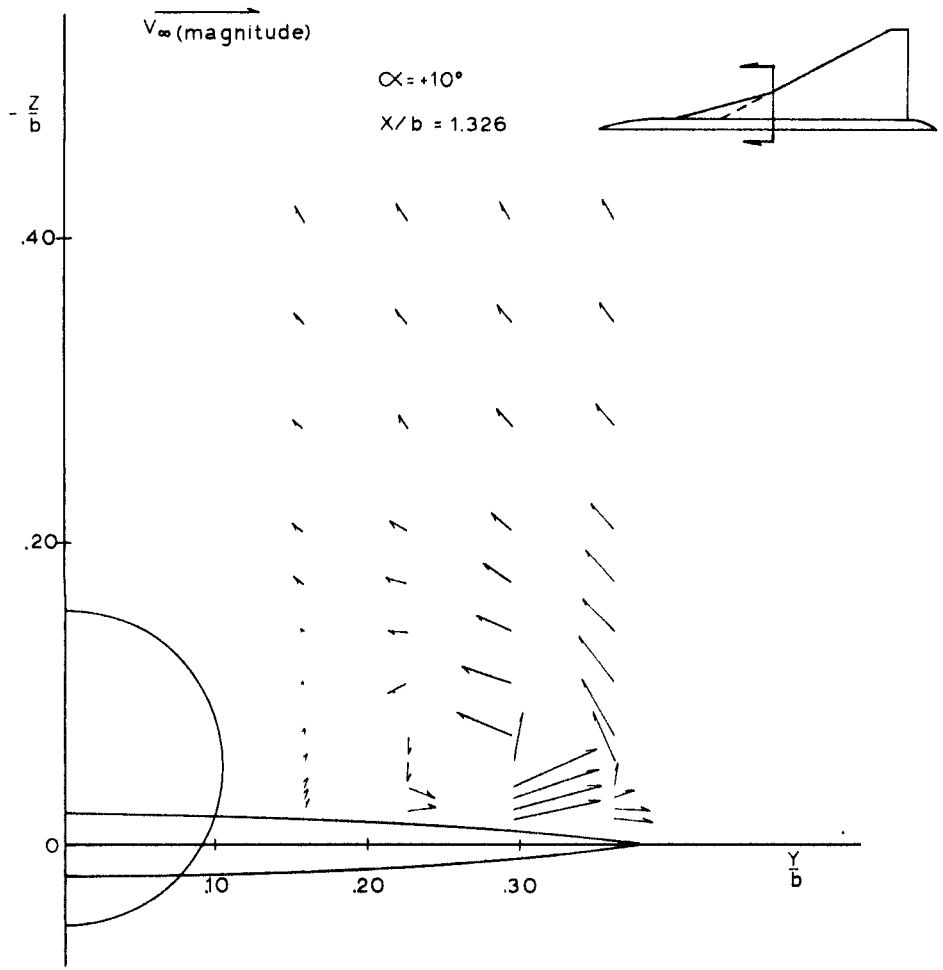

Figure 12m.- Upper surface flow field. $\alpha = 10^{\circ}$; x/b = 1.326.

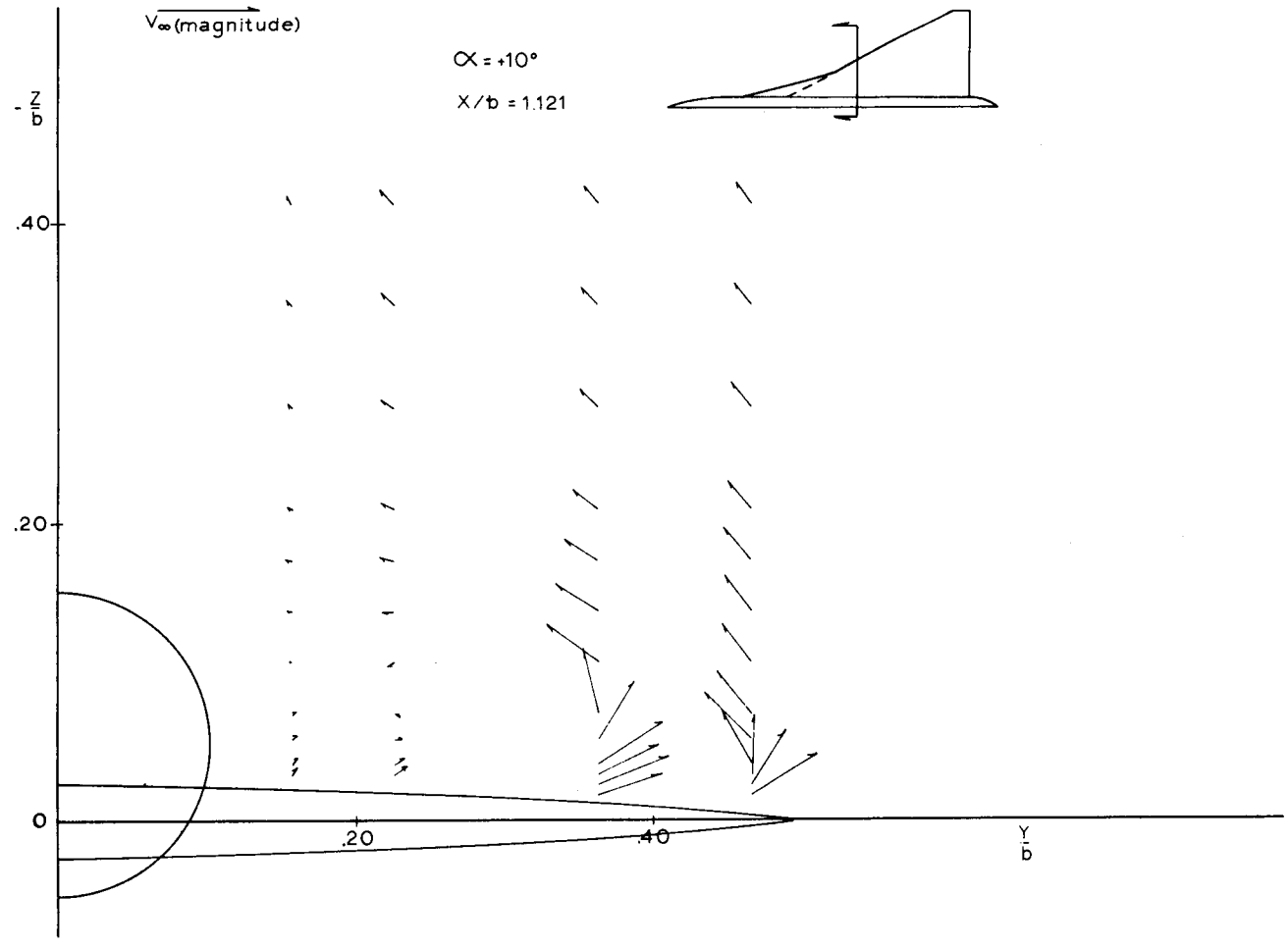

Figure 12n.- Upper surface flow field. $\alpha = 10^{o}$; x/b = 1.121.

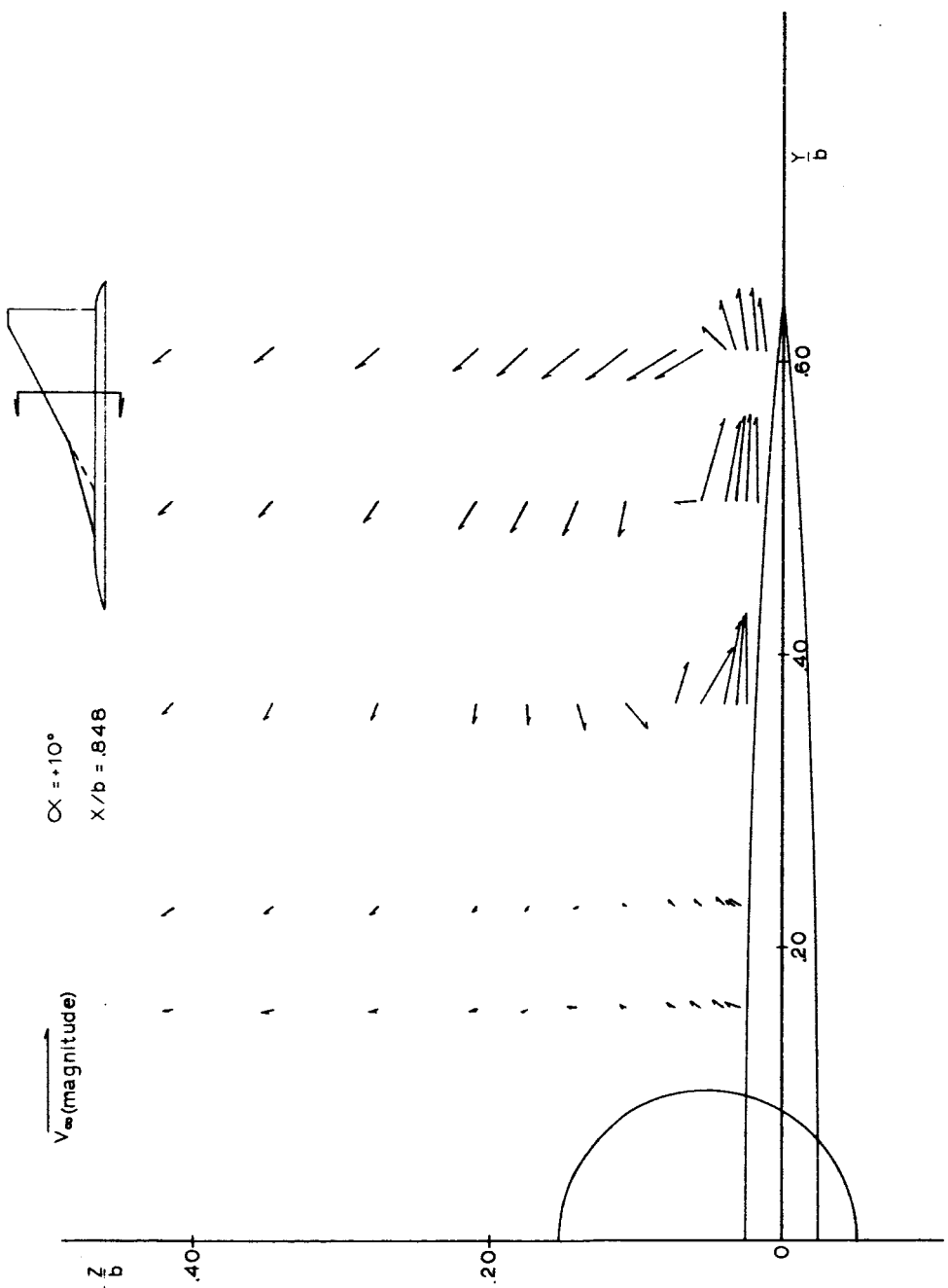

Figure 120.- Upper surface flow field. $\alpha = 10^{\circ}$; x/b = 0.848.

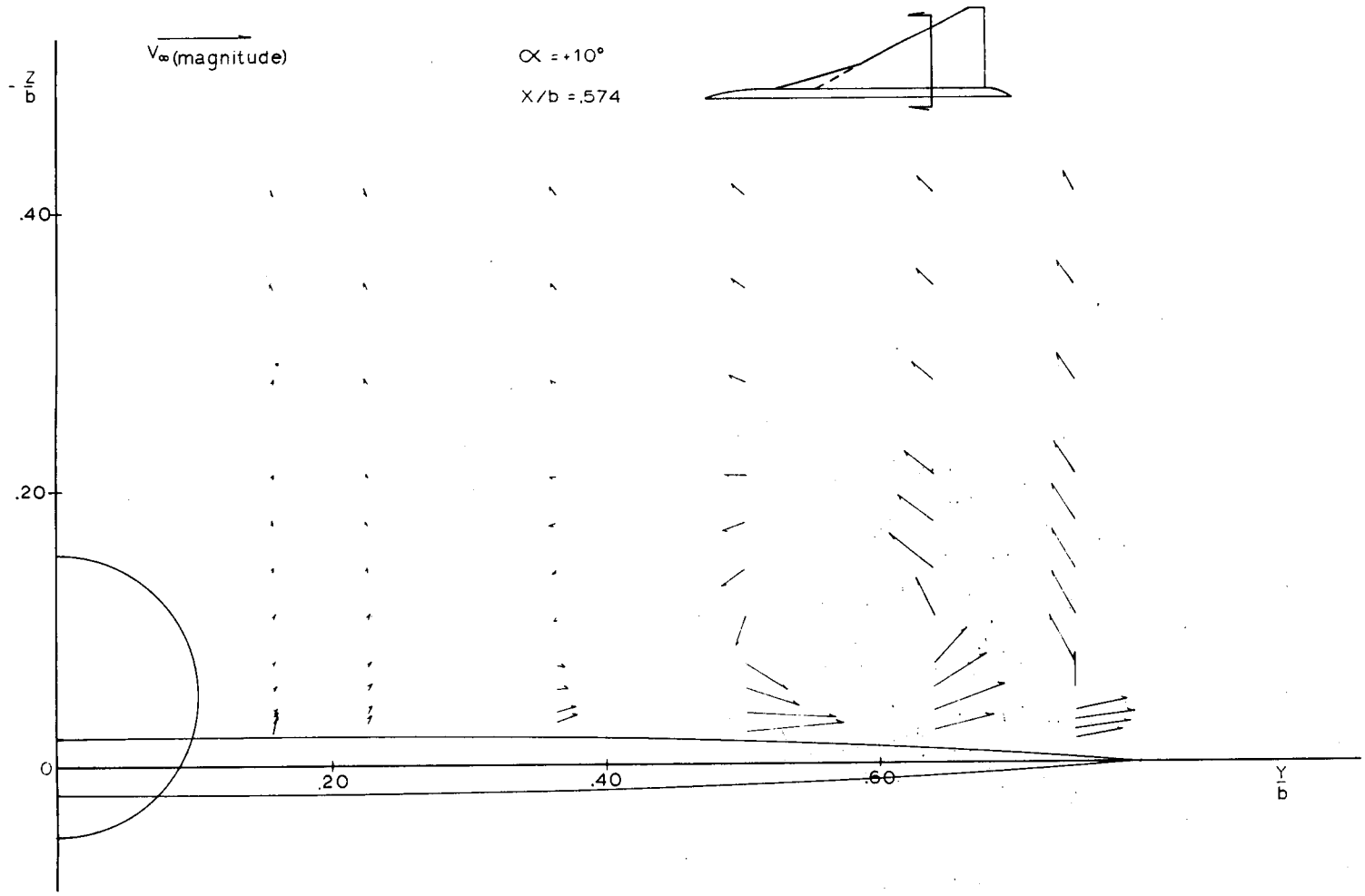

Figure 12p.- Upper surface flow field. $\alpha = 10^{\circ}$; $x/b = 0.574$.

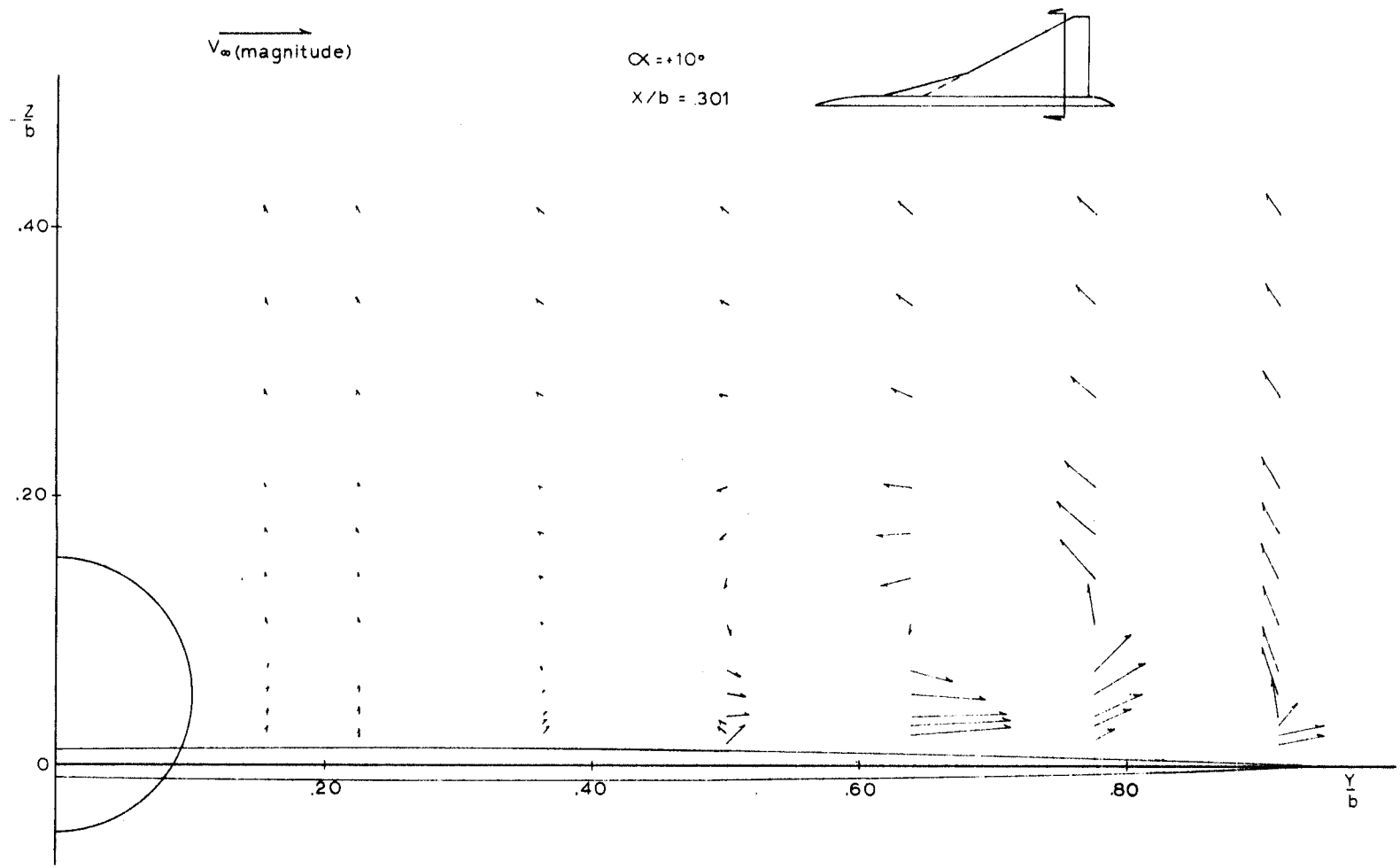

Figure 12q.- Upper surface flow field. $\alpha = 10^{\circ}$; x/b = 0.301.

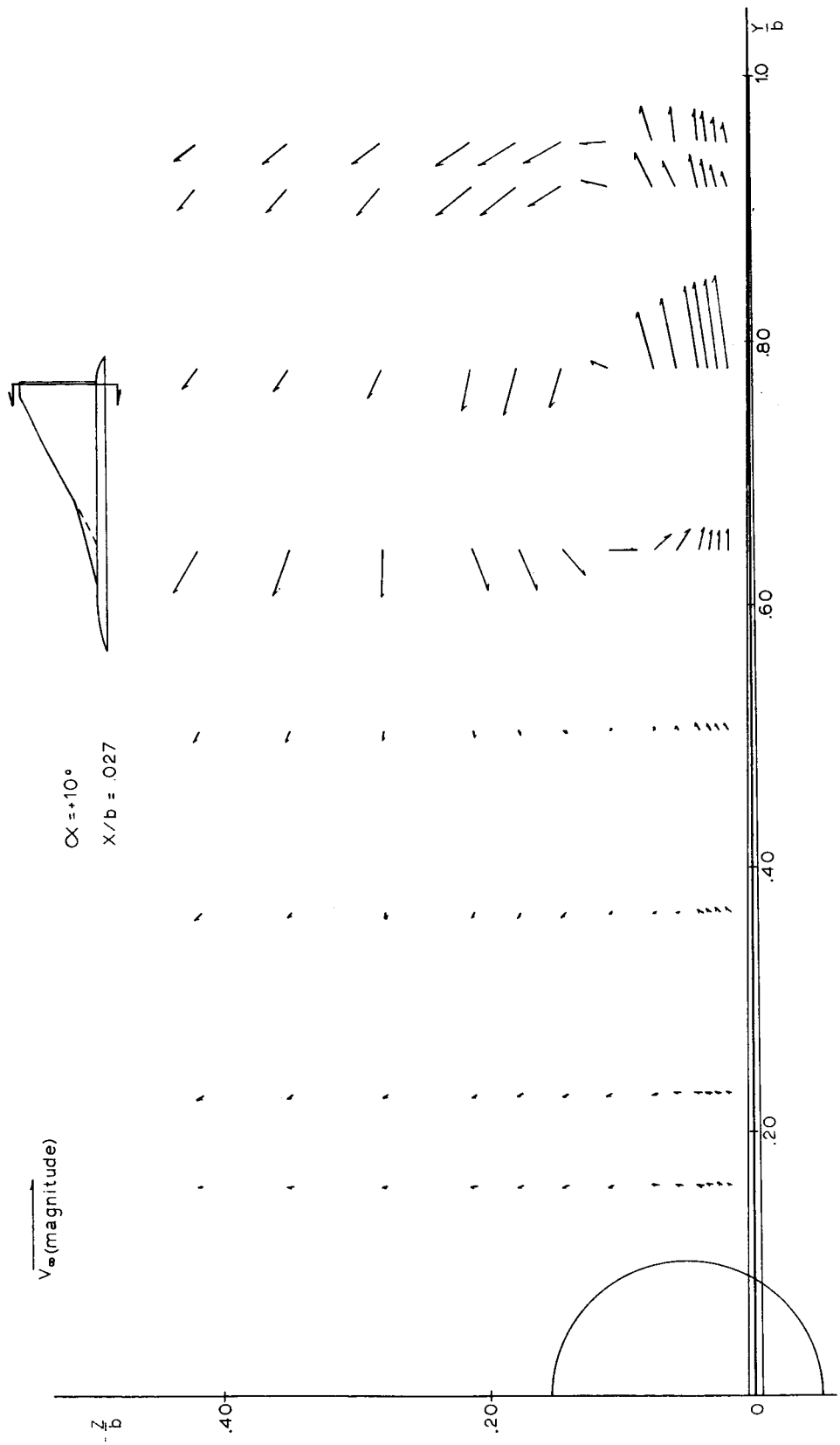

Figure 12r.- Upper surface flow field. $\alpha = 10^{o}$; x/b = 0.027.

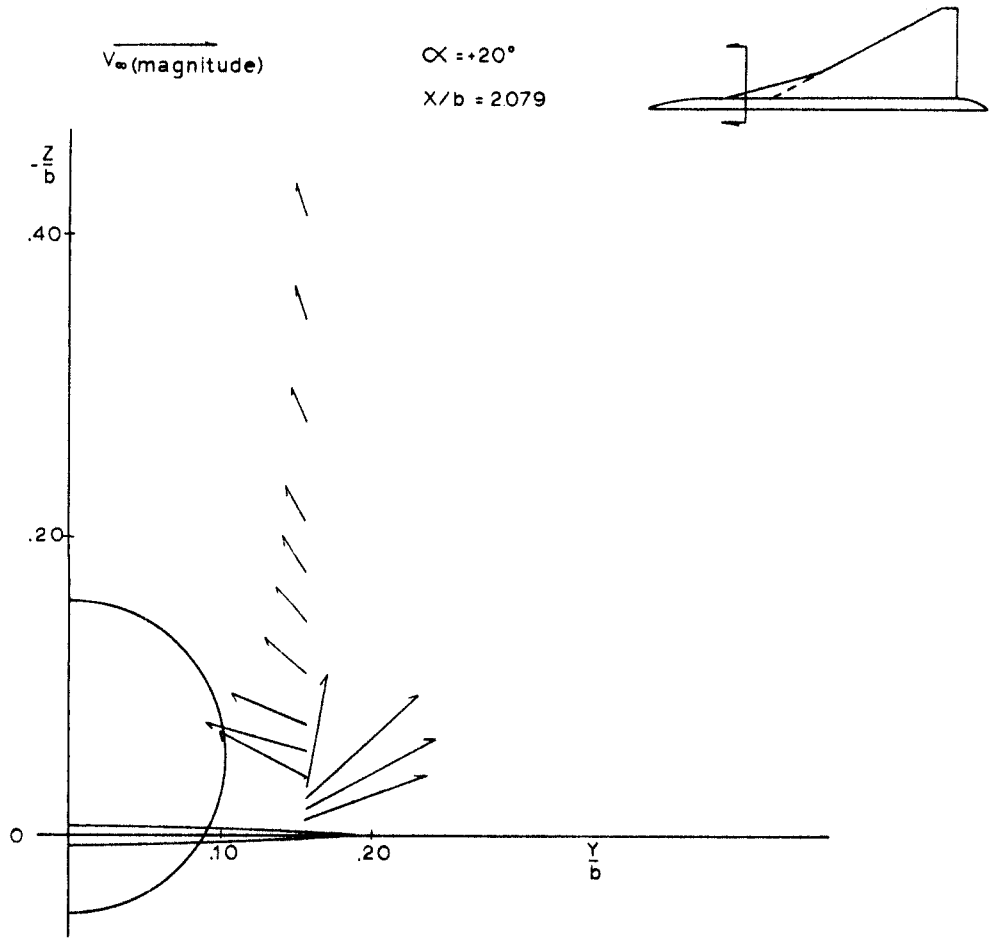

Figure 12s.- Upper surface flow field. $\alpha = 20^{\circ}$; x/b = 2.079.

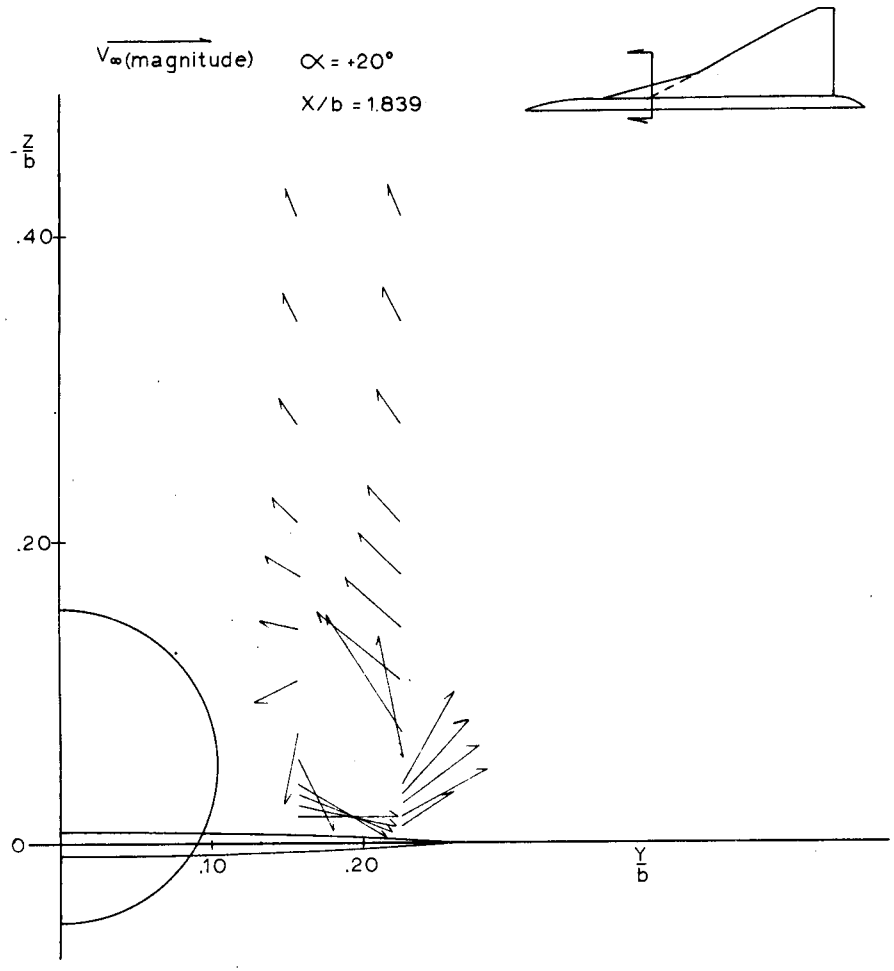

Figure 12t.- Upper surface flow field. $\alpha = 20^{\circ}$; x/b = 1.839.

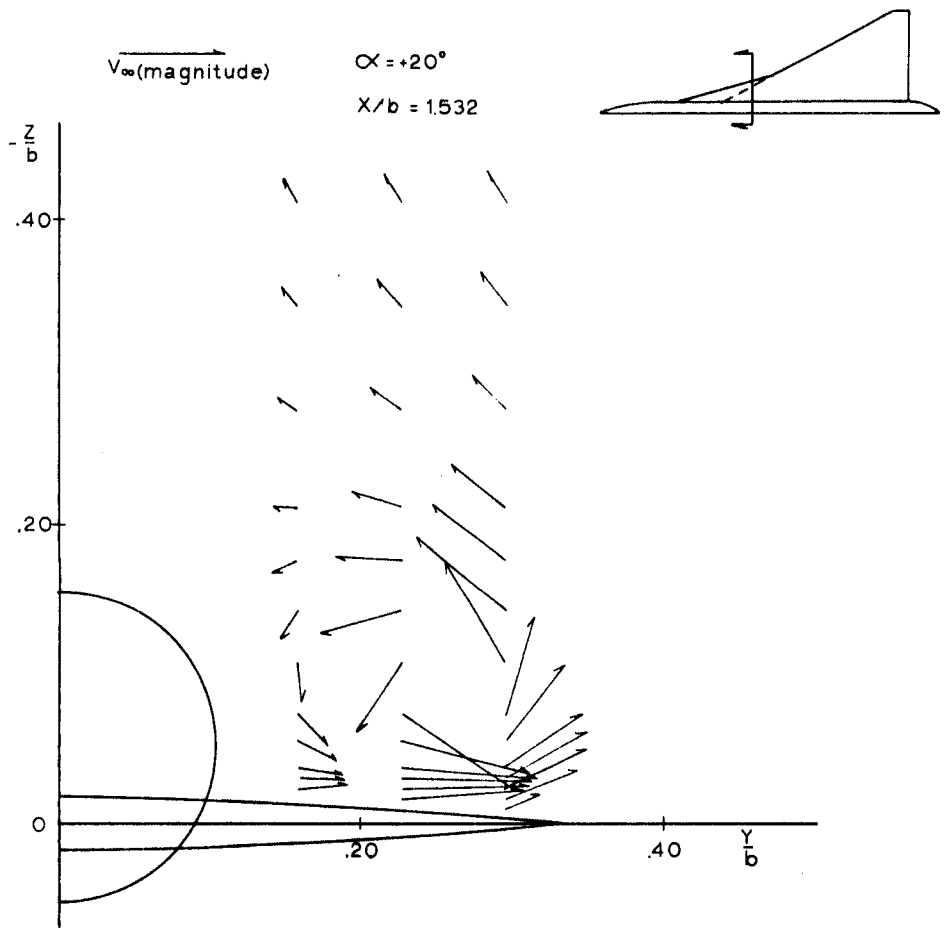

Figure 12u.- Upper surface flow field. $\alpha = 20^{\circ}$; $x/b = 1.532$.

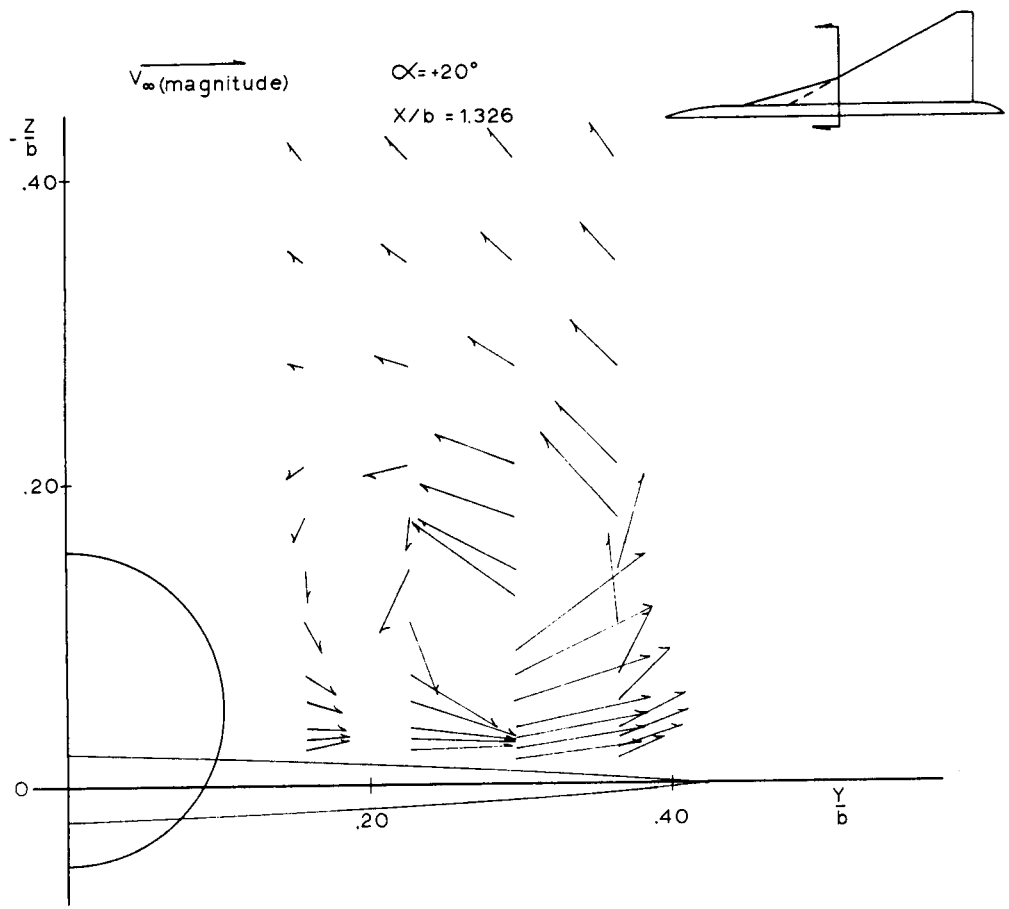

Figure 12v.- Upper surface flow field. $\alpha = 20^{\circ}$; $x/b = 1.326$.

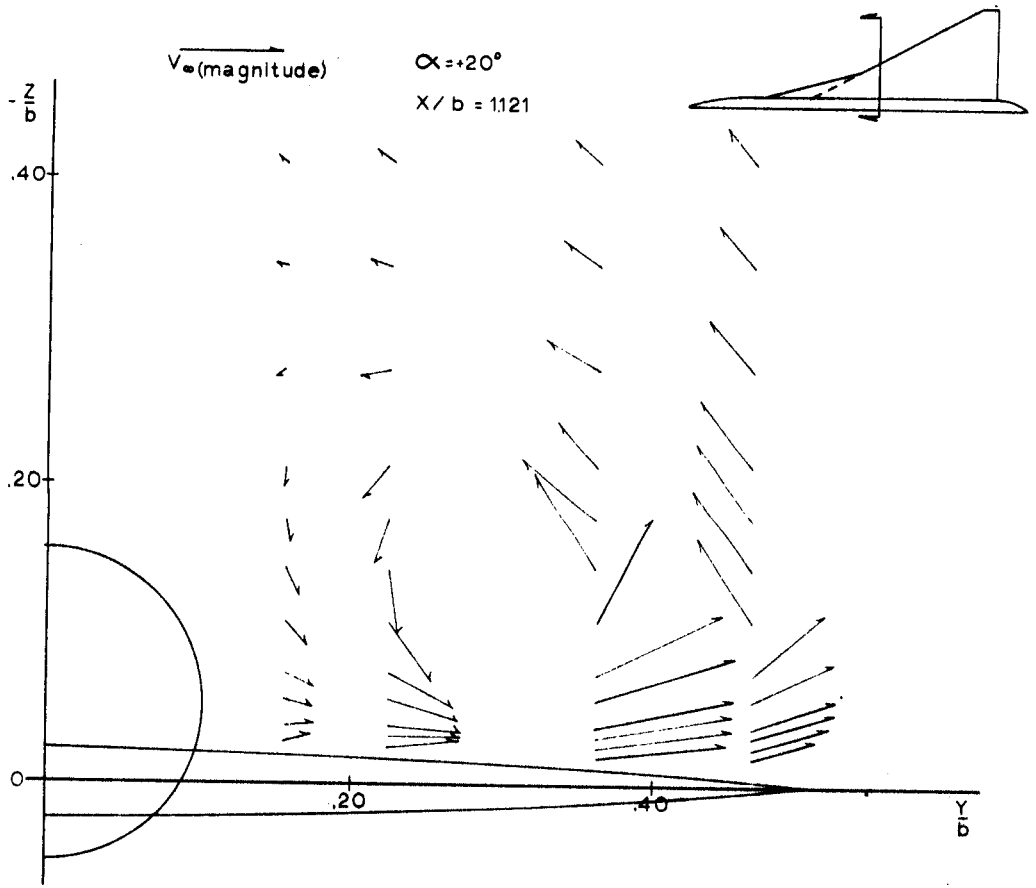

Figure 12w.- Upper surface flow field. $\alpha = 20^{\circ}$; $x/b = 1.121$.

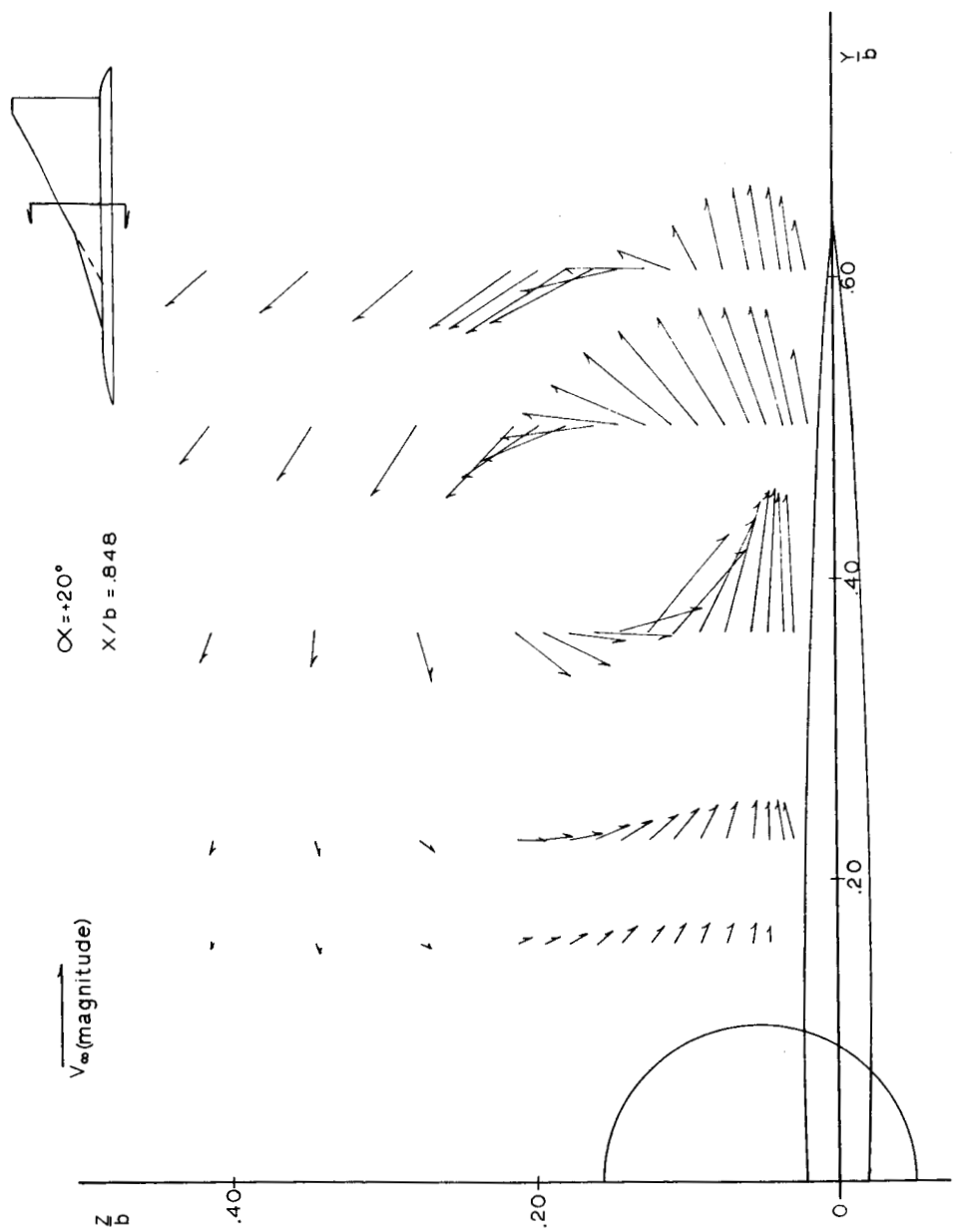

Figure 12x.- Upper surface flow field. $\alpha = 20^{\circ}$; $x/b = 0.848$.

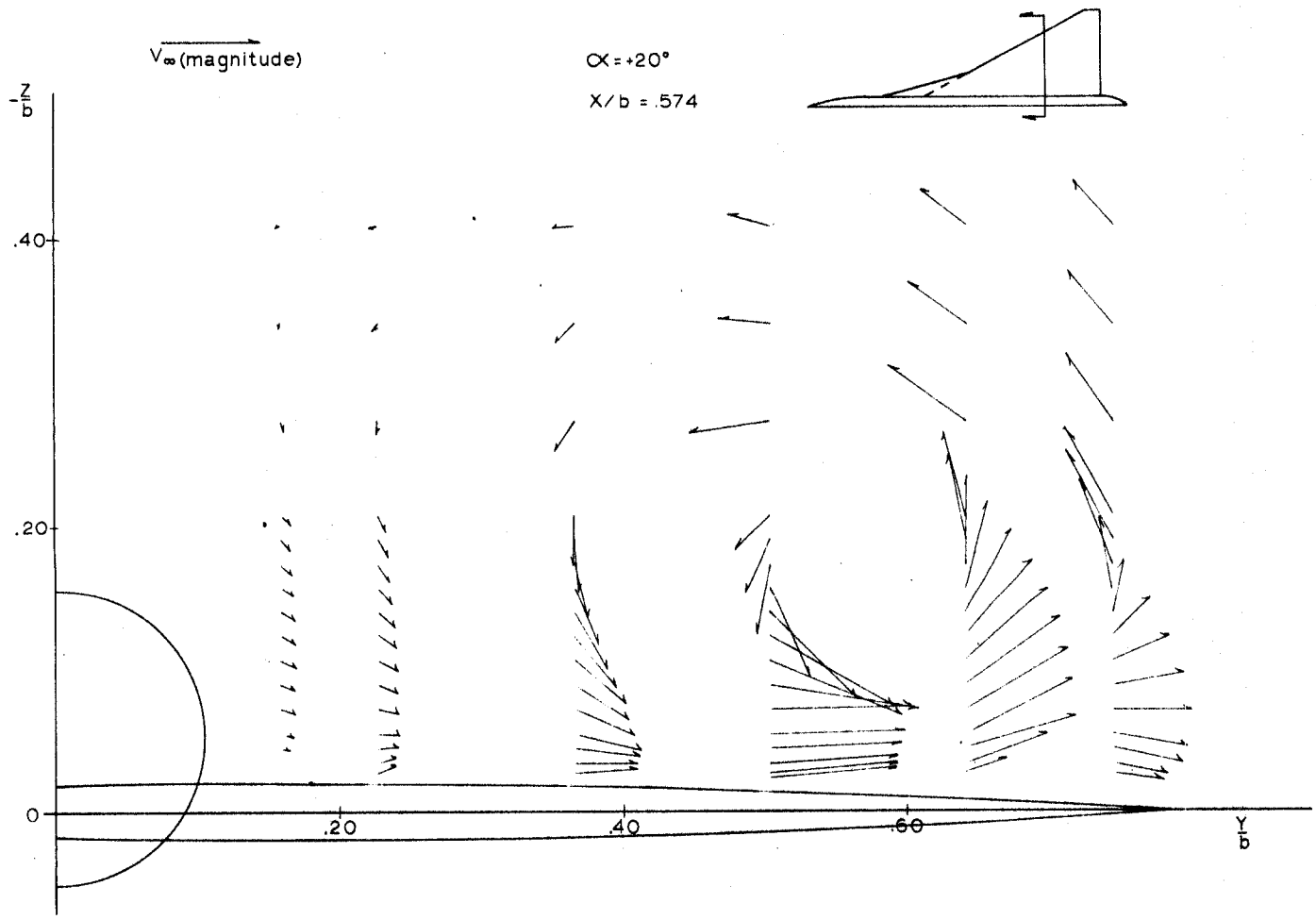

Figure 12y.- Upper surface flow field. $\alpha = 20^{\circ}$; $x/b = 0.574$.

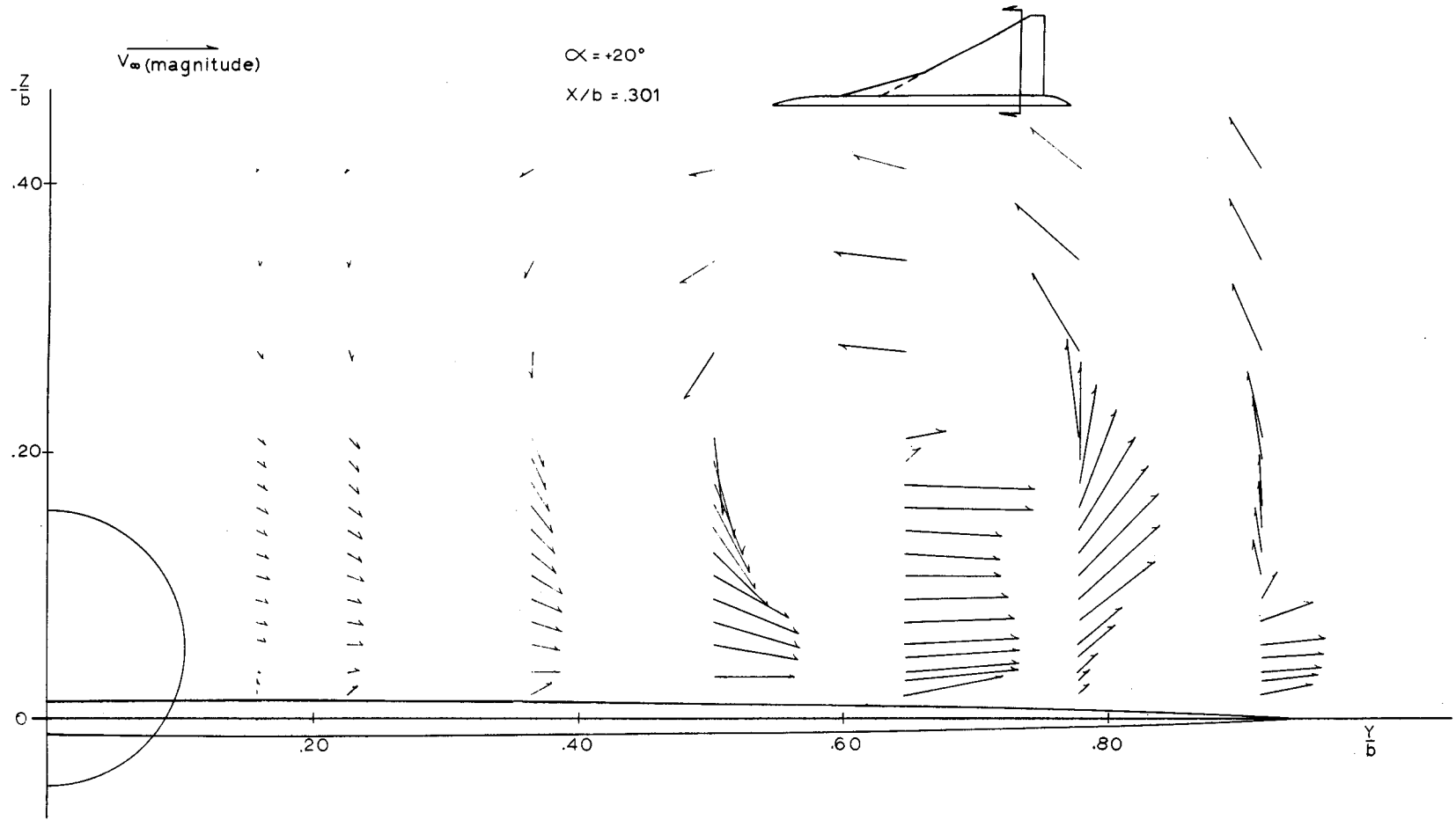

Figure 12z.- Upper surface flow field. $\alpha = 20^{\circ}$; $x/b = 0.301$.

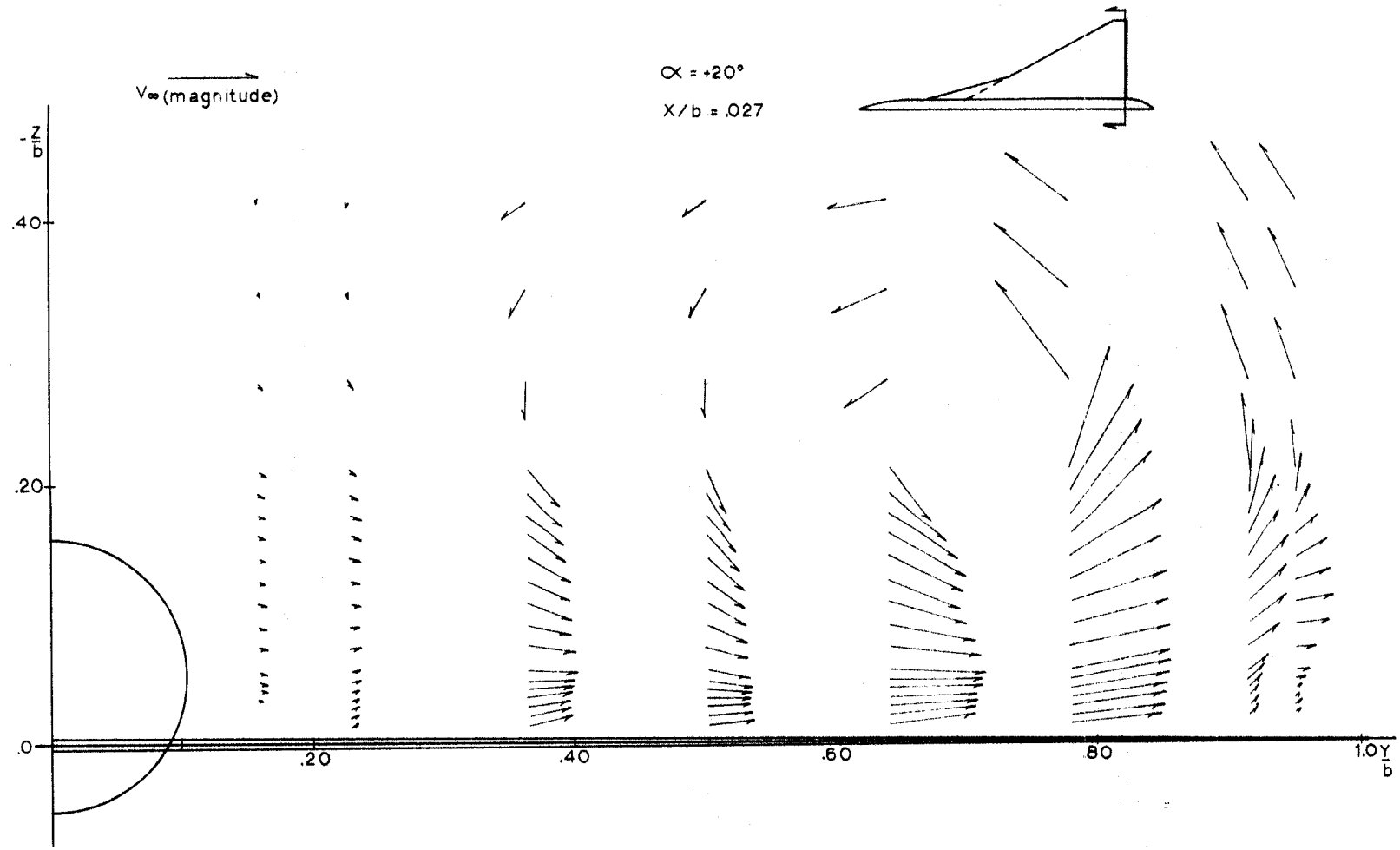

Figure 12aa.- Upper surface flow field. $\alpha = 20^{\circ}$; $x/b = 0.027$.

Figure 13a.- Upper surface flow field. $\alpha = 5^{\circ}$; $\Delta z/b = 0.0034$ above wing.

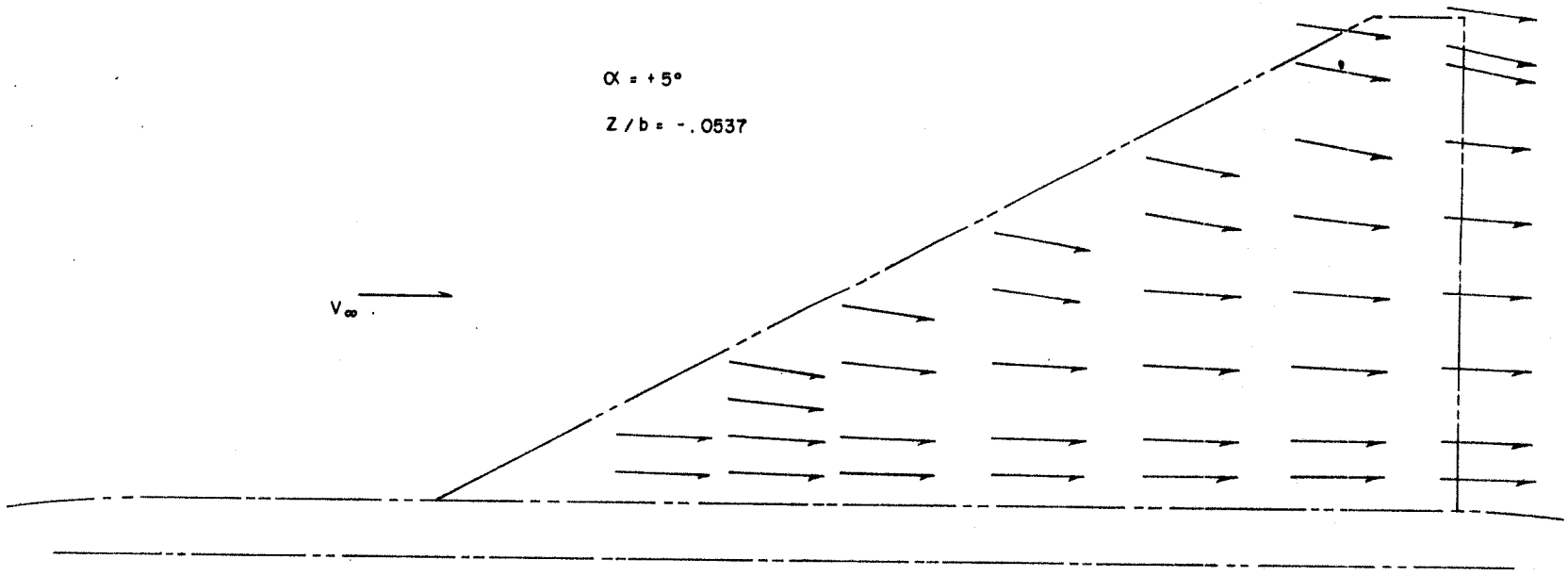

Figure 13b.- Upper surface flow field. $\alpha = 5^{\circ}$; $z/b = -0.0537$.

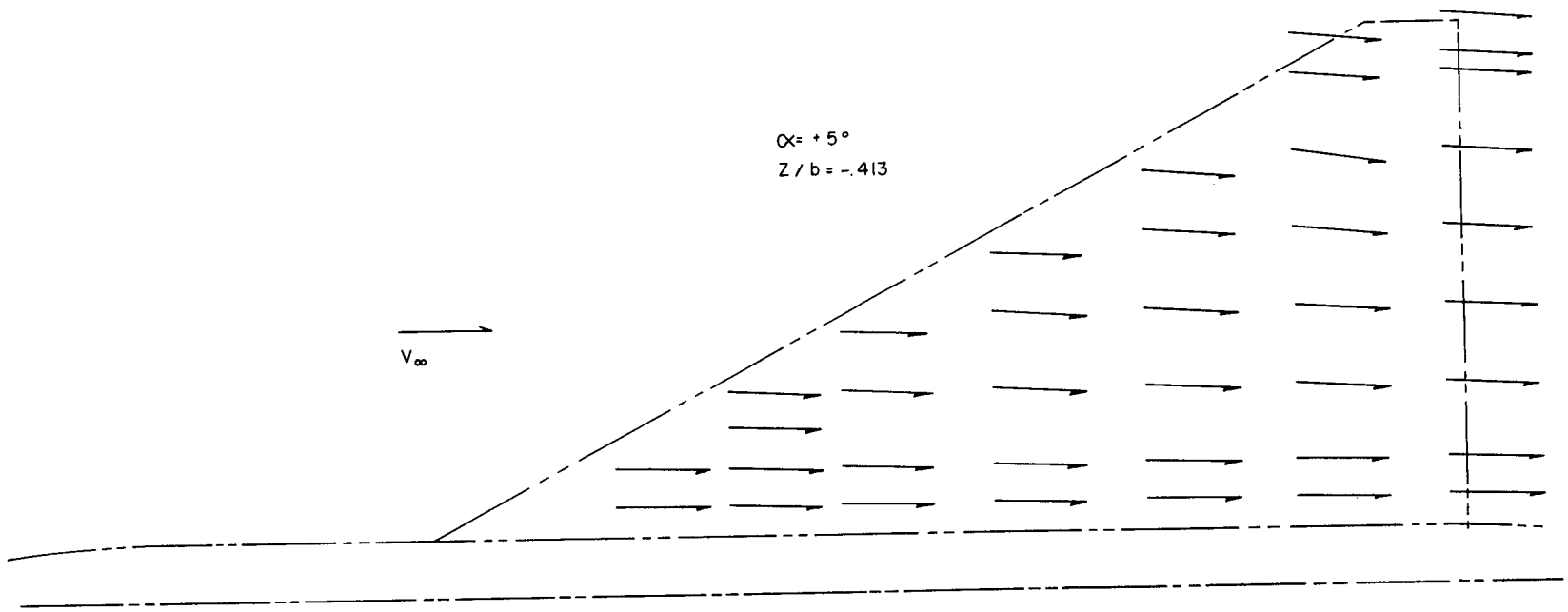

Figure 13c.- Upper surface flow field. $\alpha = 5^{o}$; $z/b = -0.413$.

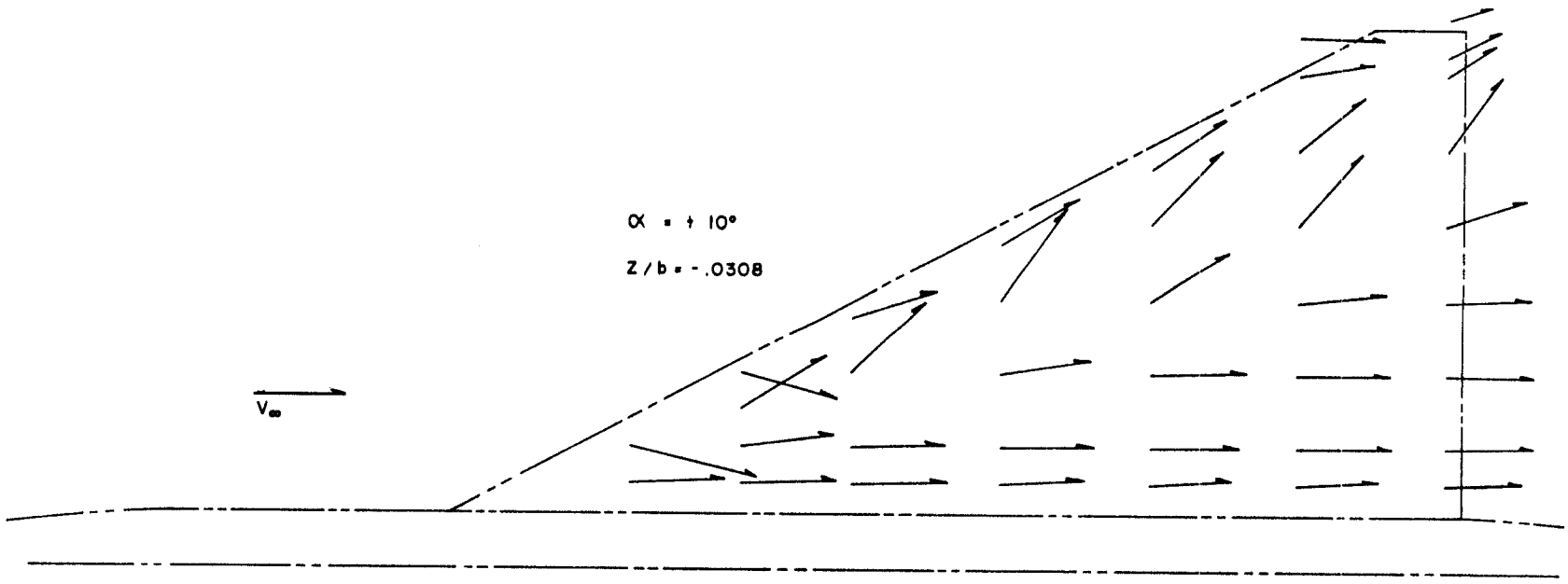

Figure 13d.- Upper surface flow field. $\alpha = 10^{\circ}$; $z/b = -0.0308$.

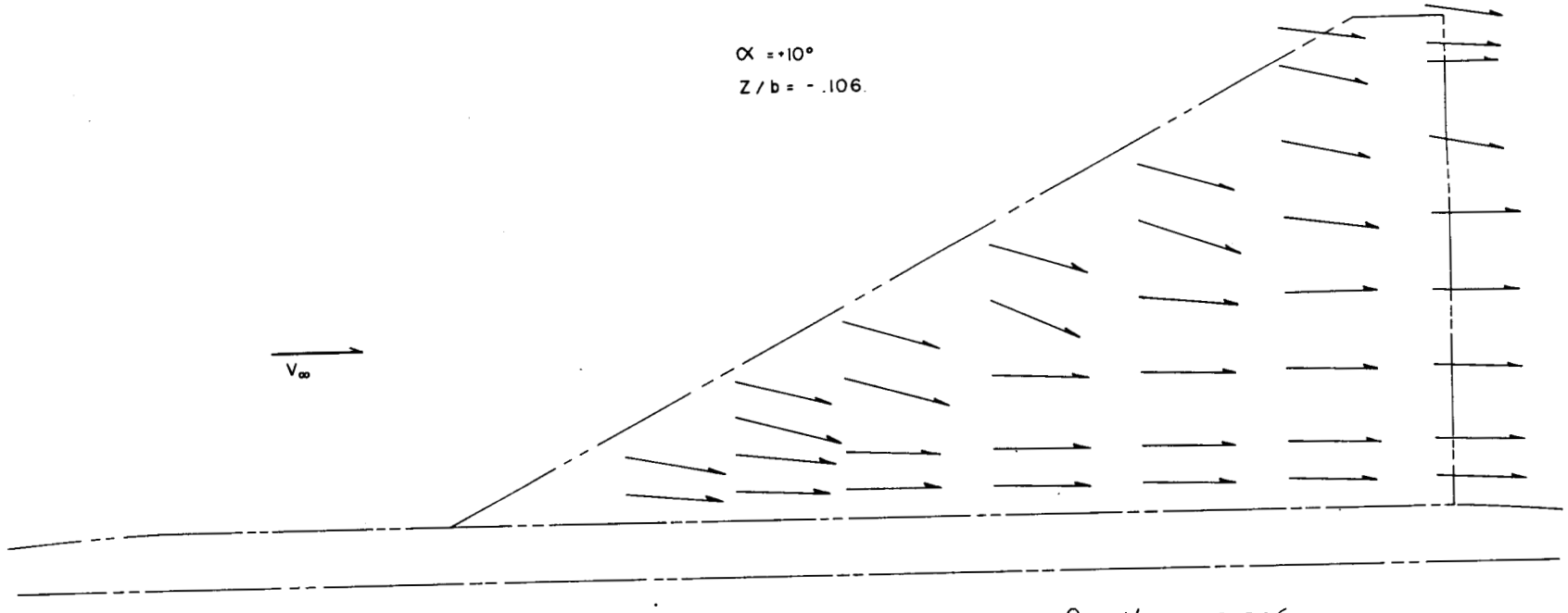

Figure 13e.- Upper surface flow field. $\alpha = 10^{\circ}$; $z/b = -0.106$.

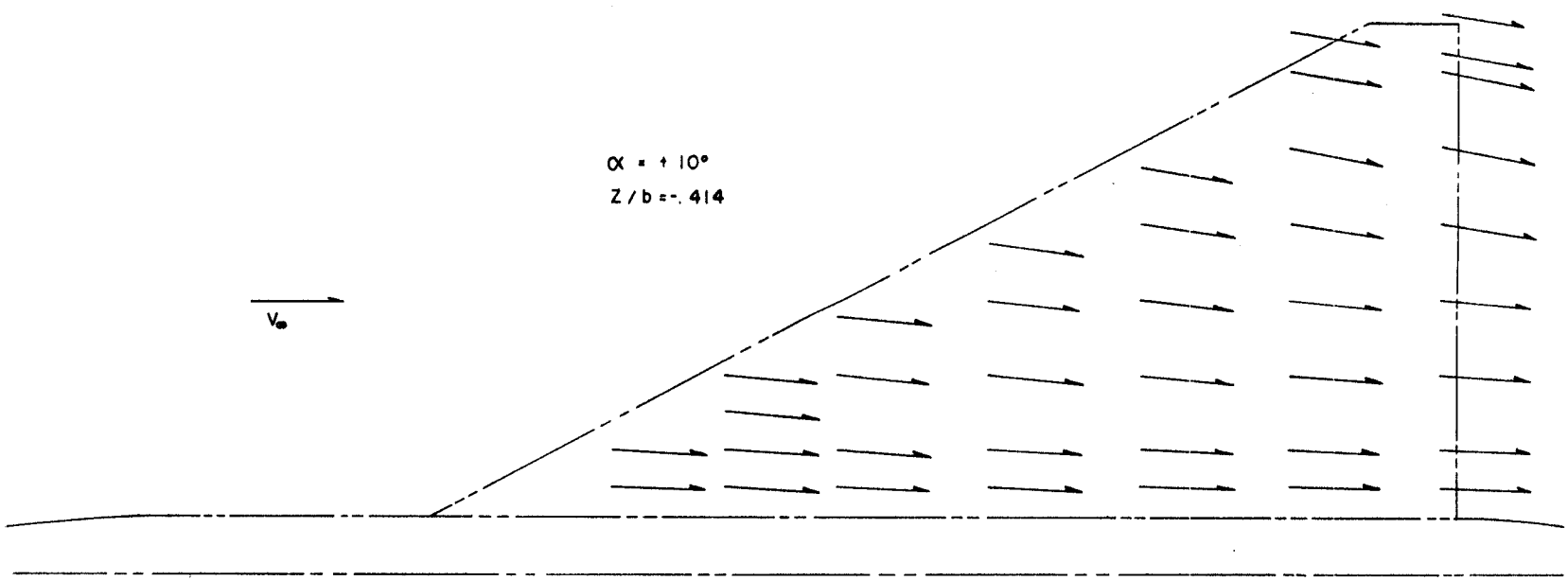

Figure 13f.- Upper surface flow field. $\alpha = 10^{\circ}$; $z/b = -0.414$.

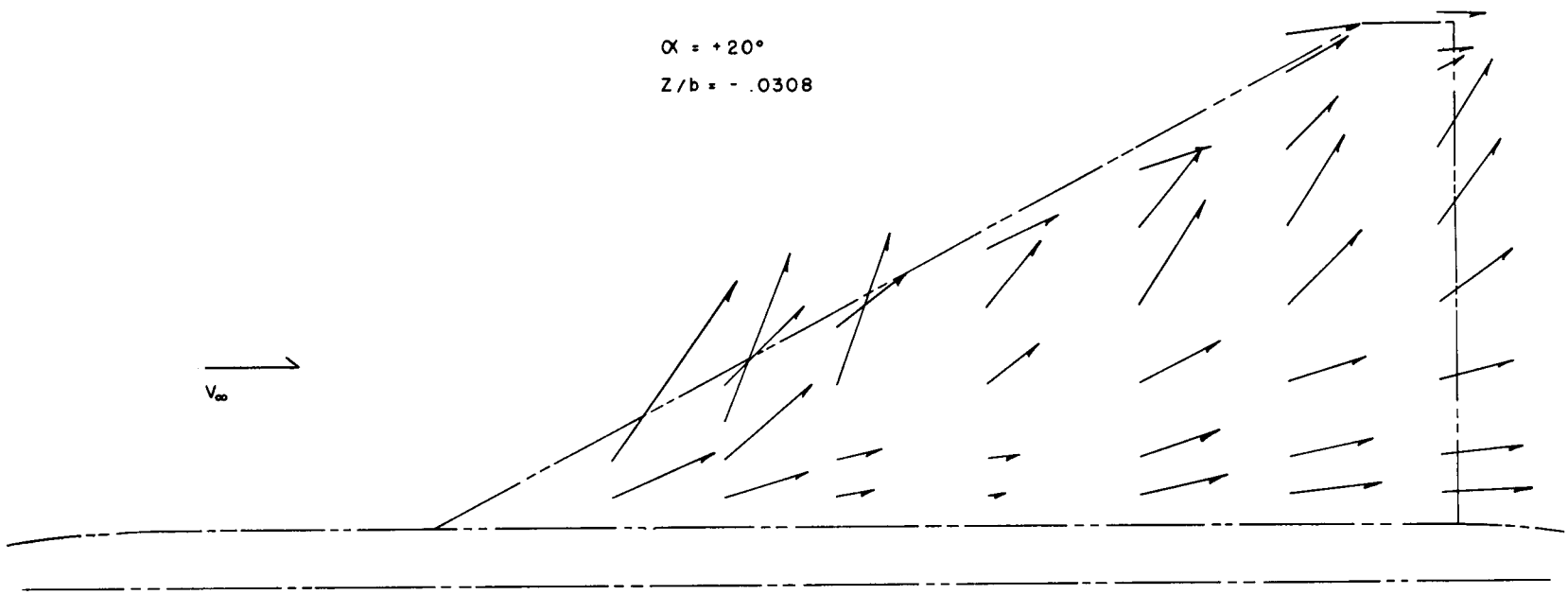

Figure 13g.- Upper surface flow field. $\alpha = 20^{\circ}$; $z/b = -0.0308$.

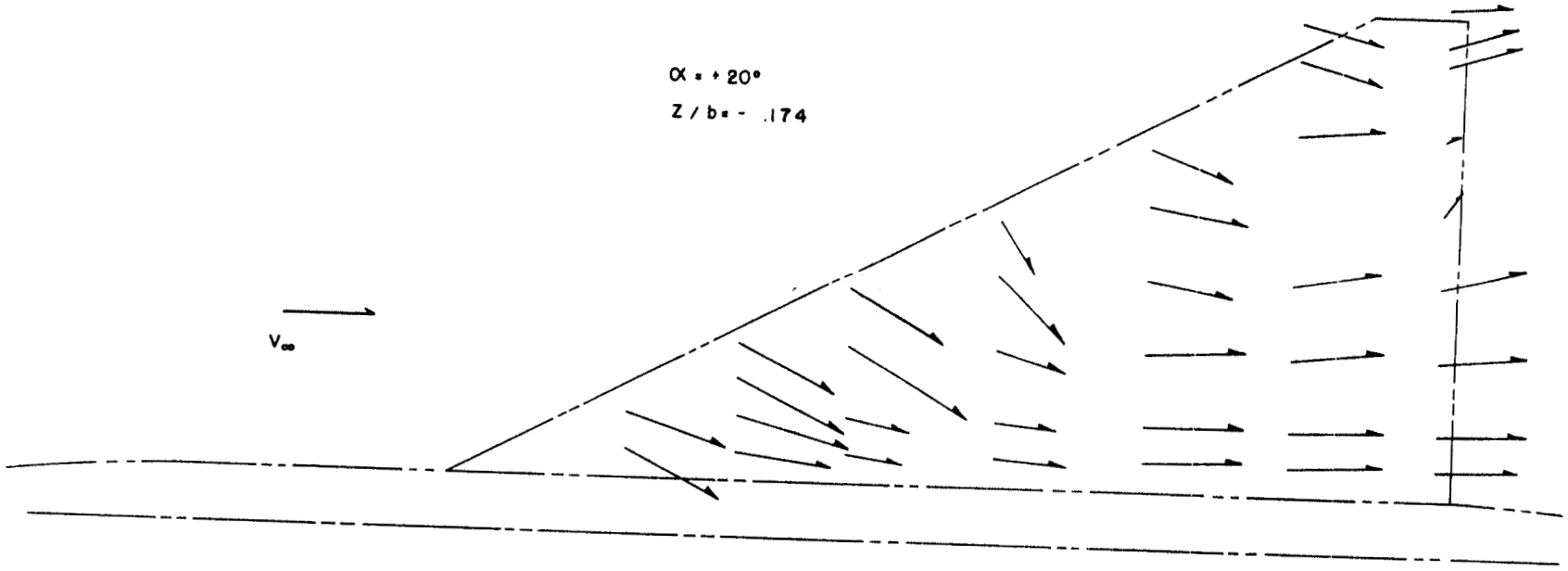

Figure 13h.- Upper surface flow field. $\alpha = 20^{\circ}$; $z/b = -0.174$.

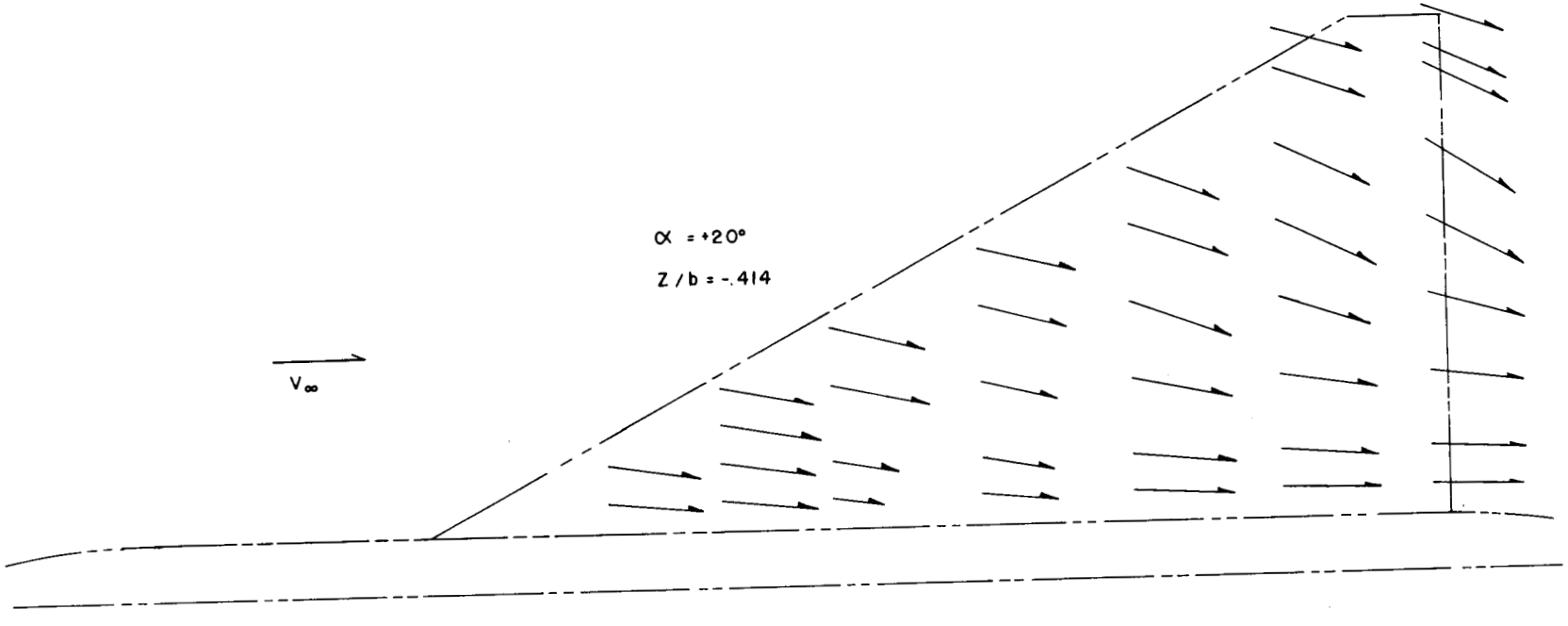

Figure 13i.- Upper surface flow field. $\alpha = 20^{\circ}$; $z/b = -0.414$.

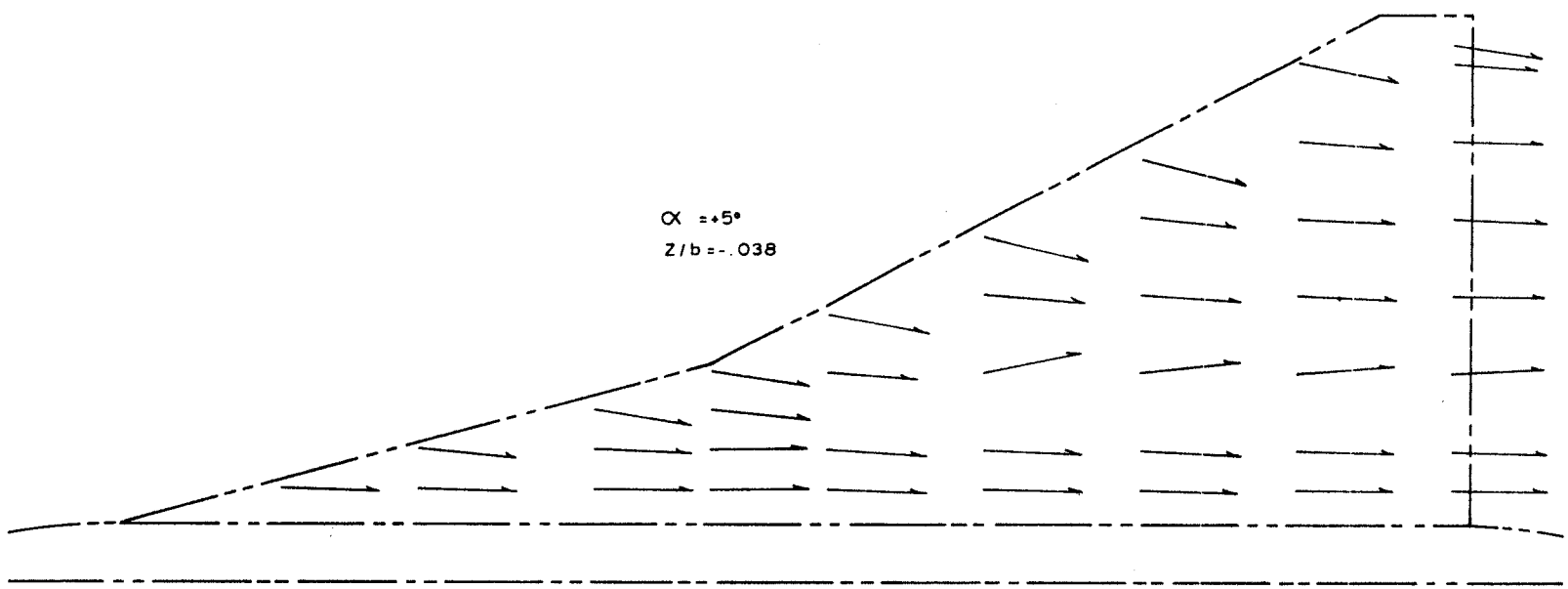

Figure 14a.- Upper surface flow field. $\alpha = 5^{\circ}$; $z/b = -0.038$.

Figure 14b.- Upper surface flow field. $\alpha = 5^{\circ}$; $z/b = -0.175$.

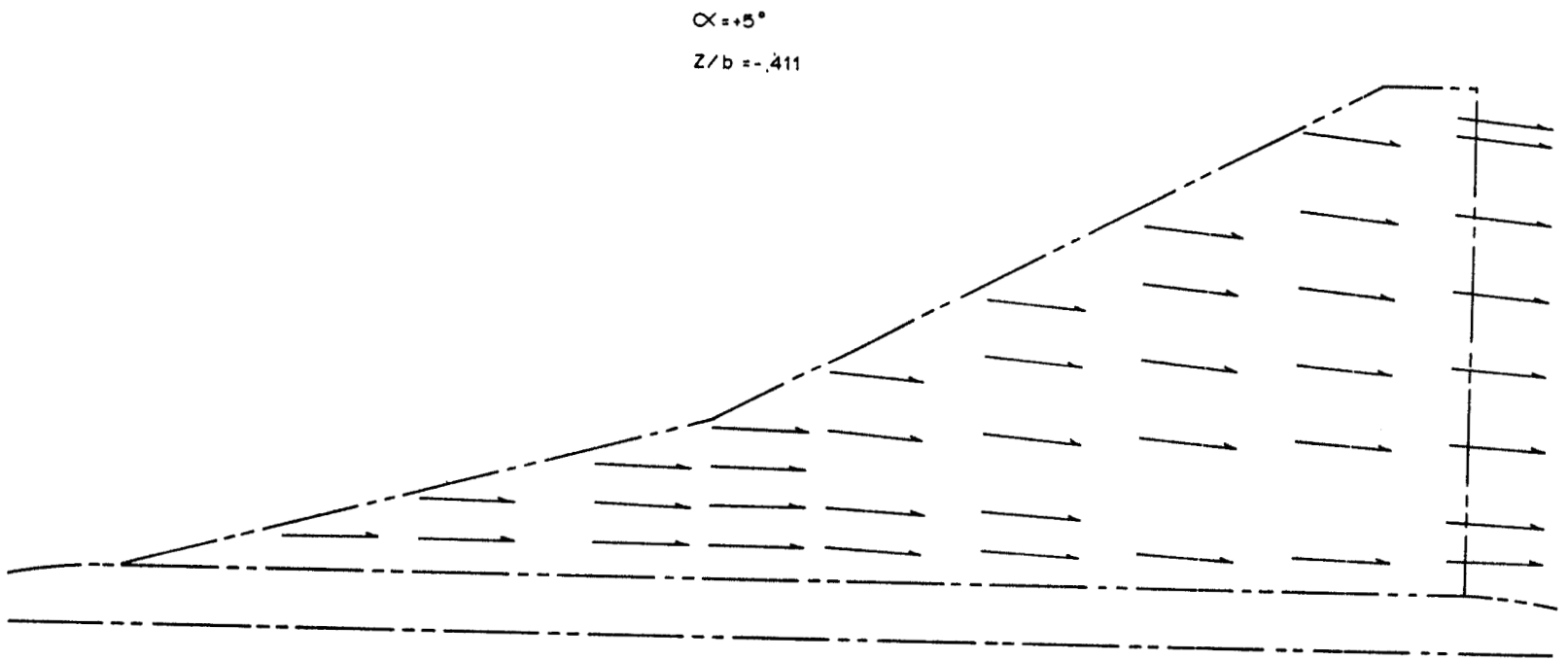

Figure 14c.- Upper surface flow field. $\alpha = 5^{\circ}$; $z/b = -0.411$.

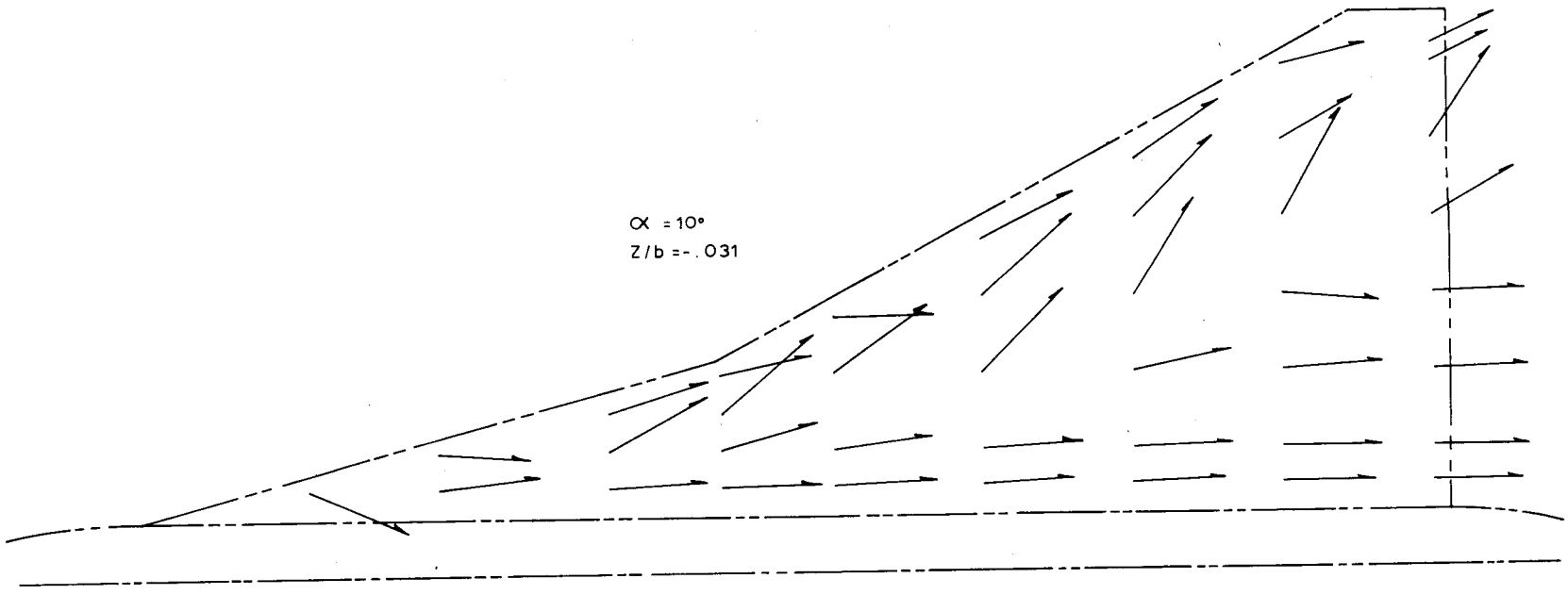

Figure 14d.- Upper surface flow field. $\alpha = 10^{\circ}$; $z/b = -0.031$.

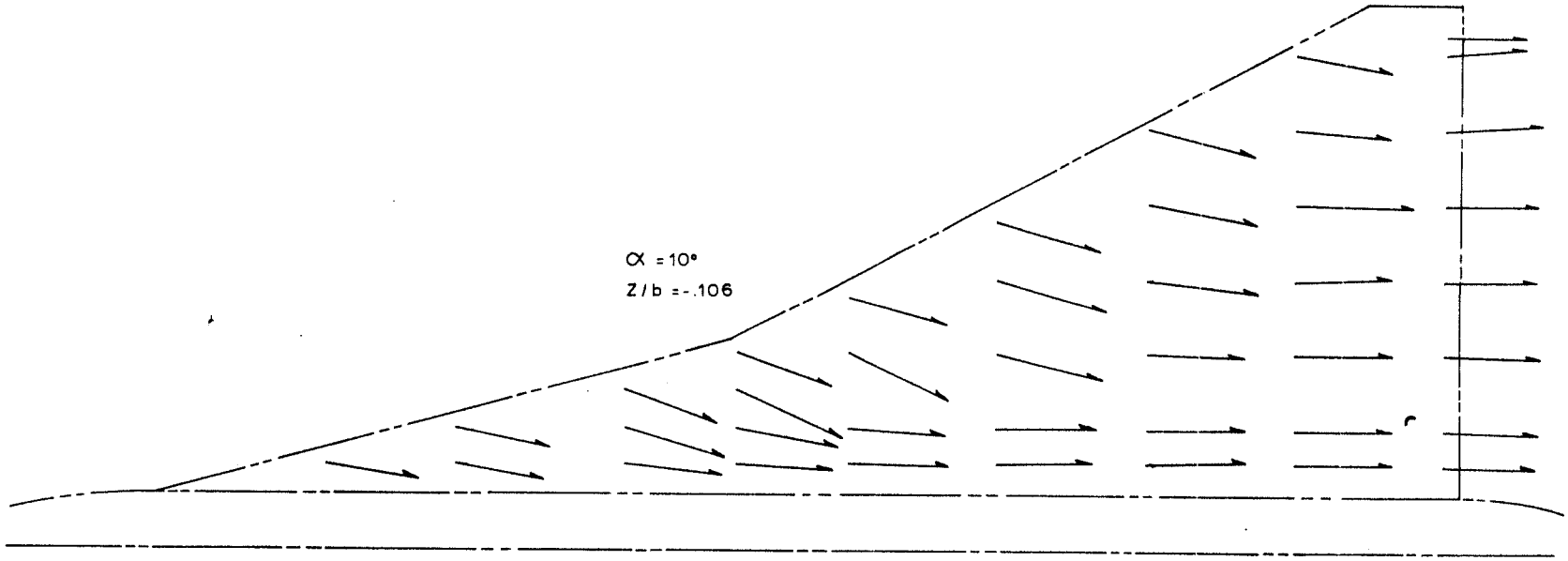

Figure 14e.- Upper surface flow field. $\alpha = 10^{o}$; $z/b = -0.106$.

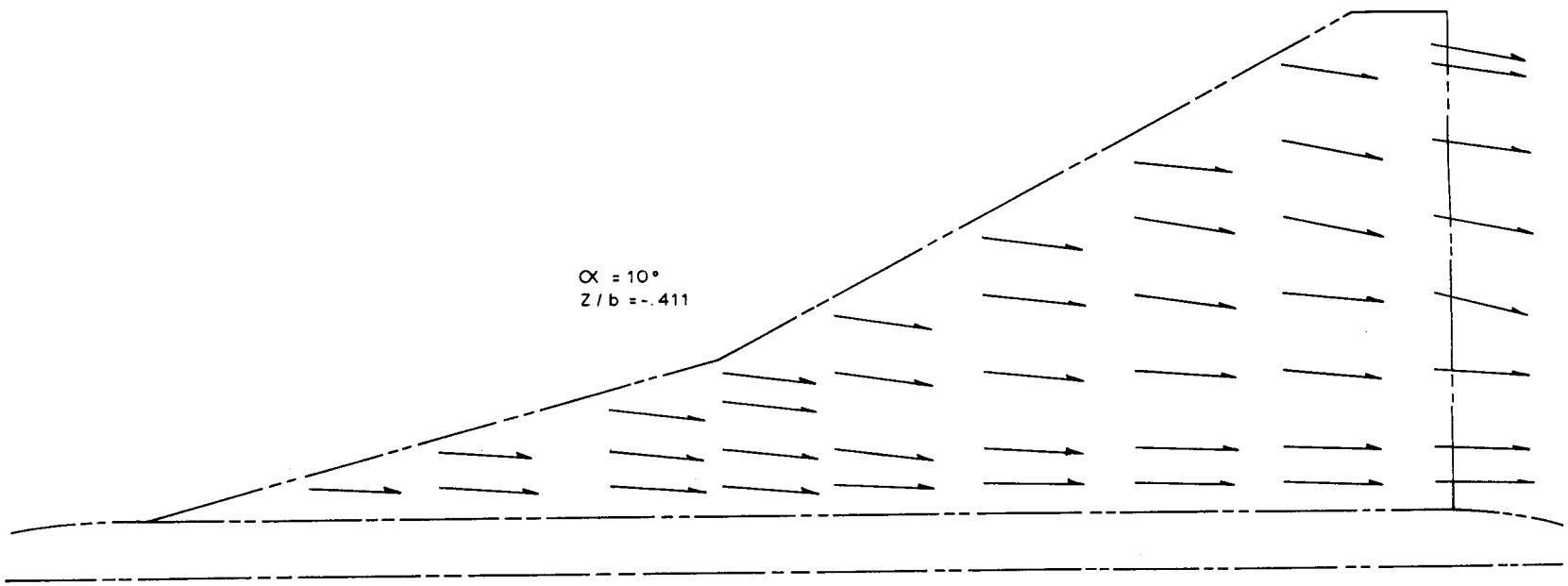

Figure 14f.- Upper surface flow field. $\alpha = 10^{o}$; $z/b = -0.411$.

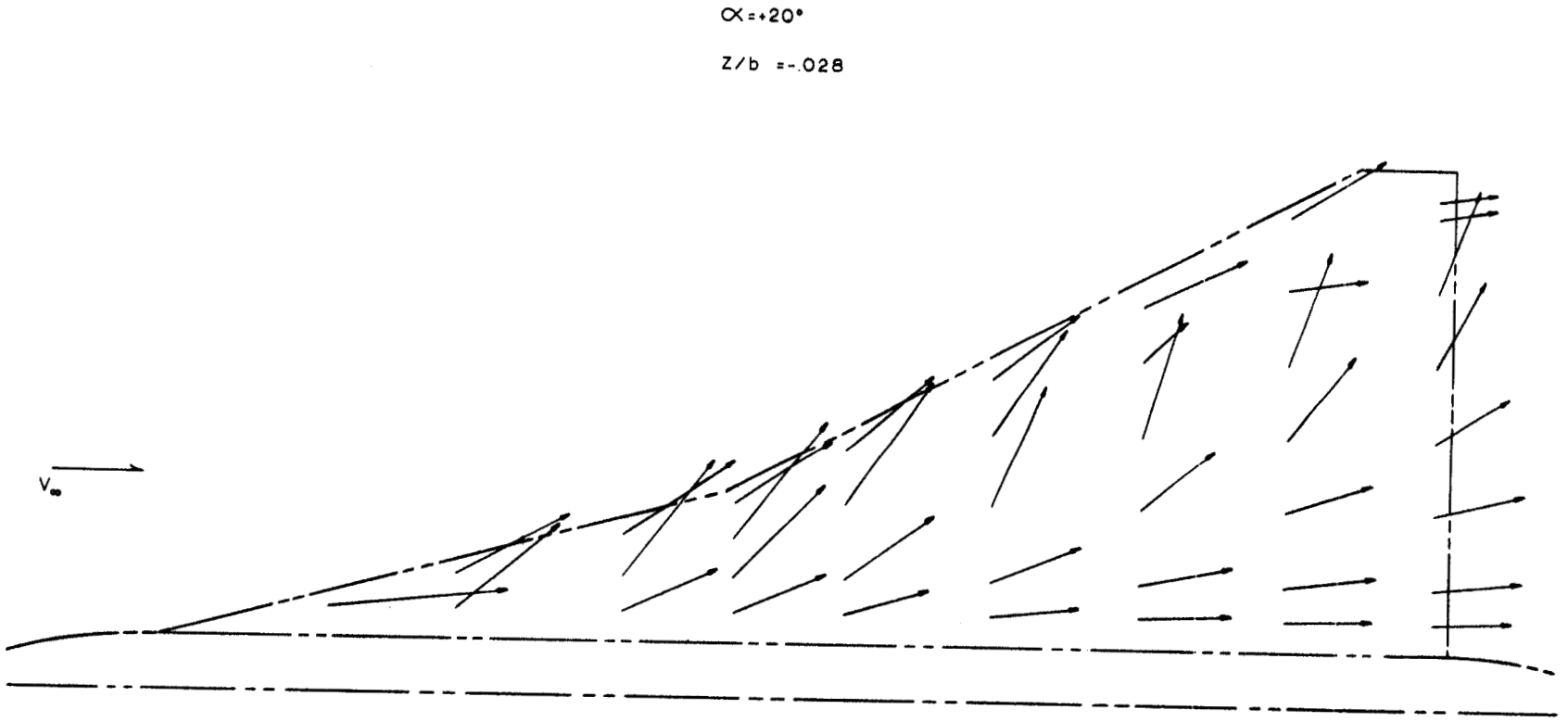

Figure 14g.- Upper surface flow field. $\alpha = +20^{\circ}$; $z/b = -0.028$.

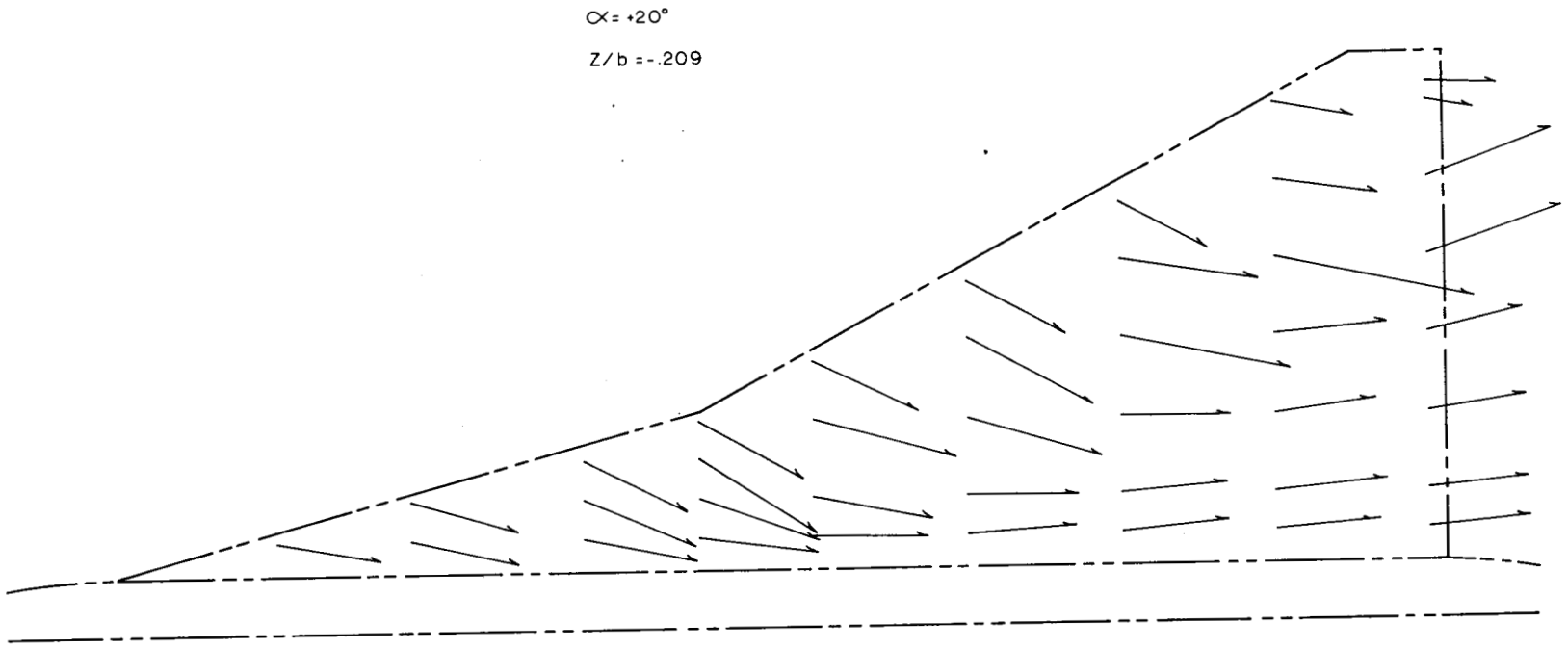

Figure 14h.- Upper surface flow field. $\alpha = 20^{\circ}$; $z/b = -0.209$.

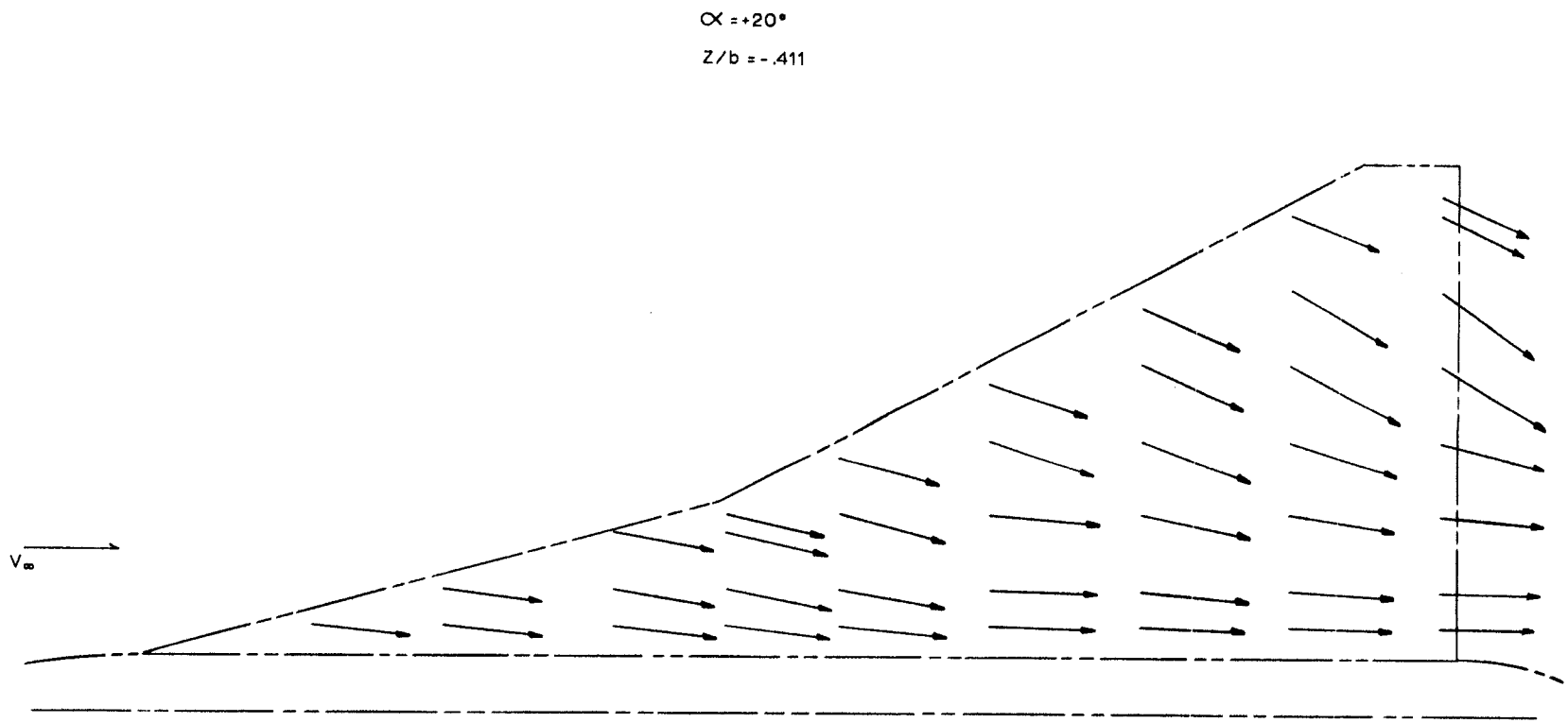

Figure 141.- Upper surface flow field. $\alpha = +20^{\circ}$; $z/b = -0.411$.

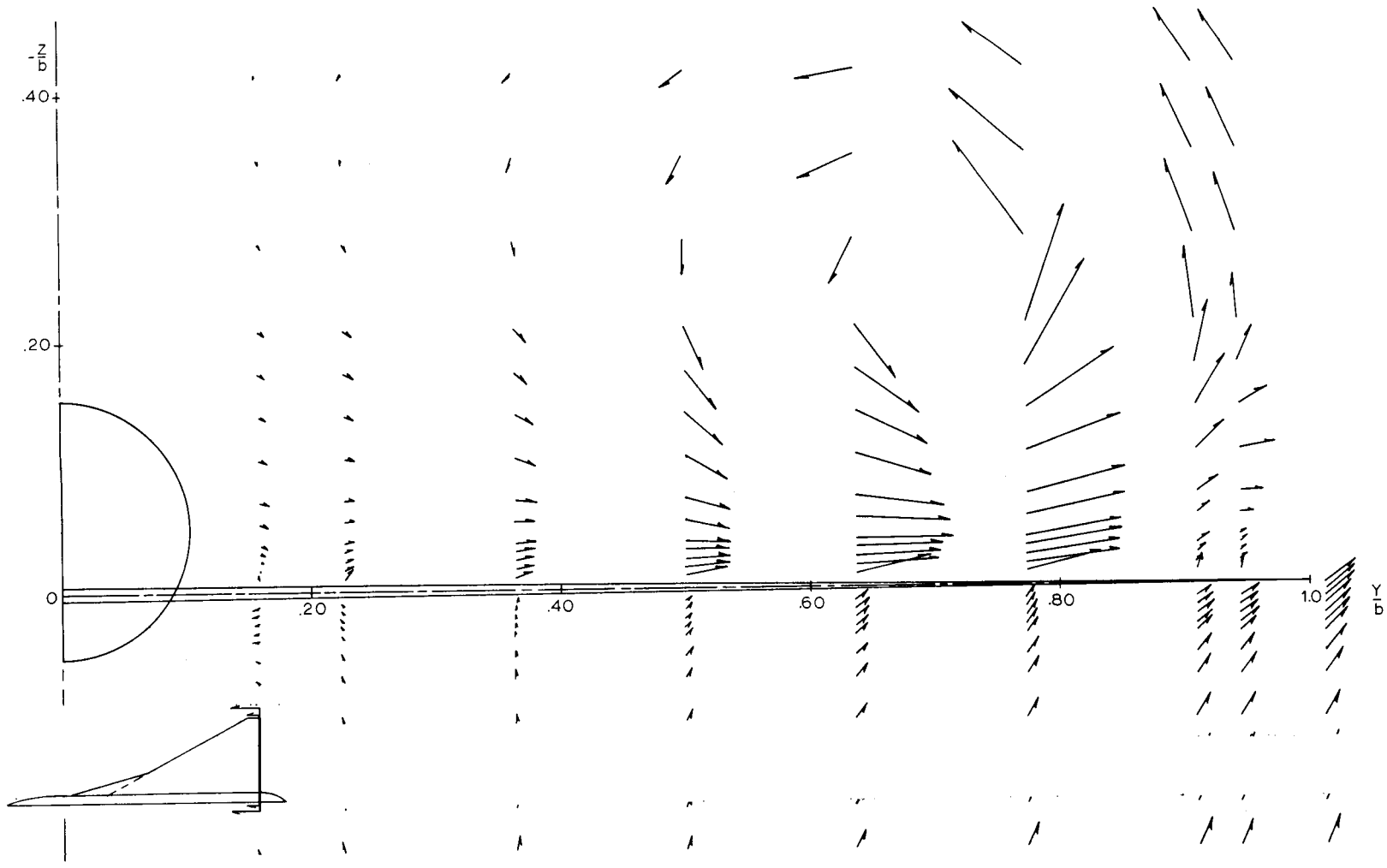

Figure 15.- Upper and lower surface flow field. $\alpha = +20^{\circ}$; x/b = 0.027 (upper surface); x/b = 0.015 (lower surface).

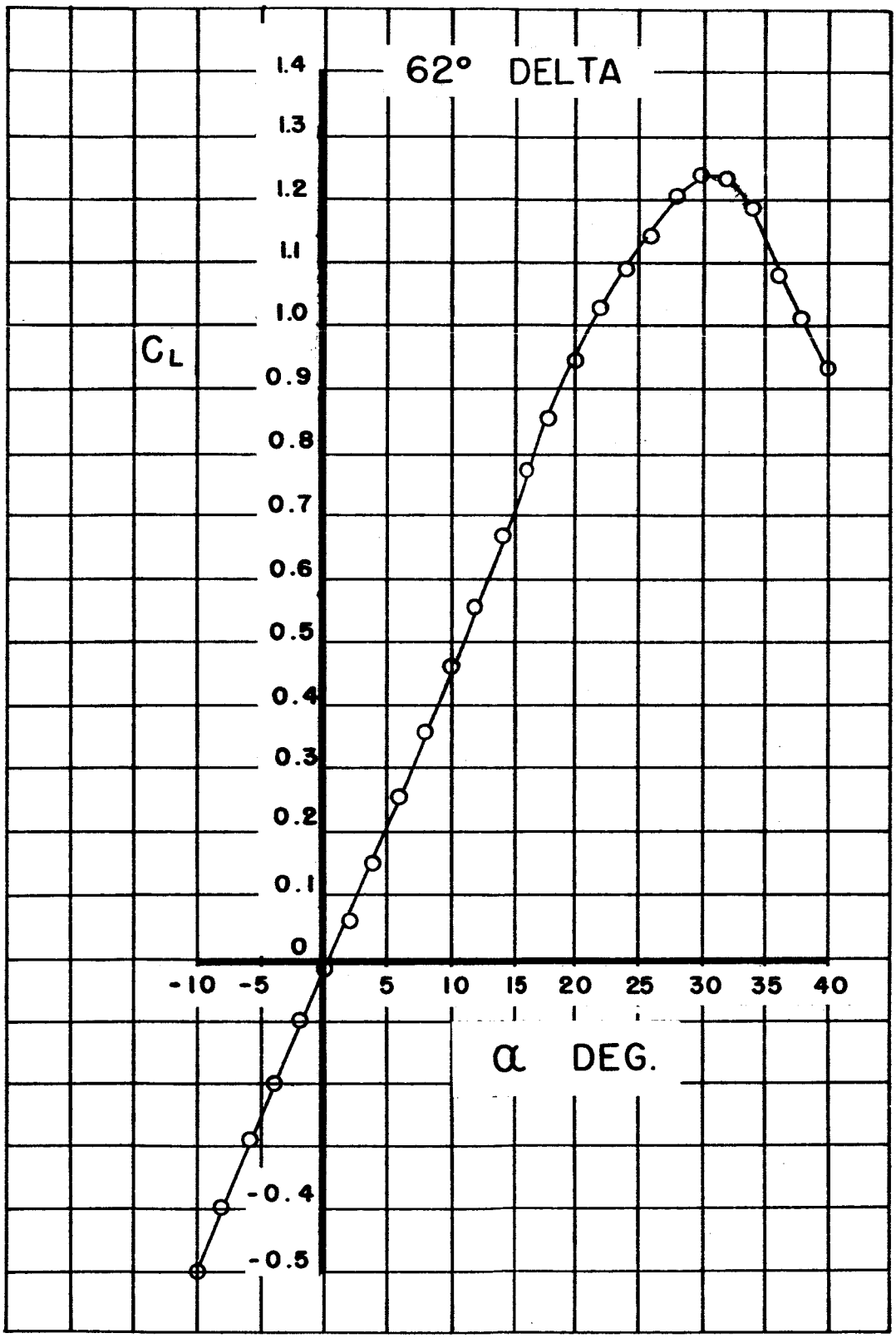

Figure 16a.- C_L vs alpha 62^o delta wing.

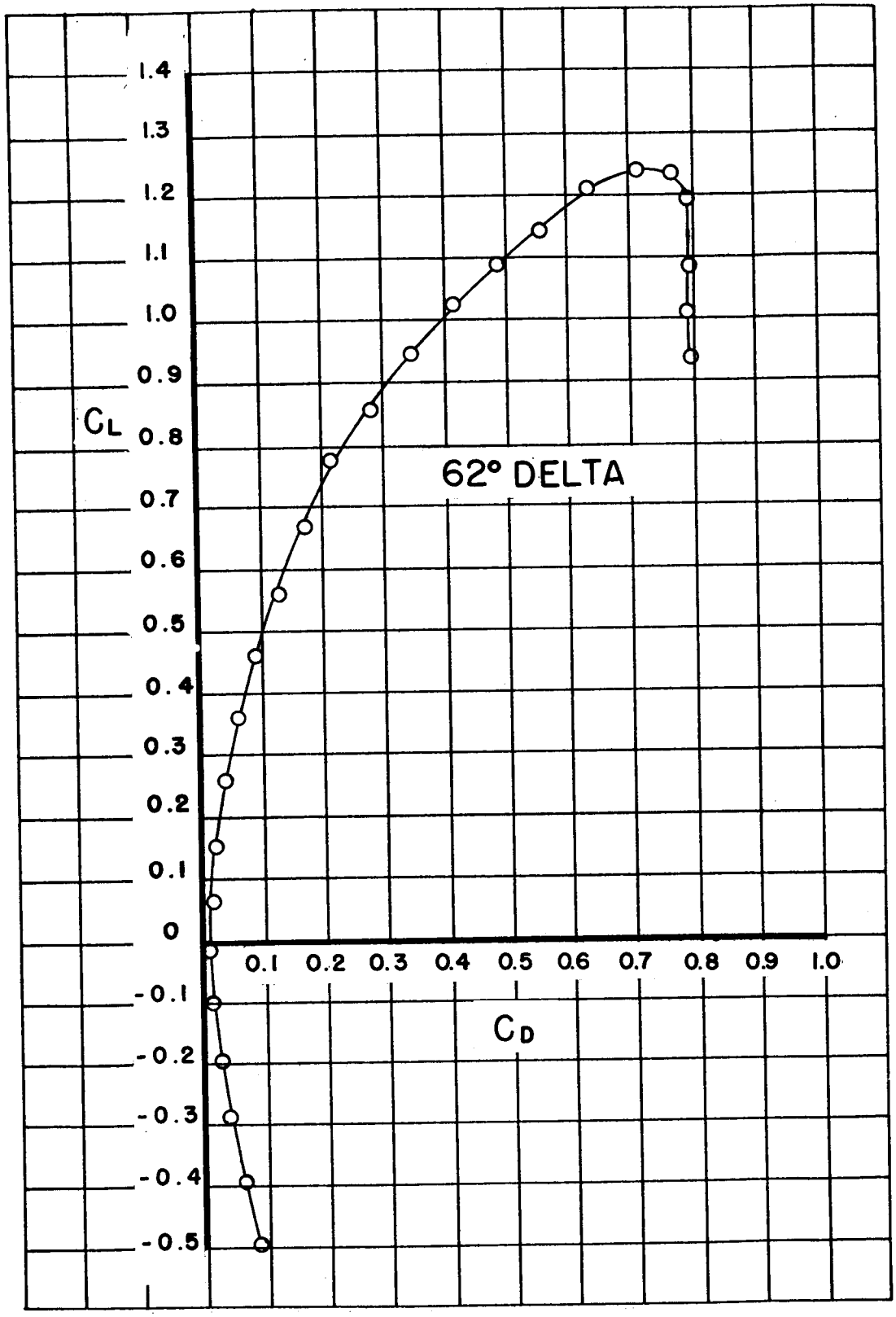

Figure 16b.- C_L vs C_D 62° delta wing.

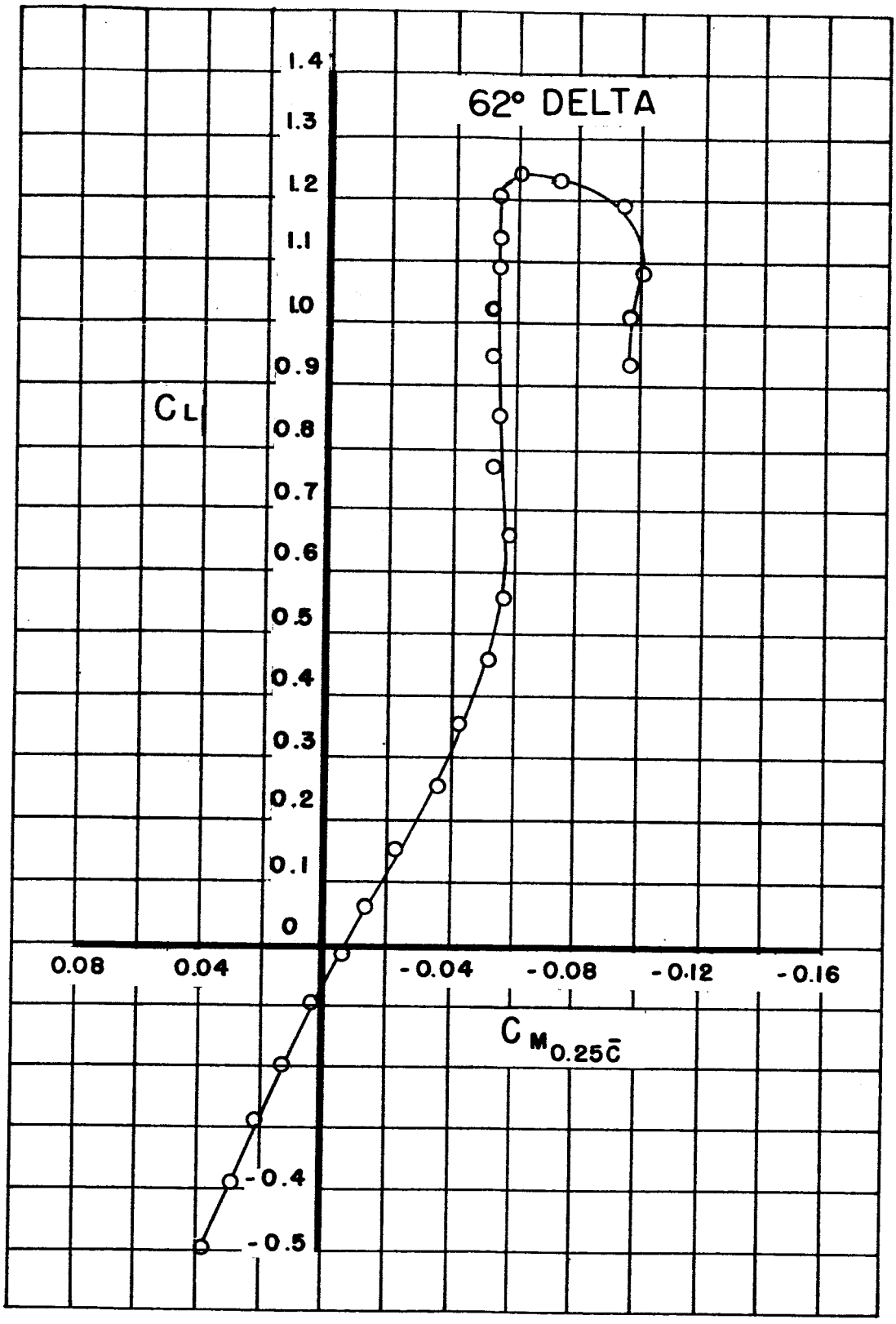

Figure 16c.- C_L vs C_M 62° delta wing.

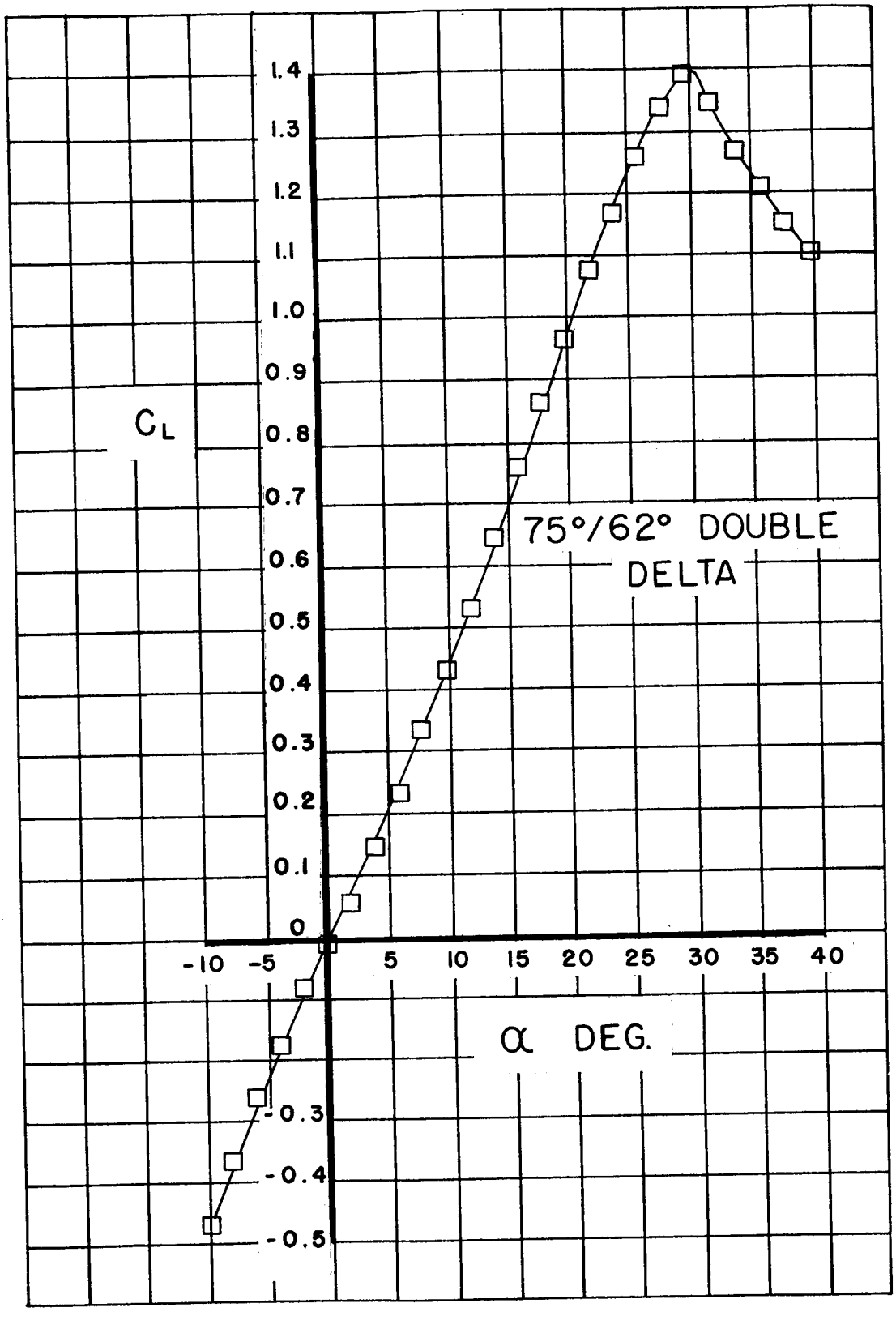

Figure 17a.- C_L vs alpha 75°/62° double-delta wing.

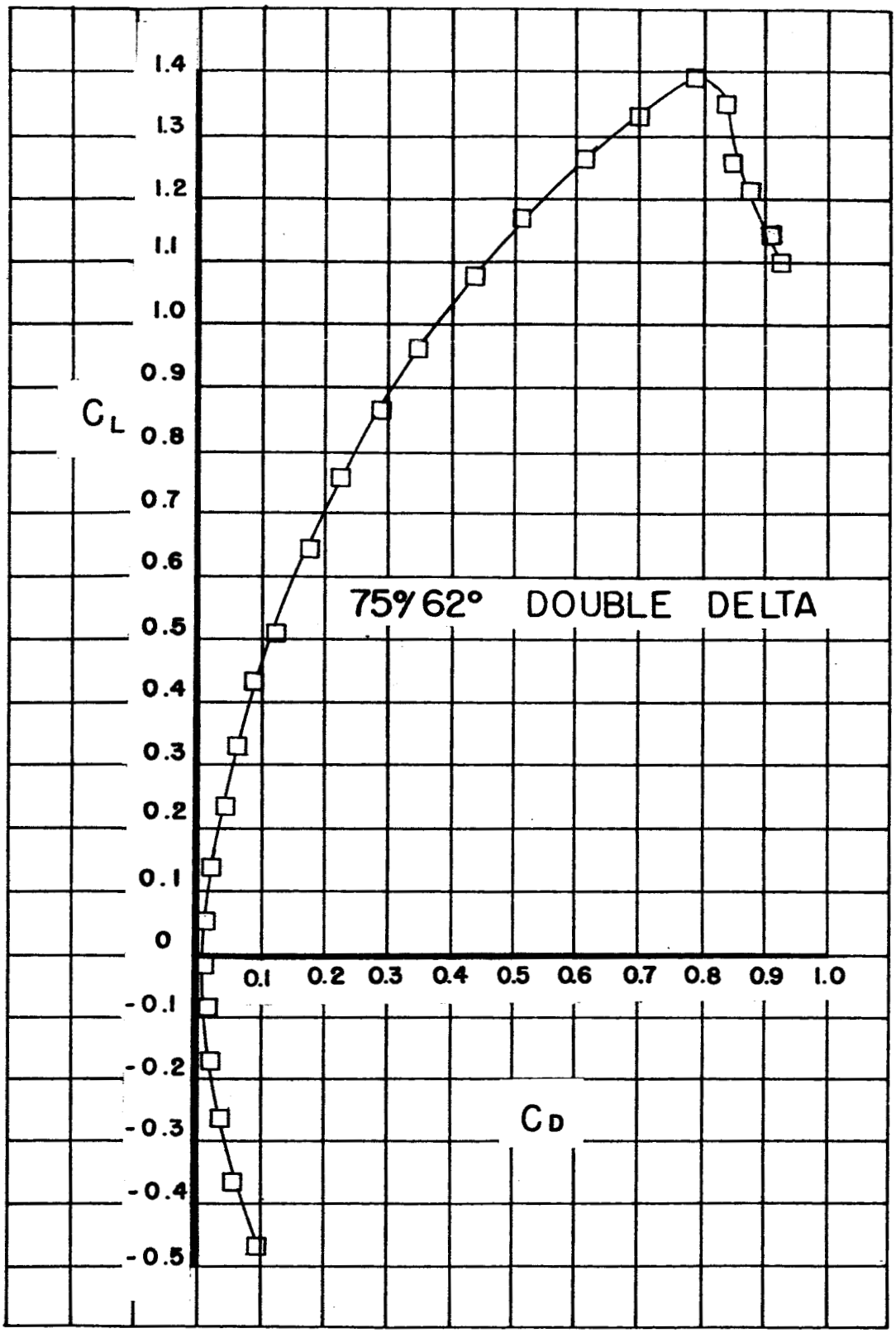

Figure 17b.- C_L vs C_D $75^\circ/62^\circ$ double-delta wing.

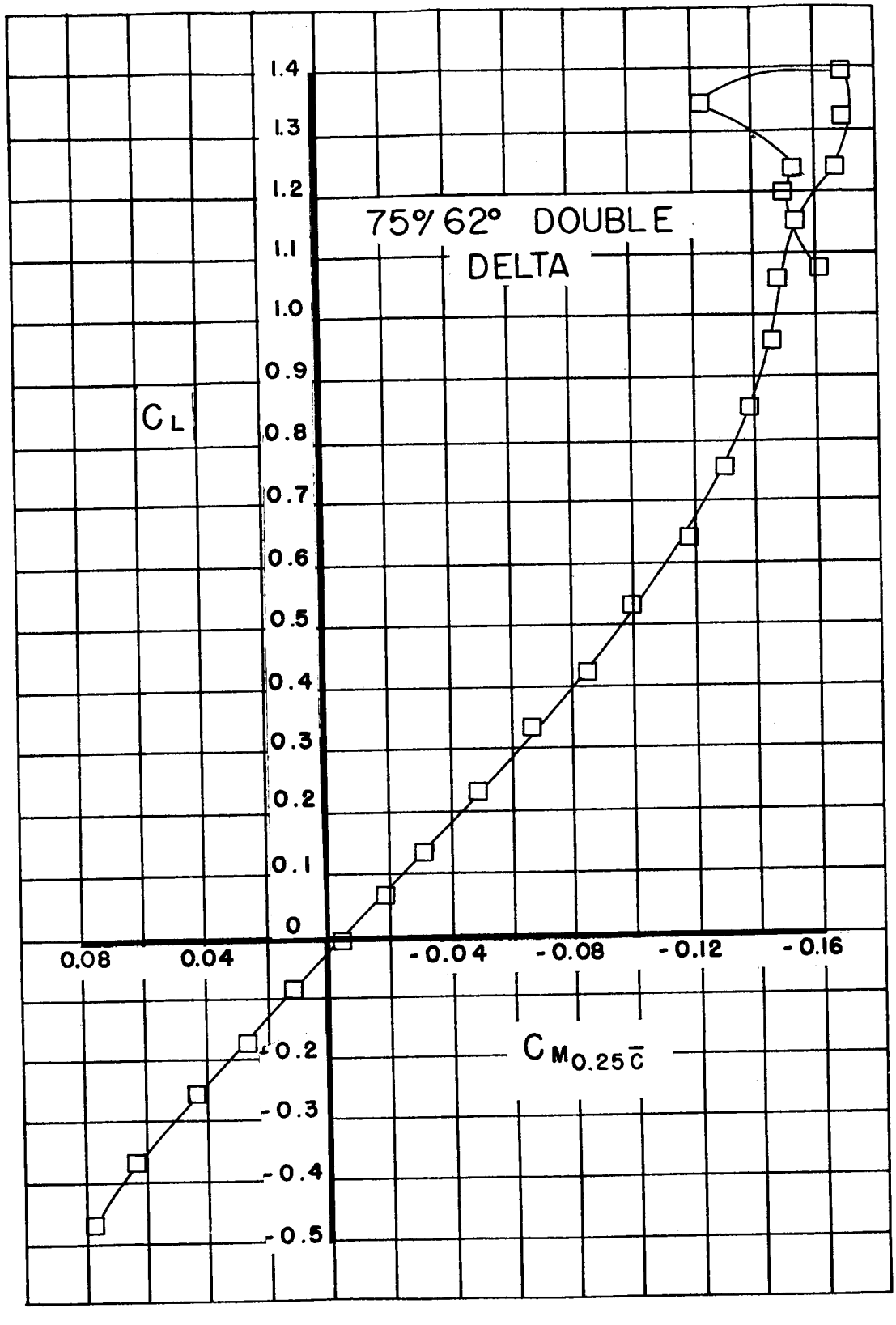

Figure 17c.- C_L vs C_M 75°/62° double-delta wing.

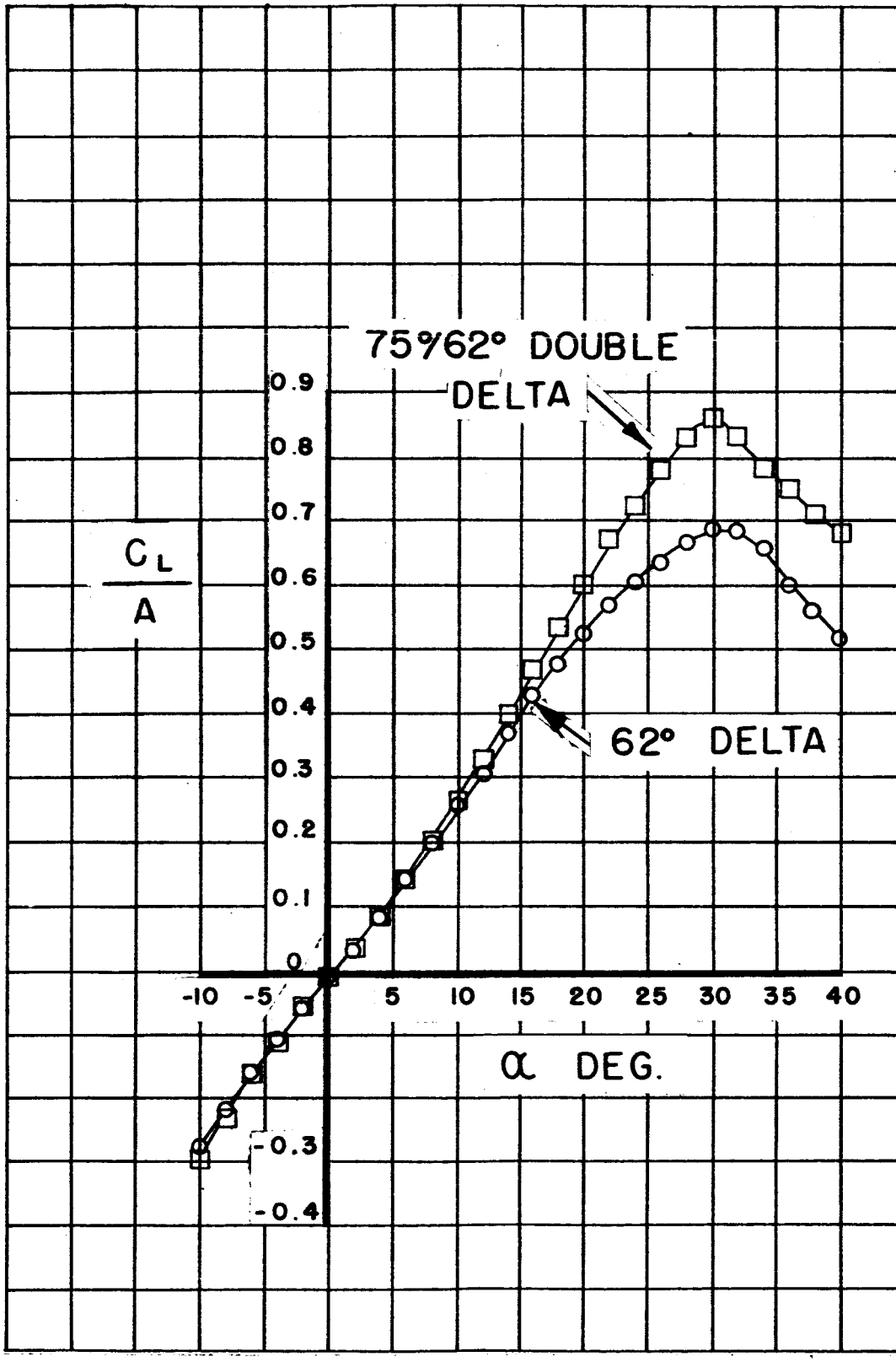

Figure 18a.- C_L/A vs alpha 62° delta wing and 75°/62° double-delta wing.

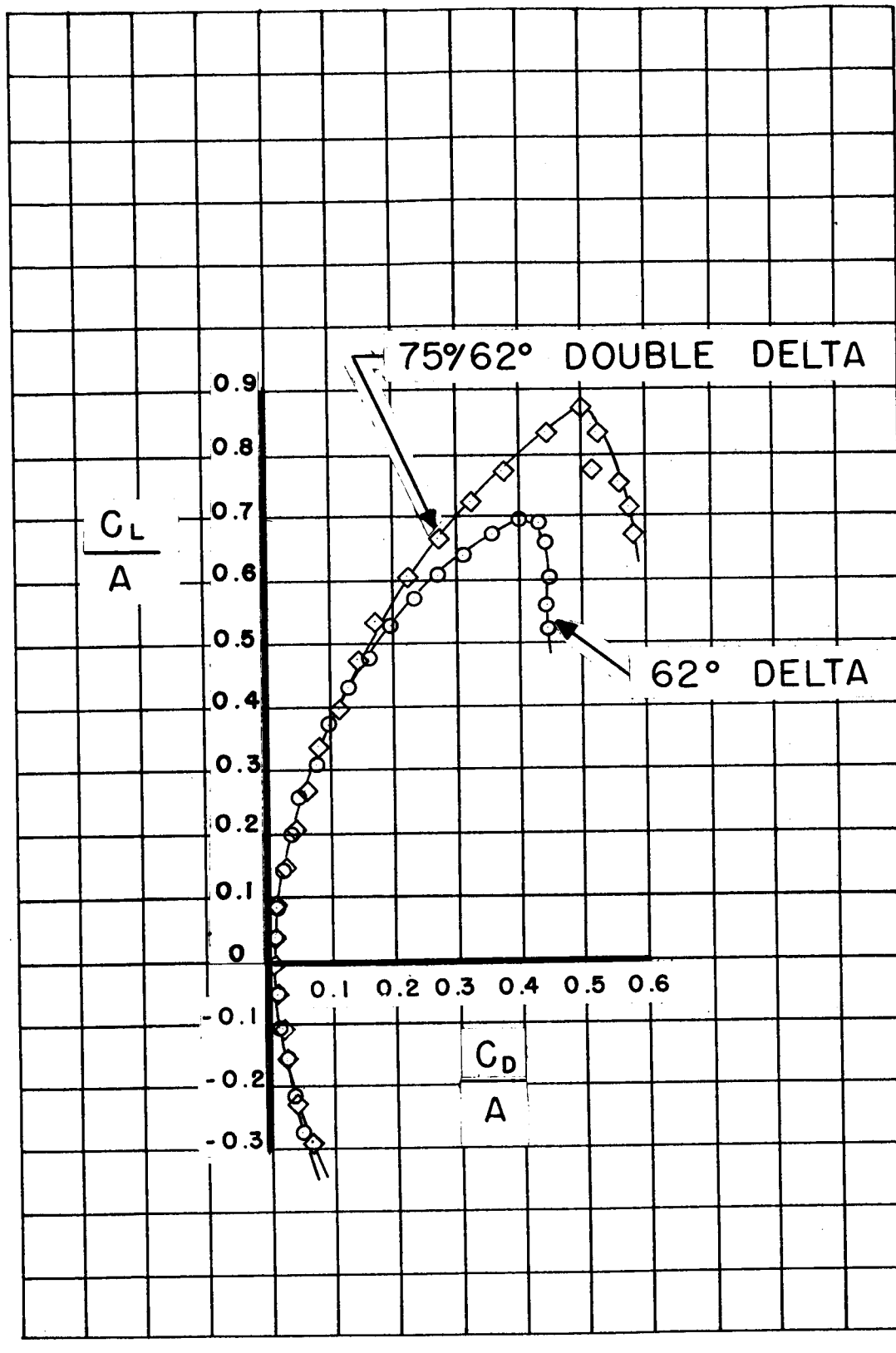

Figure 18b.- C_L/A vs C_D/A 62° delta wing and 75°/62° double-delta wing.

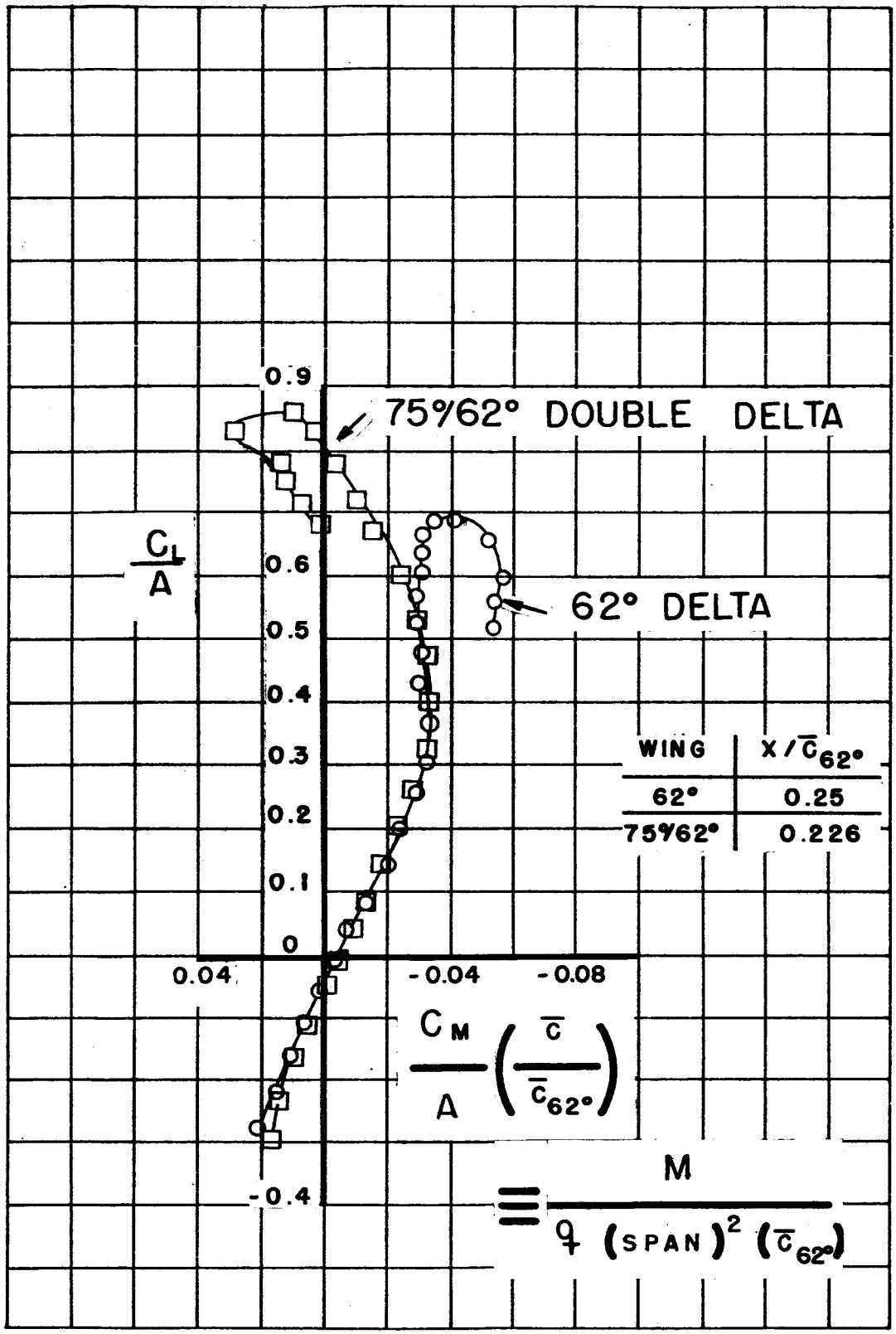

Figure 18c:- C_L/A vs $(C_M/A)\left(\bar{c}/\bar{c}_{62^\circ}\right)$ 62° delta and double-delta wings.

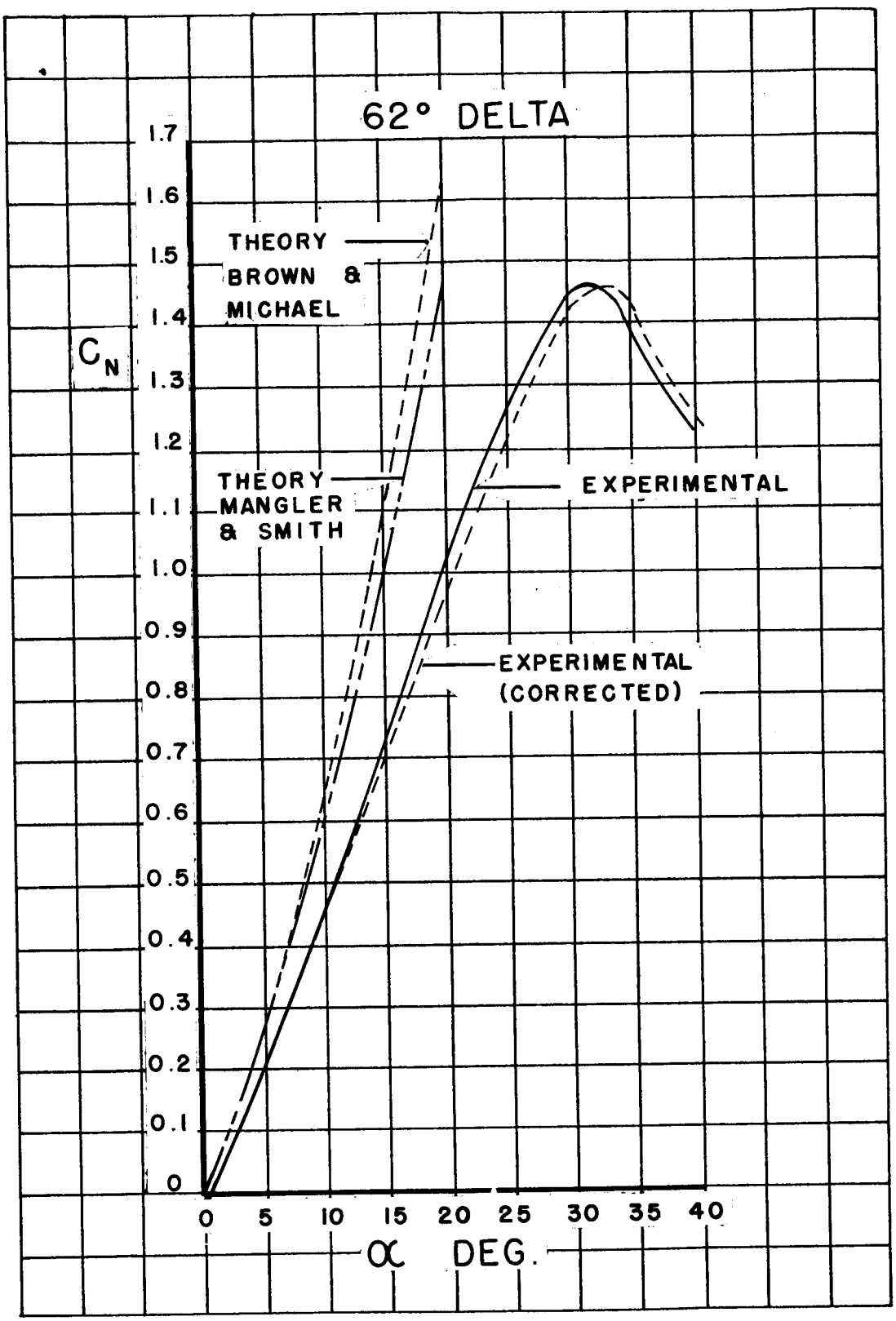

Figure 19a.- C_N vs alpha 62° delta wing.

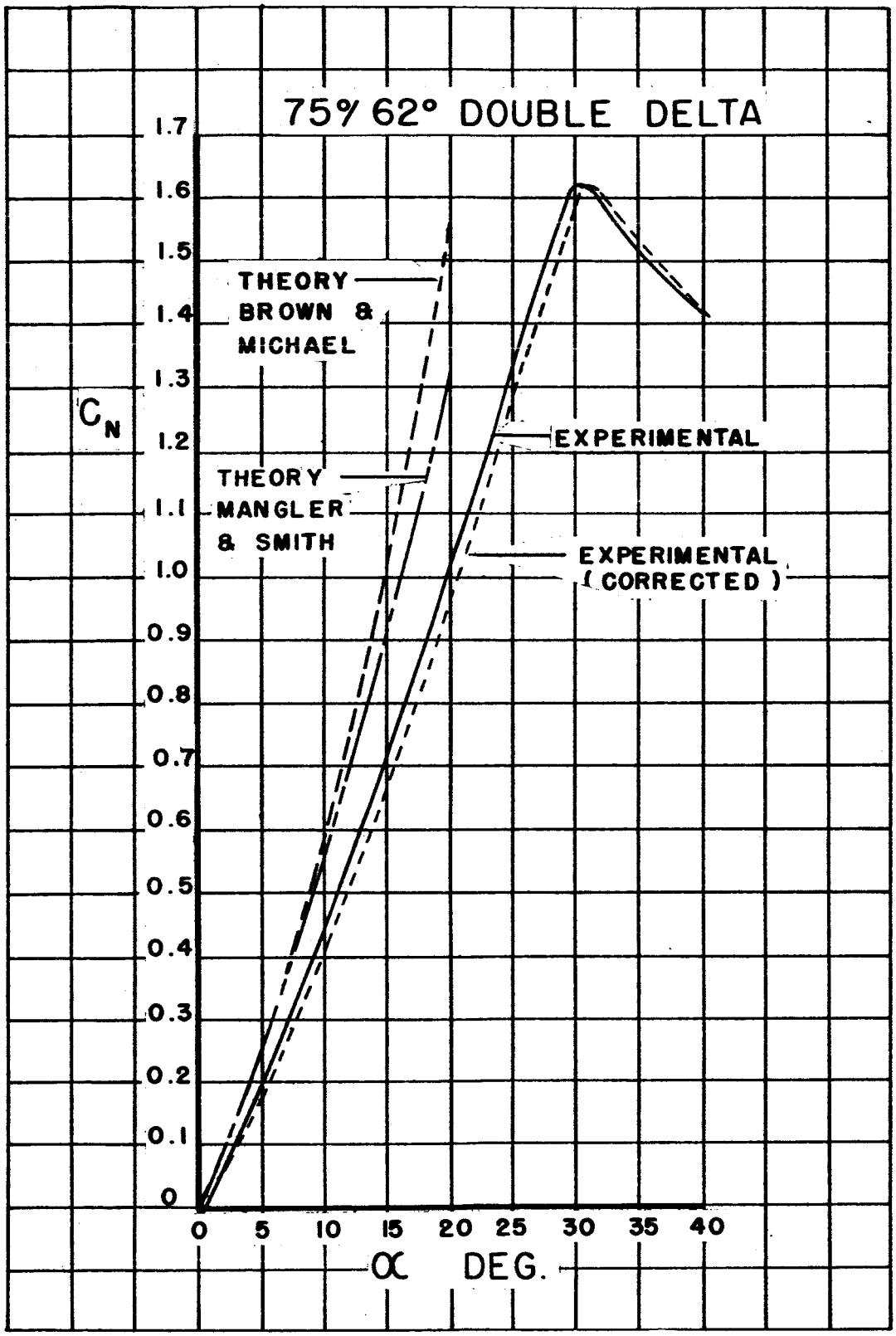

Figure 19b.- C_N vs alpha $75^\circ/62^\circ$ double-delta wing.

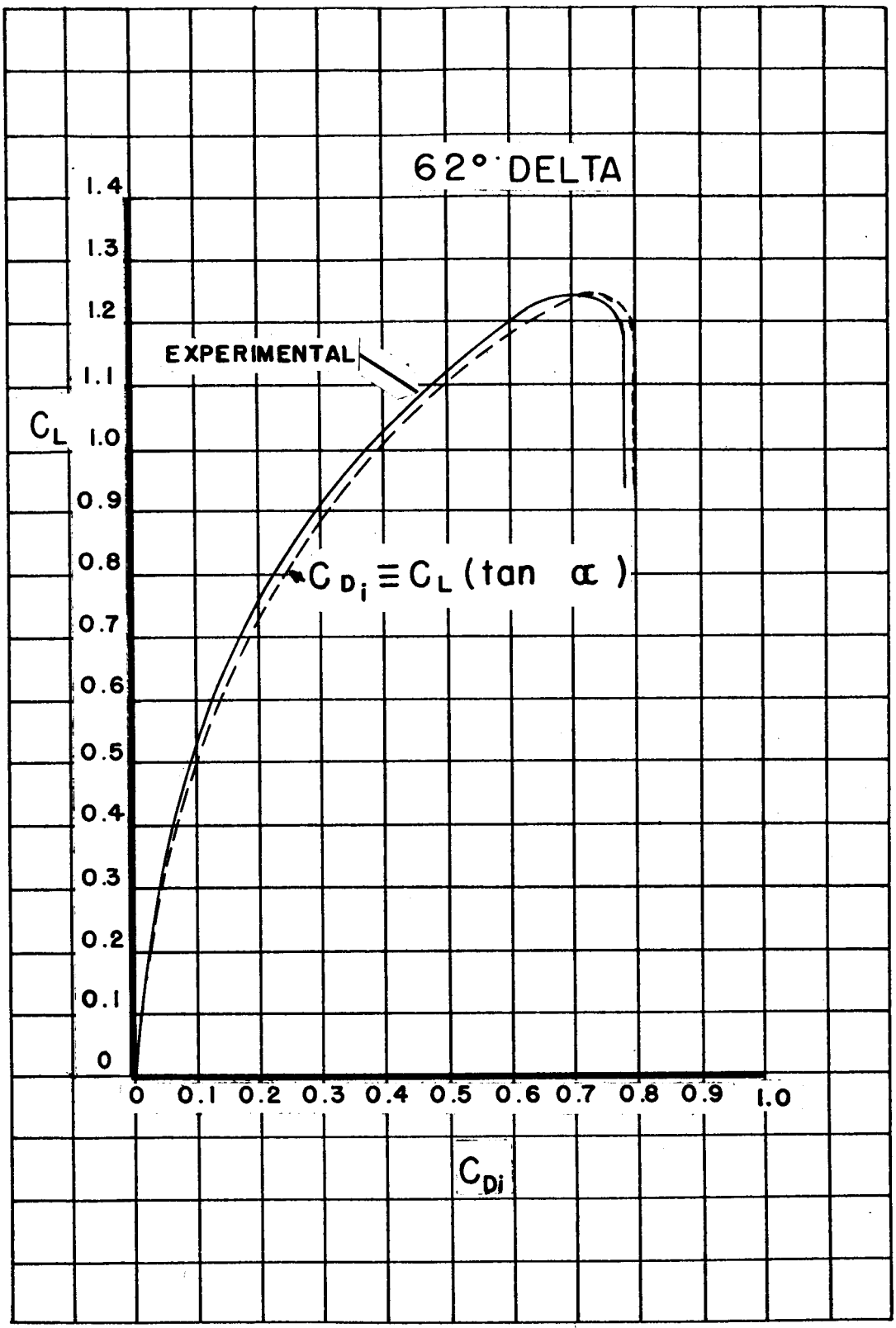

Figure 20a.- C_L vs C_{Di} 62° delta wing.

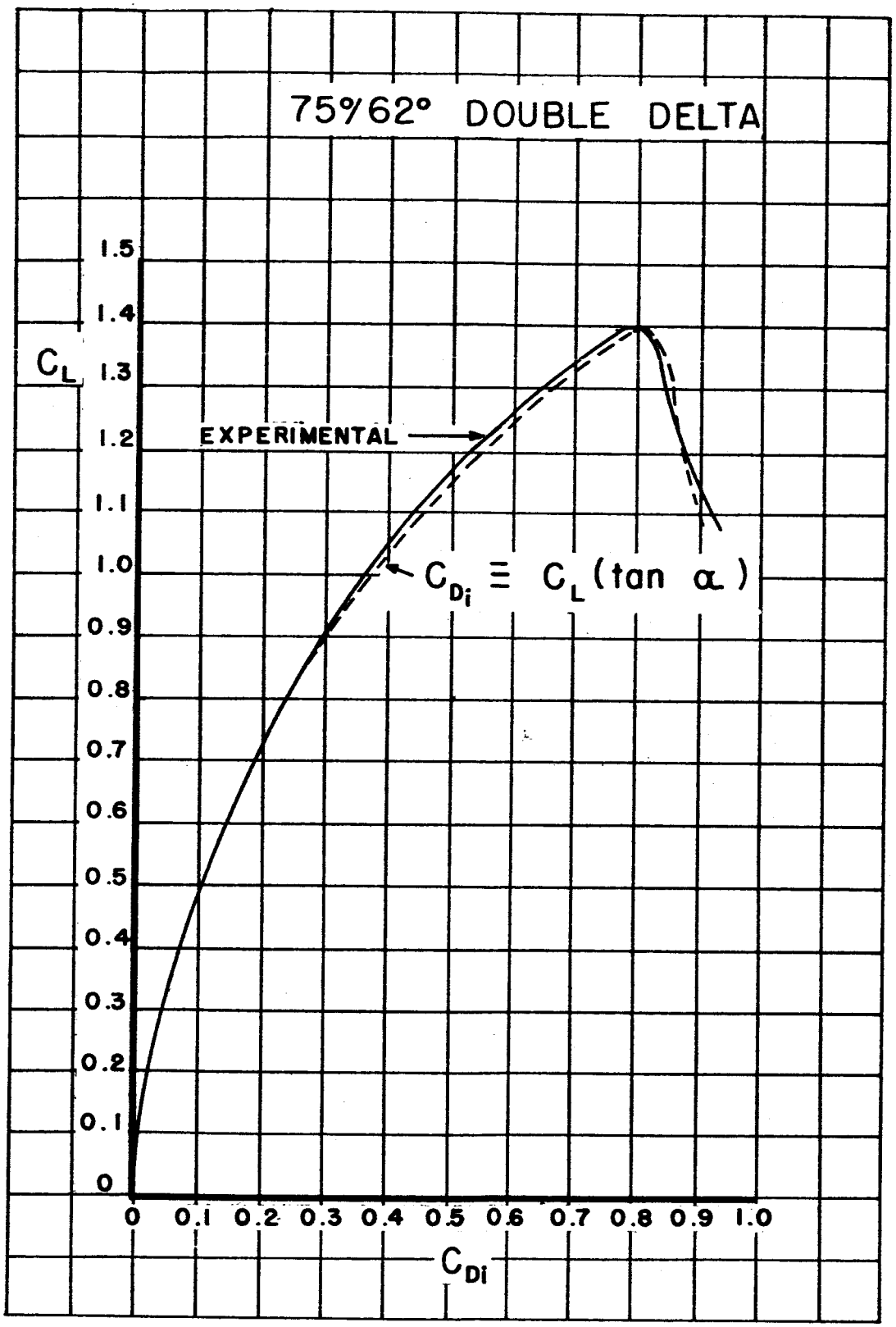

Figure 20b.- C_L vs C_{Di} $75^\circ/62^\circ$ double-delta wing.

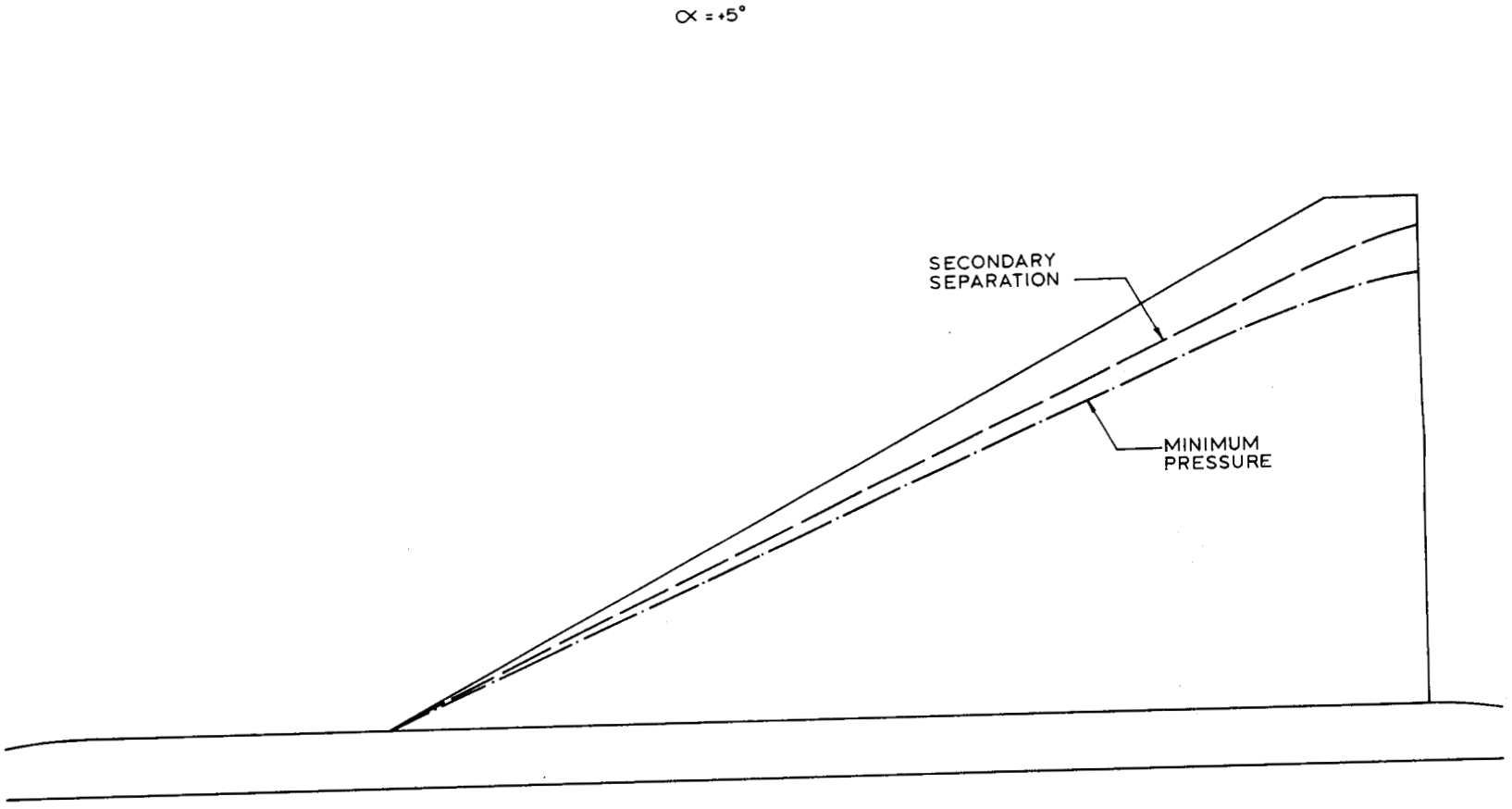

Figure 21a.- Correlation of streak patterns and pressure distribution. $\alpha = +5^{\circ}$.

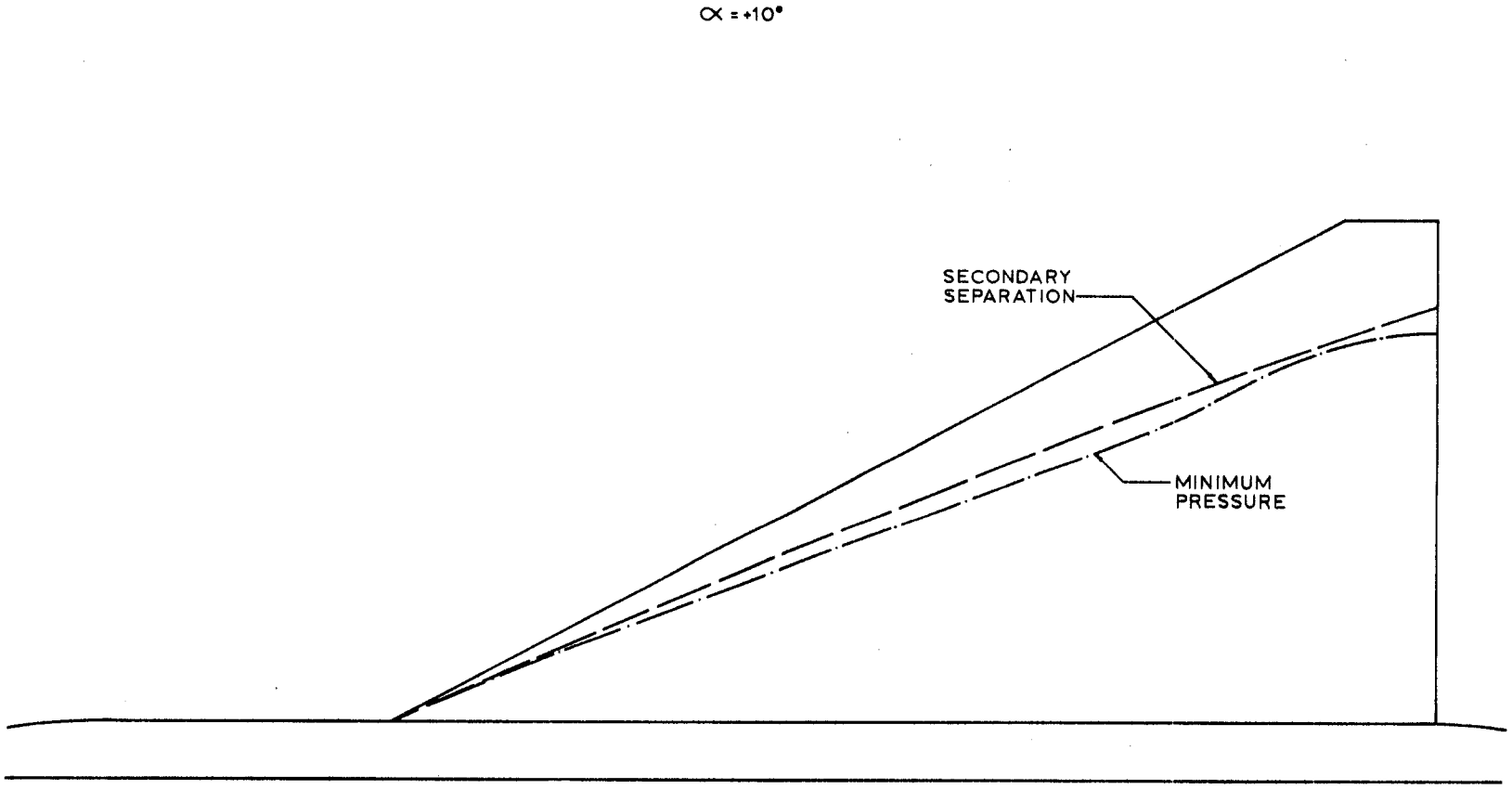

Figure 21b.- Correlation of streak patterns and pressure distribution. $\alpha = +10^{\circ}$.

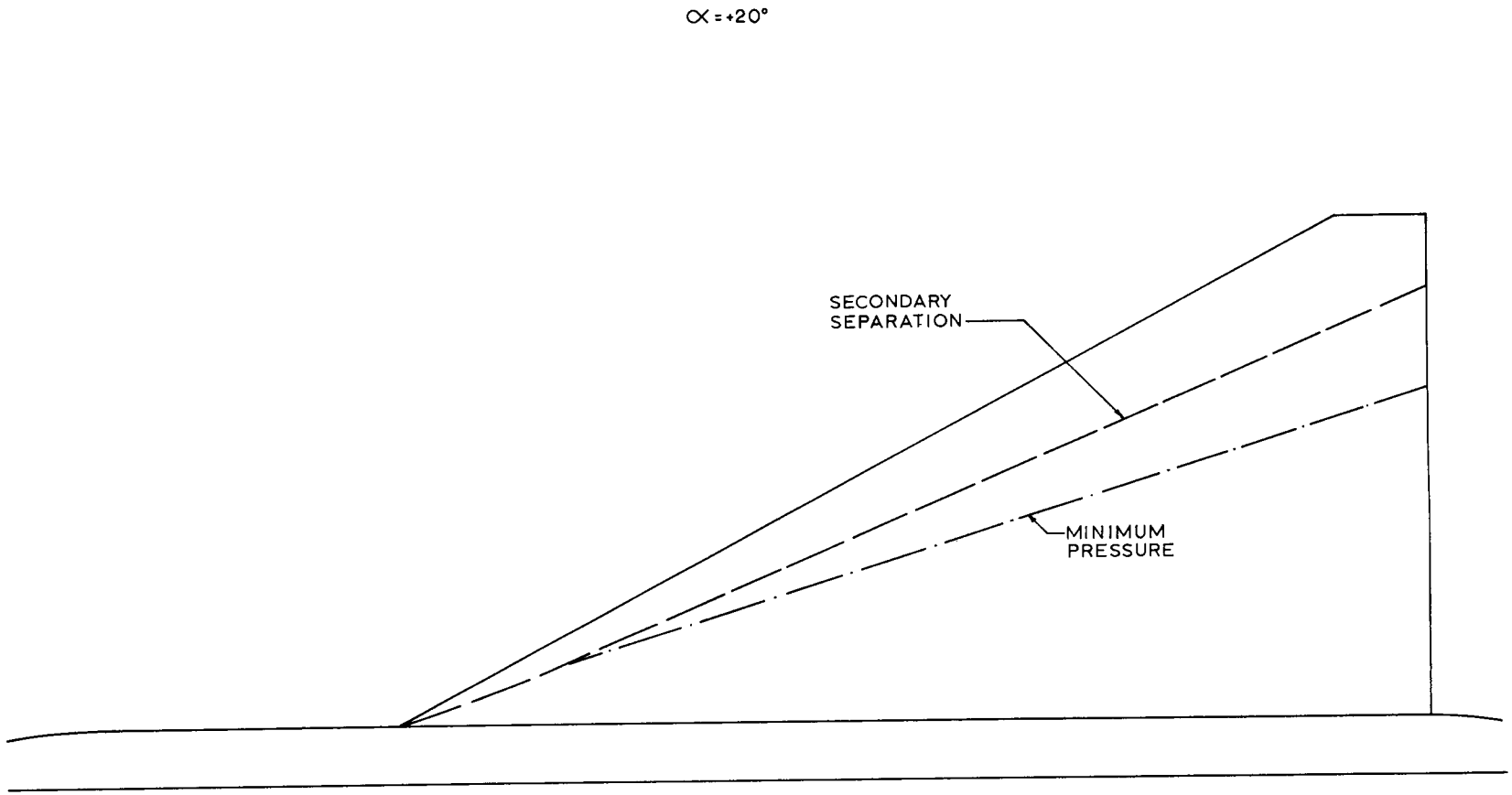

Figure 21c.- Correlation of streak patterns and pressure distribution. $\alpha = +20^{\circ}$.

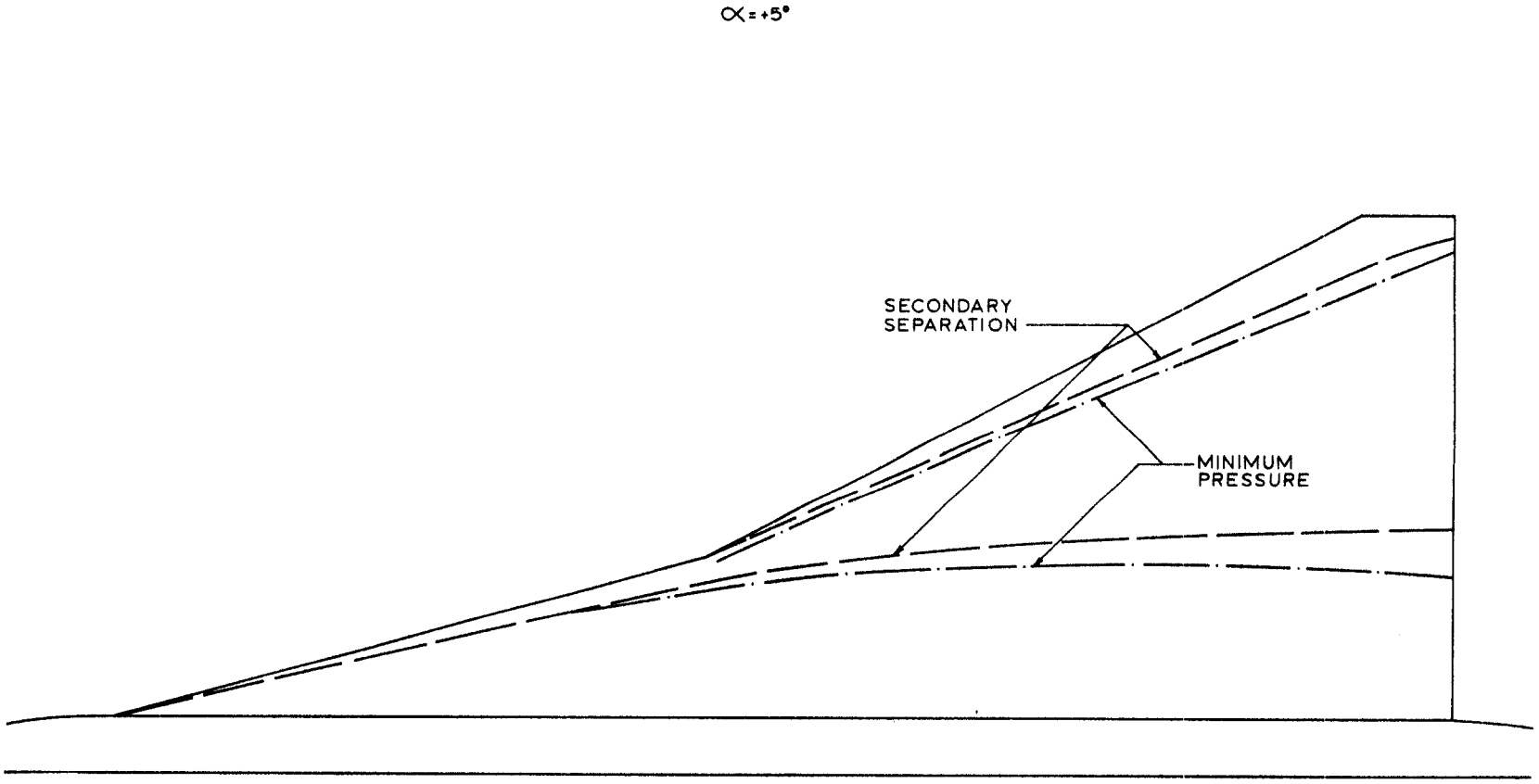

Figure 22a.- Correlation of streak patterns and pressure distribution. $\alpha = +5^{\circ}$.

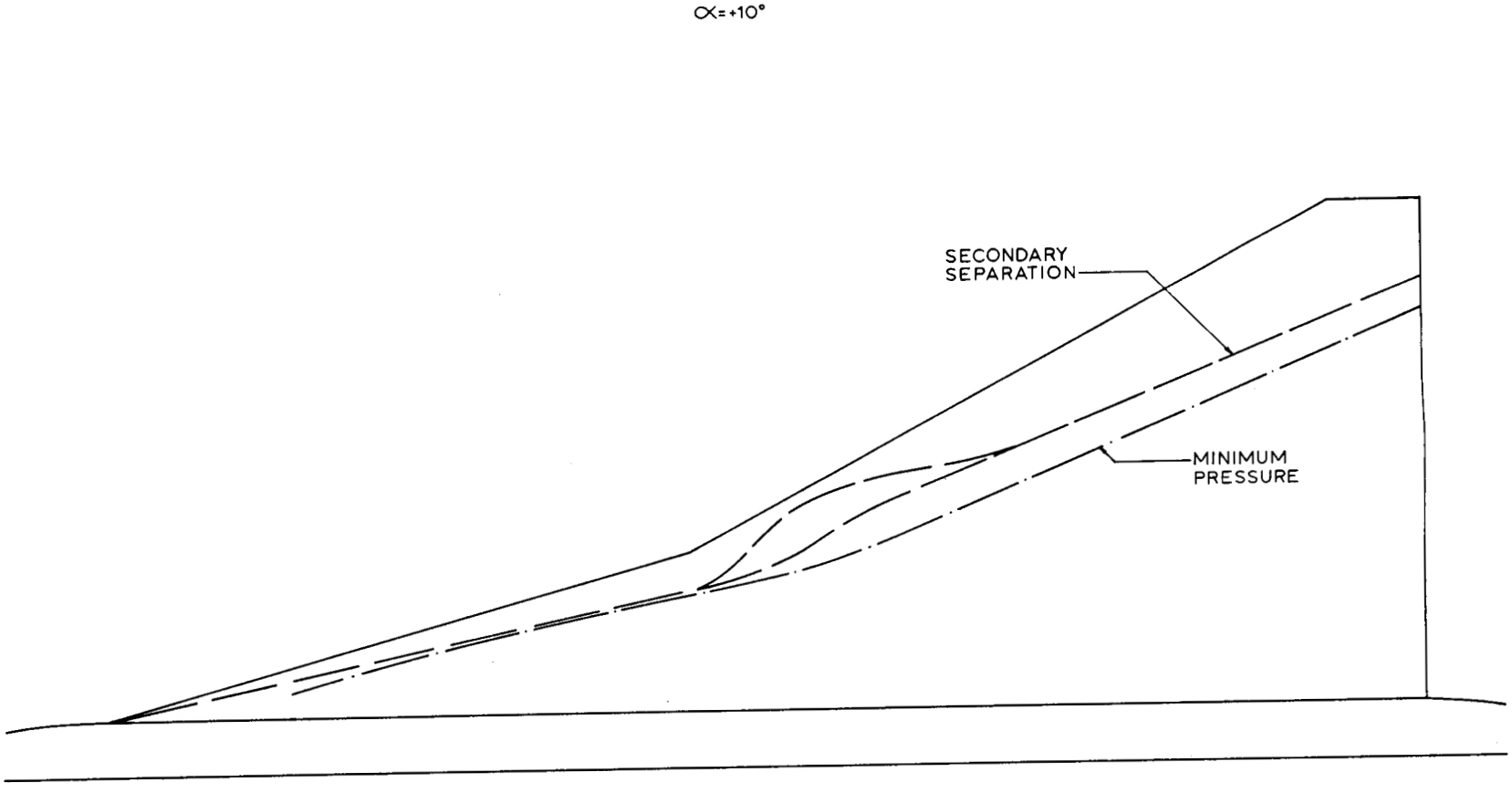

Figure 22b.- Correlation of streak patterns and pressure distribution. $\alpha = +10^{o}$.

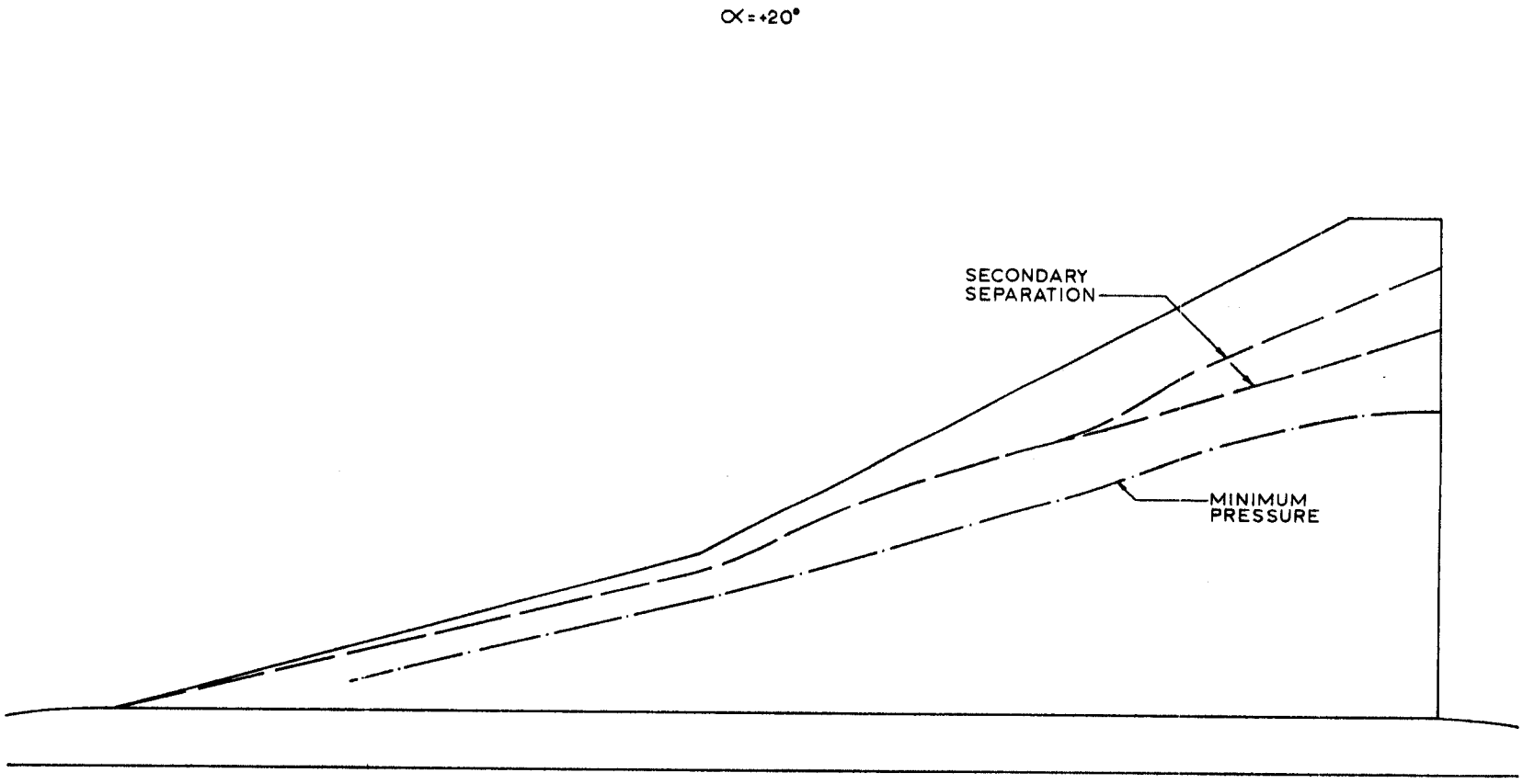

Figure 22c.- Correlation of streak patterns and pressure distribution. $\alpha = +20^{\circ}$.